DEVELOPMENT OF NANOFLUIDIC DEVICES FOR SINGLE-MOLECULE DNA DIAGNOSTICS

Franklin Ifeanyichukwu Uba

A dissertation submitted to the faculty at the University of North Carolina at Chapel Hill in partial fulfillment of the requirements for the degree of Doctor of Philosophy in the department of Chemistry in the school of Arts and Sciences.

Chapel Hill
2014

Approved by:

Steven A. Soper

James W. Jorgenson

Royce W. Murray

Valarie S. Ashby

Anne M. Taylor

Matthew R. Lockett

ABSTRACT

Franklin Ifeanyichukwu Uba: Development of Nanofluidic Devices for
Single-Molecule DNA Diagnostics
(Under the direction of Steven Soper)

Fluidic devices that possess structures less than 150 nm in one or two dimensions are generating great interest due to the unique properties afforded by this size domain not accessible at the microscale. As molecules travel through nanochannels, they undergo hydrophobic and van der Waals interactions with the channel walls at a degree that depends on the size of the channel, the surface chemistry of the wall and the debye length (governed by the ionic strength of the electrolyte solution). In this work, we report the fabrication of nanometer sized structures (nanoslits, nanochannels and nanoelectrodes) in thermoplastic and fused silica substrates for the analysis of dsNA.

In the case of thermoplastics, mixed-scale micro- and nanofluidic networks were fabricated using a simple, high resolution, single-step thermal embossing process and the fluidic structures were enclosed via low temperature fusion bonding to a cover plate. Nanochannels were chemically modified and the associated electrokinetic parameters – surface charge density, zeta potential and electroosmotic flow – were evaluated. In the fused silica substrate, we developed an integrated nanosensing device comprising of a single nanochannel and two pairs of transverse electron-conducting (~50 × 50 nm) nanoelectrodes separated by a nanometer gap (nanogap) and poised at the input and output ends of the nanochannel. This device serves a foundation for a novel technique we developing for the sequencing of DNA molecule by measuring the transit time of the monomer units entering and exiting a nanochannel (5 to 50 nanochannels) after being clipped from a single polymer digested with an enzyme. Further

experiments on single molecule electrophoresis will provide information on possible routes that can be adopted to engineer proper nanochannel wall chemistry for the enhancement or reduction of solute/wall interactions.

To God be the glory great things He has done

I dedicate this work to my lovely wife, parents and siblings for their support and prayers

ACKNOWLEDGEMENTS

I would like to express my sincere gratitude to my advisor, Professor Steven Allan Soper for his unwavering support and encouragement throughout this research work. He is the best mentor any student could ask for and his unwavering assistance has made this work a success. I am also grateful to the members of my dissertation committee, Professor James Jorgenson, Professor Royce Murray, Professor Valarie Ashby, Prof. Anne Taylor and Prof. Matthew Lockett for their time, support and insightful contributions towards the realization of my degree.

I would also like to thank Prof. Yoon-kyoung Cho and Prof. Heungjoo Shin for the invitation to embark some aspects of this research work in conjunction with the World Class University (WCU) program at Ulsan National Institute of Science and Technology. I also thank Mr. Dong-kyu Park of UNIST, Dr. Amar Kumbhar, Dr. Carrie Donley of CHANL and Dr Jennifer Marks of the Olympus research center for their assistance.

I also appreciate past and current members of the Soper research group, most importantly Dr. Rattikkan Chantiwas, Dr. Jiahao Wu, Dr. Nyote Calixte, Dr. Matt Hupert, Dr. Maggie Witek and Dr. Hong Wang and colleagues (Kumuditha Ratnayake, Bo Hu, Matt Jackson and Colleen O'Neil) for their helpful contributions. You guys are awesome!!

Thank you all.

TABLE OF CONTENTS

LIST OF TABLES

LIST OF FIGURES

LIST OF SCHEMES

LIST OF ABBREVIATIONS

AC	Alternating Current
B	Bandwidth (Hz)
C_{eq}	Equivalent Concentration
C_i	Bulk ionic Concentration of solution (mol/dm^3)
Cyt c	Cytochrome c
DC	Direct current
DL	Diffuse Layer
DLVO	Derjaguin, Landau, Verwey and Overbeek
DNA	Deoxyribonucleic acid
DRIE	Deep Reactive Ion Etching
D_u	Dukhin number
E	Electric Field strength (volts per centimeter or V/cm)
EDL	Electric Double Layer
EDTA	Ethylene Diamine Tetra Aceticacid
EKP	Electrokinetic Phenomena
EOF	Electroosmotic flow
eV	electron Volt (1 eV = 1.6026×10^{-19} J)
F	Faraday's Constant (96,485 C/mol)
F_d	Drag Force (N)
F_e	Electrical force (newton/N)
FIB	Focused Ion Beam
FITC	Fluorescein Isothicyanate

G	Conductance (Ω^{-1} or siemens)
g	Acceleration due to gravity ($9.8ms^{-2}$)
G_B	Conductivity of Buffer
I	Ionic strength of electrolytes
$I_{cond,\ bulk}$	Conduction Current from Bulk solution conductivity (A)
$I_{cond,\ surf}$	Conduction Current from Surface conductivity (A)
I_t	Tunneling Current
k_B	Boltzmann constant (1.38×10^{-23} JK^{-1})
l_p	Persistence length (nm)
L_{cont}	Contour length
m	Mass of electron ($9.10938188 \times 10^{-31}$ kg)
N_A (mol^{-1})	Avogadro's number of molecules /ions (6.02214×10^{23})
PDMS	Poly (dimethylsiloxane)
Q	Volume Flow rate (liter per min)
R ($JK^{-1}mol^{-1}$)	Molar Gas constant
RMS	Root-Mean-Square
SL	Stern Layer
T	Kelvin Temperature (Kelvin or K)
TBE	Tris(hydroxymethyl)aminomethane-borate-EDTA
u_i	Effective Ionic Mobility (m^2/sV)
u_i^{∞}	Absolute Ionic mobility
V (volts)	Applied Voltage
v_{eof} ($cm\ s^{-1}$)	Electrophoretic velocity

v_{ep}	Electrophoretic velocity
z_i	Ionic Charge
ΔG	Change in conductivity
Δp (Atm)	Pressure drop
ΔV (volts)	Voltage drop
ε_0	Electrical permittivity of vacuum
ε_e	Electrical Permittivity of a medium
ε_r	Relative dielectric constant
ε_w	Dielectric permittivity of solvent (usually water)
ζ (mV)	Zeta Potential
η	Dynamic Viscosity of solution
κ	Electrical Conductivity (siemens per centimeter or S/cm)
κ_b	Bulk electrolyte conductivity ($\Omega^{-1}m^{-1}$)
κ_d	Debye-Hückel parameter
κ_s	Surface conductivity ($\Omega^{-1}m^{-1}$)
λ_d	Debye Length
μ_{eof}	Electroosmotic flow mobility ($cm^2\ V^{-1}\ s^{-1}$)
μ_{ep}	Electrophoretic mobility ($cm^2\ V^{-1}\ s^{-1}$)
ν_{eof} (cms^{-1})	Electroosmotic Flow Velocity
ρ (Ω cm)	Resistivity at a temperature T
σ (gcm^{-3})	Density
h	Planck's Constant

CHAPTER 1: NANOFLUIDICS FOR BIOPOLYMER ANALYSIS

Introduction

Many fundamental processes in biology, for example, information storage, transcription, translation, gene regulation, mitosis, and cell communication occur in the micrometer to nanometer scale (Doherty, '03; Gilges, '94; Hwang, '08; Shenton, '01). Using micro- and nanofabrication technologies developed for the microelectronics industry, new analytical tools on these length scales have been readily developed for single molecule studies of biomolecules at a size-scale comparable to their intrinsic dimensions.

The miniaturization of analytical devices is an ongoing endeavor with the impetus focused on improving performance in a faster and cheaper fashion. The general benefits of miniaturization are the use of less reagents, parallel analysis, faster operation, and more sensitive detection (Vesel, '12). More interesting are the new qualitative possibilities that include: Single-cell analysis by integration of several biochemical steps into a micro Total Analysis System (μTAS); high-resolution analysis using local light sources and detectors or local electrical detection; and direct manipulation of relevant bio-entities such as proteins, nucleic acids, bio-molecular complexes and organelles (ribosomes and mitochondria) in addition to whole cells.

Lately, Lab-on-a-chip (LOC) systems, which are devices that contain one or more laboratory functions on a single chip, have become popular in the fields of Biology, Chemistry, Physics, Medicine and Biomedical engineering for the analysis of biological and chemical entities. An important component of LOC devices, which involves the manipulation of small amount of fluids in micrometer sized conduits, is microfluidics (Piruska, '05; Tsao, '07; Vesel, '12). Although microfluidics have been useful in several applications involving probing biology

at the single cell level (Beech, '12; Gilges, '94; Hwang, '08), and the separation of biomolecules (Effenhauser, '97; Jönsson, '10) many fundamental biological processes, such as the epigenetic and genetic control of single cells, have been reported to occur at the molecular level (*i.e.,* nano-scale). Hence, the emergence of nanofluidics – the study of fluid flows in structures with at least one dimension approaching the nanometer scale (Reisner, '05; Roy, '10).

While microfluidics have been reserved for flows in channel with dimensions ranging from 100 nm to 100 μm, nanofluidics entails flow in channels with dimensions between 1 and 100 nm (Abgrall, '08). Although, in the past, scientists have studied transport properties on fluids in the nanoscale, it is not until the last several years that this field was coined (Eijkel, '05). The invention and wide availability of many new technological tools like atomic force microscope (AFM) (Pennathur, '07) and scanning tunneling microscope (STM) (Bensimon, '95; Binnig, '82) (both for inspection and creation of nanostructures), electron (Broers, '96) and ion-beam lithographs (Dobisz, '91; Marrian, '92) and the development of new nanomachining techniques like soft lithography (Qin, '10; Whitesides, '05), bottom-up assembly methods (Du, '08) and surface science apparatus (SFA) (Derjaguin, '54) has made the study and application of nanofluidics much more accessible. Fluid conduits with at least one dimension from 1 nm to 100 nm that exist in nature include nanopores in zeolite crystals (Salavati-Niasari, '08) and nuclear membranes of biological cells to larger openings in the silica frustules of diatoms (Mazumder, '10; Yamanaka, '08). Also, molecular dynamic (MD) simulations have become a useful tool for elucidating the molecular discreteness, ion transport and fluid flow within nanochannels (Chen, '08; Li, '10). Figure 1.1 shows a number of classical disciplines where nanofluidics is currently being applied.

A unique feature of nanofluidics is that the relevant length scale is comparable to the range of surface and interfacial forces in liquids, such as electrostatic, van der Waals and steric

interactions. As the dimensions of fluidic channels approach the nanoscale, changes in the dominating forces as well as the physics of the processes for fluid/particle transport becomes more pronounced. These changes, as reported by Gad-el Hak (Conlisk, '05; Gad-el-Hak, '99), arise from an increase in the surface-to-volume ratio as dimensions are scaled down. Consequently, forces resulting from pressure, inertia, viscosity or gravity that usually plays the dominant role in macroscopic flows may become irrelevant in micro/nanofluidic systems while interfacial forces, like surface tension, become immensely dominant. As a result, it becomes difficult to transport materials (like water, ions and particles) in nanoscale systems via pressure driven flow and easier to utilize electrokinetic (EK) transport.

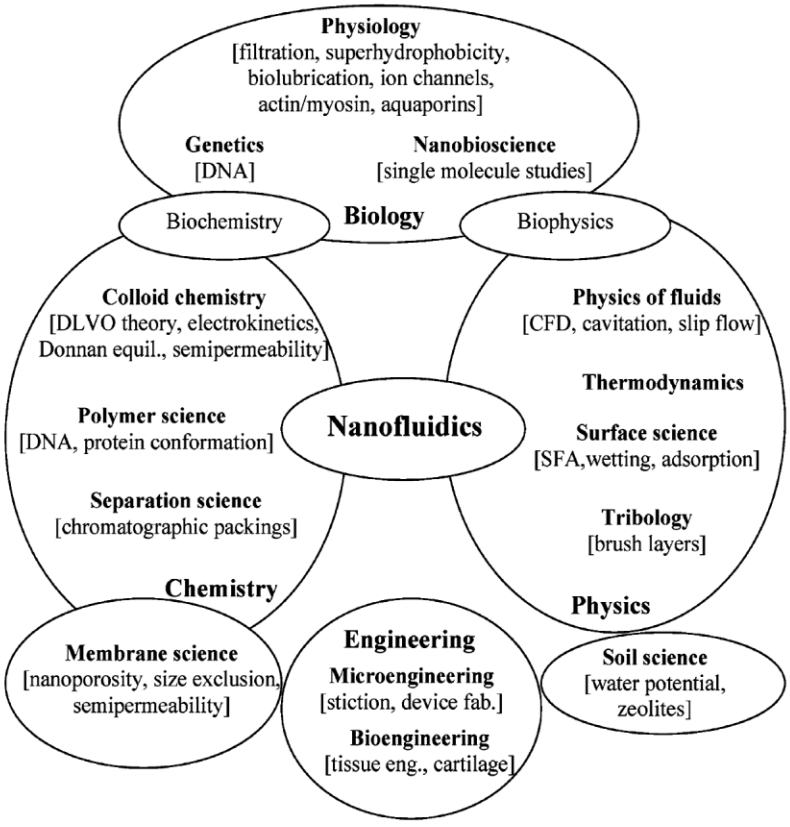

Figure 1.1 Classical disciplines relevant to nanofluidics and the different phenomena. (Reproduced from Eijkel et al., Microfluid. Nanofluid. 2005, 1, 249 – 267)

In 2005, Conlisk (Conlisk, '05) provided a graphical representation showing the pressure drop (Δp) and applied voltage (V) as a function of channel height. As shown in Figure 1.2, as the

height of the channel approaches 10 nm, for a flow-rate of 1 μl/min, the pressure drop increases from 0.006 to 3 atmospheres (~50000%), while the voltage drop increases by ~560% from 0.05 V to 0.33 V. In reality, a relatively bulky pump would be required to deliver this low flow rate at such a huge pressure drop. However, the magnitude of the voltage drop makes the electrokinetic driven flow more practical.

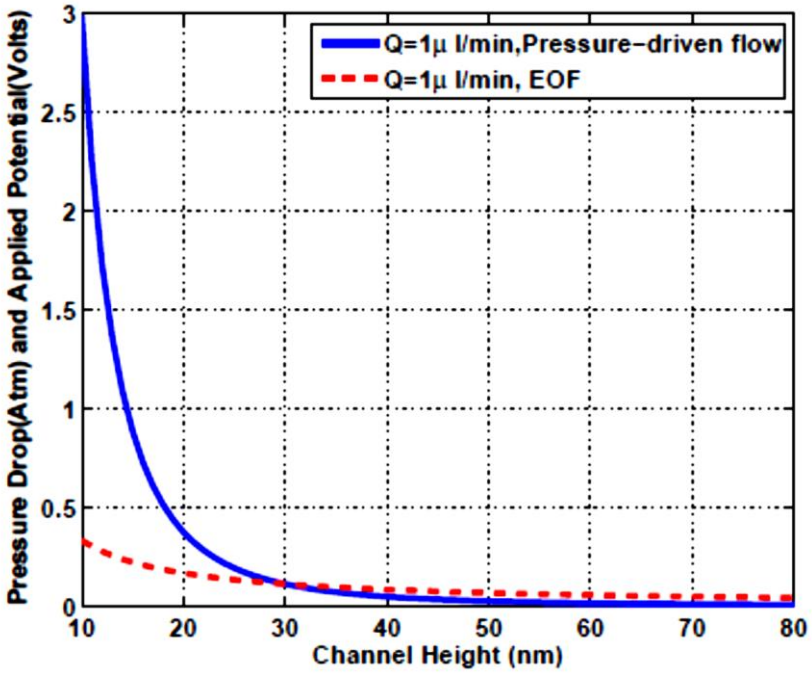

Figure 1.2 Required pressure drop and voltage drop for nanochannels with different channel heights. Nanochannel length and width are 3.5 μm and 2.3 μm, respectively, zeta potential is -11 mV for 1M NaCl solution. (Reproduced from Conlisk, A.T. *Electrophoresis* 2005, 26, 1896-1912)

1.1 Parameters in Nanofluidics

1.1.1 Electric Double Layer (EDL)

It is known that when many solid surfaces are in contact aqueous electrolyte solutions, they gain a net surface charge density arising from differences in electron (or ion) affinities between the surface and the solution, ionization of surface groups or reaction equilibria like protonation, deprotonation. For instance, a glass surface immersed in an electrolyte at pH $\geq$ 7 will acquire negative charges with a layer of electrolyte cations that strongly binds to the solid

surface. Outside this layer, another layer of mobile cations is generated as well. These two layers form a single shielding layer that is usually referred to as the Electric Double Layer (EDL) or Debye Layer. Typically, the Gouy-Chapman-Stern model (GCS) is used to describe the EDL (J.Lyklema, '95). As shown in Figure 1.3, the GCS model consists of two layers – Stern layer (SL) and diffuse layer (DL). The SL is the region next to the solid surface and ions in the SL are bound near the surface due to adsorption and Coulomb interactions while the DL is the mobile region next to the SL.

The EDL thickness is an important electrokinetic parameter, in the nanofluidics. For a channel filled with a symmetrical 1:1 electrolyte such as KCl with ionic concentration *c*, the EDL thickness or λ_D can be represented as;

$$\lambda_D = \left(\frac{\epsilon_0 \epsilon_r R T}{2 F^2 c}\right)^{1/2} \quad (1)$$

where R is the gas constant ($J \cdot mol^{-1}K^{-1}$), ϵ_0 is the permittivity of vacuum ($F \cdot m^{-1}$), ϵ_r is the dielectric constant of the medium, F is the Faraday constant ($C \cdot m^{-1}$), and T is the temperature (K). λ_D can range between 0.1 and100 nm for electrolyte concentrations between 10 and 0.01 mM.(Abgrall, '08)

The ratio of λ_D to channel height, *h* has been used to describe the state of electroneutrality of the bulk solution within the channel. For channels with heights of several micrometers to ~150 nm, it applies that $\frac{\lambda_D}{h} \ll 1$. In this case, the solution towards the center of the channel that is away from the EDL is electrically neutral, *i.e.*, equal concentration of co-ions and counter-ions within the channel, with a neutral electric potential (see Figure 1.4A). However, in the case where the channel height is on the order of the EDL thickness, that is $\frac{\lambda_D}{h} \geq 1$, there is overlap of

the EDL leading to an excess of counter-ions in the channel and loss of electroneutrality (see Figure 1.4B).

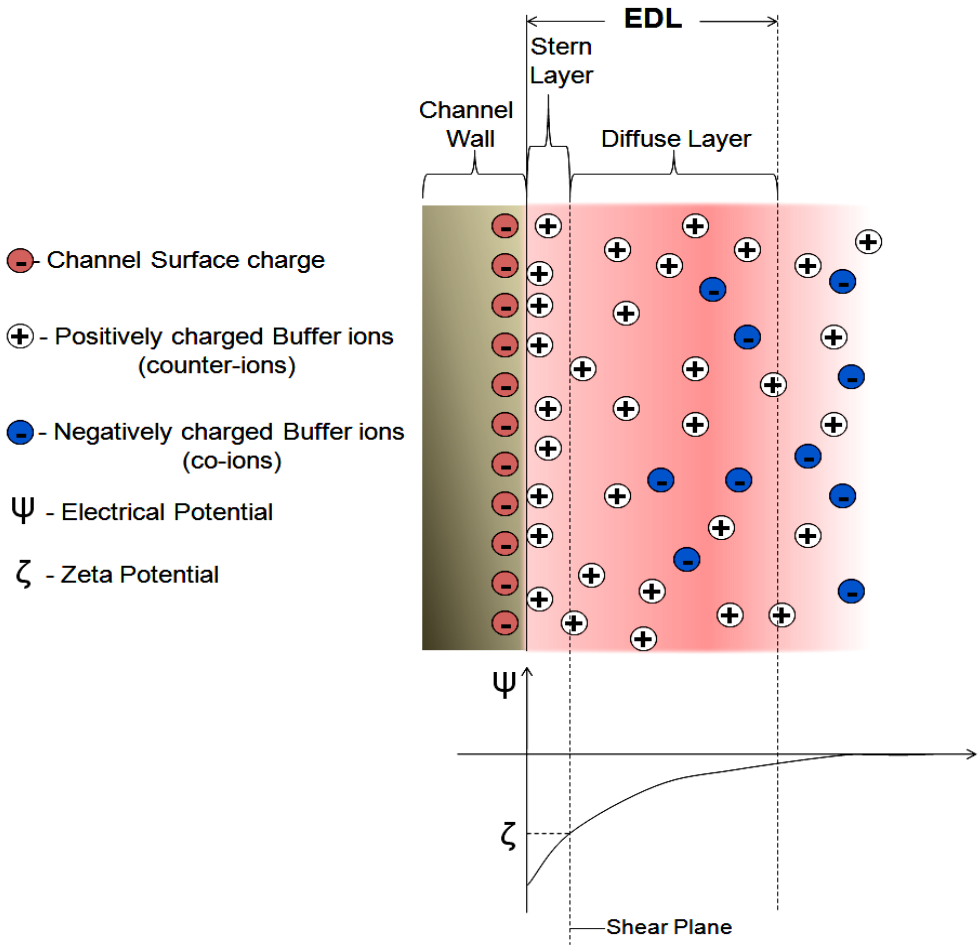

Figure 1.3 Model of the Electric Double layer at a Solid-liquid interface at a negatively charged solid surface/channel wall. (Reproduced from Lyklema J., Vol. 2 – Solid-Liquid Interfaces. First Edition ed.; Academic Press: London England, 1995)

1.1.2 Zeta Potential (or Electrokinetic Potential)

The zeta potential ζ, which measures the electric charge developed on a solid surface in contact with an aqueous solution, is the electric potential at the boundary dividing the SL and DL, also known as the shear plane (see Figure 1.3). Typically, the values of ζ can vary between -200 mV to +200 mV depending on the chemistry of the solid/liquid interface. Also, it is a property that depends on the ion concentration, ion valency and size, pH and temperature of the solution (Kirby, '04). As a result, each solid-liquid interface will have its own unique

measureable zeta potential. Sze *et al*. (Sze, '03) reported that the ζ-potential for surfaces in KCl and $LaCl_3$ aqueous solutions varied between -88 to -66 mV and -110 to -68 mV for glass and PDMS surfaces, respectively, independent of the channel size and driving voltage.

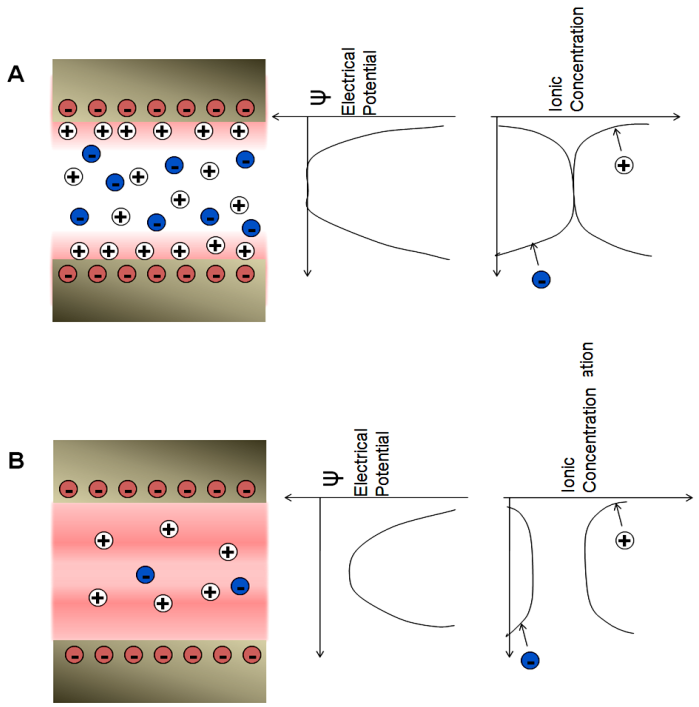

Figure 1.4 Illustration of differences in the electric potential and ionic concentrations for (A) Channels filled with moderately to highly concentrated electrolyte (and/or large channel height [$h > \lambda D$]) and (B) Channels filled with low concentrated electrolyte (and/or small channel height [$h \leq \lambda_D$]). (Reproduced from Lyklema J., Vol. 2 – *Solid-Liquid Interfaces*. First Edition ed.; Academic Press: London England, 1995)

The ζ-potential has been an important parameter in a number of applications (Erickson, '03; Ross, '01) like characterization of membrane efficiency (Reischl, '06), biomedical polymers (Werner, '99) and electrokinetic transport of particles and blood cells (Minerick, '02). Typically, it has been evaluated indirectly from other electrokinetic parameters (Alkafeef, '06; Oddy, '04; Werner, '98).

1.1.3 Electrical Conductivity

The electrical conductivity of a material (also known as specific conductance**,** κ (Sm^{-1}) measures its ability to conduct electrical current and is the reciprocal of the resistivity ρ (Ωm).

The total electrical conductivity of an electrolyte confined in a fluidic channel is a sum of the surface and bulk electrical conductivities arising from the electrically-driven motion of ions under the influence of an external electric field.

The bulk conductivity, κ_B can be computed with the Faraday's constant, (F = 96,485 C/mol), the effective mobility u_i, concentration c_i, and charge z_i of the ions present in solution using the equation (Bard, '01) (Coury, '99);

$$\kappa_B = F \sum_{|i|} |z_i| \, u_i \, c_i \qquad (2)$$

The bulk conductivity of the solution is also represented as the product of the total ionic concentration of ions in a solution and the molar conductivity, Λ.

$$\kappa_B = C_i \, \Lambda \qquad (3)$$

where; $\Lambda = z_+ \lambda_+ + z_- \lambda_-$. The molar conductivity of a dissociable solute increases with ionization, depending on the pH, and decreases by any interaction with other solutes and surfaces.(Brody, '04)

The surface conductivity, κ_S, is an additional component from the fluids tangential to the charged surface and originates from excess counter-ions in the EDL region. Ions from the electrolyte are attracted towards the wall by electrostatic forces induced by the surface charge. Higher concentrations of ions towards the wall lead to a high surface conductivity. Under thin EDL conditions, *i.e.* high electrolyte solutions, the contribution of κ_S is minimal and negligible. However, under low electrolyte concentrations or high surface charge densities, the EDL thickness increases and κ_S contributes significantly to the total conductivity. A more detailed description of κ_s has been reported by Lyklema *et al*. (J.Lyklema, '95; Lyklema, '98). Although it is possible that the motion of ions in the SL and DL contributes to the surface conductivity, the contribution of the less mobile SL is small compared to the more mobile DL. Actually, the SL contribution is sometimes called the additional surface conductivity.

The surface conductivity, just as well as the zeta potential, is a very important interfacial electrokinetic property relevant to a number of natural phenomena, such as electrode kinetics, electrocatalysis, corrosion, adsorption, crystal growth, colloid stability and flow characteristics of colloidal suspensions and electrolyte solutions through porous media and microchannels. It is therefore important to measure κ_s in studies of electrokinetic phenomena. Specific surface conductivity values reported for water in glass capillaries is on the order of $10^{-9} \sim 10^{-8}\,\Omega^{-1}\mathrm{m}^{-1}$ (Gu, '00). Researchers have successfully determined the magnitude of the surface conductivity for other important materials (Alberghi.Je, '66; Perevert.Vd, '72; Revil, '98; Stec, '10). Bikerman (Bikerman, '33) was the first to lay down a theoretical prediction for computing the surface conductivity. Squires *et al.* (Squires, '04) reported the mathematical representation as;

$$\kappa_S = 4\,\kappa_B\,\lambda_D\,(1+m)\,\mathrm{Sinh}^2\left(\frac{z_i q_i \zeta}{4\,kT}\right) \qquad (4)$$

where *m* characterizes the contribution of electro-osmosis to the motion of ions within the DL, *k* is the Boltzmann's constant and T is the temperature.

1.1.4 Electroosmotic Flow (EOF)

The EOF was first reported by Reuss (F, '09) in 1809, who showed that water could be made to percolate through porous clay diaphragms under the application of an external electric field. The mobility of water arises from the fact that clay particles acquired a surface charge when in contact with an electrolyte resulting in the formation of the EDL that induced a bulk flow of water ions. When an external electric field is applied across a capillary or channel containing counter- and co-ions, there is bulk movement of ions. The positive ions (counter) in solution are attracted towards the cathode while the negative ions (co-ions) are attracted towards the anode; however, there is an excess of counter ions in the diffuse layer of the EDL. The movements of the excess counter ions will result in a viscous drag of the surrounding liquid

molecules inducing a bulk flow of ions under the influence of the external electric field. This is referred to as the electroosmotic flow (EOF) and is illustrated in Figure 1.5a. For a thin EDL or large channel height, the EOF has a 'Plug-like' (or flat) profile. Unlike the typical hydrodynamic flow, which has a 'parabolic' profile (Figure 1.5b), this flat profile has been reported to result in high-efficiency electrokinetic separations (Jorgenson, '81; Paul, '98; Rice, '65).

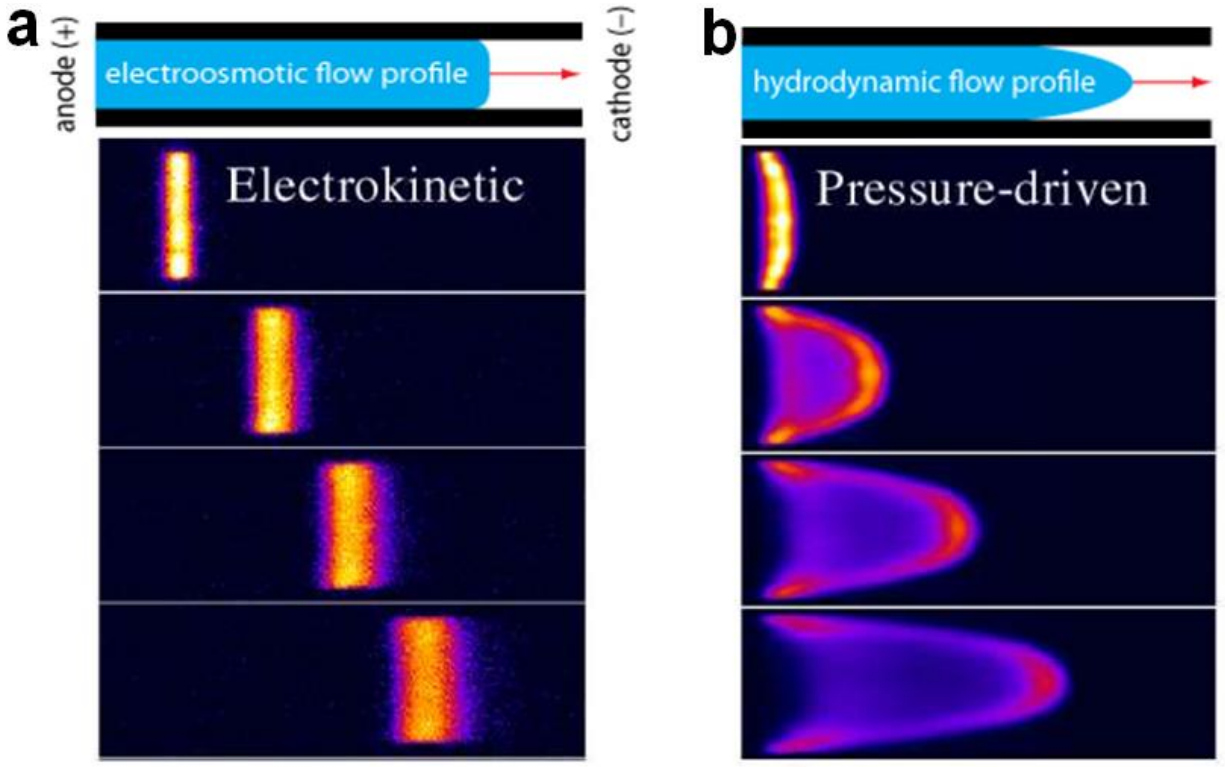

Figure 1.5 Comparison between the (a) plug-like (electrokinetic) and (b) hydrodynamic (pressure driven) flow profiles in a negatively charged channel wall imaged by nonintrusive, caged-fluorescence technique. (Reproduced from http://microfluidics.stanford.edu/Projects/Archive/caged.htm)

The direction of the EOF depends on the type of charge (positive or negative) on the channel wall. For a negatively charged wall, as shown in Figure 1.5, under the influence of an external field (E), the bulk liquid flows towards the cathode while it is reversed in a positively charged wall. The mathematical representation of the EOF velocity, v_{eof}, shown in equation 5 was generated by combining Newton's Law applied to viscous fluids and Poisson's charge distribution.

$$v_{\text{eof}} = - \frac{\epsilon_r \, E \, \zeta}{\eta} \tag{5}$$

Because the EOF mobility is the ratio of the EOF velocity and the applied field strength (*i.e.* $\mu_{eof} = v_{eof}/E$),

$$\mu_{\text{eof}} = - \frac{\epsilon_r \, \zeta}{\eta} \tag{6}$$

It can be deduced from equation 6 that μ_{eof} depends on channel wall conditions, properties of the solution (viscosity and ionic strength), pH and composition of the background electrolyte. Typically, parameters that influence the charge on the channel wall will similarly affect the zeta potential and EOF mobility.

1.2 Nanoscale Phenomena

Electrophoresis performed on the nanoscale utilizes channels with dimensions around 150 nm or less. This introduces many unique phenomena since important length scales are now comparable to the channel dimensions including the electrical double layer (EDL), characterized by the debye length. Furthermore, since the reduction in channel size increases the surface area to volume ratio, surface reactions are enhanced and the surface roughness begins to contribute to the overall flow pattern (Baldessari, '06; Movahed, '11; Pennathur, '05; Piruska, '10; Schoch, '08; Xuan, '06; Yuan, '07). Previous theories on the electrokinetic flow in microchannels utilizing Boltzmann distributions and the Poisson-Boltzmann equation cannot be directly applied to nanochannels since the concentration of co- and counter ions in nanochannels are unequal and significant EDL overlap can be easily observed (Movahed, '11). This requires the development of new theories to explain electrokinetic flows in nanochannel channels.

Currently of the most interest is the dominance of the EDL in nanofluidics. At this scale, the EDL leads to non-uniformity in the motion of the bulk/neutral solvent as well as large non-uniform transverse electric fields, resulting in Poiseuille like flow (Baldessari, '06; Piruska, '10;

Xuan, '06; Yuan, '07). This non-uniformity has drastic effects on dispersion within nanochannels due to the fact that analytes spend a significant time migrating through the EDL (Baldessari, '06). Counter-ions are more attracted to the wall and their flow is impeded, while co-ions are repelled from the wall and are transported faster (Piruska, '10; Yuan, '07). In addition to enhanced separation based on charge, separation based on size can be achieved since smaller molecules approach the wall and experience slower flow profiles than larger molecules (Piruska, '10). At this size scale, the kinetics of adsorption and desorption approaches the time required for diffusion forcing the consideration of wall adsorption; hence, the possibility of performing chromatographic separations in nanochannels (Baldessari, '06).

Furthermore, concentration polarization is a unique phenomenon observed at the interface of microchannels and nanochannels due to the increased flux of ions within the nanochannel from to the enhanced transport within the EDL of selective ions (Baldessari, '06; Piruska, '10; Yuan, '07). When the EDL spans the dimensions of the nanochannel, counterions are able to pass through the EDL while co-ions are excluded resulting in the accumulation of counter-ions and co-ions at the inlet and outlet of the nanochannel with an increased transport of divalent counterions. Doubly charge ions will be strongly attracted to the double layer; hence at the same ionic strength, the total ionic concentration of divalent counterions in the nanochannel becomes higher. Therefore, at low ionic strengths (increased EDL thickness) and non-adsorbing conditions, there will be an increase in the electric current and fluid transport while at high ionic strengths and adsorbing conditions the ζ-potential decreases leading to a decrease in the streaming current and fluid transport fluid (Yuan, '07).

Slower velocity profiles may also be observed within nanochannels when compared to microchannels due to the EDL overlap (Yuan, '07) and electroviscosity effects (Kaji, '06; Moran, '10; Yuan, '07). The decrease in channel dimensions can cause the ratio of the apparent to true

viscosities to be as high as 1.3 depending on the material of the channel wall, spatial size and shape of the channel, the ionic concentration, zeta potential, temperature, dielectric constant and other properties of the liquid. This increase in viscosity leads to an apparent decrease in the EOF within nanochannels.

1.3 DNA Molecule as a Model Polymer in Nanofluidics

In their 1953 article published in *Nature* entitled 'Molecular Structure of Nucleic acids' (Watson, '53), James Watson and Francis Crick described the Deoxyribonucleic Acid (DNA) as a long biopolymer composed of repeating units called nucleotides with two negatively charged backbones intertwined in a double helical structure. As shown in Figure 1.6, each backbone is coiled around the same axis and has a pitch of 34 Å (3.4 nm) and a radius of 10 Å (1.0 nm). In living cells, the DNA is organized into chromosomes and packaged by histones and is responsible for the encryption and transmission of hereditary information. A single nucleotide unit of DNA is composed of a nitrogenous base, a five-carbon 2'-deoxyribose sugar and one to three phosphate groups. These phosphate groups can form bonds with carbon 2, 3 or 5 of the sugar groups. A set of 46 chromosomes make up the total genome and contains 3 billion base pairs, which extends approximately 1.8 m in length (J.Lyklema, '95; Venter, '02; Venter, '01; Venter, Adams, , '01). When dealing with a DNA molecule and its associated number of degrees of freedom, it is useful to treat the behavior of this polymer by statistical quantities. The mean-square end-to-end distance (or displacement length) R_F^2 and the mean-square radius of gyration, R_G^2 are two important quantities in conformational statistics of the polymer chains that provide information about the actual size of a polymer (see Figure 1.7). A polymer chain will take up a finite volume of space, and thus the monomers will occupy an excluded volume around itself while other monomers are not allowed to enter this excluded volume due to steric hindrance, repulsive effects and interactions with the solvent.

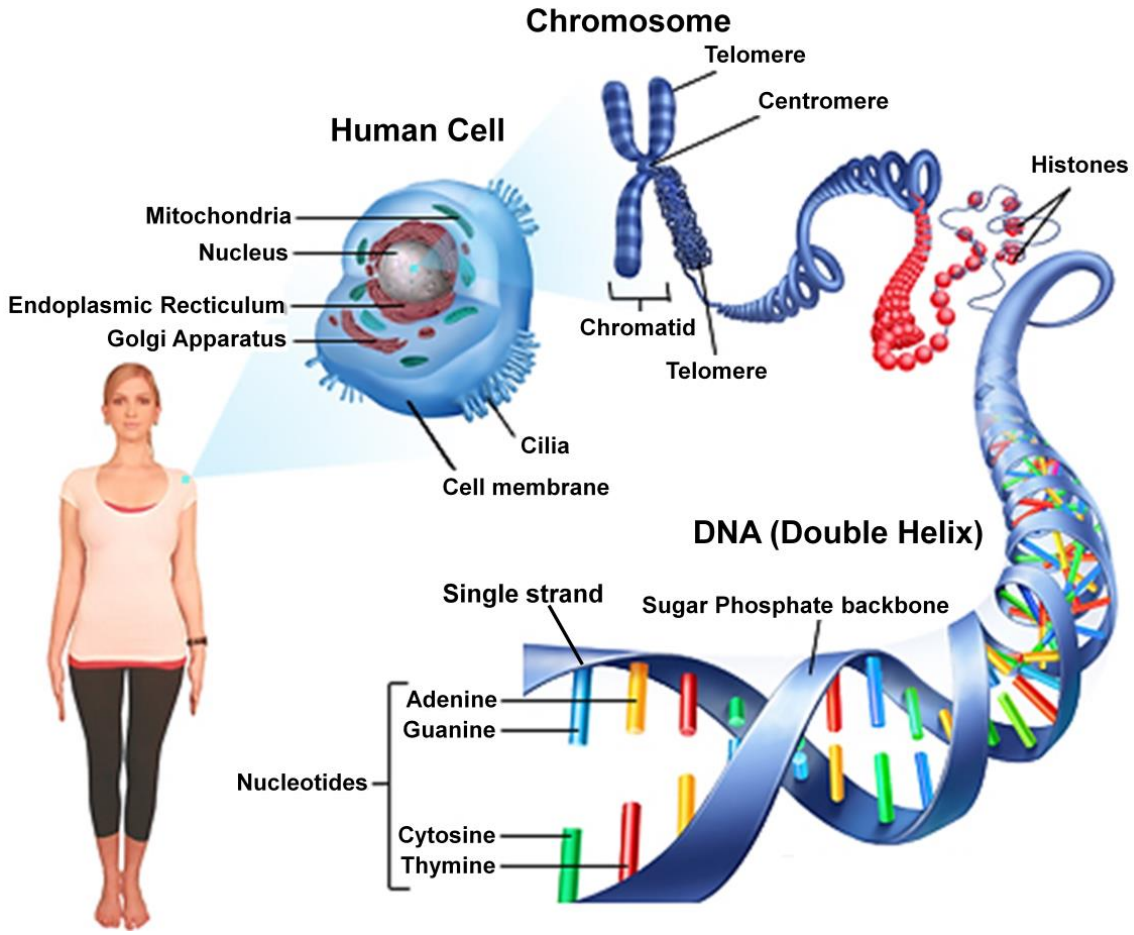

Figure 1.6 The DNA molecule is a long biopolymer which consists of several hundred million base-pairs (bp) with each base-pair contributing 0.34 nm to the total length of the molecule. The backbones of a dsDNA are held together by the bases that pair-up in a manner in which the nucleotides Adenine (A) binds to Thymine (T) and Guanine (G) binds to Cytosine (C) following the Watson-Crick based-pairs (bp). The DNA is tightly wound around proteins called histones and packaged into the nuclei of a cell in the form of chromosomes. (Reproduced from *www.virtualmedicalcentre.com*)

Although, the biological properties of a DNA molecule are very complex, the physical properties involved in the molecular dynamics can be described by three parameters; the contour length, L_c, persistence length, l_p and the effective width, w_{eff} (Reisner, '05). The contour length refers to the total length of the DNA when it is fully stretched. As stated by Watson and Crick, each base pair contributes 0.34 nm to the full contour length. Due to its double helical structure, the DNA molecule becomes locally rigid (Manning, '88).

The persistence length of DNA molecules have been extensively evaluated from light-scattering measurements of the molecular weight and the mean-square radius and with the aid of

hydrodynamic theory measurements of intrinsic viscosity and the sedimentation coefficient as reported by Hays *et al* (Hays, '69). On length scales smaller than l_P, a DNA molecule is considered rigid, while it is flexible at length scales larger than l_P. The intrinsic persistence length and width, w_0 of dsDNA in 0.1 M aqueous NaCl are ~50 nm (150 bp) and 2 nm, respectively (Manning, '06). The effect of self-avoidance on flexible polymers that are freely coiled in solution was first understood by Flory (Baumgärtner, '82; Orland, '94) and later generalized to the semi-flexible case by Schaefer *et al*. (Schaefer, '80) Flory-Pincus represented the R_F for a real polymer by the equation;

$$R_F \cong (l_p \ w_{eff})^{1/5} \ L_{cont}^{3/5} \tag{7}$$

The radius of gyration relates to R_F by;

$$R_G \cong \frac{R_F}{\sqrt{6}} \tag{8}$$

Based on the values reported by Reisner *et al*. (Reisner, '07), for 0.5× TBE buffer with 20 mM ionic concentration, w_o is 3 nm and w_{eff} was estimated to be 12 nm. It is known that the intercalation of YOYO-1 dye to dsDNA causes an extension in its contour length. At a dye concentration, of 1 dye molecule per 5 base pairs, a 20% increase in the contour and persistence length was estimated. Therefore, the adjusted persistence length will be 53 nm and the contour lengths of lambda (λ) and T4 DNA will be $L_c(\lambda)$ = 20 μm and L_c (T4) = 64 μm. Therefore, based on equations 7 and 8, the radii of gyration will be approximately ~560 nm and 1140 nm for λ and T4 DNA, respectively, in 0.5× TBE buffer.

1.4 DNA Confinement in Nanochannels

Before designing nanochannels for the study of dsDNAs, it is crucial to understand the behavior of DNA molecules in confined geometries. Previous reports have revealed that a DNA molecule confined in a nanochannel will stretch along the channel axis to a substantial fraction

of its full contour length (Reisner, '07). Confinement elongation of genomic-length DNA has several advantages over alternative techniques for extending DNA, such as flow stretching and/or stretching relying on a tethered molecule. Confinement elongation does not require the presence of a known external force because a molecule in a nanochannel will remain stretched in its equilibrium configuration allowing for continuous measurement of length (Tegenfeldt, '04).

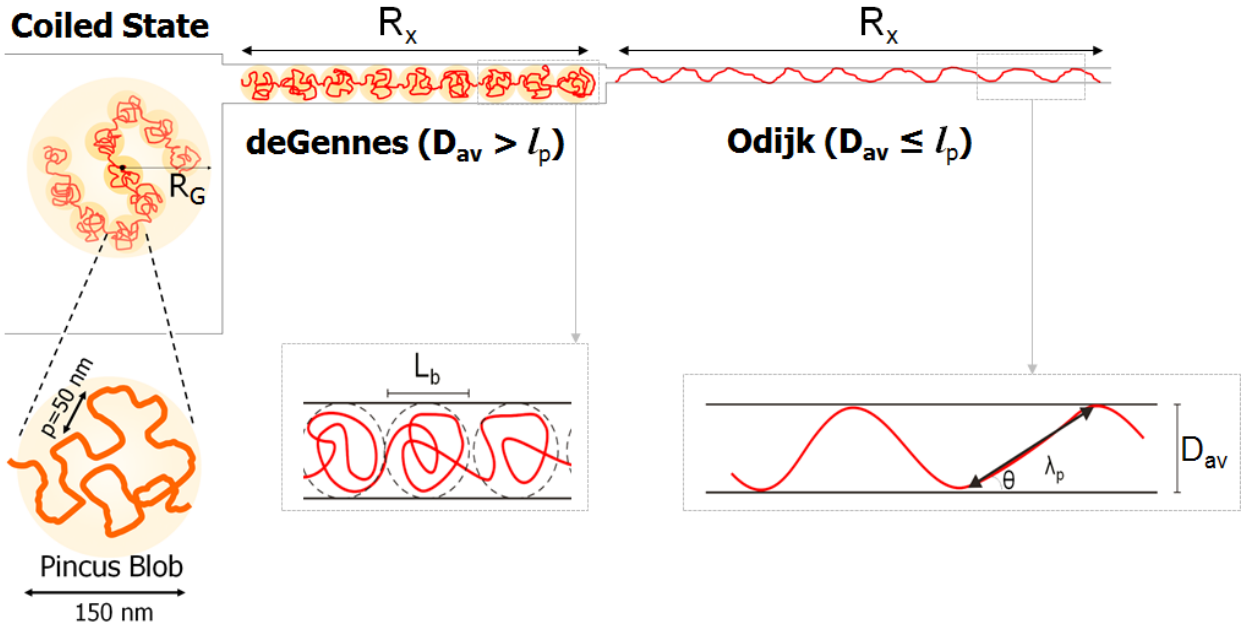

Figure 1.7 Representation of DNA molecule in the microchannel (coiled state) in a nanochannel with the average dimension greater than (deGennes regime) and less than (Odijk regime) the persistent length of dsDNA.

In confined spaces, where R_G is much larger than the geometrical average depth, D_{av}, of the nanochannel, the number of available configurations of the polymer reduces. Two main confinement regimes exists and depending on differences between the average depth and persistence length l_p. When $D_{av} >> l_p$, the molecule is free to coil within the nanochannel and stretching is entirely due to excluded volume interactions between different coiled segments of the polymer separated along the backbone. Coiling of the molecule can be envisioned to be broken up into a series of blobs with diameter L_b, while the stretching is a result of repulsion between the blobs. This is known as the deGennes regime (Martins, '13). Within the blobs, the

confinement force is only a weak perturbation while each blob retains the property of the bulk polymer. This is diagrammatically illustrated in Figure 1.7. The extension length of the molecule, R_x, can be calculated using the equation;

$$R_x = L_c \left(\frac{w_{eff}\ l_p}{D_{av}^2}\right)^{1/3} \quad (9)$$

where $D_{av} = \sqrt{D \times h}$ and is the geometrical average of the two confining dimensions in the nanochannels.

As the channel width decreases and $D_{av} << l_p$, the stretching is strictly not a result of volume exclusion but an interplay between confinement and the intrinsic elasticity of the DNA. The strong confinement prevents the molecule from forming loops within the nanochannel. Back folding becomes energetically unfavorable and stretching becomes a result of deflection of the molecules in the channel walls. The average length between these deflections is of the order of the Odijk length scale $\lambda_p \cong (D_{av}^2\ l_p)^{1/3}$. This regime is referred to as the Odijk regime (see Figure 1.7) (Odijk, '06; Odijk, '83). For a small average deflection, θ, R_x is represented as;

$$R_x = L_{cont}\ \cos\theta \cong L_{cont}\left[1 - 0.361\left(\frac{D_{av}}{l_p}\right)^{2/3}\right] \quad (10)$$

1.5 Effects of Ionic Environment on DNA Molecules

According to Reisner *et al.* (Reisner, '07),` variations in the ionic strength affect the configuration of a DNA molecule by modulating the range of electrostatic interactions between the charges on the phosphate backbone. Electrostatic interactions in electrolyte solutions are screened over a characteristic scale known as the Debye length. The geometry of the polymer results in two types of electrostatic interactions (Tegenfeldt, '04); (i) Interactions between charges separated in contours that create repulsion between back looping segments resulting in an effective DNA width (w_{eff}) that is larger than the intrinsic width w_0, and (ii) Local repulsive

interactions between charges separated by less than the Debye length in contour resulting in an increase in the persistence length to a new value for l_p. The mechanisms of these interactions determine the ionic strength variation of the extension over an ionic strength range. The Odijk-Skolnick-Fixman (Baumann, '97) equation based on single-molecule elasticity has suggested that the new persistence length of a DNA when in solution relates to the ionic strength of the solution by;

$$l_p = l_{p_o} + \frac{0.0324\ \mathrm{M}}{\mathrm{I}}\ \mathrm{nm} \qquad (11)$$

where l_{p_o} = high salt value of persistence length (≈ 50 nm). According to equation 11, l_p is roughly equal to l_{p_o} until the ionic strength drops below 10 mM. l_p increases up to about 80 nm between 10 mM and 1 mM.

Although, reports have shown that the extension of DNA in a nanochannel almost triples when the ionic strength is changed by two orders of magnitude, experiments have revealed that even over a range of 4 - 200 mM ionic strength, variation in the persistence length is not large enough to explain the observed extension of DNA. This is in contrary to a report by Krishnan *et al*. (Krishnan, '07) and explains why nanoconfinement of DNA is critical for enhanced stretching.

1.6 Nanochannel fabrication

Several review articles have discussed the numerous high resolution techniques available for the fabrication of nanofluidic devices (Chantiwas, '11; de la Escosura-Muñiz, '12; Douville, '08; Duan, '13; Mijatovic, '05; Xia, '12). For the most part, the choice of fabrication technique depends mainly on the substrate of choice, which may be inorganic (Fused Silica, glass, Silicon Nitride and Silicon) or organic (Elastomers and thermoplastics), and the desired dimension of the nanostructures.

1.6.1 Nanochannel fabrication in inorganic substrates

Inorganic substrates like glass, fused silica and silicon have been widely used as substrates for the fabrication of nanofluidic devices due to their established surface chemistry, excellent optical properties and well-entrenched fabrication techniques (Chantiwas, '11). The most prominent techniques for the fabrication of nanochannels in inorganic substrates are the top-down direct writing using focused ion beam (FIB) (Menard, '11) or electron beam lithography (EBL) (Broers, '96) followed by dry etching.

In the case of EBL, nanopatterns are initially defined in a thin layer of polymer resist using a beam of focused electrons then transferred to the underlying substrate after development and etching. EBL has been useful for the fabrication of features as small as 10 nm (Broers, '96) and with the combination of electron beam evaporation, have been used for the fabrication of nanometer sized metal electrodes (see left panel in Figure 1.8). On the other hand, nanochannels are fabricated with the FIB instrument by focusing a beam of high energy Ga ions, onto the surface resulting in the sputtering of atoms of the substrate (Menard, '11). Also, nanoelectrodes have been fabricated with the FIB by deposition using the gas injection system (Maleki, '09).

Recently, FIB was utilized for the fabrication of sub-5nm structures in fused silica substrate through a thick conductive metal layer using a 1.5 pA ion beam current (see right panel of Figure 1.8) (Menard, '11). Using EBL and/or FIB, several groups have developed nanofluidic devices in inorganic substrates for the analysis of biomolecules and the evaluation of transport phenomena in nanofluidic channels (Cabodi, '02; Levy, '10; Menard, '12; Menard, '13; Yang, '06). Though, both EBL and FIB are expensive, slow and impractical for large-scale manufacturing of nanofluidic structures. Other techniques include using nanowires as sacrificial templates,(Kyo Seon, '10) conventional machining by etching of a sacrificial strip separating a

substrate and the capping layer (Tas, '02) and self-enclosing of nanochannels using a UV laser pulse (Xia, '08).

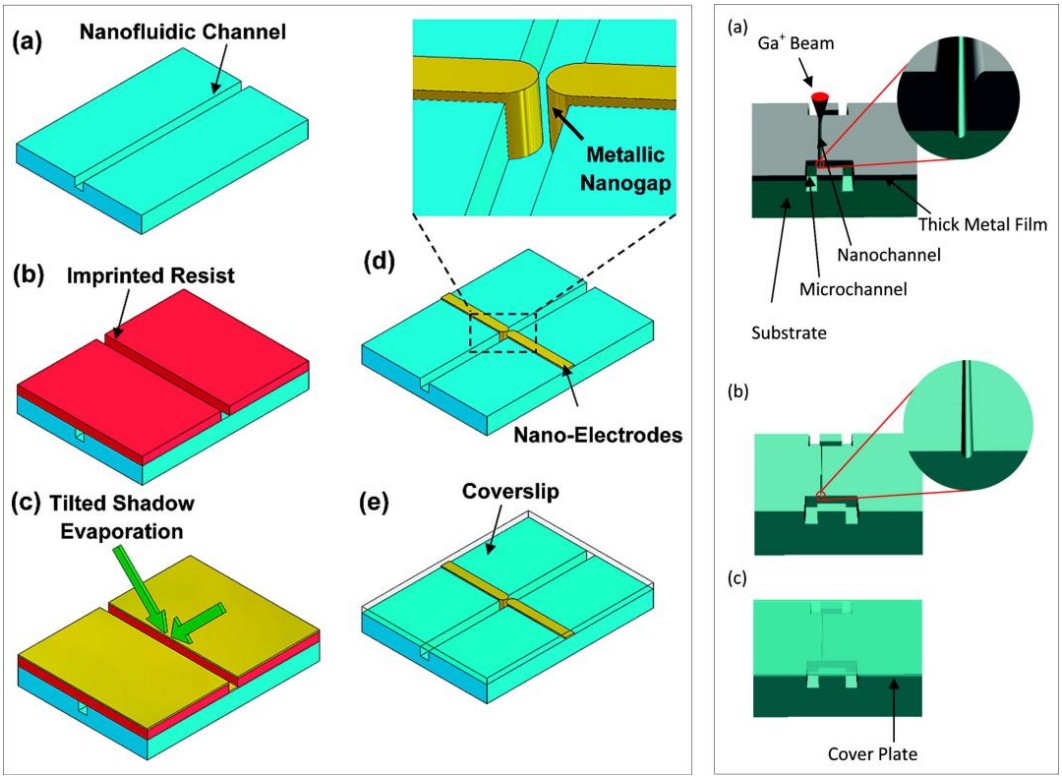

Figure 1.8 *Left panel* – Steps in the fabrication of nanogap detectors via (a) Fabrication of a single nanofluidic channel on a fused-quartz substrate using EBL; (b) imprinting of a nanotrench into the resist layer, which is perpendicularly across the nanochannel, for a subsequent mental lift-off; (c) deposition of the metals in the nanotrench via the shadow evaporation with two symmetric tilted angles; (d) after a lift-off, a pair of metallic nanowires is formed across the nanochannel with a sub-10 nm breaking gap in the channel (see inset); and (e) after making final metal contacts, the nanochannel, nanowire, and nanogap are conformably sealed by a coverslip coated with a conformable layer. (Reproduced from Liang *et al.*, *Nano Letters* 2008, 8, 1472-1476). *Right Panel* – FIB milling process scheme and subsequent fabrication steps. (a) Milling a nanochannel through the thick metal film. (b) Removal of the metal film using an etching solution. (c) Sealing of the micro- and nanochannels with a cover plate. (Reproduced from Menard *et al.*, *Nano Letters* 2010, 11, 512-517).

1.6.2 Nanochannel Fabrication in Organic Substrates

Organic substrates useful for the fabrication of nanochannels include elastomers and thermoplastics.

1.6.2.1 Elastomeric Nanofluidic Devices

Elastomers are amorphous polymers with low to moderate number of cross-links between the chains. The low Young's modulus of elastomers induces large deformation upon application

of an external load while the covalent cross-links help elastomers return to their original shape upon release of the load. Nevertheless, this property sometimes creates problems during the fabrication of nanochannels. Several efforts have been channeled towards overcoming or harnessing the deformability of elastomers for the generation of functional nanochannels. In fact, the unwanted collapse, which has traditionally been regarded as a problem in microfluidic chips, has been exploited for the fabrication of nanochannels (Lasse, '08). Mills *et al*. (Mills, '10) found that when a sheet of PDMS was mechanically stretched, exposed to oxygen plasma or U/ozone, then released, sinusoidal wrinkle patterns were generated due to the change in surface stiffness and the need to release strain. The authors modulated the amplitude of the wrinkle structures by controlling the applied strain, replicated the pattern into a UV-curable epoxy resin and transferred into PDMS. The resulting nanochannel was triangular with the base length and height of 688±79 nm and 78±18 nm, respectively. Also, nanochannels have been fabricated in PDMS substrates from Si or PDMS masters possessing the opposite (raised) tone of the structures via soft lithography (Qin, '10; Whitesides, '05).

Although, the low Young's moduli of elastomers have been advantageous for the fabrication of nanofluidic channels with tuneable dimensions (Huh, '07), this property may result in deformed nanochannels; hence, reducing the device performance. Also, elastomers like PDMS are porous and permeable to gases and liquids under high pressure and undergo hydrophobic recovery after surface treatment. These pose potential setbacks in the usability of elastomers for the development of nanofluidic devices.

1.6.2.2 Thermoplastic Nanofluidic Devices

Thermoplastics are usually high molecular weight, linear or branched chain polymers with high Young's moduli and a wide range of physicochemical properties dictated by its monomeric units. The deformability of thermoplastics make them useful substrates for the

fabrication of microfluidic channels via hot embossing, injection molding, compression molding, thermal forming and casting techniques. The most robust technique for the fabrication of nanochannels in thermoplastics is Nanoimprint Lithography (NIL).

Since its first report in the 1990s by Steven Chou and co-workers (Chou, '97; Chou, '95; Chou, '96), NIL has become an extensively used tool for the design of nanochannels in thermoplastics and has demonstrated the ability to fabricate structures with sub-10 nm sizes. The main advantage of NIL is the ability to build multi-scale micro and nanofluidic patterns in a single imprinting step at a reproducible fashion from a single stamp. Further details on NIL is presented in the review by Chantiwas *et al.* (Chantiwas, '11). Additional reported techniques for the fabrication of nanochannels in thermoplastics includes; direct proton beam writing into PMMA (Shao, '06), thermomechnical deformation of PC (Pennathur, '07), compression of PMMA microchannels (Liang, '08), sidewall lithography and hot embossing into PET (Cheng, '13), UV-lithography/O_2 plasma etching into PMMA (Nikolova, '04), hot embossing with PMMA moulds into PET (Piruska, '10), refill of PMMA microchannels (Karnik, '05) and the use of silica nanowire templates for nanochannels in PC (Brown, '06).

In summary, nanofluidic systems have been produced in both inorganic and polymer substrates; however, due to the diversities of the bulk and surface properties afforded by polymers and the overall low cost, polymer based nanofluidic devices have presented huge potential for the production of disposable, point-of-care bioanalytical systems. Also, compared to other fabrication techniques, nanoimprint lithography is cost effective and easy to integrate with microfluidic networks, achieving a lateral resolution less than 10 nm with high reproducibility. Additional details, on the experimental procedures employed for the fabrication of the nanofluidic devices used in this work is described in the subsequent chapters.

1.7 Applications of Nanochannels

Nanochannels offer great flexibility in terms of shape and size with increased robustness and surface properties, which can be tuned based on the required function (Danelon, '06; Turner, '02). Unique phenomena that occur in nano-confined environments provides some interesting opportunities for applications not readily achievable in micro-scale environments. Fundamentally, nanochannels have generated an ideal platform for investigating nanoscale physical and chemical phenomena such as concentration polarization (Kim, '07), nonlinear electrokinetic flow and ion focusing near nanofluidic channels (Piruska, '10; Zangle, '10) and mass transport in geometrically confined spaces (Kalman, '08; Schoch, '08). They have also been applied in the separation (Han, '00; Woods, '05), manipulation and detection (Bayley, '00) of single molecules and control of molecular transport and wall interactions (Kemery, '98; Kuo, '01).

1.7.1 Nanochannels for the analysis of Biopolymers

Nanofluidic channels have been useful for the analysis of biopolymers, with the DNA molecule being of the most interest. DNA molecules have been notable analytes for nanochannel applications because of their net negative charge, structural linearity and ability to conform to different stretching rates depending on the geometry of the nanochannel. Mostly all of the bioanalytical applications that use nanochannels for DNA analysis begin with DNA linearization by nanoconfinement. As depicted in Figure 1.9, DNA linearization have been achieved using a variety of nanosystems that include nanoslits (Tas, '04), nanochannels (Xu, '07), staggered densely packed circular or diamond shaped nanopillars (Cabodi, '02; Cao, '02; Turner, '02) and reconfigurable-tunable elastomeric nanochannels (Huh, '07; Qiao, '05). Unlike other traditional linearization techniques, which exert a high stretching force at an anchored end that decreases along the length of the molecules, nanoconfinement allows the entire confined DNA molecule to

be theoretically exposed to the same confinement force. This improves consistencies in measurements and allows the ability to integrate images of the DNA in its stretched state over long periods (Douville, '08).

After the DNA has been linearized in the nanoconduits, it can be probed for specific information using the optical and/or electrical detection modalities. In optical detection, the molecules are initially stained with an intercalating fluorescent dye before being confined while detection is achieved using a high magnification fluorescent microscope. However, in electrical detection modality, unstained (or stained) DNA molecules are detected via electrical signatures that may be transduced longitudinally along the nanochannel length, transversely using a pair of planar nanoelectrodes (nanogap) or using short intersecting nanochannels positioned orthogonally to the transport nanochannel. Both optical and electrical detection modalities have been employed in several bioanalytical applications.

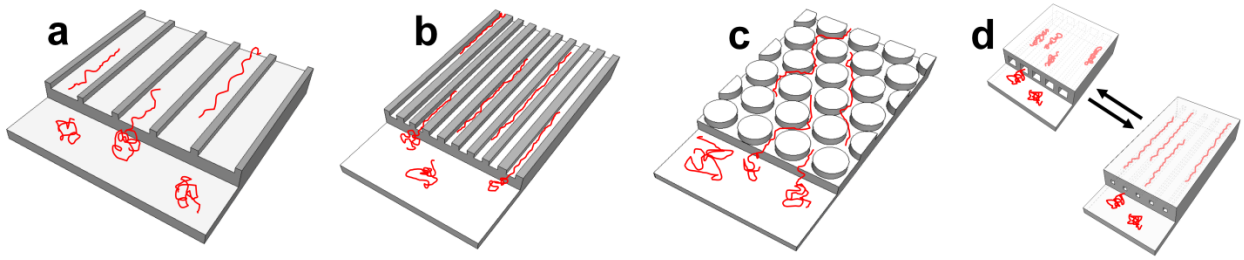

Figure 1.9 A depiction of nanofluidic device configurations used for DNA linearization by confinement. These are (a) Nanoslit (b) Nanochannel (c) Nanopillar array, and (d) Tuneable-elastomeric based nanochannels

1.7.1.1 Optical Detection

Optical imaging, which is the most commonly employed detection scheme, has the ability to distinguish different types of information based on color differences obtained from imaging with conventional (Das, '10; Lam, '12) or super-resolution (Baday, '12; Kim, '12; Neely, '10) fluorescent microscopy techniques. In early reports, optical imaging in nanochannels was used to study the transport dynamics, extent of stretching and separation of DNA molecules nanoslits

(Menard, '11; Tas, '04) and nanochannels (Schellman, '77; Yang, '06). Majority of the reported nanochannel-based separation of DNA revolve around the concept of entropic trapping reported by the Craighead group (Cabodi, '02; Meisenberg, '06). Han and Craighead in their study showed the possibility of separating DNA molecules, in size range between 5 and 160 kbp, based on their sizes using 15 mm long channels (Han, '00). Their device comprised of microchannel regions connected by narrow nanoscale regions. The authors observed that the longer the time spent in the entropic trap by the DNA molecules, the lower their overall mobilites. Longer DNA molecules with larger radius of gyration traveled faster through the system with higher overall mobility because they have a larger surface area in contact with the boundary of the nanoregion, thereby increasing their probability or entry (Han, '99). The efficiency of separation in nanochannels using micro trap entropic arrays increased at higher field strengths (Han, '00); however, the separation resolution between two peaks which was calculated by $R_s = (\Delta V/V)\sqrt{(N/16)}$, where $(\Delta V/V)$ is the fractional band velocity, decreased at higher voltages. The authors stated that the selectivity term $(\Delta V/V)$, which represents the entropic trapping effects, conquered the effect from band broadening resulting in higher resolution at low voltages.

A follow-up work was performed by Fu *et al.* (Fu, '05) for the separation of a mixture of three SDS-protein complexes based on their molecular weights. Their device possessed channels varied from 60 nm in the shallow areas to 300 nm in the wide regions. Interestingly, the smaller proteins migrated faster, which is opposite to what was previously demonstrated in DNA separation experiments. The resulting separation occurred at a length scale of 570 μm and a time of 30 s. Also, Schoch *et al.* (Schoch, '06) employed a silicon-based nanofluidic chip for the separation of proteins utilizing the diffusion characteristics of charged molecules. The diffusion of proteins becomes more significant as the nanochannel becomes smaller due to enhanced electrostatic interactions with the channel walls. Also, the pH of the solution can be adjusted to

modify the charge on the proteins and control these interactions. In brief, at low ionic strengths (thick EDL condition), the attraction/repulsion of charged molecules with the walls causes them to distribute unevenly in a way that allows for separations of the molecules; a phenomenon called the Donnan effect.

In the case of DNA electrokinetically mediated separations in nano-columns, Pennathur *et al.* (Pennathur, '07) reported the separation of a mixture of fluorescently labeled dsDNA (10, 25, 50 and 100 bp), fluorescein and fluorescein-12-UTP in fused-silica nanoslits (only one dimension in the nanoscale; three depths - 40, 100 and 1560 nm). The authors observed that the order of migration of the DNAs depended on the relative magnitude of the length of DNA (l) and λ_D with respect to the channel depth (h). They achieved the best separation performance in 100 nm fused silica channels with 1-10 mM buffers and in all cases, the EOF (moved toward the cathode) dominated over the polyanion's electrophoretic motion. In 5 mM ($\lambda_D/h \approx 0.04$) and 10 mM ($\lambda_D/h \approx 0.03$) sodium borate buffer solutions, the order of migration was Fluorescein (FL), fluorescein-UTP (UTP), followed by the 10, 25, 50 and 100 bp oligonucleotides. This results was expected since the electrophoretic mobilities are $\mu_{\mathrm{Fl}} < \mu_{\mathrm{UTP}} < \mu_{10\mathrm{bp}} < \mu_{25\mathrm{bp}} < \mu_{50\mathrm{bp}} < \mu_{100\mathrm{bp}}$. In 20 and 100 mM buffer solutions, the same elution order was observed however, the resolution degraded. The authors attributed reductions in resolution to possible changes in the electrophoretic mobility of the analytes due to increased bulk ion concentration. In 1 mM sodium borate ($\lambda_D/h \approx 0.10$), the order of elution was FL, UTP and 100, 50, 10, and 25 bp oligonucleotides. At low ionic strengths, the effects of ion density and EDL coupling compete with each other to determine the net axial migration rate; hence, transverse electromigration in the axial and transverse directions and steric-wall interactions play a role in determining the resolution.

In addition, nanochannels have been used for the separation of dye molecules. In a study, Garcia *et al*. (Garcia, '05) reported the separation of Alexa 488 (-2), and rhodamine B (neutral) dyes based on their charge and interaction with channel walls in a nanochannel with widths from 35 to 200 nm. When negatively charged molecules were introduced into these channels, they were repelled from the negative walls towards the center of the channel where fluid flow was faster. Intuitively, more negatively charged molecules will exhibit faster mobilities through the nanochannel than less negatively charged or neutral molecules, thereby, providing a mechanism for separation. Based on this, Pennathur and Santiago (Pennathur, '05) investigated various configurations of nanochannel to microchannel geometries for the separation of two negatively charged dyes fluorescein (-2) and Bodipy (-1). In agreement with the theory (Pennathur, '05), their results showed the possibility of determining the valencies and mobilites of unknown molecules based on the their transport within nanochannels.

In the case of nanochannel based enzymatic reactions, Reihn *et al.* (Riehn, '05), reported the use of 100-200 nm nanochannels for the restriction mapping of DNA molecules with restriction endonucleases. In this work, the location of the restriction reactions within the device was controlled by electrophoresis and diffusion of the enzyme cofactor Mg^{2+}. Also, the linearization and clipping of DNA was divided into separate steps by dynamically varying the concentration of Mg^{2+}. They successfully clipped and mapped λ-DNA molecules to three and four fragments using the restriction enzymes SacI and SmaI, respectively, to a resolution of 1.5 kbp.

More recently, nanochannels have gained attention in the optical mapping of DNA molecules, with size ranging from 10 kbp to 1 Mbp for the acquisition of spatial genetic and epigenetic information. A high content of optical barcodes/maps can be generated from fluorescently labeled specific sequence motifs, epigenetic marks and other genomic information

along individual DNA molecule which can be easily visualized when the DNA in linearized in the nanochannels (Levy-Sakin, '13; Michaeli, '12). As shown in Figure 1.10, optical mapping involves four main steps; (i) Sequence-specific labeling of long DNA molecules, (ii) linearization of the labeled molecules, (iii) fluorescent imaging and, (iv) map construction.

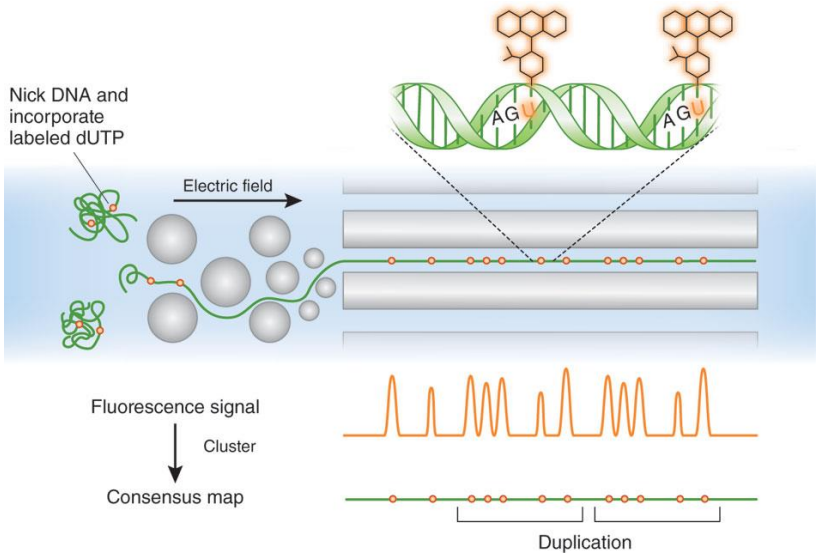

Figure 1.10 DNA molecules (green) are nicked by an enzyme at specific sequence motifs and repaired by a polymerase that incorporates fluorescently labeled nucleotides (orange dots). An applied electric field drives the molecules through a series of progressively smaller nanoscale obstacles (gray circles) that funnel the molecules into channels 45 nm in diameter. Once DNA is stretched and confined within the channels, the distances between labels can be accurately measured using a fluorescence microscope. DNA molecules with similar patterns of labels are clustered, and software is used to generate a consensus map of the sequence motifs recognized by the nicking enzyme. The maps facilitate the analysis of structural variation, such as duplications, and the *de novo* assembly of sequencing data. (Reproduced from Michaeli *et al*., Nat Biotech 2012, 30, 762-763)

In a recent technology commercialized by BioNano Genomics Inc., a device possessing ~4000 channels (0.4 mm long and 45 nm in diameter) was fabricated in Si using 193 nm lithography, and used to construct sequence motif maps of 95 bacterial artificial chromosome (BAC) clones covering the 4.7-Mb Major Histocompatibility (MHC) region from two individuals (Lam, '12). This process is fully illustrated in Figure 1.11 for a 183 kb BAC clone. First, a nicking endonuclease was used to introduce single-strand nicks in the dsDNA at specific sequence motif followed by incorporating fluorescent dye conjugated nucleotides (Alexa 546 dUTP) at these sites by Vent (exo-) polymerase (Das, '10). The labeled DNA molecules were

stained with YOYO-1 dye for visualization of the DNA molecule and size. Next, the stained DNA molecules were electrokinetically loaded into the nanochannel array where they were linearized. Locations at specific sequences were imaged as fluorescent spots along the DNA under an automated high-resolution fluorescent microscope.

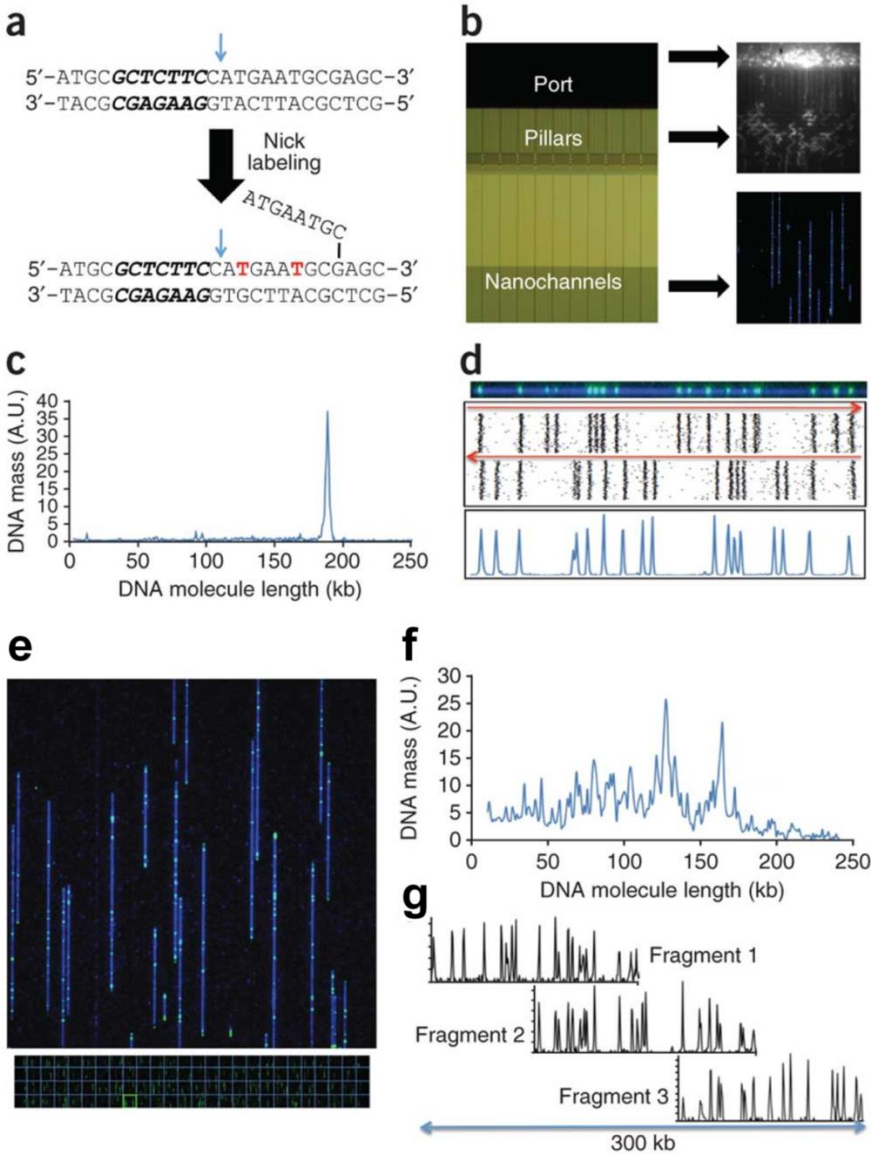

Figure 1.11 (a) Nick-labeling by Nt.BspQI and DNA polymerase is accomplished by top-strand DNA cleavage (blue arrow), one nucleotide 3′ from the recognition sequence (in bold italics), followed by incorporation of fluorescent nucleotide analogs (in red) with concomitant DNA strand displacement. (b) The DNA molecule is stained with YOYO-1 and loaded into the port of a nanoarray flowcell (left panel). The DNA molecules are introduced into the region with pillars and micrometer-scale relaxation channels by an electric field where they unwind and linearize (top right panel). Finally, the DNA molecules are pushed by a low-voltage electrical pulse, and they enter the 45-nm nanochannels, where they are stretched uniformly to 85% of the length of perfectly linear B-DNA (bottom right panel). The DNA is visualized as

blue linear structures in the nanochannels, with green labels marking the Nt.BspQI nick sites. (c) The length of the DNA molecules and the positions of nick labels on each DNA molecule are determined after automated image capture. The fragment size profile of a 183-kb BAC is shown, with the narrow peak width indicating uniform DNA linearization. (d) The DNA molecules are clustered into groups (representing individual BACs) based on nick-labeling pattern similarity. As BAC molecules can enter the nanochannels in either orientation, each BAC is represented by two clusters with opposite orientations (top panel). After combining the two clusters, histogram plots of nick-labeled DNA (bottom panel) are used to define the locations of Nt.BspQI sites. $n \approx 100$ molecules. (e) Image of a single field of view (FOV 73 × 73 μm) containing a mixture of nick-labeled DNA molecules in the nanoarray. This FOV is part of 108 FOVs shown in the bottom part of the panel (outlined in green). Each FOV can accommodate up to 250 kb of a DNA molecule from top to bottom. The images of four FOVs are stitched together so that longer molecules (up to 1 Mb) in a single channel can be analyzed whole. In all, there are 27 sets of four vertical FOVs per array scan. (f) The distribution of the DNA molecules imaged on the nanoarray by length. The majority of the molecules are 100–170 kb in length as expected from the BAC-clone sizes. (g) After clustering of DNA molecules based on nick-labeling patterns, consensus maps with overlapping patterns are assembled into contiguous-sequence motif maps. In this example, three overlapping consensus maps (each ~150 kb long) are assembled into a 300-kb map. (Reproduced from Lam *et al*., *Nature Biotech* 2012, 30, 771-776).

A single optical scan of the loaded array acquired images from 23,000 molecules, corresponding to 3 Gb of DNA sequence. The molecules ranged in size from 20–220 kb, with the majority 100–170 kb in length, as expected from the sizes of the BAC clones. By determining the order of the fluorescent labels on the backbone, the distribution of specific sequence motifs of an individual DNA molecule was inferred with great accuracy, in a manner similar to reading a bar code (Das, '10).

In addition, Lim *et al*. (Fang Lim, '11) reported the identification of methylation patterns within linearized genomic-sized dsDNA molecules. In their work, methylation patterns were detected by binding a methyl-CpG-binding domain (MBD) protein fragment labeled with Alexa 568 dye to the DNA segment possessing a 5-methyl Cytosine segment. Though this technique was limited by diffraction, the authors estimated a resolution of about 10 kbp, which is comparable to the size of a human gene.

1.7.1.2 Electrical Detection

In the electrical detection modality, biomolecules are identified by monitoring electrical conductance, resistance, capacitance and/or impedance. In most cases, the biomolecules are

unlabeled, in their native state, and detected by either observing the electrical signatures they generate due to their inherent electrical properties or measuring relative changes in the electrical properties of the buffer medium when they occupy the detection volume. Due to the inherent superiorities of electrical transduction methods, such as excellent compatibility with advanced semiconductor technology, better compatibility with scaling issues, and low cost, electrical detectors are capable of detecting single-molecules using simple instrumentation.

As depicted in Figure 1.12, nanoscale electrical detection can be performed longitudinally and/or transversely. In the case of longitudinal detection, the devices possess a single nanochannel connected to assess microchannels at the either ends (see Figure 1.12A). Biomolecules are detected by monitoring the blockage current generated when they obstruct the flux of ions while traveling through the nanochannel. This detection modality is similar to that utilized in nanopore sensing in that a single voltage source provides the required electrokinetic driving force for the introduction of the molecules into the nanochannel and the bias voltage for electrical current sensing. Using this approach, Kaji *et al*. (Kaji, '06) demonstrated the detection of λ-DNA in 1 M KCl solution in TBE buffer at pH 8. They utilized a PDMS based nanofluidic device possessing a single nanochannel, 15 μm long, 750 nm deep and 290 nm wide, fabricated by soft lithography from an FIB milled Si master (see Figure 1.12a for SEM image). The measured electrical resistance and peak-peak noise obtained in their nanochannel in the absence of the DNA were 57.2 ±0.3 MΩ and 30 pA, respectively. Transient drops in the current were observed as the DNA molecules electrokinetically travelled through the nanochannels. With longitudinal detection, it is theoretically possible to evaluate the electrophoretic mobilites and the length of DNA fragments from the translocation times and the magnitude of the change in current, respectively. However, to accurately quantify the fragment sizes, it is critical that the dimensions of the nanochannel be less than the persistent length of DNA molecule so as to

achieve a DNA extension ratio that is close to unity. Also, the length of the nanochannel may need to be as short as possible so as to minimize the electric field barrier for ease of DNA entry and maximize the current amplitude.

In the transverse electrical detection scheme, biomolecules are detected either by monitoring changes in the electrical conductance of the electrolyte within the detection volume when they occupy and displace ions of the electrolyte or by trapping them within them within the nanogap, forming molecular junctions/bridges and observing their electrical behaviors (*e.g.* resistance, impedance, capacitance, quantum mechanical tunneling, *etc*). For the case of electrical detection with transverse nanochannels (liquid-based electrodes), Menard *et al.* (Menard, '12) recently reported the detection of λ-DNA in 1 M and 125 mM KCl solutions in a fused silica nanofluidic device possessing two orthogonal, intersecting nanochannels; (i) a long nanochannel, through which DNA molecules were electrokinetically driven, and (ii) a relatively short transverse nanochannel through which the ionic conductance is monitored (see Figure 1.12b(i)). In their work, the authors developed two devices with the distance between the entrance of the transport channel and the intersection with the nanochannel respectively set at 26.6 μm (A) and 9.5 μm (B).

The authors observed current enhancements and reductions in the high and low ionic strength solutions, respectively, when the DNA molecules entered the intersection (detection region). The current amplitudes were 35 ±5 pA (~5% of baseline) and 271 ±53 pA (~27% of baseline) for the transient events in the respective devices A and B. While the distribution of event times in device A was distinctly Gaussian, with an average duration of 13 ±3 ms (0.27μs/bp), events distribution observed in Device B was broadened and skewed with an RSD of 53%. From their results, they estimated electrophoretic mobilities of 1.3×10^{-4} cm^2/Vs and 0.6

$\times 10^{-4}$ cm^2/Vs for device A and B respectively. The lower mobility in device B was attributed to the drag experienced by the molecule while still entering the nanochannel.

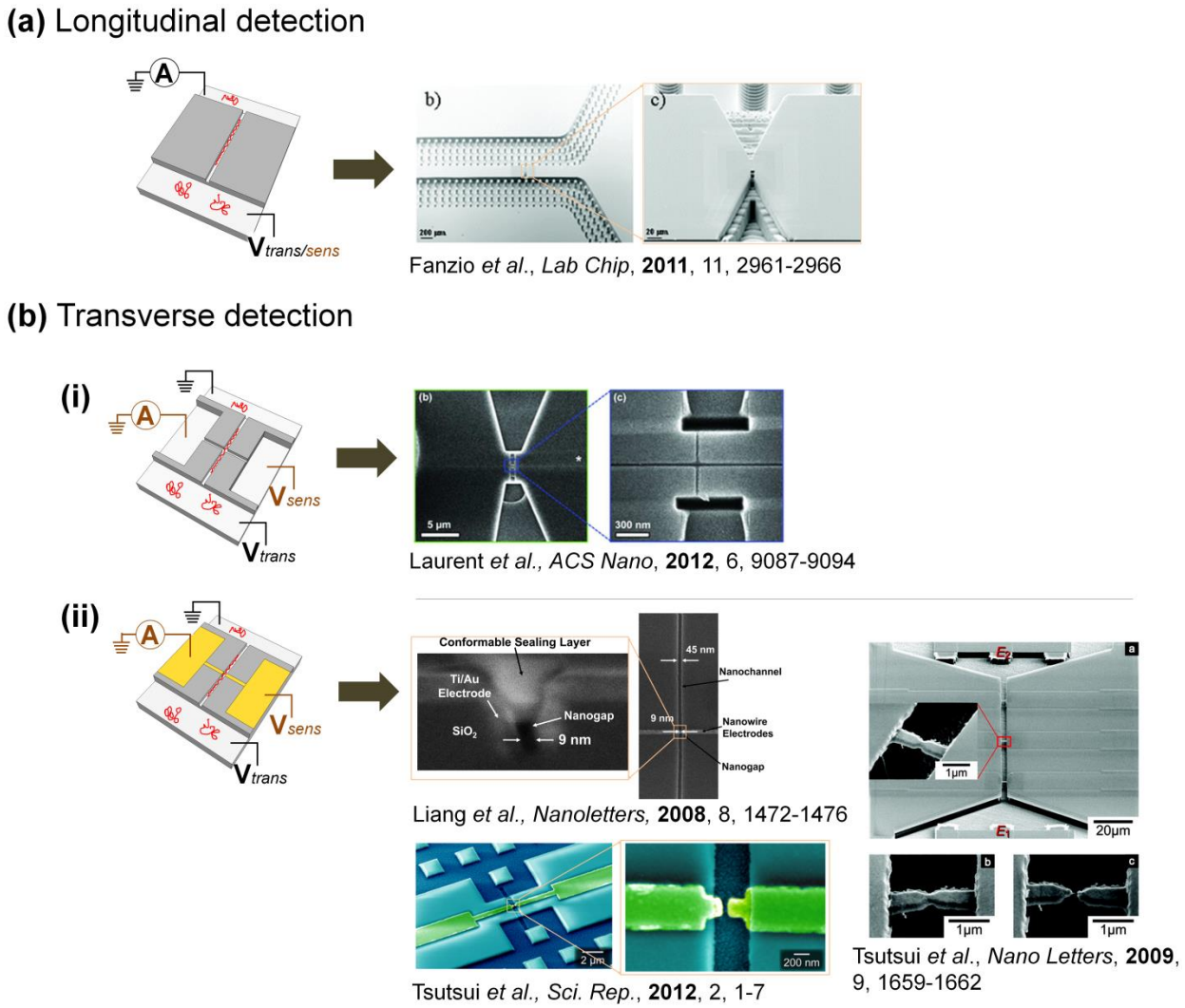

Figure 1.12 (a) A device for the longitudinal electrical detection of biomolecules with a single nanochannel connected to assess microchannels at both ends (b) A device for the transverse electrical detection of biomolecules possessing a single long nanochannel intersected with shorter nanochannels. Biomolecules generate blockage currents which are measured across the shorter nanochannels when they arrive at the intersection while electrokinetically travelling through the long nanochannels. (c) A device for the transverse electrical detection of biomolecules possessing a pair of nanometer sized metal electrodes positioned orthogonally across a single nanochannel. The nanoelectrodes are placed opposite to each other and separated by a nanometer gap. Biomolecules are detected via blockage or tunneling currents that are generated when they either block the ion-flux in the nanogap or are trapped at the nanogap to form a molecular junction, respectively

Furthermore, there have been several reports on the transverse electrical detection of biomolecules based on blockage current measurement. Liang *et al.* (Liang, '08) described the

fabrication and characterization of a nanogap detector within a 45 × 45 nm fluidic channel (50 μm length, 45 nm width and 45 nm depth) integrated with a pair of perpendicular Au electrodes of 45 nm width and 18 nm thickness with gap sizes ranging from 9 to 20 nm and heights 16 to 30 nm, respectively (see Figure 1.12b(ii)). The authors observed negative current pulses ~350 pA in the devices with nanogap cross section of 9 nm (gap) × 16 nm height with duration of ~100 μs for the DNAs that passed through the nanogap. Similarly, Kawai and co-workers developed a device with a nanogap 200 nm long, 50 nm wide and 60 nm deep for the detection of DNAs (Tsutsui, '12) and nanometer-sized particles (Tsutsui, '09) (see Figure 1.12b(ii)). DNA detection was performed in 0.1 M KCl and the current generated as a result of volume exclusion of buffer ions by DNA molecules was found to range between 35 and 75 pA with the translocation time ~0.5 ms (97 bp/μs). Both reports observed reductions in the electric current as the DNA passed through the nanogaps and explained this by the fact that DNA was more insulating than the buffer solution. However, to extend this detection scheme to smaller molecules, like nucleotides, for high resolution sensing, there is the need to further reduce the width and the depth of the gap and the flow speed of the biomolecules as they travel through the nanochannel.

1.7.2 Other applications of nanochannels

Taking advantage of the effects of streaming current and potential with flowing salt solutions, nanochannels have been used as electro-chemomechanical energy converters in batteries (Daiguji, '04) building on the report by Yang *et al.* (Yang, '03) in microchannels. When employing nanochannels, there was an increased efficiency of nearly two orders of magnitude compared to microchannels resulting from streaming currents generated within the electrical double layer of the ions and confined within the Debye length. In a similar fashion, nanochannels have been used to create nanofluidic transistors based on a metal-oxide-solution (MOSol) system, similar to a metal-oxide-semiconductor field-effect transistor (MOSFET) (Daiguji, '05).

It has been demonstrated that gate voltages are able to modulate the concentration of ions and molecules in a nanochannel and control ion conductance. Because the height of the nanochannel is on the order or smaller than the Debye length, the electric field created by the gate can penetrate the entire nanofluidic channel to precisely control ion flow. This technology has broad implications in integrated nanofluidic circuits for the manipulation of ions and biomolecules embedded within sub-femtoliter volumes (Perry, '06).

In addition, nanochannels have been applied in the development of high precision nanoengineered devices for long term zero-order release of drugs in therapeutic applications (drug delivery) (Sinha, '04), scanning nanolithography for material transport as well as distance regulation (Hong, '00), chemical experiments in a chip laboratory (Matsumoto, '98), capillary electrophoresis for chemical and biochemical analysis (Becker, '98), chemical sensing (Stern, '97), synthetic chemistry and protein dynamics in nanochannels (Gardeniers, '09) and the development of smart electrochemical nanofluidic devices (Rassaei, '11).

1.8 Overall dissertation outline

A summary of the chapters in this dissertation is presented below;

Chapter 2 – Surface charge, electroosmotic flow and DNA extension in chemically modified thermoplastic nanoslits and nanochannels.

In this chapter, we report the surface modification of thermoplastic nanochannels and an assessment of the associated surface charge density, zeta potential and electroosmotic flow (EOF). Mixed-scale fluidic networks were fabricated in poly (methylmethacrylate), PMMA. Oxygen plasma was used to generate surface-confined carboxylic acids with devices assembled using low temperature fusion bonding. Amination of the carboxylated surfaces using ethylenediamine (EDA) was accomplished via EDC coupling. XPS and ATR-FTIR revealed the presence of carboxyl and amine groups on the appropriately prepared surfaces. A modified

conductance equation for nanochannels was developed to determine their surface conductance and was found to be in good agreement with our experimental results. The measured surface charge density and zeta potential of these devices were lower than glass nanofluidic devices and dependent on the surface modification adopted, as well as the size of the channel. This property, coupled to an apparent increase in fluid viscosity due to nanoconfinement, contributed to the suppression of the EOF in PMMA nanofluidic devices by an order of magnitude compared to the micro-scale devices. Carboxylated PMMA nanochannels were efficient for the transport and elongation of λ-DNA while these same DNA molecules were unable to translocate through aminated nanochannels.

Chapter 3 – High process yields of thermoplastic nanofluidic devices using a hybrid thermal assembly technique

In this chapter, we report a novel hybrid assembly approach developed for the generation of functional thermoplastic nanofluidic devices. One major challenge associated with the development of thermoplastic nanofluidic devices is the assembly of the device, which consists of sealing a cover plate to the fluidic substrate. Typically, channel collapse or substrate dissolution results when sealing the nanofluidic substrate with the cover plate making the device inoperable. Our assembly technique involves thermally sealing a high T_g (glass transition temperature) substrate containing the nanofluidic structures to a cover plate possessing a lower T_g. For demonstration, nanofluidic devices with depths ranging between 35 nm and 250 nm were fabricated in a thermoplastic substrate (T_g = 104^{o}C) and sealed with a cover plate (T_g = 75^{o}C), possessing better optical properties than the substrate. Results obtained from sealing tests revealed that the integrity of the nanochannels remained intact after bonding and devices were useful for fluorescent imaging at high signal-to-noise. The functionality of the assembled devices

was demonstrated by studying the stretching and translocation dynamics of dsDNA in the enclosed nanofluidic channels.

Chapter 4 – Electrical detection of DNA molecules in nanofluidic devices

In this chapter, we report both the longitudinal and transverse electrical detection of DNA in polymer and fused Silica based nanofluidic devices, respectively. Nanofabrication techniques adopted for the development of the nanoelectrodes and the amplifier circuits utilized for electrical sensing were adequately described. We present results from theoretical computations performed to describe the variation of the Signal-to-Noise with the nano-electrode area and nano-gap size and show some preliminary data obtained from the transverse electrical measurement of DNA molecules using Au and Pt based nanoelectrodes.

Chapter 5 – Ongoing and Future work

In this chapter, we present a proposed sequencing scheme involving the use of dual nanoelectrodes for sequencing based on the flight times (ToF) of the clipped monomer units electrokinetically introduced into a separation nanochannel. We also describe ongoing work involving the development of nanofluidic circuits for manipulation and shaping of DNA molecules and present an alternative fabrication scheme currently being investigated for the development of nanoelectrode in insulating substrates.

REFERENCES

Abgrall, P.; Nguyen, N. T. Nanofluidic Devices and Their Applications. *Analytical Chemistry* 2008, 80, 2326-2341.

Alberghi.Je; Broudy, R. M. Surface Conductivity on Degenerate Germanium. *Physical review letters* 1966, 17, 863-&.

Alkafeef, S. F.; Alajmi, A. F. Streaming potentials and conductivities of reservoir rock cores in aqueous and non-aqueous liquids. *Colloids and Surfaces A: Physicochemical and Engineering Aspects* 2006, 289, 141-148.

Baday, M.; Cravens, A.; Hastie, A.; Kim, H.; Kudeki, D. E.; Kwok, P.-Y.; Xiao, M.; Selvin, P. R. Multicolor Super-Resolution DNA Imaging for Genetic Analysis. *Nano Letters* 2012, 12, 3861-3866.

Baldessari, F.; Santiago, J. Electrophoresis in nanochannels: brief review and speculation. *Journal of Nanobiotechnology* 2006, 4, 12.

Bard, A. J. *Electrochemical Methods: Fundamentals and Applications*. Second ed.; Wiley New York, 2001; p 856.

Baumann, C. G.; Smith, S. B.; Bloomfield, V. A.; Bustamante, C. Ionic effects on the elasticity of single DNA molecules. *Proceedings of the National Academy of Sciences* 1997, 94, 6185-6190.

Baumgärtner, A. Excluded volume effect on polymer films. *Polymer* 1982, 23, 334-335.

Bayley, H.; Martin, C. R. Resistive-Pulse SensingFrom Microbes to Molecules. *Chemical Reviews* 2000, 100, 2575-2594.

Becker, H. Planar quartz chips with submicron channels for two-dimensional capillary electrophoresis applications. *J. Micromech. Microeng.* 1998, 8, 24-28.

Beech, J. P.; Holm, S. H.; Adolfsson, K.; Tegenfeldt, J. O. Sorting cells by size, shape and deformability. *Lab on a Chip* 2012, 12, 1048-1051.

Bensimon, D.; Simon, A. J.; Croquette, V.; Bensimon, A. Stretching DNA with a Receding Meniscus: Experiments and Models. *Physical Review Letters* 1995, 74, 4754-4757.

Bikerman, J. J. Ionic theory of electroosmosis, the current flow and the surface conductivity. *Zeitschrift Fur Physikalische Chemie-Abteilung a-Chemische Thermodynamik Kinetik Elektrochemie Eigenschaftslehre* 1933, 163, 378-394.

Binnig, G.; Rohrer, H.; Gerber, C.; Weibel, E. Surface Studies by Scanning Tunneling Microscopy. *Physical review letters* 1982, 49, 57.

Brody, J. R.; Kern, S. E. History and principles of conductive media for standard DNA electrophoresis. *Analytical Biochemistry* 2004, 333, 1-13.

Broers, A. N.; Hoole, A. C. F.; Ryan, J. M. Electron beam lithography--Resolution limits. *Microelectronic Engineering* 1996, 32, 131-142.

Brown, L.; Koerner, T.; Horton, J. H.; Oleschuk, R. D. Fabrication and characterization of poly(methylmethacrylate) microfluidic devices bonded using surface modifications and solvents. *Lab on a Chip* 2006, 6, 66-73.

Cabodi, M.; Turner, S. W. P.; Craighead, H. G. Entropic Recoil Separation of Long DNA Molecules. *Analytical Chemistry* 2002, 74, 5169-5174.

Cao, H.; Tegenfeldt, J. O.; Austin, R. H.; Chou, S. Y. Gradient nanostructures for interfacing microfluidics and nanofluidics. *Applied Physics Letters* 2002, 81, 3058-3060.

Chantiwas, R.; Park, S.; Soper, S. A.; Kim, B. C.; Takayama, S.; Sunkara, V.; Hwang, H.; Cho, Y.-K. Flexible fabrication and applications of polymer nanochannels and nanoslits. *Chemical Society Reviews* 2011, 40, 3677-3702.

Chen, M.; Chen, Y.; Zhong, W.; Yang, J. Molecular dynamics simulation of ion transport in a nanochannel. *Science in China Series E: Technological Sciences* 2008, 51, 921-931.

Cheng, E.; Zou, H.; Yin, Z.; Jurcicek, P.; Zhang, X. Fabrication of 2D polymer nanochannels by sidewall lithography and hot embossing. *J. Micromech. Microeng.* 2013, 23.

Chou, S. Y.; Krauss, P. R. Imprint lithography with sub-10 nm feature size and high throughput. *Microelectronic Engineering* 1997, 35, 237-240.

Chou, S. Y.; Krauss, P. R.; Renstrom, P. J. Imprint of sub-25 nm vias and trenches in polymers. *Applied Physics Letters* 1995, 67, 3114-3116.

Chou, S. Y.; Krauss, P. R.; Renstrom, P. J. Nanoimprint lithography. *Journal of Vacuum Science & Technology B* 1996, 14, 4129-4133.

Conlisk, A. T. The Debye-Huckel approximation: Its use in describing electroosmotic flow in micro- and nanochannels. *Electrophoresis* 2005, 26, 1896-1912.

Coury, L. Conductance Measurements Part 1: Theory. *Current Separations* 1999, 18, 91-96.

Daiguji, H.; Oka, Y.; Shirono, K. Nanofluidic Diode and Bipolar Transistor. *Nano Letters* 2005, 5, 2274-2280.

Daiguji, H.; Yang, P.; Szeri, A. J.; Majumdar, A. Electrochemomechanical Energy Conversion in Nanofluidic Channels. *Nano Letters* 2004, 4, 2315-2321.

Danelon, C.; Santschi, C.; Brugger, J.; Vogel, H. Fabrication and Functionalization of Nanochannels by Electron-Beam-Induced Silicon Oxide Deposition†. *Langmuir* 2006, 22, 10711-10715.

Das, S. K.; Austin, M. D.; Akana, M. C.; Deshpande, P.; Cao, H.; Xiao, M. Single molecule linear analysis of DNA in nano-channel labeled with sequence specific fluorescent probes. *Nucleic Acids Research* 2010, 38, e177.

de la Escosura-Muñiz, A.; Merkoçi, A. Nanochannels Preparation and Application in Biosensing. *ACS Nano* 2012, 6, 7556-7583.

Derjaguin, B. V.; Titijevskaia, A. S.; Abricossova, II; Malkina, A. D. Investigations of the forces of Interaction of Surfaces in Different Media and their Application to the Problem of Colloid Stability. *Discussions of the Faraday Society* 1954, 24-41.

Dobisz, E. A.; Marrian, C. R. K. Sub-30-nm Lithography in a Negative Electron-Beam Resist with a Vacuum Scanning Tunneling Microscope. *Applied Physics Letters* 1991, 58, 2526-2528.

Doherty, E. A. S.; Meagher, R. J.; Albarghouthi, M. N.; Barron, A. E. Microchannel wall coatings for protein separations by capillary and chip electrophoresis. *Electrophoresis* 2003, 24, 34-54.

Douville, N.; Huh, D.; Takayama, S. DNA linearization through confinement in nanofluidic channels. *Anal Bioanal Chem* 2008, 391, 2395-2409.

Du, Y.; Lo, E.; Vidula, M. K.; Khabiry, M.; Khademhosseini, A. Method of Bottom-Up Directed Assembly of Cell-Laden Microgels. *Cellular and Molecular Bioengineering* 2008, 1, 157-162.

Duan, C.; Wang, W.; Xie, Q. Review article: Fabrication of nanofluidic devices. *Biomicrofluidics* 2013, 7, -.

Effenhauser, C. S.; Bruin, G. J. M.; Paulus, A.; Ehrat, M. Integrated Capillary Electrophoresis on Flexible Silicone Microdevices: Analysis of DNA Restriction Fragments and Detection of Single DNA Molecules on Microchips. *Analytical Chemistry* 1997, 69, 3451-3457.

Eijkel, J. C. T.; van den Berg, A. Nanofluidics: what is it and what can we expect from it? *Microfluid. Nanofluid.* 2005, 1, 249-267.

Erickson, D.; Li, D. Analysis of Alternating Current Electroosmotic Flows in a Rectangular Microchannel. *Langmuir* 2003, 19, 5421-5430.

F, R. F. *Memoires de la Societe Imperiale des Naturalsites de Moscou* 1809, 2, 327.

Fang Lim, S.; Karpusenko, A.; Sakon, J. J.; Hook, J. A.; Lamar, T. A.; Riehn, R. DNA methylation profiling in nanochannels. *Biomicrofluidics* 2011, 5.

Fu, J.; Mao, P.; Han, J. Nanofilter array chip for fast gel-free biomolecule separation. *Applied Physics Letters* 2005, 87, -.

Gad-el-Hak, M. The fluid mechanics of microdevices - The Freeman Scholar Lecture. *Journal of Fluids Engineering-Transactions of the Asme* 1999, 121, 5-33.

Garcia, A. L.; Ista, L. K.; Petsev, D. N.; O'Brien, M. J.; Bisong, P.; Mammoli, A. A.; Brueck, S. R. J.; Lopez, G. P. Electrokinetic molecular separation in nanoscale fluidic channels. *Lab on a Chip* 2005, 5, 1271-1276.

Gardeniers, H. G. E. Chemistry in nanochannel confinement. *Anal Bioanal Chem* 2009, 394, 385-397.

Gilges, M.; Kleemiss, M. H.; Schomburg, G. Capillary Zone Electrophoresis Separations of Basic and Acidic Proteins Using Poly(vinyl alcohol) Coatings in Fused Silica Capillaries. *Analytical Chemistry* 1994, 66, 2038-2046.

Gu, Y.; Li, D. The [zeta]-Potential of Glass Surface in Contact with Aqueous Solutions. *Journal of Colloid and Interface Science* 2000, 226, 328-339.

Han, J.; Craighead, H. G. Entropic trapping and sieving of long DNA molecules in a nanofluidic channel. *Journal of Vacuum Science & Technology A* 1999, 17, 2142-2147.

Han, J.; Craighead, H. G. Separation of Long DNA Molecules in a Microfabricated Entropic Trap Array. *Science* 2000, 288, 1026-1029.

Hays, J. B.; Magar, M. E.; Zimm, B. H. Persistence Length of DNA. *Biopolymers* 1969, 8, 531-&.

Hong, M.-H.; Kim, K. H.; Bae, J.; Jhe, W. Scanning nanolithography using a material-filled nanopipette. *Applied Physics Letters* 2000, 77, 2604-2606.

Huh, D.; Mills, K. L.; Zhu, X. Y.; Burns, M. A.; Thouless, M. D.; Takayama, S. Tuneable elastomeric nanochannels for nanofluidic manipulation. *Nat. Mater.* 2007, 6, 424-428.

Hwang, S.-J.; Tseng, M.-C.; Shu, J.-R.; Her Yu, H. Surface modification of cyclic olefin copolymer substrate by oxygen plasma treatment. *Surface and Coatings Technology* 2008, 202, 3669-3674.

J.Lyklema. *Fundamentals of Interface and Colloid Science. Vol. 2 - Solid-Liquid Interfaces*. First Edition ed.; Academic Press: London, England, 1995; Vol. Volume 2.

Jönsson, P.; Gunnarsson, A.; Höök, F. Accumulation and Separation of Membrane-Bound Proteins Using Hydrodynamic Forces. *Analytical Chemistry* 2010, 83, 604-611.

Jorgenson, J. W.; Lukacs, K. D. Zone Electrophoresis in Open-Tubular Glass-Capillaries. *Analytical Chemistry* 1981, 53, 1298-1302.

Kaji, N.; Ogawa, R.; Oki, A.; Horiike, Y.; Tokeshi, M.; Baba, Y. Study of water properties in nanospace. *Analytical & Bioanalytical Chemistry* 2006, 386, 759-764.

Kaji, N.; Ogawa, R.; Oki, A.; Horiike, Y.; Tokeshi, M.; Baba, Y. Study of water properties in nanospace. *Anal Bioanal Chem* 2006, 386, 759-764.

Kalman, E. B.; Vlassiouk, I.; Siwy, Z. S. Nanofluidic Bipolar Transistors. *Advanced Materials* 2008, 20, 293-297.

Karnik, R.; Castelino, K.; Fan, R.; Yang, P.; Majumdar, A. Effects of Biological Reactions and Modifications on Conductance of Nanofluidic Channels. *Nano Letters* 2005, 5, 1638-1642.

Kemery, P. J.; Steehler, J. K.; Bohn, P. W. Electric Field Mediated Transport in Nanometer Diameter Channels. *Langmuir* 1998, 14, 2884-2889.

Kim, S.; Gottfried, A.; Lin, R. R.; Dertinger, T.; Kim, A. S.; Chung, S.; Colyer, R. A.; Weinhold, E.; Weiss, S.; Ebenstein, Y. Enzymatically Incorporated Genomic Tags for Optical Mapping of DNA-Binding Proteins. *Angewandte Chemie International Edition* 2012, 51, 3578-3581.

Kim, S. J.; Wang, Y.-C.; Lee, J. H.; Jang, H.; Han, J. Concentration Polarization and Nonlinear Electrokinetic Flow near a Nanofluidic Channel. *Physical Review Letters* 2007, 99, 044501.

Kirby, B. J.; Hasselbrink, E. F. Zeta potential of microfluidic substrates: 1. Theory, experimental techniques, and effects on separations. *Electrophoresis* 2004, 25, 187-202.

Krishnan, M.; Mönch, I.; Schwille, P. Spontaneous Stretching of DNA in a Two-Dimensional Nanoslit. *Nano Letters* 2007, 7, 1270-1275.

Kuo, T.-C.; Sloan, L. A.; Sweedler, J. V.; Bohn, P. W. Manipulating Molecular Transport through Nanoporous Membranes by Control of Electrokinetic Flow: Effect of Surface Charge Density and Debye Length. *Langmuir* 2001, 17, 6298-6303.

Lam, E. T.; Hastie, A.; Lin, C.; Ehrlich, D.; Das, S. K.; Austin, M. D.; Deshpande, P.; Cao, H.; Nagarajan, N.; Xiao, M.; Kwok, P.-Y. Genome mapping on nanochannel arrays for structural variation analysis and sequence assembly. *Nat Biotech* 2012, 30, 771-776.

Lasse, H. T.; Anna, K.; Anders, K. Stretching DNA in polymer nanochannels fabricated by thermal imprint in PMMA. *Nanotechnology* 2008, 19, 125301.

Levy-Sakin, M.; Ebenstein, Y. Beyond sequencing: optical mapping of DNA in the age of nanotechnology and nanoscopy. *Current Opinion in Biotechnology* 2013, 24, 690-698.

Li, Y.; Xu, J.; Li, D. Molecular dynamics simulation of nanoscale liquid flows. *Microfluid. Nanofluid.* 2010, 9, 1011-1031.

Liang, X.; Chou, S. Y. Nanogap Detector Inside Nanofluidic Channel for Fast Real-Time Label-Free DNA Analysis. *Nano Letters* 2008, 8, 1472-1476.

Lyklema, J.; Minor, M. On surface conduction and its role in electrokinetics. *Colloids and Surfaces A: Physicochemical and Engineering Aspects* 1998, 140, 33-41.

Maleki, T.; Mohammadi, S.; Ziaie, B. A nanofluidic channel with embedded transverse nanoelectrodes. *Nanotechnology* 2009, 20, 105302.

Manning, G. S. The persistence length of DNA is reached from the persistence length of its null isomer through an internal electrostatic stretching force. *Biophysical Journal* 2006, 91, 3607-3616.

Manning, G. S. Three persistence lengths for a stiff polymer with an application to DNA B-Z junctions. *Biopolymers* 1988, 27, 1529-1542.

Marrian, C. R. K.; Dobisz, E. A.; Dagata, J. A. Electron-Beam Lithography with the Scanning Tunneling Microscope. *Journal of Vacuum Science & Technology B* 1992, 10, 2877-2881.

Martins, D. C.; Chu, V.; Conde, J. P. The effect of the surface functionalization and the electrolyte concentration on the electrical conductance of silica nanochannels. *Biomicrofluidics* 2013, 7, -.

Matsumoto, K.; Kawakami, T.; Nakao, M.; Hatamura, Y.; Kitamori, T.; Sawada, T. In *Nano-channel on quartz-chip laboratory using single molecular detectable thermal lens microscope*, Micro Electro Mechanical Systems, 1998. MEMS 98. Proceedings., The Eleventh Annual International Workshop on, 25-29 Jan 1998; 1998; pp 127-130.

Mazumder, N.; Gogoi, A.; Kalita, R. D.; Ahmed, G. A.; Buragohain, A. K.; Choudhury, A. Luminescence studies of fresh water diatom frustules. *Indian Journal of Physics* 2010, 84, 665-669.

Meisenberg, G. *Principles of medical biochemistry*. Mosby Elsevier: Philadelphia, 2006.

Menard, L. D.; Mair, C. E.; Woodson, M. E.; Alarie, J. P.; Ramsey, J. M. A Device for Performing Lateral Conductance Measurements on Individual Double-Stranded DNA Molecules. *ACS Nano* 2012, 6, 9087-9094.

Menard, L. D.; Ramsey, J. M. Fabrication of Sub-5 nm Nanochannels in Insulating Substrates Using Focused Ion Beam Milling. *Nano Letters* 2011, 11, 512-517.

Michaeli, Y.; Ebenstein, Y. Channeling DNA for optical mapping. *Nat Biotech* 2012, 30, 762-763.

Mijatovic, D.; Eijkel, J. C. T.; van den Berg, A. Technologies for nanofluidic systems: top-down vs. bottom-up-a review. *Lab on a Chip* 2005, 5, 492-500.

Mills, K. L.; Huh, D.; Takayama, S.; Thouless, M. D. Instantaneous fabrication of arrays of normally closed, adjustable, and reversible nanochannels by tunnel cracking. *Lab on a Chip* 2010, 10, 1627-1630.

Minerick, A. R.; Ostafin, A. E.; Chang, H.-C. Electrokinetic transport of red blood cells in microcapillaries. *Electrophoresis* 2002, 23, 2165-2173.

Moran, W.; Chi-Chang, C.; Yang, R.-J. Electroviscous effects in nanofluidic channels. *Journal of Chemical Physics* 2010, 132, 024701.

Movahed, S.; Li, D. Electrokinetic transport through nanochannels. *ELECTROPHORESIS* 2011, 32, 1259-1267.

Neely, R. K.; Dedecker, P.; Hotta, J.-i.; Urbanaviciute, G.; Klimasauskas, S.; Hofkens, J. DNA fluorocode: A single molecule, optical map of DNA with nanometre resolution. *Chemical Science* 2010, 1, 453-460.

Nikolova, D.; Dayss, E.; Leps, G.; Wutzler, A. Surface modification of cycloolefinic copolymers for optimization of the adhesion to metals. *Surface and Interface Analysis* 2004, 36, 689-693.

Oddy, M. H.; Santiago, J. G. A method for determining electrophoretic and electroosmotic mobilities using AC and DC electric field particle displacements. *Journal of Colloid and Interface Science* 2004, 269, 192-204.

Odijk, T. DNA confined in nanochannels: Hairpin tightening by entropic depletion. *Journal of Chemical Physics* 2006, 125.

Odijk, T. On the Statistics and Dynamics of Confined or Entangled Stiff Polymers. *Macromolecules* 1983, 16, 1340-1344.

Orland, H. Flory Theory Revisited. *Journal De Physique I* 1994, 4, 101-114.

Paul, P. H.; Garguilo, M. G.; Rakestraw, D. J. Imaging of Pressure- and Electrokinetically Driven Flows through Open Capillaries. *Analytical Chemistry* 1998, 70, 2459-2467.

Pennathur, S.; Baldessari, F.; Santiago, J. G.; Kattah, M. G.; Steinman, J. B.; Utz, P. J. Free-Solution Oligonucleotide Separation in Nanoscale Channels. *Analytical Chemistry* 2007, 79, 8316-8322.

Pennathur, S.; Santiago, J. Electrokinetic transport in nanochannels. 1. Theory. *Anal Chem* 2005, 77, 6772 - 6781.

Pennathur, S.; Santiago, J. G. Electrokinetic Transport in Nanochannels. 1. Theory. *Analytical Chemistry* 2005, 77, 6772-6781.

Pennathur, S.; Santiago, J. G. Electrokinetic Transport in Nanochannels. 2. Experiments. *Analytical Chemistry* 2005, 77, 6782-6789.

Perevert.Vd; Zapkov, V. T. Nature of a Surface Conductivity for Mica. *Izvestiya Vysshikh Uchebnykh Zavedenii Fizika* 1972, 121-&.

Perry, J.; Kandlikar, S. Review of fabrication of nanochannels for single phase liquid flow. *Microfluid. Nanofluid.* 2006, 2, 185-193.

Piruska, A.; Gong, M.; Sweedler, J. V.; Bohn, P. W. Nanofluidics in chemical analysis. *Chemical Society Reviews* 2010, 39, 1060-1072.

Piruska, A.; Nikcevic, I.; Lee, S. H.; Ahn, C.; Heineman, W. R.; Limbach, P. A.; Seliskar, C. J. The autofluorescence of plastic materials and chips measured under laser irradiation. *Lab on a Chip* 2005, 5, 1348-1354.

Qiao, R.; Aluru, N. R. Scaling of Electrokinetic Transport in Nanometer Channels. *Langmuir* 2005, 21, 8972-8977.

Qin, D.; Xia, Y. N.; Whitesides, G. M. Soft lithography for micro- and nanoscale patterning. *Nature Protocols* 2010, 5, 491-502.

Rassaei, L.; Singh, P. S.; Lemay, S. G. Lithography-Based Nanoelectrochemistry. *Analytical Chemistry* 2011, 83, 3974-3980.

Reischl, M.; Stana-Kleinschek, K.; Ribitsch, V. Adsorption of surfactants on polymer surfaces investigated with a novel zeta-potential measurement system. In *Advanced Materials Forum Iii, Pts 1 and 2*, Vilarinho, P. M., Ed. 2006; Vol. 514-516, pp 1374-1378.

Reisner, W.; Beech, J. P.; Larsen, N. B.; Flyvbjerg, H.; Kristensen, A.; Tegenfeldt, J. O. Nanoconfinement-enhanced conformational response of single DNA molecules to changes in ionic environment. *Physical review letters* 2007, 99.

Reisner, W.; Morton, K. J.; Riehn, R.; Wang, Y. M.; Yu, Z.; Rosen, M.; Sturm, J. C.; Chou, S. Y.; Frey, E.; Austin, R. H. Statics and Dynamics of Single DNA Molecules Confined in Nanochannels. *Physical Review Letters* 2005, 94, 196101.

Revil, A.; Glover, P. W. J. Nature of surface electrical conductivity in natural sands, sandstones, and clays. *Geophysical Research Letters* 1998, 25, 691-694.

Rice, C. L.; Whitehead, R. Electrokinetic Flow in a Narrow Cylindrical Capillary. *The Journal of Physical Chemistry* 1965, 69, 4017-4024.

Riehn, R.; Lu, M.; Wang, Y.-M.; Lim, S. F.; Cox, E. C.; Austin, R. H. Restriction mapping in nanofluidic devices. *Proceedings of the National Academy of Sciences of the United States of America* 2005, 102, 10012-10016.

Ross, D.; Gaitan, M.; Locascio, L. E. Temperature Measurement in Microfluidic Systems Using a Temperature-Dependent Fluorescent Dye. *Analytical Chemistry* 2001, 73, 4117-4123.

Roy, S.; Yue, C. Y.; Lam, Y. C.; Wang, Z. Y.; Hu, H. Surface analysis, hydrophilic enhancement, ageing behavior and flow in plasma modified cyclic olefin copolymer (COC)-based microfluidic devices. *Sensors and Actuators B: Chemical* 2010, 150, 537-549.

Salavati-Niasari, M. Host (nanopores of zeolite-Y)/guest (Ni(II)-tetraoxo dithia tetraaza macrocyclic complexes) nanocomposite materials: template synthesis and

characterization. *Journal of Inclusion Phenomena and Macrocyclic Chemistry* 2008, 62, 65-73.

Schaefer, D. W.; Joanny, J. F.; Pincus, P. Dynamics of Semiflexible Polymers in Solution. *Macromolecules* 1980, 13, 1280-1289.

Schellman, J. A.; Stigter, D. Electrical double layer, zeta potential, and electrophoretic charge of double-stranded DNA. *Biopolymers* 1977, 16, 1415-1434.

Schoch, R. B.; Bertsch, A.; Renaud, P. pH-Controlled Diffusion of Proteins with Different pI Values Across a Nanochannel on a Chip. *Nano Letters* 2006, 6, 543-547.

Schoch, R. B.; Han, J.; Renaud, P. Transport phenomena in nanofluidics. *Reviews of Modern Physics* 2008, 80, 839-883.

Shao, P. E.; van Kan, A.; Wang, L. P.; Ansari, K.; Bettiol, A. A.; Watt, F. Fabrication of enclosed nanochannels in poly(methylmethacrylate) using proton beam writing and thermal bonding. *Applied Physics Letters* 2006, 88, -.

Shenton, M. J.; Lovell-Hoare, M. C.; Stevens, G. C. Adhesion enhancement of polymer surfaces by atmospheric plasma treatment. *Journal of Physics D: Applied Physics* 2001, 34, 2754.

Sinha, P. M. Nanoengineered device for drug delivery application. *Nanotechnology* 2004, 15, S585-S589.

Squires, T. M.; Bazant, M. Z. Induced-charge electro-osmosis. *Journal of Fluid Mechanics* 2004, 509, 217-252.

Stec, K.; Szroeder, P.; Benzhour, K. High Temperature Surface Conductivity of Hydrogenated Diamond Films Exposed to Humid Air. *Acta Physica Polonica A* 2010, 118, 511-514.

Stern, M. B.; Geis, M. W.; Curtin, J. E. Nanochannel fabrication for chemical sensors. *Journal of Vacuum Science & Technology B* 1997, 15, 2887-2891.

Sze, A.; Erickson, D.; Ren, L. Q.; Li, D. Q. Zeta-potential measurement using the Smoluchowski equation and the slope of the current-time relationship in electroosmotic flow. *Journal of Colloid and Interface Science* 2003, 261, 402-410.

Tas, N. R.; Haneveld, J.; Jansen, H. V.; Elwenspoek, M.; van den Berg, A. Capillary filling speed of water in nanochannels. *Applied Physics Letters* 2004, 85, 3274-3276.

Tegenfeldt, J. O.; Prinz, C.; Cao, H.; Chou, S.; Reisner, W. W.; Riehn, R.; Wang, Y. M.; Cox, E. C.; Sturm, J. C.; Silberzan, P.; Austin, R. H. The dynamics of genomic-length DNA molecules in 100-nm channels. *Proceedings of the National Academy of Sciences of the United States of America* 2004, 101, 10979-10983.

Tsao, C. W.; Hromada, L.; Liu, J.; Kumar, P.; DeVoe, D. L. Low temperature bonding of PMMA and COC microfluidic substrates using UV/ozone surface treatment. *Lab on a Chip* 2007, 7, 499-505.

Tsutsui, M.; He, Y.; Furuhashi, M.; Rahong, S.; Taniguchi, M.; Kawai, T. Transverse electric field dragging of DNA in a nanochannel. *Sci. Rep.* 2012, 2.

Tsutsui, M.; Taniguchi, M.; Kawai, T. Transverse Field Effects on DNA-Sized Particle Dynamics. *Nano Letters* 2009, 9, 1659-1662.

Turner, S. W.; Cabodi, M.; Craighead, H. G. Confinement-induced entropic recoil of single DNA molecules in a nanofluidic structure. *Physical review letters* 2002, 88, 128103.

Turner, S. W. P.; Cabodi, M.; Craighead, H. G. Confinement-Induced Entropic Recoil of Single DNA Molecules in a Nanofluidic Structure. *Physical Review Letters* 2002, 88, 128103.

Venter, J. C. The sequence of the human genome (vol 291, pg 1304, 2001). *Science* 2002, 295, 1466-1466.

Venter, J. C. The sequence of the human genome (vol 292, pg 1304, 2001). *Science* 2001, 292, 1838-1838.

Venter, J. C.; Adams, M. D.; Myers, E. W.; Li, P. W.; Mural, R. J.; Sutton, G. G.; Smith, H. O.; Yandell, M.; Evans, C. A.; Holt, R. A.; Gocayne, J. D.; Amanatides, P.; Ballew, R. M.; Huson, D. H.; Wortman, J. R., *et al.* The sequence of the human genome. *Science* 2001, 291, 1304-+.

Vesel, A.; Mozetic, M. Surface modification and ageing of PMMA polymer by oxygen plasma treatment. *Vacuum* 2012, 86, 634-637.

Watson, J. D.; Crick, F. H. C. Molecular Structure of Nucleic Acids: A Structure for Deoxyribose Nucleic Acid. *Nature* 1953, 171, 737-738.

Werner, C.; Jacobasch, H. J. Surface characterization of polymers for medical devices. *International Journal of Artificial Organs* 1999, 22, 160-176.

Werner, C.; Körber, H.; Zimmermann, R.; Dukhin, S.; Jacobasch, H.-J. Extended Electrokinetic Characterization of Flat Solid Surfaces. *Journal of Colloid and Interface Science* 1998, 208, 329-346.

Whitesides, G. M.; Gates, B.; Mayers, B.; Xu, Q. B. Soft lithography and nanofabrication. *Abstracts of Papers of the American Chemical Society* 2005, 229, 204-POLY.

Woods, L. A.; Gandhi, P. U.; Ewing, A. G. Electrically Assisted Sampling across Membranes with Electrophoresis in Nanometer Inner Diameter Capillaries. *Analytical Chemistry* 2005, 77, 1819-1823.

Xia, D.; Yan, J.; Hou, S. Fabrication of Nanofluidic Biochips with Nanochannels for Applications in DNA Analysis. *Small* 2012, 8, 2787-2801.

Xu, F.; Datta, P.; Wang, H.; Gurung, S.; Hashimoto, M.; Wei, S.; Goettert, J.; McCarley, R. L.; Soper, S. A. Polymer Microfluidic Chips with Integrated Waveguides for Reading Microarrays. *Analytical Chemistry* 2007, 79, 9007-9013.

Xuan, X. L., D. . Electrokinetic transport of charged solutes in micro- and nanochannels: The influence of transverse electromigration. *Electrophoresis* 2006, 27, 5020-5031.

Yamanaka, S.; Yano, R.; Usami, H.; Hayashida, N.; Ohguchi, M.; Takeda, H.; Yoshino, K. Optical properties of diatom silica frustule with special reference to blue light. *Journal of Applied Physics* 2008, 103.

Yang, J. Electrokinetic microchannel battery by means of electrokinetic and microfluidic phenomena. *J. Micromech. Microeng.* 2003, 13, 963-970.

Yang, S. C. Effects of surface roughness and interface wettability on nanoscale flow in a nanochannel. *Microfluid. Nanofluid.* 2006, 2, 501-511.

Yuan, Z.; Garcia, A. L.; Lopez, G. P.; Petsev, D. N. Electrokinetic transport and separations in fluidic nanochannels. *Electrophoresis* 2007, 28, 595-610.

Zangle, T. A.; Mani, A.; Santiago, J. G. Theory and experiments of concentration polarization and ion focusing at microchannel and nanochannel interfaces. *Chemical Society Reviews* 2010, 39, 1014-1035.

CHAPTER 2: SURFACE CHARGE, ELECTROOSMOTIC FLOW AND DNA EXTENSION IN CHEMICALLY MODIFIED THERMOPLASTIC NANOSLITS AND NANOCHANNELS[1]

Introduction

Fluidic channels with one or two dimensions in the nanometer scale, nanoslits or nanochannels, respectively, have generated great interest because of unique phenomena that occurs in nano-confined space such as nanocapillarity (van Honschoten, '10), concentration polarization (Anand, '11; Mani, '09) and electrical double layer (EDL) overlap (Kim, '09; Kim, '07; Pu, '04; Wang, '05). These properties arise when the channel size is comparable to either the length scales of electrostatic interactions in solution or the size of the molecules being transported through them. Some of the interesting applications that arise from the use of nanochannels include single-molecule analysis (Craighead, '06; Craighead, '03; Menard, '12; Saleh, '03), molecular pre-concentration (Zangle, '10), chemical analyses of mass-limited samples (Piruska, '10; Tsukahara, '10), DNA electrophoresis (Keyser, '10; Menard, '13; Pennathur, '07), desalination (Kim, '13), nanofluidic diodes (Cheng, '10), real-time probing of biomolecules (Levy, '10; Levy, '08; Liang, '08; Persson, '10; Reccius, '05), ionic transport (Daiguji, '10) and entropic trapping for DNA separations (Han, '00). Controlled fabrication of nanochannels has facilitated the study of charge-based phenomena like ion enrichment and depletion and surface-charge-governed transport (Karnik, '05; Plecis, '05; Stein, '04).

---

[1]This chapter previously appeared as an article in Analyst (RSC). The original citation is as follows: Uba, F. I.; Pullagurla, S.; Sirasunthorn, N.; Wu, J.; Park, S.; Chantiwas, R.; Cho, Y.-K.; Shin, H.; Soper, S. A. "Surface charge, electroosmotic flow and DNA extension in chemically modified thermoplastic nanoslits and nanochannels," *Analyst* (September 2014) 139.

As described by Chantiwas *et al.* (Chantiwas, '11), thermoplastic nanofluidic devices offer an attractive alternative to glass/quartz devices due to the materials' diverse physiochemical properties and the fabrication techniques available to design the prerequisite structures. A commonly employed modality for the fabrication of thermoplastic nanofluidic devices is nanoimprint lithography (NIL) (Abgrall, '07; Chantiwas, '10; Chou, '95; Wu, '11). This technique takes advantage of the deformability of the substrate at temperatures above the glass transition temperature (Tg) of the substrate to produce multi-scale structures in a relatively high production mode over large areas at moderate cost (Rotting, '02).

Another benefit of using thermoplastics for nanofluidics is the diversity in their surface chemistry, which is determined by the identity of the monomer units comprising the polymer chains such as poly (methylmethacrylate), PMMA, containing methyl ester monomer units. In addition, a diverse range of simple activation techniques can be employed to generate functional groups that alter the surface chemistry (Hawthorne, '00; Henry, '00; Jackson, '14; Llopis, '07; Soper, '02). Common surface activation protocols for polymer fluidic devices are ultraviolet (UV) and plasma activation (Chai, '04; Chan, '96; Wei, '05). These activation techniques have been reported to generate a host of surface oxygen-containing species, such as carbonyls (aldehydes, ketones and carboxylic acids) and alcohols following a sequence of free-radical photo-initiated oxidation reactions (Chai, '04; Xu, '07).

Surface activation of polymer substrates possessing nanofluidic structures requires careful control of the dose to minimize activation-induced nano-scale roughness that may affect the operational characteristics of the device (Yang, '06). Plasma treatment has been the method of choice for nanofluidic surface activation and low-temperature assembly of nanofluidic devices as it induces minimal surface root-mean-square (RMS) roughness, lacks diffraction limitations and shadowing effects as reported for UV activation of polymer microchannels (Jackson, '14),

and allows for low temperature assembly of the device to maintain surface functionality and minimize nanostructure deformation (Abgrall, '07). Exposing PMMA to controlled O_2 plasma conditions can generate surface carboxylic acids (Chai, '04), which remain accessible for subsequent modification reactions after device thermal assembly.

In a previous work, we reported the generation of positively charged surfaces in PMMA microchannels following both chemical (*N*-lithiodiaminoethane reaction) (Henry, '00) and photochemical (UV) pathways (Llopis, '07), To the best of our knowledge, most of the work on nanochannel surface modification has involved functionalization of surface silanol groups in glass or fused silica (Stein, '04), particularly for the immobilization of biomolecules (Daiguji, '10; Karnik, '05; Martins, '13). Glass possesses well-established surface chemistry, hydrophilicity, non-conductivity, rigidity, minimal surface defects, non-deformability at high pressures and well-established top-down fabrication techniques (Menard, '11; Tas, '02). However, with the growing interests in elastomeric (Chung, '08; Huh, '07; Park, Lee, , '09; Park, Huh, , '09), thermoplastic (Chantiwas, '10) and membrane-based (Kwak, '11; Shao, '06) nanofluidic devices, it becomes necessary to understand the effects of surface modification on the charge density and surface charge-governed transport in thermoplastic nanofluidic channels, especially when considering such devices for many of the applications discussed previously (Schoch, '05; Stein, '04).

In this work, we report the surface modification of thermoplastic nanoslits and nanochannels and the determination of the surface charge density, zeta potential and electroosmotic flow (EOF) in these devices. The nanofluidic devices were fabricated in PMMA using a simplified protocol that did not require UV or thermal NIL, significantly simplifying the production of devices, even for devices with structures to ~20 nm. Carboxyl groups were generated on the walls of PMMA nanoslits and nanochannels under controlled conditions,

including the plasma exposure time and oxygen gas flow rate (Chai, '04; Xu, '07). The surface-confined carboxyl groups were subsequently aminated by reaction with a solution of ethylenediamine (EDA). The extent of roughness induced by surface activation was assessed in a nanoslit device using atomic force microscopy (AFM). Surface conductance plots were generated for the fluidic devices using a range of KCl concentrations. In agreement with our measurements, a modified model of ion transport in nanofluidic devices based on Schoch *et al*. (Schoch, '05) was presented. In addition, we investigated the effects of solution pH on the surface charge density and the EOF and assessed the ability of these devices for DNA translocation.

2.1 Experimental Methods

2.1.1 Materials and Reagents

PMMA sheets and cover plates were purchased from Good Fellow (Berwyn, PA), Cyclic olefin copolymer (COC 6017) was purchased from TOPAS Advanced Polymers (Florence KY) and Si <100> wafers were purchased from University Wafers (Boston, MA). Isopropanol, 1-ethyl-3-[dimethylaminopropyl] carbodimide hydrochloride (EDC), 2-(4-morpholino)-ethane sulfonic acid (MES), ethylenediamine (EDA), tripropylene glycol diacrylate (TPGA), trimethylolpropane triacrylate (TMPA), Irgacure 651 (photo-initiator), 50% potassium hydroxide (KOH), hydrochloric acid (HCl) and potassium chloride (KCl) were obtained from Sigma-Aldrich (St. Louis, MO). An anti-adhesion monolayer of (tridecafluoro – 1,1,2,2 – tetrahydrooctyl) tricholorosilane (T-silane) was purchased from Gelest, Inc. Tris buffer (pH = 8.0) and 2-(*N*-morpholino)ethanesulfonic acid (MES) buffer (pH 5.0) were obtained from Fisher Scientific (Houston, TX) and Life Technologies (Carlsbad, CA), respectively. All required dilutions were performed using 18 MΩ/cm milliQ water (Millipore) and buffer solutions were filtered using a 0.2 μm filter.

2.1.2 Fabrication of Nanofluidic Devices

Device fabrication involved four steps. First, a Si master was developed by initially patterning two V-shaped access microfluidic channels, 55 µm wide, 12 µm deep and 1.5 cm long in a Si <100> wafer using standard photolithography and anisotropic etching with 50% KOH. Next, the nanofluidic channels were milled using a Helios NanoLab 600 DualBeam instrument (FEI) Focused Ion Beam (FIB) instrument. In most cases, a beam current of 9.7 pA (diameter FWHM of 14 nm at 30 keV Ga^+ ions at normal incidence) and a dwell time of 1 µs were used to fabricate the desired nanochannels. For nanochannels <50 nm, an Al film with sputtering yield of 0.30 $\mu m^3/nC$ was deposited onto the Si wafer. The type and thickness of conductive film were chosen based on a previous report.(Menard, '11) After FIB milling, the Al layer was removed using an Al etching solution, cleaned with copious amounts of water and dried with N_2 gas.

The patterned Si wafer, which served as the master for producing the resin stamp, was coated with an anti-adhesion monolayer of T-silane from the gas phase in a desiccator under vacuum for 2 h. The structures were then transferred into a UV-curable resin containing 68 wt% TPGA as the base, 28 wt% TMPA as a crosslinking agent and 4 wt% Irgacure 651 as photo-initiator that on a COC backbone. To produce resin stamps with protrusive structures, the Si master was covered with the UV resin by dispensing with a pipette followed by gentle pressing of the COC plate on the resin-coated master to ensure complete filling of the resin into mold cavities. This was followed by exposure to a 365 nm UV light (10 J/m^2) through the COC plate for 5 min in a CL-100 Ultraviolet crosslinker. After curing, the UV-curable resin was gently demolded from the Si master.

The patterned UV-curable resin was used as the stamp to hot emboss structures into a 1.5 mm-thick PMMA sheet with access holes for reservoirs drilled prior or after embossing. Embossing was performed using a Hex03 hot embosser (JenOptik) at a pressure of 1910 kN/m^2

for 120 s with the top and bottom plates maintained at a temperature of 125°C. The pressure was applied after 30 s preheating of the stamp and the substrate at the desired molding temperature and was maintained during the imprinting process until cooled to 40°C. After cooling, the PMMA replica was demolded from the UV-resin stamp. For enclosing the fluidic substrate, a 175 µm thick PMMA sheet was used as a cover plate. Both the patterned PMMA sheet and cover plate were pre-activated using oxygen plasma at 50 W for 35 s and 5.5 sccm oxygen gas flow rate. Thermal assembly was performed at 80°C for 400 s at a pressure of 370 kN/m^2.

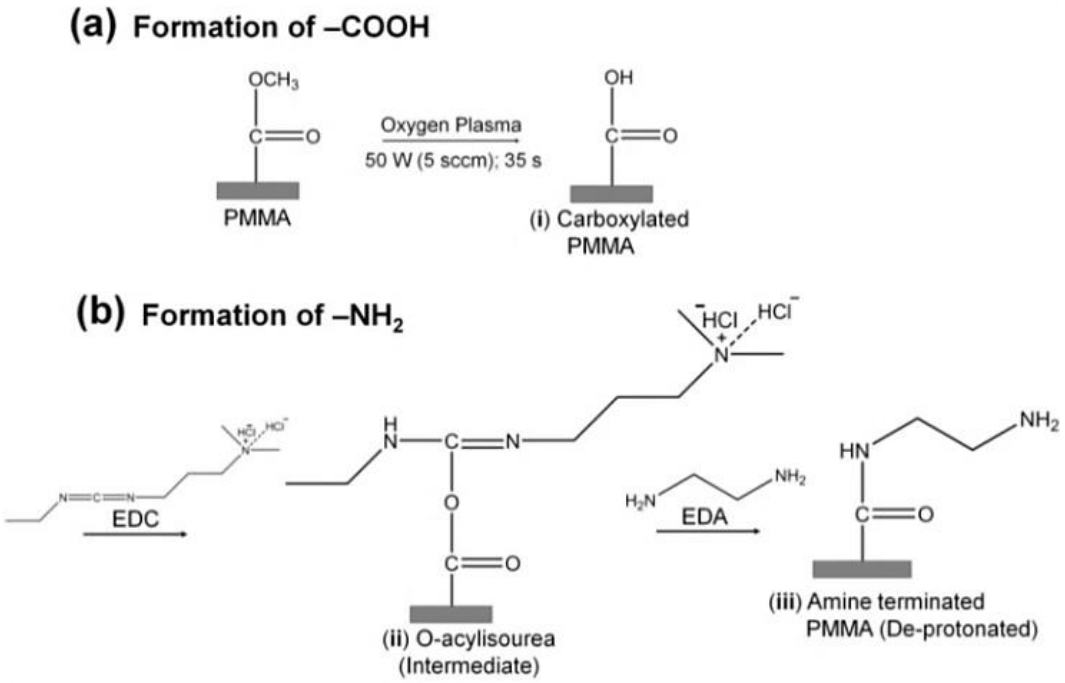

Scheme 2.1 Protocol for the surface modification of PMMA with (a) carboxyl groups by plasma activation, and (b) amine groups by chemical reaction with ethylenediamine through EDC coupling chemistry to the plasma activated PMMA.

2.1.3 Surface Modification

Surface amination reactions were initially tested on planar PMMA substrates (1 cm × 1 cm). PMMA substrates were exposed to 50 W (5.5 sccm) O_2 plasma for 35 s to generate the carboxylic acid functional scaffolds necessary for the amination reaction (Scheme 2.1). The plasma modified samples were then soaked in 5 ml buffered solution (100 mM MES, pH 5.0)

containing 250 mg EDC and 330 µl EDA (density = 0.899 g/cm^3) for 20 min at room temperature. After incubation, samples were rinsed with deionized water and air dried. The same protocol was adopted for the amination of assembled PMMA nanofluidic devices containing either nanoslits or nanochannels. In this case, the assembled devices were immediately filled with the EDA-EDC/MES solution and allowed to incubate for 20 min and rinsed with deionized water prior to experiments.

2.1.4 Water Contact Angle and Surface Energy Determinations

The wettability of unmodified and modified PMMA surface was assessed by water contact-angle measurements using a VCA Optima instrument (AST Products). PMMA sheets (1.5 mm thick) were cut to 1 cm × 1 cm and the surfaces modified as described above. A volume of 2.0 µL nanopure water (18.2MΩ·cm at 25^{o}C) was dispensed onto the substrate and the photograph of each droplet was captured immediately for analysis using the software provided by the manufacturer. The measurements were repeated at least five times at separate positions on the substrate and the values reported as the mean ±one standard deviation. Surface energies of the surfaces were deduced from the Zismann plot created by measuring the contact angle of a series of liquids with known liquid-vapor surface tensions (γ_{lv}). The liquids used were water (γ_{lv} ~ 72.80 mJ/m^2), glycerol (γ_{lv} ~ 64.00 *m*J/m^2) and DMSO (γ_{lv} ~ 43.54 *m*J/m^2) (see SI for more information).

2.1.5 Atomic Force Microscopy (AFM) Measurements

The topologies of untreated PMMA (u-PMMA), Plasma modified PMMA (O_2-PMMA) and amine modified PMMA (NH_2-PMMA) planar surfaces and the bottom surface of nanoslits were investigated using the Asylum Research MFP-3D Atomic Force Microscope (tip radius ~2 nm) in repulsive tapping mode at a rate of 1.0 Hz. The Tap300A1-G cantilever tips (Ted Pella) had a frequency of 300 kHz and force constant of 40 N/m. For the planar surfaces, the scans

were taken over a 3.5 μm × 3.5 μm scan size and the RMS surface roughness computed using the manufacturer's software. In the nanoslit, a scan size of 4 μm × 500 nm was acquired.

2.1.6 Scanning Electron Micrographs (SEM) Measurements

For SEM, the resin stamp and PMMA substrate were pre-coated with a 2-3 nm Au/Pd layer and imaged under high vacuum with an FEI Quanta 200 field emission gun at a 5 kV accelerating voltage.

2.1.7 Surface Charge Measurements

Direct current conductance plots were used to determine the surface charge of the nanoslits and nanochannel devices. Prior to all measurements, fluidic devices were flushed with a binary mixture of methanol/ultrapure water (50% v/v). Nanochannel filling was aided by capillary pulling from the inlet reservoir and vacuum suction from the outlet reservoir to ensure complete filling and the elimination of air-bubbles. Finally, fluidic channels were rinsed several times with deionized water before filling with the desired electrolyte.

Next, pre-cleaned devices were filled with the KCl solutions and Ag/AgCl electrodes were immersed into the access reservoirs poised at the ends of microchannels. Electrolyte solutions were allowed to equilibrate for 3-5 min evidenced by a stable resistance value under a bias voltage. The conductance values were determined by fitting the slope of the ionic current as a function of the applied voltage, which was stepped from -1V to 1V with 50 mV step size and a 5 s holding time for each data point. All measurements were achieved with a low noise Axopatch 200B amplifier coupled to a digidata 1440A digitizer with signal acquisition and analysis performed with the pClamp10 control software. The measurements were performed five times with repeated draining and filling. The mean conductance was plotted against the electrolyte concentration in a log-log plot and the surface charge determined from these graphs. This experiment was also performed with KCl solutions prepared over a pH range of 3.5 to 12 to

investigate the effects of pH on surface charge. The solution pH was adjusted using HCl or KOH. No pressure difference across the nanochannel was induced during the measurements. To avoid carry-over errors, each measurement was performed using a new device.

2.1.8 Electroosmotic Flow (EOF) Measurements

Two devices, one possessing a single PMMA nanoslit (138 μm long, 50 nm deep and 1 μm wide) and a single nanochannel (138 μm long, 120 nm high and 120 nm wide) connecting two opposite V-shaped access microchannels were fabricated as previously described. Fluidic channels were activated and the EOF was assessed using the current monitoring method. EOF values were measured using 0.1 and 0.05 M KCl solutions in 10 mM Tris buffer at pH 7.8. First, the pre-cleaned primed device was filled with 0.1 M solution and allowed to equilibrate for 3 min under a 1 V DC bias. Next, one access reservoir was emptied and 0.05 M KCl was introduced. Ag/AgCl electrodes were placed in the reservoirs across the channels under a 200 mV DC bias. Signals were acquired using the Axopatch 200B amplifier with a pClamp10 software and Digidata 1440A digitizer set at 10 kHz sampling frequency.

2.1.9 Transport Dynamics of λ-DNA through Thermoplastic Nanochannels

To study the electrokinetic parameters and extension length of λ-DNA, 100 × 100 nm nanochannels were used. λ-DNA (Promega Corporation) were stained with the bis-intercalating dye, YOYO-1 (Molecular Probes, Eugene, OR) at a base-pair/dye ratio of 5:1 in an electrolyte solution of 1× TBE (89 mM Tris, 89 mM Borate, 1 mM EDTA) with the addition of 4% v/v β-mercaptoethanol as a radical scavenger to minimize photo-induced damage (photobleaching and/or photonicking). Experiments were performed using 0.75 pM DNA solutions. Fluorescence microscopy was performed with an inverted microscope (Olympus IX81 TIRF microscope, Olympus, Pennsylvania, PA) equipped with a 100×/1.49 NA oil immersion objective and 488 nm laser light for excitation and a Sedat laser filter set LF488/561-2X2M-B-000 (Semrock).

Images were acquired at ~150 fps using a Hamamatsu EMCCD digital camera with EM gain and analyzed using Metamorph software.

Buffer solution was initially added into the pre-cleaned chip then the buffer solution in one of the microchannels was replaced with a solution containing the stained λ-DNA. Lambda DNA was electrokinetically driven through the nanochannels by immersing platinum electrodes into reservoirs situated on either side of the nanochannel and applying a DC bias voltage using a variable voltage power supply.

To study the degree of extension of λ-DNA confined in the PMMA nanochannels, the λ-DNA was initially driven from the microchannel into the nanochannel under a field strength of 100 V/cm. Once the DNA molecule had fully entered the nanochannel, the DC field was switched off. The molecule was allowed to relax until it reached its equilibrium extension length inside the channel before an image was acquired at a 50 ms exposure time. The end-to-end distance of the fluorescence image was measured using ImageJ software and displayed in a histogram.

2.2 Results and Discussion

2.2.1 Device Fabrication

The fabrication steps adopted for building the thermoplastic nanofluidic devices are depicted in Figures 2.1a – c. This fabrication strategy is a simplified scheme of an NIL process previously reported in our group (Wu, '11). The resin stamp was made by casting the non-cured UV resin against a Si master and appyling pressure to the resin using a COC plate. UV curing was accomplished with a benchtop UV crosslinking chamber. Thermal embossing was used to transfer the nanofluidic structures into PMMA from the UV-curable resin stamp and the device was sealed with a PMMA cover plate using low-temperature plasma assisted bonding to build the enclosed mixed-scale device (Figure 2.1c). Shown are SEMs of devices possessing an array

of 4 nanoslits (Figure 2.1d – f) or 7 nanochannels (Figure 2.1g – i). The nanostructures, which were fabricated by FIB milling into the Si master, were designed with dimensions (width × depth) of 1 µm × 50 nm and 120 nm × 120 nm for the nanoslits and nanochannels, respectively (Wu, '11).

This fabrication scheme was also used to produce 40 × 40 nm and approximately 20 × 20 nm nanochannels in PMMA substrates – the smallest reported nanofluidic channel to date fabricated in a thermoplastic substrate. Figure 2.1j shows the cross-sectional image of the 20 × 20 nm nanochannel FIB milled into a Si master through an 80 nm thick Al layer after removal of the conductive layer. The top-view of the channel after transfer into the thermoplastic is shown in Figures 2.1k.

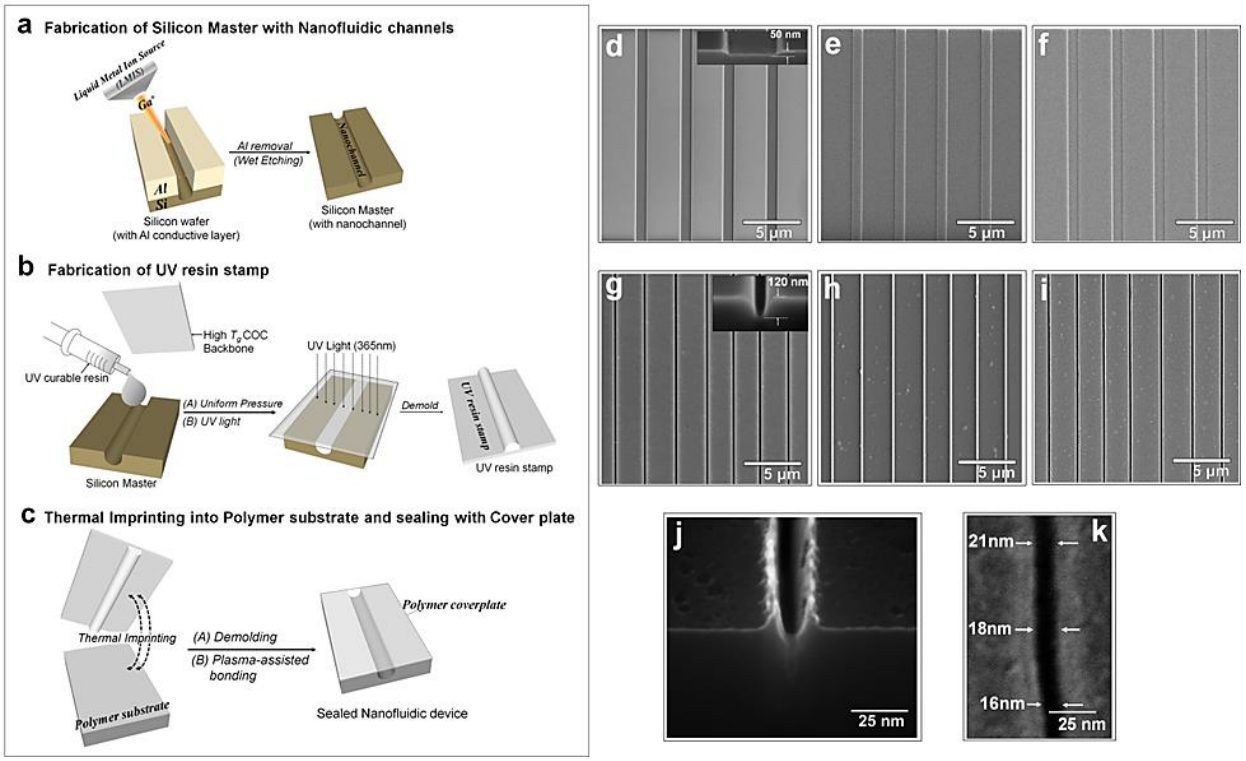

Figure 2.1 Process scheme for the fabrication and assembly of thermoplastic nanofluidic devices. (a) Fabrication of the Si master, which consisted of micron-scale access channels and the nanochannels/nanoslits; (b) fabrication of the protrusive polymer stamp in a UV-curable resin from the Si master; (c) generation of the fluidic structures in the thermoplastic substrate from the resin stamp by thermal embossing and plasma-assisted bonding of the substrate to the cover plate. SEMs of the Si master, resin stamp and PMMA substrate for the nanoslits (d, e, f) and nanochannels (g, h, i),

respectively. Inset shows the off–axis (52°) cross section SEM images of the Si masters. The dimensions ($l \times w \times h$) were 22 μm × 1 μm × 50 nm for each of the 4 nanoslits and 45 μm × 120 nm × 120 nm for each of the 7 nanochannels. Series of SEMs for a 18 × 23 nm nanochannel in Si (j) and (k) the embossed nanochannel in PMMA. The roughness seen in the SEMs for the stamp and substrate are artifacts from coating with 3 nm AuPd for imaging.

We observed that the final width and depth of the thermoplastic nanochannels following this fabrication scheme were sensitive to: (i) Surface uniformity of the sputtered Al film; (ii) the extent of uniformity of the silane layer vapor deposited onto the Si master; (iii) required dosage for complete curing of the UV resin; (iv) the strength of adhesion between the cured resin stamp and the COC back plate - strong adhesion was achieved by slightly roughening the COC with a very fine sandpaper, cleaning with water and drying prior to pressing onto the deposited uncured resin; (v) uniformity of the applied force over the entire substrate area during thermal embossing; and (vi) the cooling temperature during demolding - a temperature 40 to 50^{o}C less than the embossing or assembly temperatures was found to yield the most intact and uniform nanofluidic structures after demolding. Sub-30 nm channels were sensitive to any minor variation in these parameters as evidenced by small differences in the channel width measured along the 20 nm deep nanochannel (Figure 2.1k).

Compared to using the patterned Si directly as the embossing stamp, the UV resin stamp possesses a lower Young's modulus (600-800 MPa) (Amirsadeghi, '11) and a thermal expansion coefficient that is similar to that of PMMA (6×10^{-5}/°C). This leads to a reduction in the adhesion and thermal stress during thermal embossing of the nanofluidic device (Becker, '08; Chan-Park, '03) producing nanofluidic devices with high structural integrity. A single 4 inch Si wafer could contain 10 - 15 patterned devices with each Si master used repeatedly to fabricate > 20 UV resin stamps. Each resin stamp could be then be used for the embossing of >20 replicas in PMMA without noticeable damage.

PMMA substrates were sealed using plasma-assisted low temperature thermal fusion bonding (Figure 2.2a). The formation of leak-free fluidic devices or discontinuities due to channel collapse during assembly was evaluated by introducing 5 mM fluorescein in 0.5X TBE buffer into the fluidic network. As shown in Figures 2.2b and 2.2c, the nanoslits and nanochannels did not reveal any leakage or discontinuity along the channel length. Current-voltage plots acquired after filling with 1 mM KCl (Figure 2.2d) revealed that the measured currents for voltages of opposite polarity had similar absolute values and good linearity (non-rectification). The absence of voltage gating and rectification indicated homogeneity in surface charge along the walls of the PMMA nanoslits and nanochannels when using symmetrical electrolyte conditions.

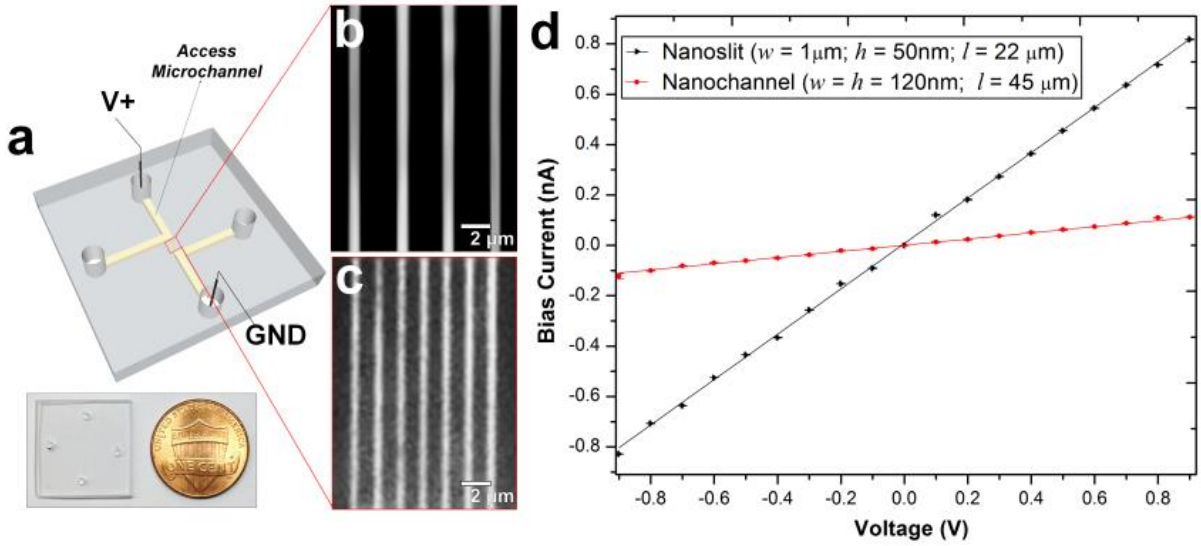

Figure 2.2 (a) Photograph of a thermally assembled nanofluidic devices fabricated in PMMA. The fluorescence images for the sealed nanoslit (b) and nanochannel (c) devices seeded with 5 mM FITC in 0.5× TBE buffer. (d) I/V plot generated between -0.9 V to 0.9 V for the nanofluidic device filled with 1 mM KCl revealing an electrical conductance of 90.08 ±5.7 nS and 12.26 ±12.3 nS for the nanoslits and nanochannels, respectively. The measured currents have similar absolute values for the respective voltages of opposing polarities; hence, the channels are symmetric (absence of rectification).

2.2.2 Effects of Thermal Fusion Bonding Temperature on the Wettability of O_2-PMMA

Previous reports have shown that the temperature used to thermally fusion bond a cover plate to a nanofluidic substrate affects the surface wettability/solid surface tension of plasma

treated polymer surfaces (Jackson, '14). We therefore investigated the effects of temperature on the wettability of O_2-PMMA (50 W, 5.5 sccm gas flow rate for 35 s) by measuring the water contact angle at temperatures between 75˚C and 100˚C, the typical temperature range utilized for thermal assembly of PMMA nanofluidic devices. As reported by Chai *et al.*(Chai, '04) the interpretation of contact angles in terms of the wettability relies on the validity of Young's equation, which interrelates the Young's contact angle, θ_Y, with the interfacial tension of a liquid-vapor, γ_{lv}, solid-vapor, γ_{sv}, and solid-liquid, γ_{sl} (see equation 1 and Figure 2.3);

$$\cos\theta_Y = \frac{\gamma_{sv} - \gamma_{sl}}{\gamma_{lv}} \tag{1}$$

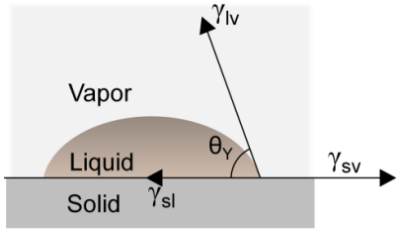

Figure 2.3 Schematic showing the interfacial tensions in Young's equation

Typically, θ_Y is expected to be a good approximation of the measured contact angle for a surface when the RMS roughness ≤5 nm.(Kwok, '99) γ_{sl} can be determined by;(Kwok, '99)

$$\gamma_{sl} = \gamma_{lv} + \gamma_{sv} - 2\sqrt{\gamma_{lv}\gamma_{sv}}\left(1 - \beta\left(\gamma_{lv} - \gamma_{sv}\right)^2\right) \tag{2}$$

γ_{sv} can be calculated using the water contact angle and equations 1 and 2;

$$\gamma_{sv}\left(1 - \beta(\gamma_{lv}-\gamma_{sv})^2\right) = \frac{[\gamma_{lv}(1+\cos\theta_Y)]^2}{4\gamma_{lv}} \tag{3}$$

where β is 1.057×10^{-4} $(m^2/mJ)^2$ and γ_{lv} for water is 72.70 mJ/m^2.

As shown in Figure 2.4a, there was a gradual increase in the water contact angle as the temperature of the plasma treated PMMA was increased. Heating the plasma treated substrate to temperatures ≤80˚C did not result in a significant change in the surface wettability. However, at temperatures ≥85˚C, there was a significant increase in γ_{sl} (see Figure 2.4b) As described by

Jackson *et al.* (Jackson, '14), this increase arises because the functional groups generated after plasma treatment (≤10 nm from the surface) undergo thermally induced rearrangement and are buried into the bulk substrate when heated to elevated temperatures. To avoid this, we performed fusion bonding of devices at 80˚C for 400 s. The wettability was primarily retained using these conditions and allowed the device to fill easily with aqueous solvents by capillary action and low pressure suction. Therefore, using low thermal bonding temperatures (~80°C) also minimized the amount of surface reorganization of the polar functional groups following plasma treatment.

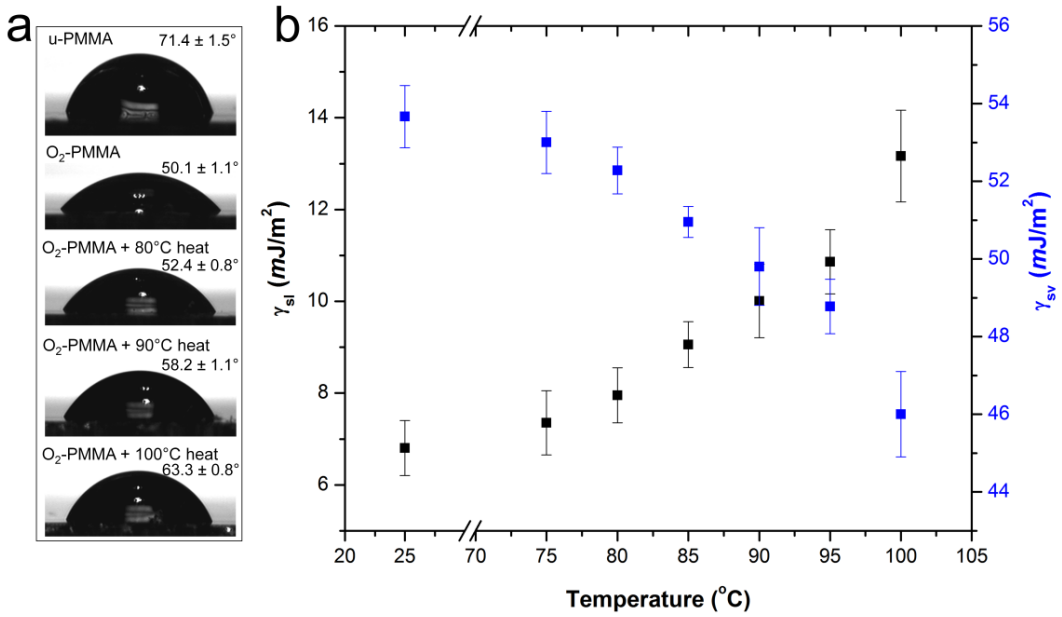

Figure 2.4 Variation of the water contact angle (a) and surface tension forces (b) with temperature for O_2-PMMA. Planar PMMA pieces were activated using an O_2 plasma with the following conditions; power level of 50 W, 5.5 sccm gas flow rate and treatment time of 35 s. Each reported value represents the average of five values measured at different positions on the substrate and the vertical bars represent one standard deviation unit.

2.2.3 Surface Energy (SE) of u-PMMA and O_2-PMMA surfaces

As proposed by Zisman (Kwok, '99), the SE of a solid surface can be estimated by measuring the contact angle of a series of liquids with known γ_{lv}. A graph of the water contact angles as a function of γ_{lv} is called a Zisman plot. The liquid-vapor surface tension at $\cos\theta_Y = 1$, also called the critical surface tension, γ_c, gives the SE of the solid surface. A test liquid with $\gamma_{lv} \sim \gamma_c$ will completely spread over the surface. Figure 2.5 shows Zisman plots for u- and O_2-

PMMA. The graph was generated by depositing 2.0 µl of three liquids, water (γ_{lv} ~ 72.80 mJ/m^2), glycerol (γ_{lv} ~ 64.00 *m*J/m^2) and DMSO (γ_{lv} ~ 43.54 mJ/m^2) onto the solid surface. The results revealed that the SE increased from ~27.02 mJ/m^2 for u-PMMA to 38.88 mJ/m^2 after plasma treatment suggesting the incorporation of oxygen containing polar functional groups onto the polymer surface. We speculate that this will approximately be the SE experienced in the plasma modified nanoslit and nanochannels and, as suggested from the previous section, expect it to remain relatively unchanged after device assembly when the assembly temperature was ≤80^o.

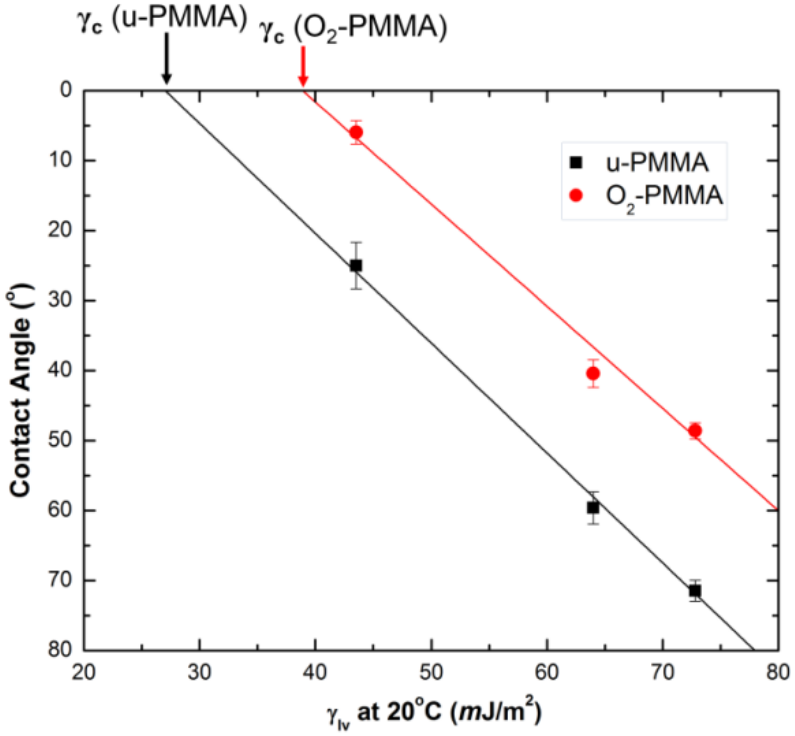

Figure 2.5 Zisman plot for u-PMMA (black trace) and O_2-PMMA (red trace) measured with water (γ_{lv} ~ 72.80 mJ/m^2), glycerol (γ_{lv} ~ 64.00 mJ/m^2) and DMSO (γ_{lv} ~ 43.54 mJ/m^2). Each point represents the average of five values measured at different positions on the substrate and the vertical bars represent one standard deviation unit.

2.2.4 Surface Modification of Poly (methyl methacrylate) (PMMA)

The surface wettability and solid surface tensions for the unmodified (u), plasma (O_2) and amine (NH_2)-modified PMMA were assessed using water contact angle measurements. u-

PMMA showed a contact angle of 71.4 ±1.5°, which corresponded to a solid-vapor surface tension, γ_{sv}, of ~40.4 mJ/m^2. After plasma treatment, the contact angle decreased to 50.1 ±1.1° indicating an increase in γ_{sv} to ~54.6 *m*J/m^2. Amine modification led to an increase in the water contact angle to 62.9 ±2.0° (γ_{sv} = 45.8 mJ/m^2). The observed trends were consistent with literature data (Henry, '00). We employed XPS and FTIR to analyze the u-PMMA, O_2-PMMA and NH_2-PMMA surfaces to verify the fidelity of the surface modification.

2.2.4.1 X-ray Photoelectron Spectroscopy (XPS) Analysis of Plasma treated PMMA Substrates and Nanoslits

The O/C and N/C ratios were used to assess the extent of surface modification of PMMA surfaces. For XPS measurements, C1s, O1s and N1s photoelectron signals were acquired using an Axis Ultra DLD X-ray photoelectron spectrometer (Kratos Analytical) under ultra-high vacuum conditions (10^{-8} to 10^{-10} Torr) with a monochromatic Al Kα X-ray source, 20 eV pass energy, 370 s acquisition time, 1,600 ms dwell time and 20° electron take-off angle. Given an inelastic mean free path of 3-4 nm, ~95% of the resultant signal originated 9-12 nm from the surface (Mitchell, '94; Powell, '94; Seah, '79). For all XPS spectra, Shirley backgrounds were subtracted by averaging at least 10 data points associated with the background.

As shown in Figure 2.6a for planar PMMA surfaces, O_2-PMMA led to an increase in the O/C ratio confirming the generation of oxygen-containing groups (Chai, '04). For amination of the O_2-PMMA, several conditions involving EDC or EDC-NHS coupling chemistries were evaluated with concentrations ranging between 0.1 and 1 M ethylene diamines (EDA). In all cases, there were decreases in the O/C ratios (Figure 2.6a); however, depending on the amination conditions, the amount of N-containing groups differed. As depicted in Figure 2.6b, the highest N/C ratio was observed for animation involving the reaction of O_2-PMMA with 1 M EDA in EDC.

To identify the surface functionalities generated after the O_2-PMMA, the C1s spectra were processed based on previously published work (Seidel, '99). The u-PMMA C1s spectrum showed the presence of four Gaussian components: (1) 284.6 eV aliphatic C-C and C-H; (2) 285.2 eV quaternary C-C α to the pristine ester; (3) 286.4 eV methoxy C-O ester; and (4) 288.7 eV carbonyl C=O ester (Figure 2.6c).

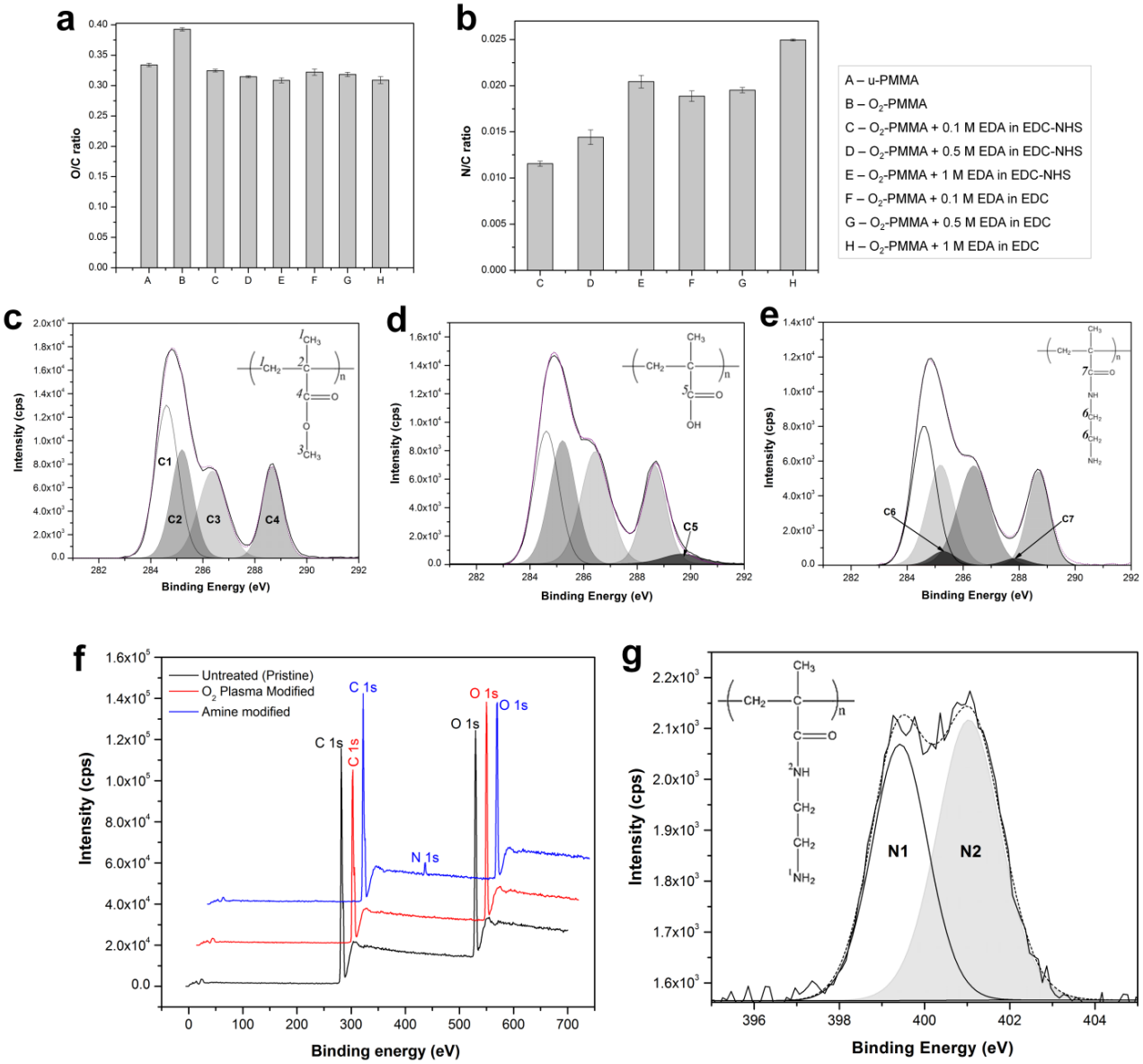

Figure 2.6 Bar graphs showing (a) O/C and (b) N/C ratios for different surface modification schemes for both u-PMMA (unmodified) and O_2-PMMA (plasma treated PMMA) obtained from XPS data. Deconvoluted C1s spectra for (c) u-PMMA, (d) O_2-PMMA and (e) NH_2-PMMA. PMMA peaks were labeled and assigned to the polymer's monomer. Spectra for the plasma activated PMMA contained an additional peak for carboxyl functionalities and the amine-modified surface showed the presence of two

peaks corresponding to the C-N bond of an amine and amide. **(**f) XPS survey spectrum of u-PMMA (black trace), O_2-PMMA (red trace) and NH_2-PMMA (blue trace) nanoslits. (g) N1s deconvoluted spectrum showing two forms of nitrogen atoms. The insert shows the chemical structure of the aminated PMMA surface with the nitrogens labeled N1 and N2.

This fitting was in good agreement with previous literature. Nevertheless, the theoretical peak area ratio of the C1s components (1) - (4) of 2:1:1:1 was found to be 1.90:1.18:1.20:1.00 in our data. The slight deviation may have been attributed to additives and/or plasticizers introduced into the substrate by the manufacturer (Ben, '00). Furthermore, in addition to the peaks listed above for u-PMMA, the deconvoluted C1s peak of O_2-PMMA showed the presence of a peak at a binding energy of 289.7 eV (Figure 2.6d). This peak corresponded to the OC=O of a carboxylic acid. After amination, the deconvoluted C1s peak showed the absence of the carboxylic acid peak and the presence of two peaks; (1) 285.8 eV, C-N bond of an amine, and (2) 287.9 eV O=C-N bond of an amide (Figure 2.6e).

The combined survey spectra are shown in Figure 2.6f for an unassembled PMMA nanoslit device. The trace for u-PMMA showed the presence of only two peaks at 284.8 eV and 532.0 eV indicative of C1s and O1s core levels, respectively. After exposure to 50 W (5.5 sccm) O_2 plasma for 35 s, there were observable changes in the individual intensities of the C1s and O1s peaks when compared to the u-PMMA (red trace in Figure 2.6f). There was an increase in the O/C atomic ratio from 0.331 ±0.006 for u-PMMA to 0.403 ±0.003 for O_2-PMMA indicating the incorporation of oxygen containing chemical groups on the PMMA surface. The survey spectrum taken for the NH_2-PMMA surface (blue trace) showed the presence of a new peak centered at 399.69 eV in addition to the C1s and O1s peaks. This peak is characteristic of surfaces possessing nitrogen-containing functionalities (N1s core level) (Gröning, '94; Henry, '00).

Further analysis of the XPS data revealed that the atomic ratio of the peak area of the O1s peak to the C1s peak was 0.309 ±0.006 with the ratio of the O1s to C1s peak areas ~10.9% less

for NH_2-PMMA compared to u-PMMA. This result demonstrated that not only was nitrogen successfully incorporated onto the surface of a PMMA nanoslit, but the amount of oxygen present on the surface was less than what was present for the u-PMMA or O_2-PMMA. The N/C ratio was 0.025 ±0.001. The N1s peak obtained was deconvoluted as shown in Figure 2.6g. This peak consisted of two individual peaks, one centered at 399.1 eV and the other at 400.9 eV. The peak at the lower binding energy corresponded to the N1s core level of an amine (N1), while the higher energy peak was assigned to an amide (N2) (Henry, '00).

Overall, the observations in the XPS data indicated the presence of fewer ester groups for O_2-PMMA and NH_2-PMMA. Collectively, these results indicated successful oxidation and amination of the PMMA nanoslit surfaces and were similar to the results secured for the planar PMMA surface.

2.2.4.2 Fourier Transform Infra-red (FTIR) spectra

To examine the molecular nature of the treated and untreated surfaces, FTIR studies were employed using pre-cut Si wafers coated with a 200 nm Au layer. Commercial PMMA sheets were dissolved in dichloromethane and diluted to yield a solution with a final concentration of 0.5 mg PMMA/mL. This was spin coated onto a Au wafer at 2500 rpm for 60 s to yield a 5 nm thick polymer layer. The coated Au-wafers were allowed to dry in an oven after which they were ready for surface modification and analysis. This approach minimized interference from bulk material in the IR spectra. FTIR spectra were collected at a resolution of 2 cm^{-1} on a 670-IR spectrophotometer (Varian, US) using a monolayer/grazing-angle specular reflectance accessory.

A FTIR spectrum of u-PMMA with the characteristic peaks between 4000 and 650 cm^{-1} is shown in Figure 2.7a. The most prominent band was ν(C=O) at 1733 cm^{-1} assigned to the ester stretch. The absorption bands at 1270, 1241 cm^{-1} and 1195, 1153 cm^{-1} could be assigned to ν(C–O) and ν(COC) stretching of an ester. This spectrum correlates well with the FTIR spectrum of

PMMA documented in the literature (Henry, '00). After plasma treatment, there was the appearance of a band at 3430 cm^{-1} and 1700 cm^{-1}, which could be assigned to the ν(O-H) and ν(C=O) of a carboxylic acid (Figure 2.7b). Amination with EDA led to the appearance of bands at 3396 cm^{-1} and 1675 cm^{-1} corresponding to the ν(N-H) stretch of a primary amine and ν(C=O) of an amide (Figure 2.7c). These support the XPS results and confirm successful surface modification of PMMA using EDA.

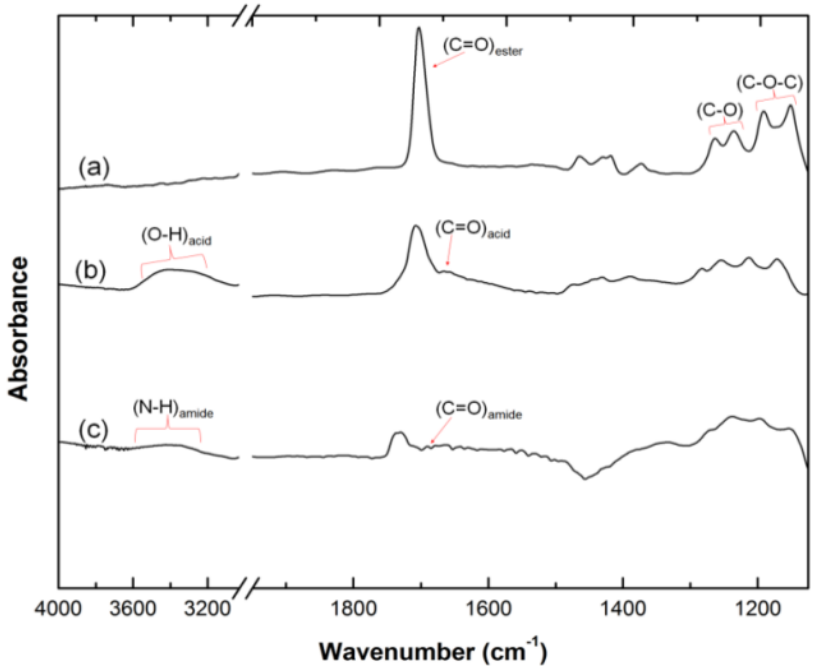

Figure 2.7 ATR-FTIR spectra for (a) untreated (b) plasma-treated and (c) amine-modified PMMA.

2.2.5 Surface Topographical Studies of Modified PMMA Nanoslits

Surface modification reactions induce not only chemical changes but also some topographical changes. These changes are in the form of nanometer or sub-nanometer random surface roughness on solid walls with roughness amplitude a_r. Results obtained from previously reported molecular dynamic simulations showed that roughness may affect the wettability of surfaces and the EOF in nanofluidic channels depends on the magnitude of a_r (Messinger, '10). For cases where λ_D/a_r <<1, where λ_D is the Debye length, the EOF can be significantly different compared to λ_D/a_r ~1; the presence of a rough surface that is comparable to λ_D can alter the EDL

near the surface and reduce the EOF (Ziarani, '08) and streaming potential (Park, '12). For a homogeneously charged rough channel surface, the EOF is expected to decrease when a_r is >5% of the channel width irrespective of the value of λ_D/a_r (Wang, '07). Alterations in the EOF become insignificant for surfaces with λ_D/a_r >1 (Kim, '06; Messinger, '10). Also, the water contact angle is expected to be altered by rough surfaces compared to a smooth surface with identical chemical properties (Kwok, '99; Wenzel, '49).

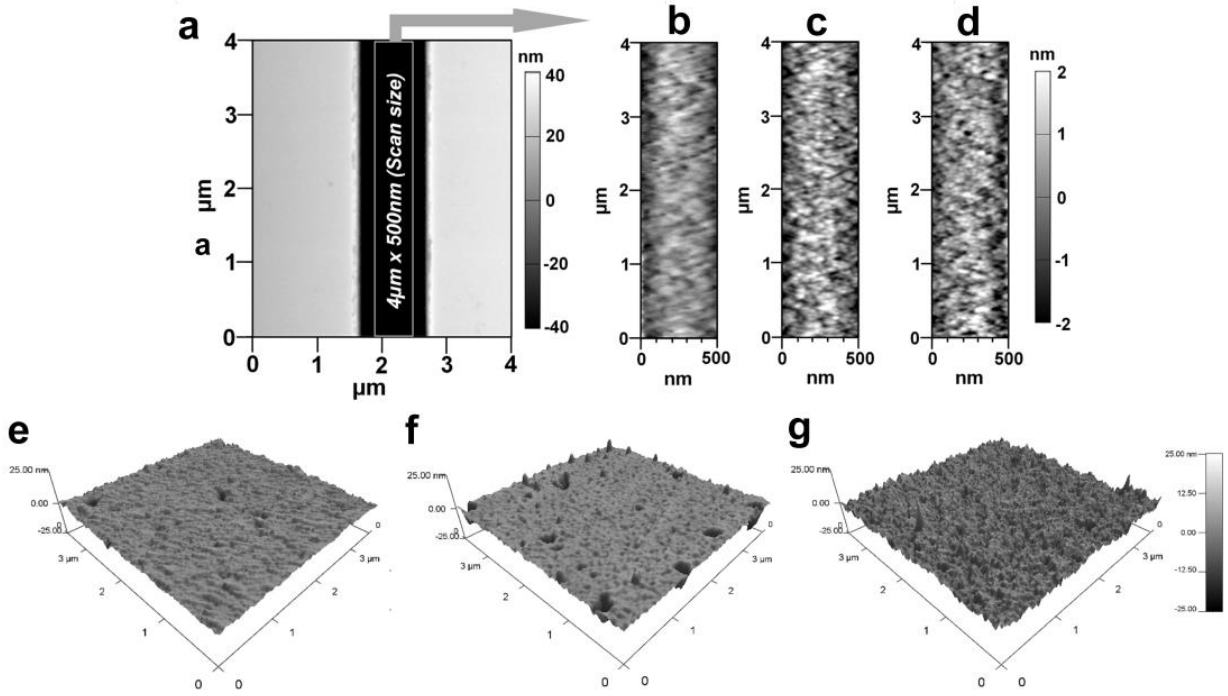

Figure 2.8 AFM characterization of a PMMA nanofluidic device with 1 μm x 50 nm nanoslit (a) for: (b) u-PMMA; (c) O_2-PMMA; and (d) NH_2-PMMA. The image shown is 4 μm x 500 nm. The measured root-mean-square (RMS) surface roughness was 0.80 nm, 0.95 nm and 1.03 nm, respectively, for these three devices. Also shown are AFM images for planar PMMA; (e) u-PMMA (f) O_2-PMMA and (g) NH_2-PMMA. Images on the planar PMMA were scanned over an area of 3.5 × 3.5 μm.

The roughness was measured by AFM for PMMA nanoslits because the bottom surface could be easily profiled without tip-wall interactions compared to nanochannels. Figure 2.8a shows a representative AFM image of a nanoslit. For the u-PMMA nanoslit shown in Figure 2.8b, the measured RMS surface roughness was 0.75 nm. This value was approximately equal to the measured roughness obtained from the bottom surface of the FIB milled nanoslit in the

original Si master (data not shown). However, this value was less than that of the planar u-PMMA (1.16 nm, see Figure 2.8e). After surface activation and modification, there was an increase in the RMS roughness to 0.96 nm and 1.08 nm for the O_2- and NH_2-PMMA nanoslits, respectively (Figures 2.8c and 2.8d). This increase in surface roughness for O_2-PMMA was due to etching by the oxygen plasma while the surface roughness for the aminated surface can be attributed to slight swelling and/or dissolution of the PMMA by the EDA solution and the additional C-C bonds introduced onto the surface from EDA.

An increase in the surface roughness was also observed on the planar O_2-PMMA and the NH_2-PMMA compared to u-PMMA (see Figures 2.8f-g). Nevertheless, because the experiments were performed at solution ionic strengths where λ_D <10× the channel dimension but slightly larger than the wall roughness (λ_D ~1.5 nm) (Menard, '13; Schoch, '08), we expect the contributions of surface roughness to wettability and EOF in our PMMA nanoslit and nanochannel devices to be insignificant relative to contributions from changes in surface charge.

2.2.6 Electrical Model of the Nanofluidic Device for Conductance Measurement

Figure 2.9a shows the experimental setup of the nanofluidic device configured for making conductance measurements and the equivalent circuit for the nanofluidic device (Figure 2.9b). The device contained two opposing V-shaped access microchannels (with equal dimensions) with two reservoirs each fabricated at both ends of the microchannel for introducing fluids into the nanochannels or nanoslits. We represented the total voltage applied across reservoirs 1 and 3 as $\boldsymbol{V}$ and the voltage drop across the micro- and nanochannel as $\boldsymbol{V_{mc}}$ and $\boldsymbol{V_{nc}}$, respectively. In this study, the microchannel dimensions were configured such that most of the voltage drop occurred within the nanochannel. The measured electrical resistance, R, across reservoirs 1 and 3 for a given electrolyte was expressed as a combination of the resistance of the

access microchannel, R_{mc}, and the resistance of each nanochannel, R_{nc} (array of parallel resistors each with R_{nc}):

$$R = \frac{R_{nc}}{n} + R_{mc} \quad (4)$$

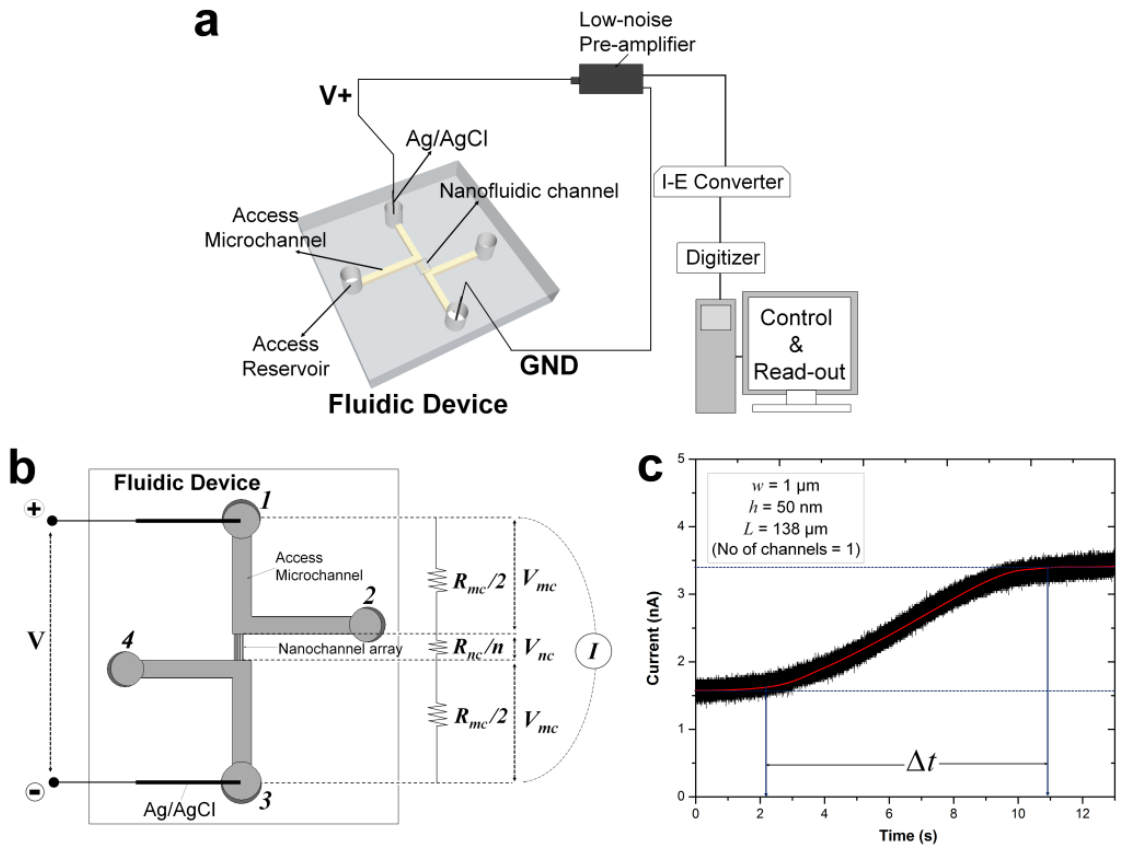

Figure 2.9 (a) Schematic showing the experimental setup for measuring the resistance of the nanochannels. The nanofluidic device was interfaced to an Axopatch 200B amplifier connected to a Digidata 1440A and computer for readout. Each nanochannel of the array was assumed to have the same geometrical size. (b) Diagram showing the voltage drop and resistances across micro- and nanochannels. (c) Current versus time trace showing the current generated across a nanoslit arising from the replacement of a low ionic strength buffer (0.05 M KCl in 10 mM Tris buffer) with a higher ionic strength buffer (0.1 M KCl in 10 mM Tris) for an O_2-PMMA nanoslit. Buffer replacement within the nanoslit arose from the EOF associated with the device.

To determine the percent voltage drop across each nanofluidic array, the mixed-scale devices were filled with 0.5 M KCl and the values of R_{mc} and R measured using an Axopatch 200B amplifier. From these values, R_{nc}/n was calculated for the nanoslit (n = 5) and nanochannel (n = 7) using equation (S4) and the percent voltage drop calculated from;

$$\%V = \left[\left(\frac{R_{nc}}{n}\right)/R\right]\times 100 \quad (5)$$

The data is summarized in Table 2.1.

Table 2.1 Measured and calculated electrical resistances across the microchannel R_{mc}, nanoslit/nanochannel R_{nc} and percent voltage drop across nanochannels or nanoslits. The nanofluidic device consisted of a single nanoslit or nanochannel.

Device	Dimensions of Nanofluidic device ($l \times w \times h$)	R_{mc} (kΩ)	R (MΩ)	$\frac{R_{nc}}{n}$ (MΩ)	Voltage drop (%V)
Nanoslit	22 μm × 1 μm × 50 nm	501.7 ± 10.2	19.9 ± 1.2	18.9 ± 1.1	95.2 ± 1.1
Nanochannel	45 μm × 50 nm × 50 nm	997.2 ± 12.5	60.9 ± 1.8	58.9 ± 1.6	96.7 ± 1.2

2.2.7 Surface Charge and pH Effects

As shown in Figure 2.9, the nanofluidic device was comprised of input/output microchannels interconnected by an array of nanochannels with the majority of the voltage drop occurring across the nanochannels (see Table 2.1 for resistance values of the fluidic network). Therefore, the majority of the electrokinetic flow occurred within the nanochannels, which can be heavily influenced by surface charge and λ_D to name a few. The surface charge can be a significant determinant of the fluid dynamics for devices possessing high surface-to-volume ratios. Depending on the solution pH and the surface chemistry, the solid can have either a positive or negative surface charge density, σ_s, described by $\sigma_s = \sum_i q_i/A$; where $q_i = z_i e$ and q_i is the net charge of ion i, z_i is the valency of ion i, e is the electron charge, and A is the surface area; this can be used to compute the number of charged sites per unit area, Γ in nm^{-2} (Schoch, '08). Due to wall surface charge, an EDL develops to maintain the electroneutrality at the solid/liquid interface (Sonnefeld, '95). For a channel filled with a symmetrical 1:1 electrolyte such as KCl with ionic concentration c, the EDL thickness or λ_D is;

$$\lambda_D = \left(\frac{\epsilon_0 \epsilon_r R T}{2 F^2 c}\right)^{1/2} \quad (6)$$

where R is the gas constant ($J \cdot mol^{-1}K^{-1}$), ϵ_0 is the permittivity of vacuum ($F \cdot m^{-1}$), ϵ_r is the dielectric constant of the medium, F is the Faraday constant ($C \cdot m^{-1}$), and T is the temperature (K). λ_D can vary from <1 nm at high ionic strength to a few tens of nm at low ionic strength (Plecis, '05).

Electrical conductance measurements across nanofluidic channels filled with ionic salt solutions have been used to deduce the magnitude of the surface charge density. Here, we present a modified electrokinetic model based on the report from Stein *et al.* (Stein, '04) for determining σ_s. When an external electric field is applied across a nanochannel filled with an ionic salt solution, the measured electrical conductance (G_T) is the sum of the bulk conductance (G_B) and the surface conductance (G_S). At high salt concentrations, the surface charges in the nanochannel are shielded by the mobile ions and have negligible influence on the ion concentration in the nanochannel. In this case, transport is dominated by the ions in the bulk solution and G_B depends on the nanochannel dimensions and electrolyte concentration according to (Martins, '13; Schoch, '08; Schoch, '05);

$$G_B = 10^3 \left(\mu_{K^+} + \mu_{Cl^-}\right) c\, N_A\, e \cdot \frac{n\, w\, h}{L} \qquad (7)$$

where *w, L* and *h* are the nanochannel width, length and height, respectively, N_A is Avogadro's number, *c* is the electrolyte concentration in mol/L, *n* is the number of nanochannels in the device and μ_{K+} and μ_{Cl^-} are the ion mobilities of K^+ and Cl^- ions, respectively ($\mu_{K+} = 7.619 \times 10^{-8}$ $m^2/V\ s$ and $\mu_{Cl^-} = 7.912 \times 10^{-8}$ $m^2/V\ s$).

However, at low salt concentrations, the nanochannels become predominantly filled with counterions. For electroneutrality within the nanochannel, excess counterions in the EDL compensate for the net surface charge, which governs the counterion concentration inside the channel (Daiguji, '03). The EDL becomes very thick and overlaps leading to co-ion exclusion

effects. The nanoslit/nanochannel becomes predominantly filled with counterions of concentration c_e (mol/L) and the contribution of G_B to G_T becomes negligible (*i.e.* $G_T \approx G_S$). From the principle of conservation of charge, the number of surface charges should be approximately equal to the number of counterions. Therefore, c_e can be represented as;

$$c_e = 10^{-3} \frac{(\text{number of surface charges})}{(\text{volume of nanochannel})} = \left(\frac{2\ w\ L\ \sigma_s}{e\ N_A} + \frac{2\ h\ L\ \sigma_s}{e\ N_A}\right) \frac{1}{L\ w\ h}$$

$$c_e = 10^{-3}\ \frac{2\ \sigma_s\ (w + h)}{e\ N_A \cdot w\ h} \tag{8}$$

where σ_s is the surface charge density. G_B becomes negligible and σ_s governs the total ion conductance in the nanochannel. For 1D nanoslits such as reported by Stein *et al.*,(Stein, '04) Schoch *et al*. (Schoch, '05), Karnik *et al*. (Karnik, '05), and Martins *et al*. (Martins, '13), $h << w$; hence $(w + h) \approx w$. However, for 2D nanochannels with $h \leq w$, hence, both w and h contribute to c_e and G_S. Therefore, the surface conductivity, κ_{surf} (S/m), is given by;

$$\kappa_{surf} = 10^3 \left(\mu_{opp}\right) c_e\ N_A\ e \tag{9}$$

where μ_{opp} is the mobility of the counterion (solution cations or anions for the negatively or positively charged surfaces, respectively). Substituting equation 8 into 9, κ_{surf} (S/m) can also be represented in terms of the surface charge density as;

$$\kappa_{surf} = 2\ \mu_{opp}\ \frac{\sigma_s\ (w + h)}{w\ h} \tag{10}$$

And G_S is represented as;

$$G_S = \kappa_{surf} \times \frac{n\ w\ h}{L} \tag{11}$$

or

$$G_S = 2\ \mu_{opp} \sigma_s\ n \frac{(w + h)}{L} \tag{12}$$

Therefore, substituting equations 7, 10 and 12 into equation S6, we have;

$$G_T = 10^3 \left(\mu_{K^+} + \mu_{Cl^-}\right) c\, N_A\, e \cdot \frac{n\, w\, h}{L} + 2\, \mu_{opp} \sigma_s\, n \frac{(w + h)}{L} \quad (13)$$

When $G_B \approx G_S$, a transition ion concentration, c_t, is observed on a log-log plot of G_T versus the ion concentration (Schoch, '05).

We investigated the effects of surface modification of polymer nanofluidic devices by experimentally measuring σ_s of modified PMMA nanoslits and nanochannels by monitoring ionic conductance plots. Figures 4a and 4b show the conductance traces for an array of surface modified nanoslits (22 μm × 1 μm × 50 nm) and nanochannels (45 μm × 120 nm × 120 nm) measured over a range of KCl concentrations (10^{-5} M – 1 M in Tris buffer, pH = 7.8). In both devices, the conductance results obtained before and after surface modification differed essentially in the low ionic concentration regime. This effect was characterized by a shift of the plateau conductance suggesting a change in the surface charge dependent on the nature of the modification. When the modified surfaces were in contact with an electrolyte at pH 7.8, ~99.9% of the surface carboxyl groups (pK_a = 4.66) would be deprotonated and ~99.0% of the amine groups (pK_a = 10.42) would be protonated (Meisenberg, '06). At extreme pH values and low buffer concentrations, the counterions in solution necessary to maintain electroneutrality are H^+ and K^+ for O_2-PMMA devices and Cl^- and OH^- for the NH_2-PMMA devices. However, at pH 7.8 and KCl concentration $\geq 10^{-5}$ M, $[K^+] >> [H^+]$ and $[Cl^-] >> [OH^-]$. Therefore in equation 13, $\mu_{opp} \approx \mu_{K+}$ or μ_{Cl-} for the deprotonated and protonated carboxyl and amine surfaces, respectively (Zangle, '10).

At a KCl concentration greater than 10^{-2} M, the measured ionic conductance in both the nanoslits and nanochannels fit linearly to the theoretical bulk conductance (see Figure 2.10) and was reproducible from one device to another. This confirmed that there was no significant change in the dimensions of the fluidic channels during thermal embossing, device assembly and

surface chemical modification. However, at low electrolyte concentrations (surface charge-governed regime), the nanochannel conductance deviated from linearity and plateaued for both the plasma and amine treated devices with the measured surface conductance lower for the $-NH_3^+$ terminated devices compared to the $-COO^-$ terminated devices. For the nanoslit devices, the average surface conductance at this region was 7.5×10^{-10} S for the O_2-PMMA device. After amination, the conductance dropped to 3.8×10^{-10} S, ~50.7 % of its original value (Figure 4A).

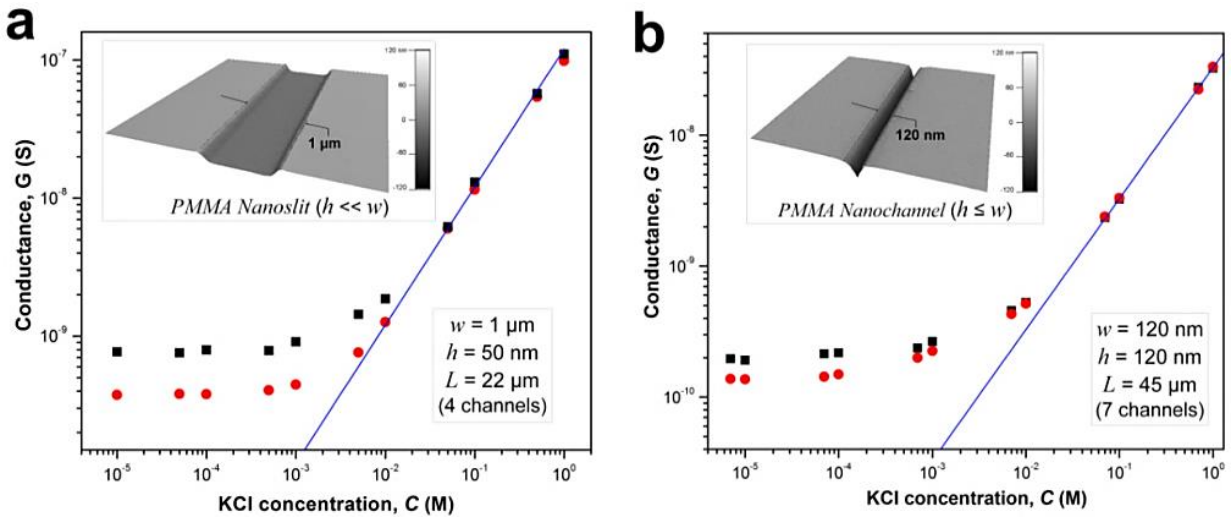

Figure 2.10 Conductance plots obtained from surface modified devices consisting an array of (a) four nanoslits (each 1 µm wide, 50 nm deep and 22 µm long), and (b) seven nanochannels (each 120 nm wide, 120 nm deep and 45 µm long) square and circle markers represent the data obtained for the plasma and amine modified surfaces, respectively. The solid blue line represents the trace of the theoretical bulk conductance calculated with equation (2). Each data point represents an average of five measurements with a scatter in the data within 5-8% of the mean value. From the graph, the effective surface charge density as calculated from the transition concentration, c_t, was 38.2 mC/m^2 for plasma treated nanoslit, 28.4 mC/m^2 for amine treated nanoslit, 40.5 mC/m^2 for plasma treated nanochannel and 22.9 mC/m^2 for the amine treated nanochannel.

The transition concentration, c_t, used to compute σ_s was approximately 6.60 mM and 3.52 *m*M for the O_2- and NH_2-PMMA surfaces, respectively. For O_2-PMMA nanoslits, we obtained $|\sigma_s|$ ~38.2 mC/m^2, which was less than 60 mC/m^2 reported by Stein *et al.*(Stein, '04) and 214 mC/m^2 reported by Schoch *et al.*(Schoch, '05) for glass-based nanoslits measured at pH 8. For the NH_2-PMMA nanoslit, $|\sigma_s|$ was 28.4 mC/m^2. In the nanochannels, the conductance in the low ionic strength region for the amine-modified device dropped to ~67.6% of its O_2-PMMA device.

The surface charge densities were 40.5 mC/m^2 and 22.9 mC/m^2 for the O_2- and NH_2-PMMA devices, respectively.

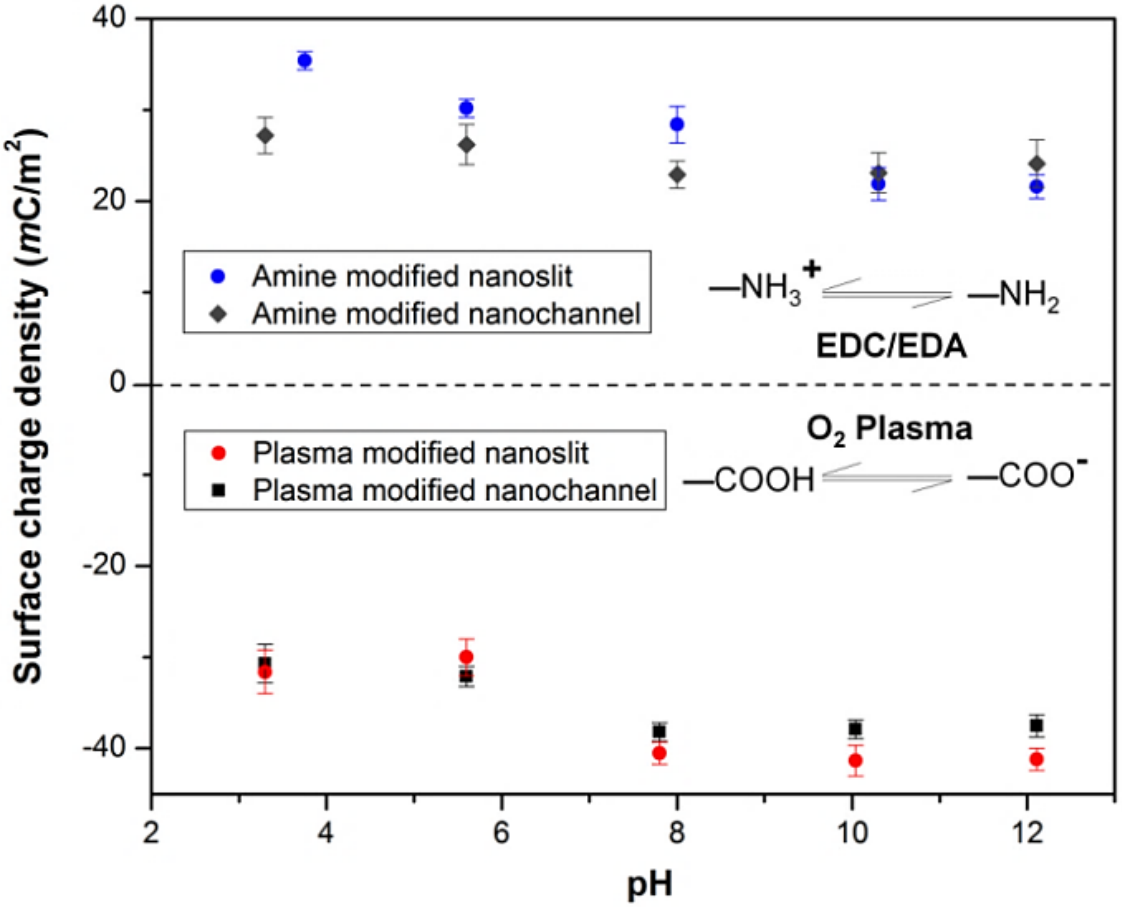

Figure 2.11 Plot showing the effect of pH on the surface charge density σ_s, in plasma and amine modified nanoslits and nanochannels.

We also monitored the effect of pH on $\sigma_s$of PMMA nanoslits and nanochannels. As depicted in Figure 2.11, the plasma modified nanoslits and nanochannels indicated that the surface charge density gradually increased as the pH of the electrolyte solution increased because at low pH the surface carboxyl groups were converted to their protonated form. This leads to a corresponding decrease in the surface conductance as less counterions are attracted into the fluidic channel. At high pH, the carboxyl groups become deprotonated thereby increasing σ_s. An opposite trend was observed for the amine modified surfaces. The measured surface conductance was higher at low pH and lower at high pH. This is most likely due to the conversion of the –

NH_2 groups to $-NH_3^+$ groups at low pH. At pH ≥8, the surfaces of the O_2-PMMA devices were fully deprotonated and the $|\sigma_s|$ for the nanochannel was found to be greater than the nanoslits. The values were 38.3 mC/m^2 ($\Gamma \approx 4.2$ nm^{-2}) and 40.5 mC/m^2 ($\Gamma \approx 4.0$ nm^{-2}) for the fully deprotonated PMMA nanoslit and nanochannel, respectively. These values were found to remain relatively constant at pH >10. In the nanochannel, the width is comparable to the height, therefore, the surface charge density of the vertical walls, which is typically neglected in the nanoslit, also contributes to the ion transport within the channel (Craighead, '06). Surplus counterions would be attracted into the nanochannel and more coions would be excluded.

2.2.8 Electroosmotic Flow (EOF) Measurements

The EOF can be described in terms of a mobility, $\boldsymbol{\mu}_{eof} = \boldsymbol{\upsilon}_{eof}/E$, where $\boldsymbol{\upsilon}_{eof}$ is the steady-state bulk EOF. At low λ_D, $\boldsymbol{\mu}_{eof}$ can be represented in terms of the bulk solvent viscosity η_o, and the zeta potential ζ by the Helmholtz-Smoluchowski relation (Slater, '10);

$$\boldsymbol{\mu}_{eof} = \frac{\epsilon_0 \epsilon_r \zeta}{\eta_o} \tag{14}$$

Also, the zeta potential can be represented in terms of σ_s and λ_D for different electrolyte solutions by combining equations (9) into (10):(Chai, '04)

$$\zeta = \frac{2\ k_B T}{e} \ln\left[\frac{2\ e\ \sigma_s\ \lambda_D}{\epsilon_r\ \epsilon_0\ k_B\ T} + \sqrt{1+\left[\frac{\left(e\ \lambda_D / \epsilon_r\ \epsilon_0\ k_B\ T\right)^2}{4}\right]} \right] \tag{15}$$

With ϵ_0 and ϵ_r constants, conditions that change σ_s, ζ, λ_D, or η will alter the magnitude of the EOF. $\boldsymbol{\mu}_{eof}$ was measured using the current monitoring method.(Huang, '88) For the EOF measurement, we used PMMA devices possessing a single nanofluidic channel 138 µm long and 0.1 M and 0.05 M KCl solutions to allow for the generation of a large amount of readable current (see Figure 2.9c for a typical current trace) and to ensure that the measurement was performed at a region where equation 14 is valid ($\lambda_D \leq 2$ nm). This single channel geometry eliminates errors

in migration time that may arise due to preferential filling across an array of nanochannels during electrolyte replacement. A negative EOF value indicated that the EOF was from cathode to anode and consistent with a positively charged fluidic channel wall while a positive EOF value indicated a negatively charged wall. Molecular Dynamics (MD) simulations reported by Qiao *et al*. (Zangle, '10) have revealed that differences in the distribution of counterions for negatively charged O_2-PMMA devices when compared to the positively charged NH_2-PMMA is influenced by the finite size of the ions - K^+ (0.27 nm) and Cl^- (0.36 nm) and the EOF is influenced by surface fluid interactions.

Table 2.2 Measured and expected EOF values as well as surface charge and zeta potentials for the plasma activated and amine terminated devices investigated at pH 7.8

Device	**Terminating groups**	**σ_s (mC/m^2)**	**ζ (mV)**	**μ_{eof} (cm^2/Vs) × 10^{-4}**	
				Expected*	**Measured**
Nanoslit	O_2-PMMA	- 38.3	- 57.1	4.53	0.93 ± 0.025
	NH_2-PMMA	28.4	45.8	- 3.63	- 0.82 ± 0.012
Nanochannel	O_2-PMMA	- 40.5	- 59.8	4.74	1.02 ± 0.017
	NH_2-PMMA	22.9	38.3	- 3.04	- 0.75 ± 0.021

*Calculated from equation (15) using the values for σ_s and ζ

In previous work, we have shown that exposing PMMA microchannels to controlled plasma conditions can generate carboxylate groups with a surface coverage of 2.7 ± 0.5 × 10^{-9} mol/cm^2 (Xu, '07). We have also reported the EOF at pH 7.4 for carboxylated and NH_2-terminated PMMA microfluidic devices to be 4.43 ±0.58 × 10^{-4} cm^2/ Vs and -1.34 ±0.21 × 10^{-4} cm^2/Vs, respectively (Llopis, '07). As shown in Table 2.2, we obtained an EOF of 0.93 ±0.03 × 10^{-4} cm^2/Vs and -0.82 ±0.01 × 10^{-4} cm^2/Vs for O_2- and NH_2-PMMA nanoslits, respectively. For the O_2- and NH_2-PMMA nanochannels, the EOF was found to be 1.02 ±0.02 × 10^{-4} cm^2/Vs and -0.75 ±0.02 × 10^{-4} cm^2/Vs, respectively. The trend and magnitude of the EOF observed in the PMMA nanofluidic devices scales with the measured $\sigma_s$in the nanochannel and was consistent

with molecular dynamic simulations reported by Qiao *et al.*(Menard, '12). The values reported for the O_2-PMMA nanochannels were similar to that reported by Menard *et al*. (Menard, '13) for fused silica nanochannels (≤100 nm) measured using 2× TBE with 2% polyvinylpyrrolidone acting as an EOF suppressor ($0.79 \pm 0.01 \times 10^{-4}$ cm^2/Vs) and ~35.8 ±4.4% lower when compared to fused silica channels measured with 2× TBE only ($1.58 \pm 0.01 \times 10^{-4}$ cm^2/Vs). A possible reason for the lower EOF observed in the PMMA nanofluidic devices is the low ζ. This conclusion is supported by the results from the continuum theory based on the Poisson–Boltzmann equation for the ion distribution, Navier–Stokes equations for fluid transport (Slater, '10) and atomistic simulations (Menard, '12). Both models showed that the EOF in a nanofluidic channel varies almost linearly with ζ with the latter model true for surface charge densities ≤80 mC/m^2 (Menard, '12). Furthermore, ζ depends on the chemistry of the solid–liquid interface and is related to the surface charge density by parameters such as the ionic strength, density of charged sites on the surface, their pK_a values and the solution pH, which modulates the extent of dissociation of the surface groups (Figure 2.10).

In addition, recent reports have shown that reducing the size of fluidic channels can result in reductions of the EOF due to the apparent increase in the viscosity of a fluid upon confinement in charged nanoconduits (Craighead, '03; Kaji, '06; Kim, '09; Wang, '05), an effect not considered in equation 14. In most cases, this phenomenon makes the ratio of the apparent to predicted or bulk viscosity, represented as η_{app}/η_o, to exceed 1.3 with this ratio dependent on the material of the channel walls, size and shape of the channel, the ionic concentration, ζ, temperature, and dielectric constant (Kim, '09). Due to the relatively higher ζ in glass-based devices, η_{app}/η_o is expected to be greater when compared to thermoplastic devices. This may explain why the EOF measured in glass nanoslits at pH 8.5 (~1.3×10^{-4} cm^2/Vs) was lower than

those of fused silica micro-capillaries (5×10^{-4} cm^2/Vs) (Hug, '06) or glass microchannels (4.82×10^{-4} cm^2/Vs) (Pu, '04).

2.2.9 Transport Dynamics of λ-DNA through Thermoplastic Nanochannels.

The majority of applications explored in nanofluidic devices have focused on investigating the transport properties of dsDNA confined in fused silica glass (Chan, '96; Martins, '13; Menard, '13; Menard, '11; Tas, '02; Xu, '07; Yang, '06) and elastomeric (Qiao, '05; Wang, '10) nanochannels. However, because thermoplastics possess dissimilar surface properties compared to glass-based devices (Chantiwas, '11), it becomes necessary to explore the transport properties of dsDNA in these devices. Although, a few studies have utilized PMMA-based nanoslits (Chantiwas, '10) and nanochannels (Kaji, '06; Tas, '04) for DNA stretching, the electrokinetic parameters of dsDNA in surface modified thermoplastic 2D nanochannels is yet to be reported. Understanding the effects of $\sigma_s$and the charge polarity on these parameters and on the stretching properties of dsDNA in thermoplastic nanochannels is necessary for assessing the viability of these devices for applications in DNA sizing or mapping.

First, we assessed the degree of extension of dsDNA confined in O_2-PMMA nanochannels seeded with 2× TBE buffer (pH 7.5). When a DNA molecule with width *w* was driven from a microchannel into the nanochannel under a constant field, upon initial entrance (also called DNA injection), the molecule was observed to stretch because the pulling electric force acted against the resistance due to the entropic interface and frictional forces experienced by the portion of the molecule resident in the microchannel (red trace and insert in Figure 2.12a) (Chan, '96). When the field was turned off after the molecule had fully entered the nanochannel, the molecule underwent elastic relaxation and attained an equilibrium extension length shorter than the injection length (blue trace and insert of Figure 2.12a).

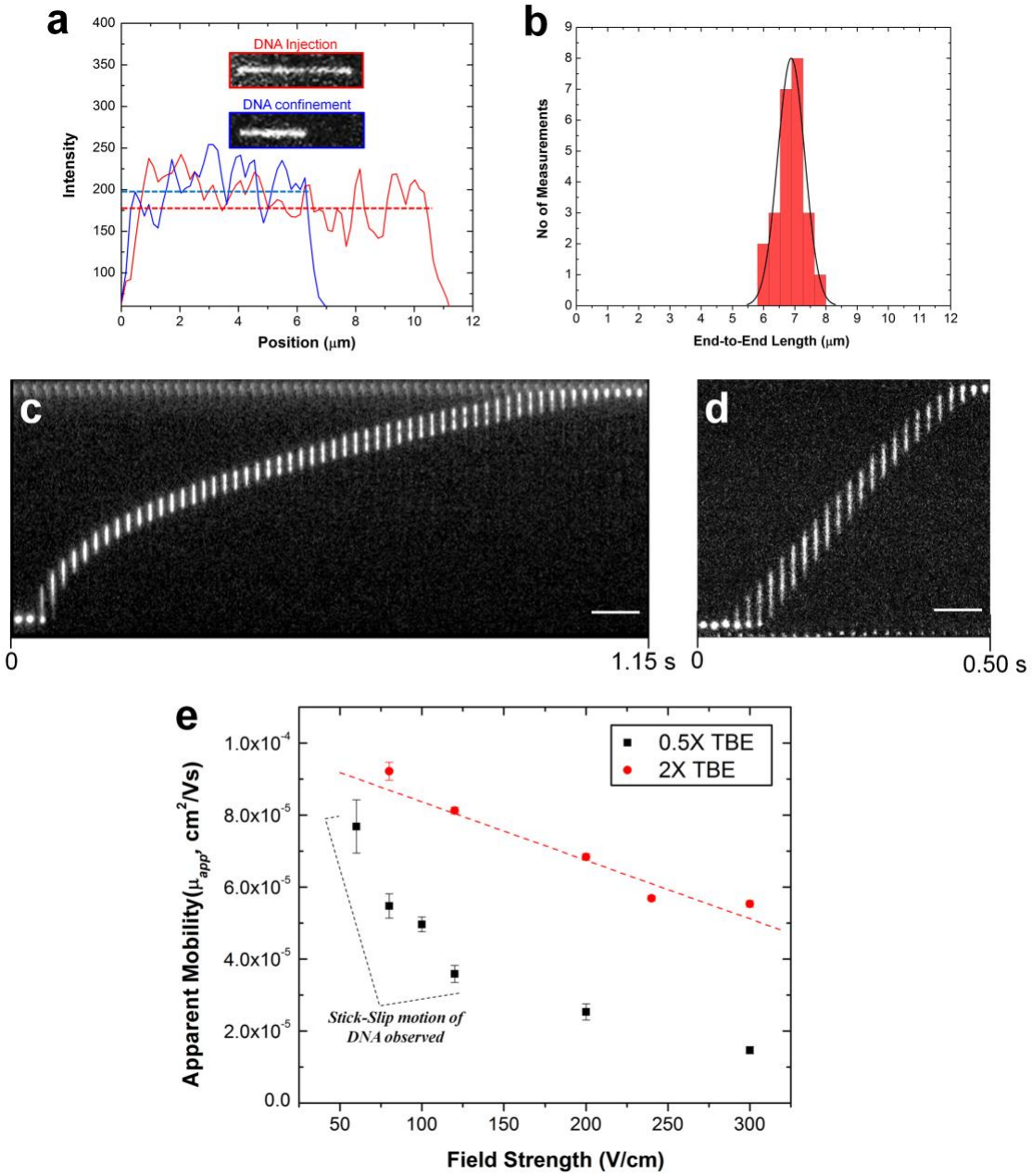

Figure 2.12 (a) Representative fluorescence intensity profile of an individual YOYO-1 stained λ-DNA molecule after injection (red line) and confinement (blue line) in the plasma modified nanochannel filled with 2X TBE buffer. Complete injection into the nanochannel produced an initial molecule length of 11.25 ±1.68 μm (calculated from n=20 events). However, when the voltage was turned off, the DNA relaxed to its equilibrium length. (b) Histogram of the measured end-to-end length of relaxed λ-DNA molecules confined in the PMMA nanochannel. The average equilibrium length determined by the Gaussian curve fit (black line) was ~ 6.88 ±0.43 μm. Representative frames of fluorescently stained λ-DNA molecules translocating through a 100 nm × 100 nm plasma modified PMMA nanochannel and imaged in (c) 0.5× and (d) 2× TBE buffer at 80 V/cm and 120 V/cm, respectively. The time between frames is approximately 20 ms and scale bars are 10 μm. (e) Plots of DNA apparent mobility against the electric field strength for DNA translocation through the single nanochannel filled with 0.5× (black markers) and 2× (red markers) TBE buffer. Error bars represent the standard deviations in the measurements (n = 10)

Assuming that the nanochannel has a depth D, which is less than the free-solution radius of gyration but greater than the persistence length l_p of the molecule, due to self-avoidance the confined molecule will extend in such a way that it divides into a series of non-interpenetrating blobs with the molecular mass distributed along the channel with relatively uniform density (Martins, '13). We estimated the extension factor ε of the confined DNA molecule possessing an equilibrium extension length L_E and a contour length L_C with the equation;

$$\frac{L_E}{L_C} \approx \frac{(l_p\, w)^{1/3}}{D^{2/3}} \qquad (16)$$

Although, the total contour length of an unstained λ-DNA molecule (48.5 kbp) is 16.3 μm, at our intercalating dye concentration, we expect a 23% increase in length to 20 μm (Xu, '07). Therefore, from equation 16, we expect the extension factor for a stained λ-DNA molecule with a width of 3 nm (Kwak, '11) and persistence length of 50 nm confined in a 100 × 100 nm nanochannel to be ~0.25. Nevertheless, we note that equation 16 does not account for ionic effects, like the buffer ionic strength and viscosity, on the elasticity and wall wettability, roughness and frictional drag on the overall extension of the DNA molecule (Baumann, '97; Bilenberg, '05; Yang, '06).

In our experiment, we observed that when stained λ-DNA molecules were completely introduced into the O_2-PMMA nanochannels, it stretched to ~11.25 ±1.68 μm at initial entry (calculated from n = 20). When the field was turned off, the DNA molecules remained confined in the nanochannel but relaxed to an overall average extension length of 6.88 μm, determined from a Gaussian curve fit of the histogram shown in Figure 2.12b. The experimental extension factor was 0.34, a value ~40% greater than that predicted by the de Gennes theory. The enhanced stretching of the confined DNA molecule was likely due to additional interfacial surface forces

in the form of surface energy acting on the DNA molecule from the charged nanochannel walls. The measured surface energy for O_2-PMMA devices was ~38.9 mJ/m^2 (see Figure 2.5).

Next, we investigated the electrophoretic properties of DNA molecules electrokinetically driven through nanochannels using 50 µm long, 100 nm × 100 nm channels. All DNA movements represented in the frames shown in Figures 2.12c and 2.12d were observed without the need of an EOF suppressor. The apparent electrophoretic mobility μ_{app} of DNA in the nanochannel was due to the electrophoretic mobility of DNA, μ_{ep}, and the EOF.

Figure 2.12e shows the variation of μ_{app} for λ-DNA traveling through O_2-PMMA nanochannels filled with 0.5× (black squares) and 2× (red circles) TBE. Our results revealed that the apparent mobility of λ-DNA was lower in the channel filled with 0.5× TBE than that of 2× TBE. One possible reason for this was that as the ionic strength of the buffer solution in the charged nanochannel was reduced, there was a corresponding increase in λ_D (~30 nm for 0.5× and ~8 nm for 2× TBE, estimated from classical theory) (Schoch, '05; van Honschoten, '10). This led to a larger EOF for the lower ionic strength buffer thereby reducing μ_{app} of λ-DNA molecules through the nanochannel. We observed that in the devices filled with 2× TBE, the DNA moved through the nanochannel with a constant velocity (Figure 2.12d) and an almost linear variation of the electrophoretic mobility for the entire range of electric field strengths studied (red trace in Figure 2.12e). This confirmed the absence of dielectrophoretic trapping sites along the channel wall, which was supported by the low nanochannel wall roughness. Interestingly, in the nanochannels seeded with 0.5× TBE, we observed intermittent (stick-slip) motion of the DNA molecules through the nanochannel similar to previous reports (Chantiwas, '10; Tas, '02) at measurements performed <150 V/cm (Figure 2.12c). Based on MD simulations(Luan, '10) and theoretical computations (Binquan, '13), a highly negatively charged DNA molecule translocating through a nanochannel interacts both electrically (attractive or repulsive forces) and

hydrodynamically with the channel wall. Therefore, we attributed the intermittent motion of DNA to latent electrical interactions between the charged DNA molecule and the thick EDL and this presents the possibility that at this field strength, the driving force was less than the interfacial force. This observation is yet to be reported for DNAs translocating through glass nanofluidic devices at this field strength because the threshold field strength required to introduce DNA into nanochannels without the addition of an EOF suppressor was >200 V/cm for 100 nm nanochannels (Menard, '13). However, at field strengths greater than 200 V/cm, we did not observe intermittent motion of DNA in these devices with 0.5× TBE. It is possible that at these fields, the driving force overwhelmed the interfacial force causing the DNA to move through the nanochannel with continuous velocity or that the wall interactions occurred so fast they were not detectable at our imaging frame rate.

Finally, we performed translocation experiments in a NH_2-PMMA device using 2× TBE (pH 7.4). At this pH, we observed that λ-DNA adsorbed onto the surface of the assess microchannels and remained immobile even with the application of a large bias voltage. This sticking is probably due to strong electrostatic interactions between the negatively charged DNA backbone and the positively charged amine groups. When the solution pH was increased to 10, there were significant reductions in DNA sticking in the microchannel and several λ-DNA molecules were observed to move towards the entrance of the nanochannel. However, when the DC voltage was turned on, the DNA molecules initially attempted to enter the nanochannel but paused at first entry (Figure 2.13). No further movement was observed at higher fields and even with reversed DC voltages. This is likely due to strong wall interactions with residual $–NH_3^+$ groups or hydrogen bonding between the DNA and the deprotonated $–NH_2$ groups overwhelming the electrokinetic driving force.

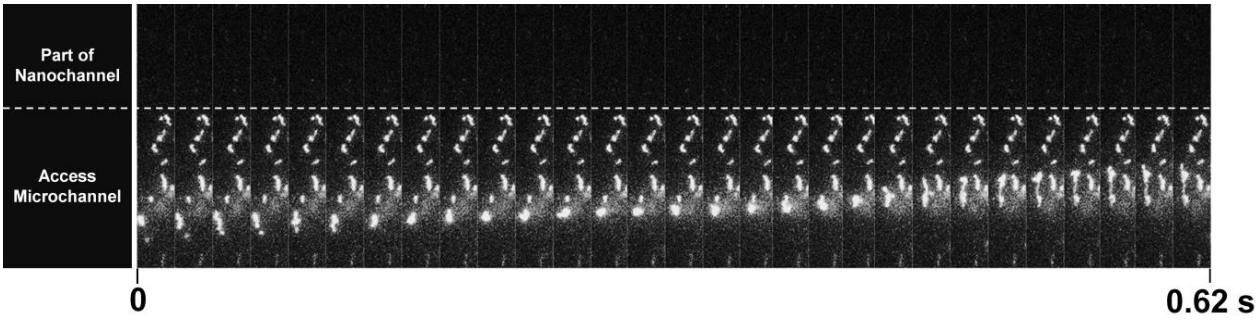

Figure 2.13 Representative frames of translocation events of λ-DNA in amine modified nanofluidic devices in the presence of a bias electric field (20 V) in a 2X TBE buffer (pH ≈ 10).

2.3 Conclusion

In this work, we report a simple and robust fabrication strategy that can be used to produce thermoplastic nanofluidic devices with structures below 20 nm. Furthermore, because the fabrication steps were successfully achieved using simple bench top UV curing and thermal embossing instruments, the cost of device fabrication was significantly reduced compared to conventional NIL techniques. We demonstrated the successful modification of thermoplastic nanoslits and nanochannels using oxygen plasma to produce carboxylic acid moieties that could be subsequently converted into amino groups by reaction with EDA. For the conditions reported in this work, the plasma treated polymer nanoslits and nanochannels were observed to possess $|\sigma_s|$ of 38.2 mC/m^2 and 40.5 mC/m^2, respectively, at pH 7.8. These values were lower than that reported for their glass-based counterparts. The low surface charge densities in polymer nanofluidic devices helped to minimize artifacts arising from ion exclusion due to concentration polarization. The ability to generate positively charged moieties in a simple modification scheme with $|\sigma_s|$ of 28.4 mC/m^2 in the nanoslits and 22.9 mC/m^2 in the nanochannels offers a unique venue for performing nanochannel chromatography by generating the proper stationary phase.

The reduced EOF observed in PMMA nanofluidic devices compared to polymer microchannels and glass nanochannels was likely due to lower surface charge density (and zeta potential) and apparent increases in fluid viscosity due to nanoconfinement. Generally, lower

EOF values are desirable in applications involving DNA analysis for mapping and sequencing because it enables the introduction of these biomolecules into the fluidic channels without the need for EOF suppressors.

REFERENCES

Abgrall, P.; Low, L.-N.; Nguyen, N.-T. Fabrication of planar nanofluidic channels in a thermoplastic by hot-embossing and thermal bonding. *Lab on a Chip* 2007, 7, 520-522.

Amirsadeghi, A.; Lee, J. J.; Park, S. Surface adhesion and demolding force dependence on resist composition in ultraviolet nanoimprint lithography. *Applied Surface Science* 2011, 258, 1272-1278.

Anand, R. K.; Sheridan, E.; Knust, K. N.; Crooks, R. M. Bipolar Electrode Focusing: Faradaic Ion Concentration Polarization. *Analytical Chemistry* 2011, 83, 2351-2358.

Baumann, C. G.; Smith, S. B.; Bloomfield, V. A.; Bustamante, C. Ionic effects on the elasticity of single DNA molecules. *Proceedings of the National Academy of Sciences* 1997, 94, 6185-6190.

Becker, H.; Gärtner, C. Polymer microfabrication technologies for microfluidic systems. *Anal Bioanal Chem* 2008, 390, 89-111.

Ben, A. S.; Baud, G.; Jacquet, M.; Nanse, G.; Fioux, P.; Nardin, M. XPS characterization of plasma-treated and alumina-coated PMMA. *Appl. Surf. Sci.* 2000, 153, 172-183.

Bilenberg, B.; Hansen, M.; Johansen, D.; Özkapici, V.; Jeppesen, C.; Szabo, P.; Obieta, I. M.; Arroyo, O.; Tegenfeldt, J. O.; Kristensen, A. Topas-based lab-on-a-chip microsystems fabricated by thermal nanoimprint lithography. *Journal of Vacuum Science & Technology B* 2005, 23, 2944-2949.

Binquan, L.; Gustavo, S. An electro-hydrodynamics-based model for the ionic conductivity of solid-state nanopores during DNA translocation. *Nanotechnology* 2013, 24, 195702.

Chai, J.; Lu, F.; Li, B.; Kwok, D. Y. Wettability Interpretation of Oxygen Plasma Modified Poly(methyl methacrylate). *Langmuir* 2004, 20, 10919-10927.

Chan-Park, M. B.; Yan, Y.; Neo, W. K.; Zhou, W.; Zhang, J.; Yue, C. Y. Fabrication of High Aspect Ratio Poly(ethylene glycol)-Containing Microstructures by UV Embossing. *Langmuir* 2003, 19, 4371-4380.

Chan, C. M.; Ko, T. M.; Hiraoka, H. Polymer surface modification by plasmas and photons. *Surface Science Reports* 1996, 24, 1-54.

Chantiwas, R.; Hupert, M. L.; Pullagurla, S. R.; Balamurugan, S.; Tamarit-Lopez, J.; Park, S.; Datta, P.; Goettert, J.; Cho, Y.-K.; Soper, S. A. Simple replication methods for producing nanoslits in thermoplastics and the transport dynamics of double-stranded DNA through these slits. *Lab on a Chip* 2010, 10, 3255-3264.

Chantiwas, R.; Park, S.; Soper, S. A.; Kim, B. C.; Takayama, S.; Sunkara, V.; Hwang, H.; Cho, Y.-K. Flexible fabrication and applications of polymer nanochannels and nanoslits. *Chemical Society Reviews* 2011, 40, 3677-3702.

Cheng, L.-J.; Guo, L. J. Nanofluidic diodes. *Chemical Society Reviews* 2010, 39, 923-938.

Chou, S. Y.; Krauss, P. R.; Renstrom, P. J. Imprint of sub-25 nm vias and trenches in polymers. *Applied Physics Letters* 1995, 67, 3114-3116.

Chung, S.; Lee, J. H.; Moon, M.-W.; Han, J.; Kamm, R. D. Non-lithographic wrinkle nanochannels for protein preconcentration. *Adv. Mater. (Weinheim, Ger.)* 2008, 20, 3011-3016.

Craighead, H. Future lab-on-a-chip technologies for interrogating individual molecules. *Nature (London, U. K.)* 2006, 442, 387-393.

Craighead, H. G. Nanostructure science and technology: Impact and prospects for biology. *J. Vac. Sci. Technol., A* 2003, 21, S216-S221.

Daiguji, H. Ion transport in nanofluidic channels. *Chemical Society Reviews* 2010, 39, 901-911.

Daiguji, H.; Yang, P.; Majumdar, A. Ion Transport in Nanofluidic Channels. *Nano Letters* 2003, 4, 137-142.

Gröning, P.; Collaud, M.; Dietler, G.; Schlapbach, L. Plasma modification of polymethylmethacrylate and polyethyleneterephthalate surfaces. *Journal of Applied Physics* 1994, 76, 887-892.

Han, J.; Craighead, H. G. Separation of Long DNA Molecules in a Microfabricated Entropic Trap Array. *Science* 2000, 288, 1026-1029.

Hawthorne, S. B.; Yang, Y.; Grabanski, C. B.; Miller, D. J.; Lee, M. L. Response to comments on adsorption versus absorption of polychlorinated biphenyls onto solid-phase microextraction coatings. *Anal. Chem.* 2000, 72, 642-643.

Henry, A. C.; Tutt, T. J.; Galloway, M.; Davidson, Y. Y.; McWhorter, C. S.; Soper, S. A.; McCarley, R. L. Surface Modification of Poly(methyl methacrylate) Used in the Fabrication of Microanalytical Devices. *Analytical Chemistry* 2000, 72, 5331-5337.

Huang, X.; Gordon, M. J.; Zare, R. N. Current-monitoring method for measuring the electroosmotic flow rate in capillary zone electrophoresis. *Anal. Chem.* 1988, 60, 1837-8.

Hug, T.; Rooij, N. d.; Staufer, U. Fabrication and electroosmotic flow measurements in micro- and nanofluidic channels. *Microfluid. Nanofluid.* 2006, 2, 117-124.

Huh, D.; Mills, K. L.; Zhu, X. Y.; Burns, M. A.; Thouless, M. D.; Takayama, S. Tuneable elastomeric nanochannels for nanofluidic manipulation. *Nat. Mater.* 2007, 6, 424-428.

Jackson, J. M.; Witek, M. A.; Hupert, M. L.; Brady, C.; Pullagurla, S.; Kamande, J.; Aufforth, R. D.; Tignanelli, C. J.; Torphy, R. J.; Yeh, J. J.; Soper, S. A. UV activation of polymeric high aspect ratio microstructures: ramifications in antibody surface loading for circulating tumor cell selection. *Lab on a Chip* 2014, 14, 106-117.

Kaji, N.; Ogawa, R.; Oki, A.; Horiike, Y.; Tokeshi, M.; Baba, Y. Study of water properties in nanospace. *Anal Bioanal Chem* 2006, 386, 759-764.

Karnik, R.; Castelino, K.; Fan, R.; Yang, P.; Majumdar, A. Effects of Biological Reactions and Modifications on Conductance of Nanofluidic Channels. *Nano Letters* 2005, 5, 1638-1642.

Keyser, U. F.; van Dorp, S.; Lemay, S. G. Tether forces in DNA electrophoresis. *Chemical Society Reviews* 2010, 39, 939-947.

Kim, D.; Darve, E. Molecular dynamics simulation of electro-osmotic flows in rough wall nanochannels. *Physical Review E* 2006, 73, 051203.

Kim, S. J.; Ko, S. H.; Kang, K. H.; Han, J. Direct seawater desalination by ion concentration polarization (vol 5, pg 297, 2010). *Nat. Nanotechnol.* 2013, 8, 609-609.

Kim, S. J.; Li, L. D.; Han, J. Amplified Electrokinetic Response by Concentration Polarization near Nanofluidic Channel. *Langmuir* 2009, 25, 7759-7765.

Kim, S. J.; Wang, Y.-C.; Lee, J. H.; Jang, H.; Han, J. Concentration Polarization and Nonlinear Electrokinetic Flow near a Nanofluidic Channel. *Physical Review Letters* 2007, 99, 044501.

Kwak, R.; Kim, S. J.; Han, J. Continuous-Flow Biomolecule and Cell Concentrator by Ion Concentration Polarization. *Anal. Chem. (Washington, DC, U. S.)* 2011, 83, 7348-7355.

Kwok, D. Y.; Neumann, A. W. Contact angle measurement and contact angle interpretation. *Advances in Colloid and Interface Science* 1999, 81, 167-249.

Levy, S. L.; Craighead, H. G. DNA manipulation, sorting, and mapping in nanofluidic systems. *Chem. Soc. Rev.* 2010, 39, 1133-1152.

Levy, S. L.; Mannion, J. T.; Cheng, J.; Reccius, C. H.; Craighead, H. G. Entropic Unfolding of DNA Molecules in Nanofluidic Channels. *Nano Letters* 2008, 8, 3839-3844.

Liang, X.; Chou, S. Y. Nanogap Detector Inside Nanofluidic Channel for Fast Real-Time Label-Free DNA Analysis. *Nano Letters* 2008, 8, 1472-1476.

Llopis, S. L.; Osiri, J.; Soper, S. A. Surface modification of poly(methyl methacrylate) microfluidic devices for high-resolution separations of single-stranded DNA. *ELECTROPHORESIS* 2007, 28, 984-993.

Luan, B.; Afzali, A.; Harrer, S.; Peng, H.; Waggoner, P.; Polonsky, S.; Stolovitzky, G.; Martyna, G. Tribological Effects on DNA Translocation in a Nanochannel Coated with a Self-Assembled Monolayer. *The Journal of Physical Chemistry B* 2010, 114, 17172-17176.

Mani, A.; Zangle, T. A.; Santiago, J. G. On the Propagation of Concentration Polarization from Microchannel−Nanochannel Interfaces Part I: Analytical Model and Characteristic Analysis. *Langmuir* 2009, 25, 3898-3908.

Martins, D. C.; Chu, V.; Conde, J. P. The effect of the surface functionalization and the electrolyte concentration on the electrical conductance of silica nanochannels. *Biomicrofluidics* 2013, 7, -.

Meisenberg, G. *Principles of medical biochemistry*. Mosby Elsevier: Philadelphia, 2006.

Menard, L. D.; Mair, C. E.; Woodson, M. E.; Alarie, J. P.; Ramsey, J. M. A Device for Performing Lateral Conductance Measurements on Individual Double-Stranded DNA Molecules. *ACS Nano* 2012, 6, 9087-9094.

Menard, L. D.; Ramsey, J. M. Electrokinetically-Driven Transport of DNA through Focused Ion Beam Milled Nanofluidic Channels. *Analytical Chemistry* 2013, 85, 1146-1153.

Menard, L. D.; Ramsey, J. M. Fabrication of Sub-5 nm Nanochannels in Insulating Substrates Using Focused Ion Beam Milling. *Nano Letters* 2011, 11, 512-517.

Messinger, R. J.; Squires, T. M. Suppression of Electro-Osmotic Flow by Surface Roughness. *Physical Review Letters* 2010, 105.

Mitchell, D. F.; Clark, K. B.; Bardwell, J. A.; Lennard, W. N.; Massoumi, G. R.; Mitchell, I. V. Film thickness measurements of SiO2 by XPS. *Surface and Interface Analysis* 1994, 21, 44-50.

Park, H. M.; Lee, H. D. Effects of wall roughness and velocity slip on streaming potential of microchannels. *International Journal of Heat and Mass Transfer* 2012, 55, 3295-3306.

Park, K. D.; Lee, S. W.; Takama, N.; Fujii, T.; Kim, B. J. Arbitrary-shaped nanochannels fabricated by polymeric deformation to achieve single DNA stretching. *Microelectron. Eng.* 2009, 86, 1385-1388.

Park, S.-m.; Huh, Y. S.; Graighead, H. G.; Erickson, D. A method for nanofluidic device prototyping using elastomeric collapse. *Proc. Natl. Acad. Sci. U. S. A.* 2009, 106, 15549-15554, S15549/1-S15549/6.

Pennathur, S.; Baldessari, F.; Santiago, J. G.; Kattah, M. G.; Steinman, J. B.; Utz, P. J. Free-Solution Oligonucleotide Separation in Nanoscale Channels. *Analytical Chemistry* 2007, 79, 8316-8322.

Persson, F.; Tegenfeldt, J. O. DNA in nanochannels-directly visualizing genomic information. *Chem. Soc. Rev.* 2010, 39, 985-999.

Piruska, A.; Gong, M.; Sweedler, J. V.; Bohn, P. W. Nanofluidics in chemical analysis. *Chemical Society Reviews* 2010, 39, 1060-1072.

Plecis, A.; Schoch, R. B.; Renaud, P. Ionic Transport Phenomena in Nanofluidics: Experimental and Theoretical Study of the Exclusion-Enrichment Effect on a Chip. *Nano Letters* 2005, 5, 1147-1155.

Powell, C. J.; Jablonski, A.; Tanuma, S.; Penn, D. R. Effects of elastic and inelastic electron scattering on quantitative surface analyses by AES and XPS. *Journal of Electron Spectroscopy and Related Phenomena* 1994, 68, 605-616.

Pu, Q.; Yun, J.; Temkin, H.; Liu, S. Ion-Enrichment and Ion-Depletion Effect of Nanochannel Structures. *Nano Letters* 2004, 4, 1099-1103.

Qiao, R.; Aluru, N. R. Scaling of Electrokinetic Transport in Nanometer Channels. *Langmuir* 2005, 21, 8972-8977.

Reccius, C. H.; Mannion, J. T.; Cross, J. D.; Craighead, H. G. Compression and Free Expansion of Single DNA Molecules in Nanochannels. *Physical Review Letters* 2005, 95, 268101.

Rotting, O.; Ropke, W.; Becker, H.; Gartner, C. Polymer microfabrication technologies. *Microsyst. Technol.* 2002, 8, 32-36.

Saleh, O. A.; Sohn, L. L. An artificial nanopore for molecular sensing. *Nano Lett.* 2003, 3, 37-38.

Schoch, R. B.; Han, J.; Renaud, P. Transport phenomena in nanofluidics. *Reviews of Modern Physics* 2008, 80, 839-883.

Schoch, R. B.; Renaud, P. Ion transport through nanoslits dominated by the effective surface charge. *Applied Physics Letters* 2005, 86, 25311 1-3.

Seah, M. P.; Dench, W. A. Quantitative electron spectroscopy of surfaces: A standard data base for electron inelastic mean free paths in solids. *Surface and Interface Analysis* 1979, 1, 2-11.

Seidel, C.; Kopf, H.; Gotsmann, B.; Vieth, T.; Fuchs, H.; Reihs, K. Ar plasma treated and Al-metalized polycarbonate: a XPS, mass spectroscopy and SFM study. *Appl. Surf. Sci.* 1999, 150, 19-33.

Shao, P. E.; van Kan, A.; Wang, L. P.; Ansari, K.; Bettiol, A. A.; Watt, F. Fabrication of enclosed nanochannels in poly(methylmethacrylate) using proton beam writing and thermal bonding. *Applied Physics Letters* 2006, 88, -.

Slater, G.; Tessier, F.; Kopecka, K. The Electroosmotic Flow (EOF). In *Microengineering in Biotechnology*, Hughes, M. P.; Hoettges, K. F., Eds. Humana Press: 2010; Vol. 583, pp 121-134.

Sonnefeld, J.; Göbel, A.; Vogelsberger, W. Surface charge density on spherical silica particles in aqueous alkali chloride solutions. *Colloid Polym Sci* 1995, 273, 926-931.

Soper, S. A.; Henry, A. C.; Vaidya, B.; Galloway, M.; Wabuyele, M.; McCarley, R. L. Surface modification of polymer-based microfluidic devices. *Analytica Chimica Acta* 2002, 470, 87-99.

Stein, D.; Kruithof, M.; Dekker, C. Surface-Charge-Governed Ion Transport in Nanofluidic Channels. *Physical Review Letters* 2004, 93, 035901.

Tas, N. R.; Berenschot, J. W.; Mela, P.; Jansen, H. V.; Elwenspoek, M.; van den Berg, A. 2D-Confined Nanochannels Fabricated by Conventional Micromachining. *Nano Letters* 2002, 2, 1031-1032.

Tas, N. R.; Haneveld, J.; Jansen, H. V.; Elwenspoek, M.; van den Berg, A. Capillary filling speed of water in nanochannels. *Applied Physics Letters* 2004, 85, 3274-3276.

Tsukahara, T.; Mawatari, K.; Kitamori, T. Integrated extended-nano chemical systems on a chip. *Chemical Society Reviews* 2010, 39, 1000-1013.

van Honschoten, J. W.; Brunets, N.; Tas, N. R. Capillarity at the nanoscale. *Chemical Society Reviews* 2010, 39, 1096-1114.

Wang, M.; Chang, C.-C.; Yang, R.-J. Electroviscous effects in nanofluidic channels. *The Journal of Chemical Physics* 2010, 132, -.

Wang, M.; Wang, J.; Chen, S. Roughness and cavitations effects on electro-osmotic flows in rough microchannels using the lattice Poisson–Boltzmann methods. *Journal of Computational Physics* 2007, 226, 836-851.

Wang, Y.-C.; Stevens, A. L.; Han, J. Million-fold Preconcentration of Proteins and Peptides by Nanofluidic Filter. *Analytical Chemistry* 2005, 77, 4293-4299.

Wei, S.; Vaidya, B.; Patel, A. B.; Soper, S. A.; McCarley, R. L. Photochemically Patterned Poly(methyl methacrylate) Surfaces Used in the Fabrication of Microanalytical Devices. *J. Phys. Chem. B* 2005, 109, 16988-16996.

Wenzel, R. N. Surface Roughness and Contact Angle. *The Journal of Physical and Colloid Chemistry* 1949, 53, 1466-1467.

Wu, J.; Chantiwas, R.; Amirsadeghi, A.; Soper, S. A.; Park, S. Complete plastic nanofluidic devices for DNA analysis via direct imprinting with polymer stamps. *Lab on a Chip* 2011, 11, 2984-2989.

Xu, F.; Datta, P.; Wang, H.; Gurung, S.; Hashimoto, M.; Wei, S.; Goettert, J.; McCarley, R. L.; Soper, S. A. Polymer Microfluidic Chips with Integrated Waveguides for Reading Microarrays. *Analytical Chemistry* 2007, 79, 9007-9013.

Yang, S. C. Effects of surface roughness and interface wettability on nanoscale flow in a nanochannel. *Microfluid. Nanofluid.* 2006, 2, 501-511.

Zangle, T. A.; Mani, A.; Santiago, J. G. Theory and experiments of concentration polarization and ion focusing at microchannel and nanochannel interfaces. *Chemical Society Reviews* 2010, 39, 1014-1035.

Ziarani, A. S.; Mohamad, A. A. Effect of wall roughness on the slip of fluid in a microchannel. *Nanoscale and microscale thermophysical engineering* 2008, 12, 154-169.

CHAPTER 3: HIGH PROCESS YIELDS OF THERMOPLASTIC NANOFLUIDIC DEVICES USING A HYBRID THERMAL ASSEMBLY TECHNIQUE[2]

Introduction

Nanofluidic devices have generated great interest for investigating several unique physical and chemical phenomena that are not readily obtainable in micro-scale environments. For example, nanofluidic devices have served as viable platforms for the analysis of biopolymers, especially DNAs (Abgrall, '08; Prakash, '08). When a double-stranded DNA (dsDNA) is contained in a microchannel, it will assume a randomly coiled-state (low entropy) with a radius of gyration (R_g) defined by the ionic strength of the solution and the contour length of the molecule (Han, '99). However, when confined in a nanochannel with dimensions (width × depth) comparable to its persistence length, ~50 nm for a dsDNA, the molecule stretches with the degree of stretching inversely proportional to the nanochannel dimensions (Guo, '03; Odijk, '08; Reisner, '05; Reisner, '07). This phenomenon has generated interesting applications such as rapid probing of conformational, dynamic and entropic properties of DNA molecules for the determination of the spatial location of genetic information (Levy, '10), identification of methylation patterns within dsDNA (Fang Lim, '11), restriction mapping of genomic DNA (Riehn, '05), DNA fragment sizing (Foquet, '02), localization of transcription factors for protein synthesis to a specific gene or binding site (Li, '03), and high signal-to-noise ratio detection of DNA with minimal multiple occupancy artifacts (Tegenfeldt, '04).

---

[2]This chapter is currently submitted as an article in Lab-On-a-Chip (RSC) and a Provisional patent filed on September 15, 2014 in the United States Patent and Trademark Office (U.S. Provisional application number 62/050,237).

Recently, polymer-based materials, especially thermoplastics – linear or branched polymers with high molecular weights – have become viable substrates for the fabrication of nanofluidic devices. Thermoplastics such as poly(methyl methacrylate) (PMMA), polycarbonate (PC), cyclo-olefin copolymer (COC) and polyethylene terephthalate (PET) possess glass transition temperatures (T_g) that are significantly smaller than glass allowing for the fabrication of nanostructures using nanoimprint lithography (NIL), which is conducive to high production rates at low-cost and with good replication fidelity (Chantiwas, '11). NIL has been successful in patterning structures down to the sub-10 nm scale with the ultimate resolution seemingly determined by the minimum feature size associated with the molding tool (Abgrall, '07; Chantiwas, '10; Chou, '95; Wu, '11). Other modalities that can be used to fabricate thermoplastic nanochannels include proton beam writing (Shao, '06), thermomechnical deformation (Sivanesan, '05), compression of microchannels (Li, '13), sidewall lithography and hot embossing (Cheng, '13), UV-lithography/O_2 plasma etching (Junshan, '12), hot embossing with thermoplastic molding tools (Liu, '13), refill of microchannels (Li, '12), and the use of silica nanowire templates (Zhang, '08).

The aforementioned techniques for producing nanochannels in thermoplastics employed a top-down approach and as such, require an assembly step to enclose the fluidic network. Unfortunately, challenges associated with assembling devices with the cover plates have limited the use of thermoplastic-based nanofluidic devices with the smallest operational 2D thermoplastic nanochannel reported till date being 71 × 77 nm (width × depth). In a typical fluidic device production pipeline, the final step involves bonding the thermoplastic substrate possessing the fluidic network to a second plastic material (cover plate) that encloses the channels. The common modes employed for enclosing thermoplastic nanochannels are thermal or solvent-assisted fusion bonding (Cho, '10). Thermal fusion bonding the substrate to a cover

plate of the same material has been executed by; (i) heating the substrate and cover plate to slightly above its T_g while applying a constant pressure, thereby allowing polymer chains to diffuse between the contact surfaces; or (ii) bonding at a temperature lower than the T_g of the material by using UV or oxygen plasma treatment of the substrate and cover plate prior to chip assembly, thereby reducing the T_g of the first few layers of material (Abgrall, '07; Chantiwas, '10; Hu, '11; Lasse, '08; Wu, '11). Although both approaches have been reported to produce high tensile strengths between the cover plate and substrate, the first approach is typically discouraged for assembly of thermoplastic nanofluidic devices because it results in bulk polymer flow and significant deformation or collapse of the nanochannels (40% and 60% deformation for PMMA and COC, respectively) rendering devices unusable in most cases. The second approach is commonly used for enclosing thermoplastic nanochannels; however, the resulting bond strength is often lower than desired and thus, are unable to withstand high pressure or electric fields for extended periods of time (Chantiwas, '10). Preliminary results obtained from our group have revealed that nanochannels experience reduction in depths (6% for PMMA and 9% for COC) when sealed with cover plates of the same material by fusion bonding at a temperature below its bulk T_g after plasma treatment (Chantiwas, '10). Unfortunately, these channel dimensional changes increased as the nanochannel dimensions dropped below 50 nm and resulted in low process yield rates (*i.e.*, low rates of producing successful devices). Likewise, solvent-assisted bonding suffers from problems associated with dimensional stability because the solvent can soften and embrittle the plastic material leading to material dissolution (Cho, '10). Hence, there remains the need for the development of methods for sealing thermoplastic nanochannels with high bond strength while maintaining structural integrity and producing high process yield rates.

Herein, we report a robust mode for the assembly of thermoplastic nanofluidic devices in which a high T_g thermoplastic substrate possessing the nanofluidic structures is bonded to a

cover plate with a T_g lower than that of the substrate. Although, a similar scheme was proposed for sealing COC-based microsystems (Bilenberg, '05) and recently reported for sealing PMMA nanochannels using a PET cover plate (Cheng, '14), the smallest assembled nanochannels were ~85 nm and the functionality of these devices for biological applications were not demonstrated. In this study, COC (T_g = 75^{o}C) was used as the cover plate due to its excellent optical transmissivity (with low propagation loss at λ >300 nm), low autofluorescence (Khanarian, '01; Piruska, '05), excellent biocompatibility, low moisture uptake (< 0.01%), high temperature tolerance, chemical resistance and ease of surface modification via UV activation or plasma treatment. The T_g of COC depends on the norbornene content and can range from 65 – 180°C for norbornene contents ranging from 60 – 85 wt%, respectively (Bilenberg, '05; Jena, '12). Nanofluidic channels were fabricated in a substrate (PMMA; T_g = 105^{o}C or COC; T_g = 178^{o}C) via a single imprinting step as previously reported (Uba, '14). Device assembly was achieved by bonding the plasma treated cover plate (COC; T_g = 75^{o}C) to the untreated substrate at a temperature ~5^{o}C lower than the T_g of the cover plate. In contrast to the high temperature, time-consuming and long processing steps required for enclosing glass nanofluidic devices (Suni, '02; Tong, '96), our assembly process was performed directly on the thermoplastic substrate following embossing without the need of pre-cleaning or cleanroom conditions in a total time of 15 min. With this assembly approach, we demonstrated the utilization of sub-50 nm thermoplastic nanochannels for high SNR fluorescent imaging and DNA stretching. Bond strengths higher than those of the native polymers assembled at a temperature above its T_g were achieved with a process yield – percent of working assembled devices that retained the nanochannel dimensions predefined in the original Si master – >90% without deformation or collapse of the nanostructures. Finally, nanochannels were successfully modified via UV-

activation through the cover plate post-assembly and the functionality of the assembled devices was assessed by investigating the transport dynamics of dsDNA through the nanochannels.

3.1 Experimental Methods

3.1.1 Materials and Reagents

PMMA sheets (T_g = 105^{o}C), 1.5 mm and 0.175 mm thick, were purchased from Good Fellow (Berwyn, PA). Cyclic olefin copolymer (COC) 6017 ($T_g \approx 178^oC$), 5010 ($T_g \approx 108^oC$) and 8007 ($T_g \approx 78^oC$; 0.13 mm) sheets were purchased from TOPAS Advanced Polymers (Florence KY). Si <100> wafers were purchased from University Wafers (Boston, MA). Tripropylene glycol diacrylate (TPGA), trimethylolpropane triacrylate (TMPA), Irgacure 651 (photo-initiator), 50% potassium hydroxide (KOH), hydrochloric acid (HCl) and potassium chloride (KCl) were obtained from Sigma-Aldrich (St. Louis, MO). The anti-adhesion monolayer of (tridecafluoro – 1,1,2,2 – tetrahydrooctyl) tricholorosilane (T-silane) was purchased from Gelest, Inc. Tris buffer (pH = 8.0) was obtained from Fisher Scientific (Houston, TX). All dilutions were performed using 18 MΩ/cm milliQ water (Millipore).

3.1.2 Device Fabrication

Nanofluidic structures were fabricated in thermoplastic substrates using a scheme previously reported by our group (Uba, '14). Briefly, access microchannels and nanochannels were fabricated in a Si wafer (master) by optical lithography and focused-ion beam milling, respectively. Next, resin stamps were produced from the Si master by curing a UV-resin (68 wt% TPGA, 28 wt% TMPA and 4 wt% Irgacure 651) under 365 nm light coated onto a COC 6017 plate. Subsequently, fluidic structures were imprinted into the polymer substrate by thermal embossing at 125^{o}C for 120 s under 1910 kN/m^2 pressure using a Hex03 hot embosser (JenOptik). In the final fabrication step, fluidic structures were enclosed with a low T_g thermoplastic cover plate using the setup shown in Figure. 3.1.

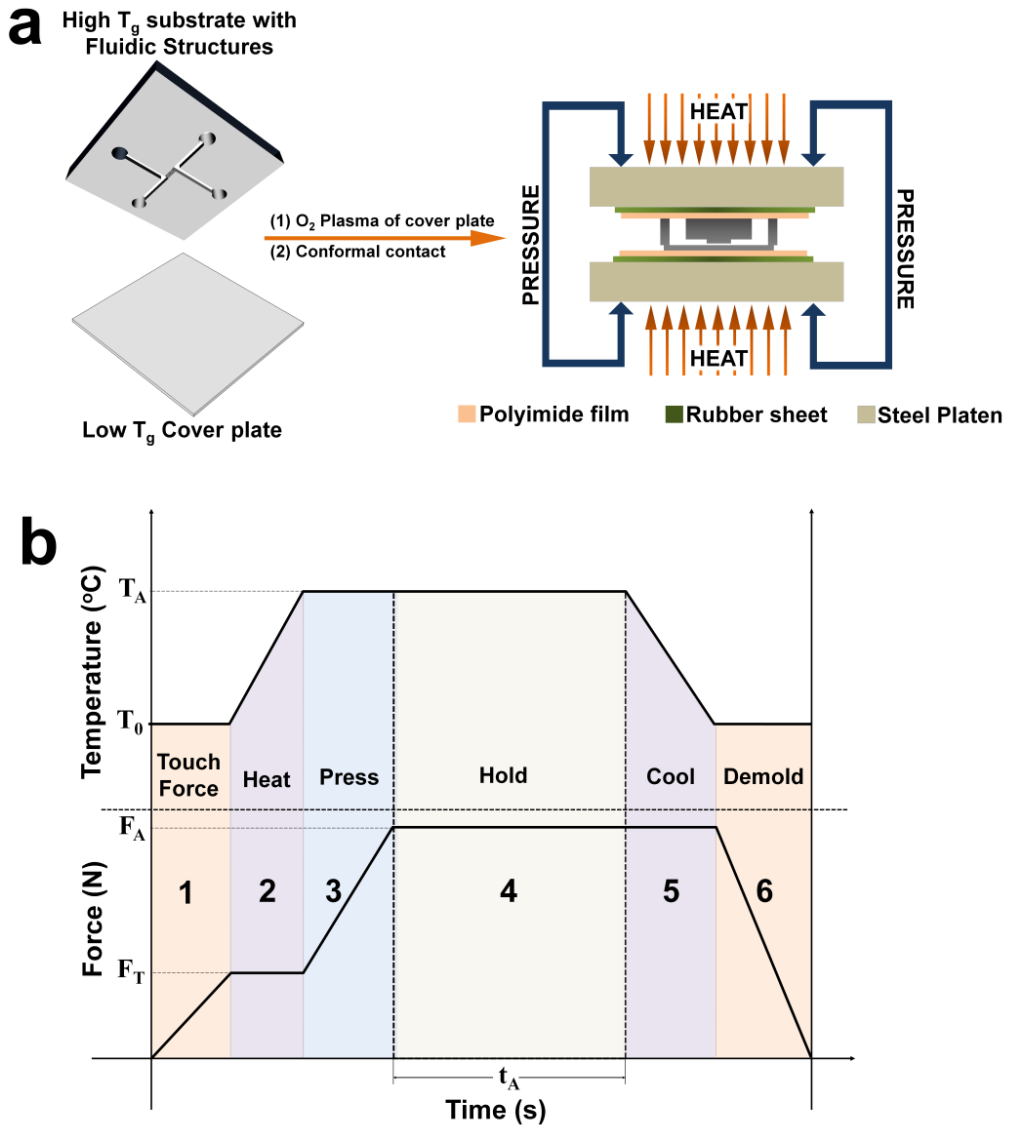

Figure 3.1 (a) Schematic illustration of the device assembly using the thermal press instrument. (b) Temperature-pressure process profile showing the six stages for the bonding cycle.

The assembly scheme used an untreated substrate possessing the fluidic structures and an oxygen plasma treated cover plate that were brought into conformal contact and then placed in a vacuum seal bag for 20 min to eliminate air pockets from the contacted substrate/cover plate. Next, the partially bonded device (determined by the lack of Newton rings) was sandwiched between a pair of polyimide films, rubber sheets and placed between the platens of the thermal embosser (see Figure 3.1a). We found that the rubber sheets promoted bond uniformity across the entire surfaces while the polyimide film prevented sticking of the thermoplastic nanofluidic

device to the rubber sheets. The temperature, pressure and time were found to be important process parameters, which depended primarily on the thermal, mechanical, physical and surface properties of the cover plate.

As shown in Figure 3.1b, the temperature–pressure process program used for enclosing the fluidic structures was partitioned into six stages:

1) Touch force stage – This was incorporated to facilitate heat conduction across the surfaces prior to thermal fusion bonding. The top and bottom embosser platens were advanced towards the assembly and used to clamp the pre-assembled substrate and cover plate near room temperature at a pressure of 180kN/m^2, which was lower than the required assembly pressure.
2) Heating Stage – The top and bottom platens were heated to the optimized assembly temperature (70^{o}C when using the COC 8007 cover plate) at a defined ramp rate of 3^{o}C/s while holding the clamped device at the touch force.
3) Pressure stage – Once the desired assembly temperature was reached, the pressure was immediately increased to the intended optimum pressure of 680 kN/m^2.
4) Holding stage – The assembly temperature and pressure were maintained for 900 s.
5) Cooling stage – Once assembly was complete, the temperature was gradually reduced to ≤35^{o}C at a rate of 1^{o}C/s while holding the device at the assembly pressure. This reduced stress imposed on the cover plate and prevented collapse into the fluidic channels.
6) Demolding stage – After the assembled device was cooled, the platens were slowly withdrawn.

3.1.3 Water Contact Angle Measurements

The wettability of the polymer surfaces, effect of plasma power and exposure time and the ageing of the cover plate were assessed by water contact angle measurements using a VCA

Optima instrument (AST Products). A volume of 2.0 µL nanopure water (18.2 MΩ·cm at 25°C) was dispensed onto 1 cm × 1 cm thermoplastic surfaces and a photograph of each droplet captured immediately for analysis using the software provided by the manufacturer. The measurements were repeated five times at different positions on the substrate with the values reported as the mean ±one standard deviation.

3.1.4 Bond Strength Measurements

A common technique used to evaluate the bond strength is the double cantilever beam test also known as the crack opening method (Ramm, '12; Tsao, '07). In this technique, a razor blade of known thickness t_b is inserted between the bonded substrate and cover plate inducing an interfacial fracture (or equilibrium crack) with a length L from the edge of the razor. If the elastic moduli of the substrate and cover plate is represented by E_s and E_p, respectively, the bond strength γ (J/cm^2) defined by the interfacial surface energy is given by;

$$\gamma = \frac{3t_b^2 E_s t_s^3 E_p t_p^3}{16L^4\left(E_s t_s^3 + E_p t_p^3\right)} \quad (1)$$

where t_s and t_p are the thicknesses of substrate and cover plate, respectively. In this work, all tests were performed using a stainless steel single edge razor blade with a thickness of 0.009" and the crack lengths were measured using a calibrated upright microscope with a 5× objective lens. Bond strengths were calculated using equation 1 with elastic moduli of 3.3 GPa for PMMA, 2.60 GPa for COC 8007 and 3.0 GPa for COC 5010 as provided by the manufacturer of the thermoplastics. Measurements were performed in triplicate and values were plotted against the assembly temperature (°C), time (s) and pressure (N/m^2).

3.1.5 Surface Charge Measurements

Direct current (DC) conductance measurements were used to evaluate the surface charge density in the nanochannel before and after UV activation. Conductance plots were generated

using KCl solutions in the concentration range of 10^{-6} to 0.1 M KCl following the procedure previously reported (Uba, '14; Vesel, '12). For UV activation of the nanochannels, assembled devices were placed in a 265 nm UV chamber with the cover plate facing the light source, then exposed to a 350 *m*J/cm^2 dose of UV light through the COC cover plate. In all cases, fluidic devices were initially flushed with a binary mixture of methanol/ultrapure water (50% v/v) followed by rinsing with deionized water. Pre-cleaned devices were filled with KCl solutions with Ag/AgCl electrodes immersed into the access reservoirs poised at the ends of microchannels. Electrolyte solutions were allowed to equilibrate for 3-5 min as evidenced by a stable current value under a fixed bias voltage. Current-voltage plots were generated by fitting the slope of the ionic current as a function of the applied voltage stepped from -0.5 V to 0.5 V with 50 mV steps and a 5 s holding time. All measurements were performed using the Axopatch 200B amplifier coupled to a Digidata 1440A digitizer with signal acquisition and analysis performed with the pClamp10 software. The average conductance generated from five trials was plotted against the electrolyte concentration in a log-log plot and the surface charge (σ_s) determined by fitting the graphs with the conductance equation;(Uba, '14)

$$G_T = 10^3 \left(\mu_{K^+} + \mu_{Cl^-}\right) c\, N_A\, e \cdot \frac{n\, w\, h}{L} + 2\, \mu_{opp} \sigma_s\, n \frac{(w + h)}{L} \qquad (2)$$

where G_T is the total measured conductance in the nanochannel, *w, L* and *h* are the nanochannel width, length and height, respectively, N_A is Avogadro's number, *e* is the electron charge (1.602 × 10^{-19} C), *c* is the electrolyte concentration in mol/L, *n* is the number of nanochannels in the device and μ_{K+} and μ_{Cl}^- are the ion mobilities of K^+ and Cl^- ions, respectively (μ_{K+} = 7.619 × 10^{-8} m^2/V s and μ_{Cl}^- = 7.912 × 10^{-8} m^2/V s) and $\mu_{opp} \approx \mu_{K+}$ for the deprotonated carboxyl surface. Finally, we assessed the effects of electrolyte pH on the surface conductance using KCl solutions prepared over a pH range of 5 – 9 adjusted using HCl or KOH solutions.

3.1.6 Atomic Force Microscopy (AFM) and Scanning Electron Micrographs (SEMs)

The topologies of the nanofluidic channels and the roughness of the polymer surfaces were investigated using an Asylum Research MFP-3D Atomic Force Microscope (tip radius ~2 nm) in repulsive tapping mode at a rate of 1.0 Hz. The Tap300A1-G cantilever tips (Ted Pella) had a frequency of 300 kHz and force constant of 40 N/m. For SEM, the non-conductive resin stamps and thermoplastic substrates were pre-coated with a 2-3 nm Au/Pd layer and imaged using a FEI Helios FIB/SEM.

3.1.7 Nanofluidic Devices and DNA Translocation

All fluorescence imaging experiments were performed using an inverted microscope (Olympus IX81 TIRF microscope, Olympus, Pennsylvania, PA) equipped with a 100×/1.49 NA oil immersion objective and 488 nm laser light for excitation, Sedat laser filter set (LF488/561-2X2M-B-000, Semrock) and a Hamamatsu EMCCD digital camera with Metamorph software for data acquisition. All images were analyzed using Fiji software. λ-DNA (Promega Corporation) and T4 DNA (Wako Chemcials) were stained with the bis-intercalating dye, YOYO-1 (Molecular Probes, Eugene, OR) at a base-pair/dye ratio of 5:1 in an electrolyte solution of 1× TBE (89 mM Tris, 89 mM Borate, 1 mM EDTA) with the addition of 4% v/v β-mercaptoethanol as a radical scavenger to minimize photo-induced damage (photobleaching and/or photonicking).

Nanochannels with depths between 25 and 200 nm were fabricated in PMMA and sealed using the assembly scheme previously described. Devices were seeded with 5 mM FITC in 1× TBE and allowed to equilibrate for 3 min before imaging through the cover plate with an exposure time of 2 s. Unprocessed images were imported into Fiji software and the fluorescence SNR was computed for each nanochannel using the relation;(Firbank, '99)

$$SNR = 0.655 \frac{S_{avg}}{\sigma_{noise}} \quad (3)$$

where S_{avg} is the mean pixel intensity of the signal and σ_{noise} is the standard deviation in the background pixel intensity. The factor 0.655 arises because the (Gaussian) noise present on the raw data is centered about zero (Firbank, '99). The selected area in all cases was 18 μm^2 and the measured σ_{noise} under these imaging conditions were respectively ~2.589 and 5.822 for the COC and PMMA cover plates.

We investigated the degree of extension of T4-DNA molecules confined in nanochannels designed with a range of predefined sizes. The DNA molecules were driven from the microchannels into the nanochannel under low field strengths. Once they had fully entered the nanochannel, the DC field was switched off. The molecule was allowed to relax until it reached its equilibrium extension length before an image was acquired. The end-to-end distance of the fluorescence image was measured using Fiji software. Although the total contour length (L_c) of an unstained λ-DNA molecule (166 kbp) is ~56.6 µm, at our intercalating dye concentration, the expected length is ~64 µm (Reisner, Morton, , '05). Finally, the velocities of λ-DNA molecules (0.75 pM) electrokinetically driven through an untreated and UV-activated hybrid device was evaluated from time-lapse images acquired at ~120 fps.

3.2 Results and Discussions

3.2.1 Water Contact Angle Measurements

In a typical nanofluidic device assembly process, the maximum bond strength between the substrate and cover plate is in part a function of the difference in hydrophobicitiy/hydrophilicity of the surfaces in contact. In our initial bonding tests performed using a low T_g untreated COC cover plate and the high T_g untreated substrate, we were only able to achieve bonding when the devices were assembled at temperatures greater than the T_g of the

cover plate by 5°C or more (data not shown). However, at these temperatures the nanochannels were severely deformed and the cover plate completely collapsed, rendering the device nonfunctional. Therefore, before device assembly, oxygen plasma was used to pre-activate the hydrophobic COC cover plate to make it more hydrophilic and thus, improve its adhesion to the PMMA substrate, which was not plasma activated.

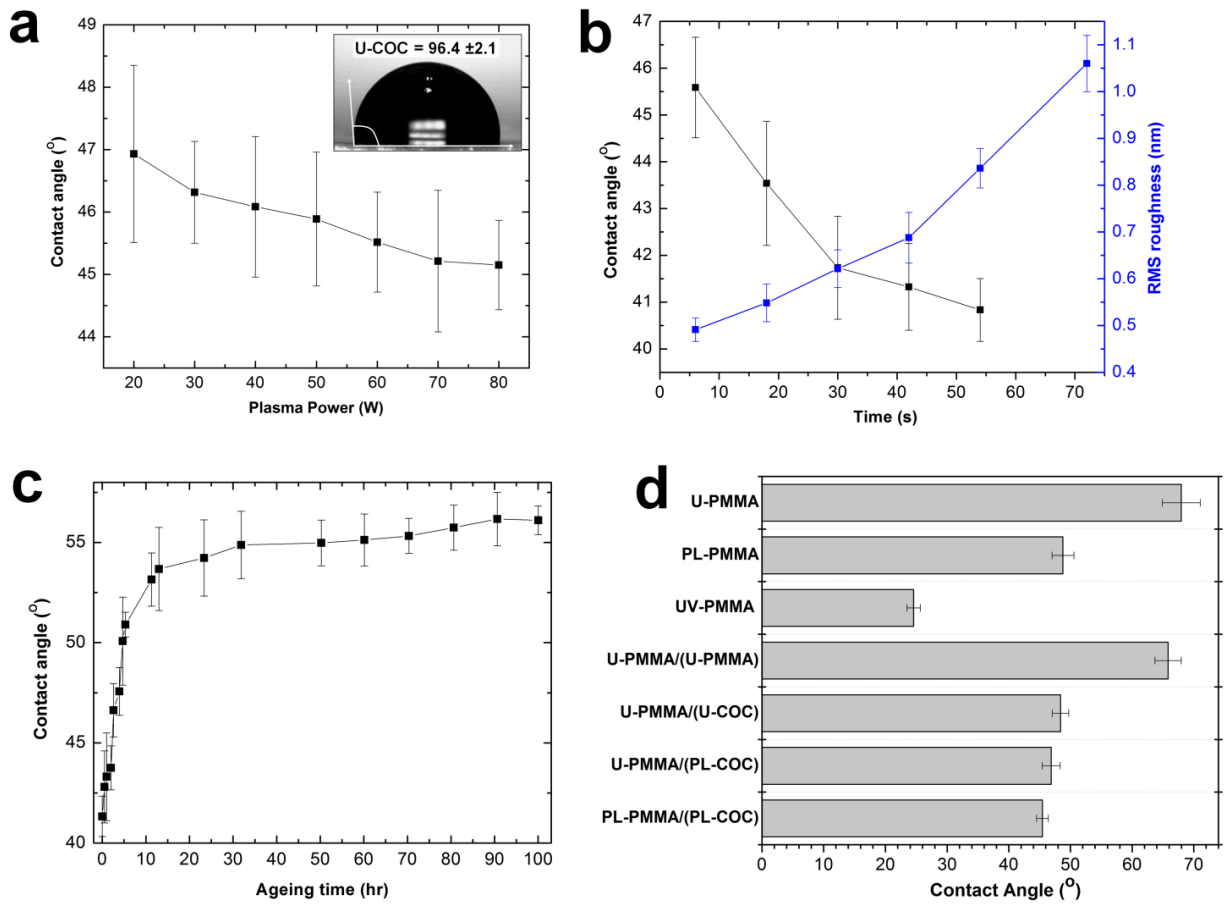

Figure 3.2 (a) Plot of the variation between the contact angle and RF power of the oxygen plasma at 10 sccm gas flow and a constant exposure time of 10 s. (b) Plot of the relationship between the water contact angle (black trace) and the RMS roughness (blue trace) versus the plasma exposure time at 50 W for 10 sccm gas flow. (c) Effect of ageing under room temperature conditions on the water contact angle of treated COC cover plate surface for plasma treatments condition of 50 W at 30 s under 10 sccm oxygen flow rate. (d) Water contact angle measurements on the PMMA substrate under different surface modification conditions with and without the COC cover plate. ('U-PMMA' is untreated PMMA substrate, 'PL-PMMA' is plasma treated PMMA substrate, 'UV-PMMA' is UV-activated PMMA substrate, 'U-PMMA/(U-PMMA)' is untreated PMMA substrate UV-activated through an untreated PMMA cover plate, 'U-PMMA/(U-COC)' is untreated PMMA substrate UV-activated through an untreated COC cover plate, 'U-PMMA/(PL-COC)' is untreated PMMA substrate UV-activated through a plasma treated COC cover plate and 'PL-PMMA/(PL-COC)' is plasma treated PMMA substrate UV-activated through a plasma treated COC cover plate)

It is well-established that oxygen plasma generates oxygen-containing polar functional groups on thermoplastic surfaces by inducing free radical reactions between the polymer chains and atomic oxygen in the plasma (Chai, '04; Hwang, '08). It also known that as the plasma power and treatment times are increased, the surface not only becomes richer in oxygen containing groups but also rougher. The RMS roughness is a parameter that can result in distortion of the electroosmotic flow in nanochannels, especially when the ratio of the RMS roughness to the electric double layer (EDL) thickness >1 (Vesel, '12). For these reasons, water contact angle and AFM measurements were used to assess the hydrophilicity and surface roughness, respectively, for determining the optimum plasma RF power and exposure time for treatment of the COC cover plate under a constant oxygen gas flow of 10 sccm.

Figure 3.2a shows the relationship between the water contact angle and the plasma power at a 10 s exposure time. As shown in the graph, oxygen plasma treatment resulted in a decrease in the water contact angle of 96.4 $\pm 2.1^{o}$ for the untreated COC surface to 46.9 $\pm 1.4^{o}$ and 45.2 $\pm 0.7^{o}$ for surfaces treated at 20 W and 80 W RF power, respectively, indicating an increase in the surface energy (Hwang, '08). However, we observed that the effect of the plasma RF power on the hydrophilicity of the COC surface was not very significant when compared to the exposure time. The black trace in Figure 3.2b shows the variation of the water contact angle with the exposure time in the range of 6 to 60 s at 50 W plasma power. As can be seen, there was a distinct decrease in the contact angle from 45.6 $\pm 1.1^{o}$ to 41.7 $\pm 1.0^{o}$ when the treatment time was increased from 6 s to 30 s. Above 30 s, the contact angle slightly decreased to a constant value of 40.8 $\pm 0.7^{o}$ at 54 s. However, as shown in Figure 3.2c (blue trace), the surface roughness increased almost linearly from 0.49 ±0.03 nm for the untreated COC surface to 1.06 ±0.06 nm for the surface treated for 60 s. As a result, we used an oxygen plasma condition of 50 W RF power with a 30 s exposure time under 10 sccm oxygen flow rate to treat the COC cover plate.

Because the EDL thickness for most ionic solutions used in nanofluidics varies between 1-100 nm and the RMS roughness of the COC surface treated at the above plasma condition was low (~0.62 ±0.04 nm), we speculate that distortions in the EOF profile arising from the surface roughness on the nanochannel cover plate would be minimal while still maintaining high adhesive capacity. Based on XPS data from previous reports, the density of polar functional groups on COC at this treatment condition is relatively low when compared to higher exposure times and gas flow rates (Hwang, '08).

Although the surface properties of thermoplastics can be modified by plasma treatment without affecting its bulk properties, treated surfaces have been shown to undergo ageing when stored in air. This is due to reorientation of the polar surface functional groups causing their movement into the bulk thermoplastic or movement of small chain polymer segments into the bulk causing the thermoplastic surface to lose its hydrophilic property (Roy, '10; Vesel, '12). Ageing studies were performed on treated COC cover plates to determine whether oxidation continued to occur after assembly and if assembled nanofluidic devices could be stored under vacuum conditions to improve shelf-life. The results obtained after treating the COC cover plate with 50 W RF power and 30 s exposure time are shown in Figure 3.2c. These results revealed that the contact angle changed from 41.33 ±1.00^{o} to 53.15 ±1.33^{o} during the first 10 h following treatment. Over a period of 100 h, the contact angle remained at 56.10 ±0.72^{o}. The hydrophilicity was not completely lost over the storage time evaluated as the contact angle was still 35-40^{o} lower than that of the untreated COC surface. Also, we did not experience any difficulty in filling devices used 5 days after assembly and these devices yielded results similar to those obtained from the devices that were used immediately after sealing.

Because we were interested in post-assembly modification of the nanochannels by UV-activation through the COC cover plate, we assessed the wettability of a PMMA substrate before

and after exposure to UV light with and without a COC cover plate. We used U-, PL- and UV- prefixes to indicate untreated, plasma treated and UV-activated surfaces, respectively, and represented the assembled devices as 'substrate/(cover plate)'. For example, untreated PMMA substrate bonded to an oxygen plasma treated COC cover plate was represented as 'U-PMMA/(PL-COC)'. As can be seen in Fig. 3.2d, U-PMMA showed a water contact angle of 68.0 $\pm 3.1^{o}$. Direct exposure to RF oxygen plasma under the above conditions resulted in a decrease in the contact angle to 48.8 $\pm 1.8^{o}$. However, direct exposure to 350 mJ/cm^2 of UV light resulted in a reduction in the contact angle to 24.6 $\pm 1.1^{o}$ with an observed yellowing of the polymer. When the PMMA substrate was activated through an untreated PMMA cover plate, the measured water contact angle was 65.9 $\pm 2.1^{o}$, a value similar to that obtained for U-PMMA. This was not surprising considering that PMMA has been shown to only transmit 10-15% of light at a wavelength of 265 nm.(Piruska, '05) The measured contact angles for U-PMMA/(U-COC) and U-PMMA/(PL-COC) were 48.4 $\pm 1.3^{o}$ and 46.9 $\pm 1.5^{o}$, respectively; these contact angles were not statistically different but were lower than U-PMMA by 15 – 20^{o}. These results not only revealed that the underlying PMMA substrates were successfully activated through the COC cover plate by the UV light, but also showed that plasma treatment of the cover plate had no considerable effect on the bulk transmittance of the material, because it only affects 5 – 15 nm of the polymer surface (Hwang, '08). When the PMMA substrate was plasma treated prior to UV-activation through the plasma treated COC cover plate, the measured water contact angle was 45.5 $\pm 0.9^{o}$. Because this value was slightly lower than that obtained for U-PMMA/(U-COC), it is either likely that under UV-activation, more polar groups were incorporated onto the PMMA surface (Jackson, '14) or less polar groups generated on the PMMA via plasma activation (Chai, '04) were converted to more polar hydrophilic groups via free-radical pathways.

3.2.2 Bond Strength Determinations

The critical parameters in any fusion bonding scheme adopted for enclosing fluidic devices are the bonding pressure, temperature and time. In this work, we optimized these parameters to obtain high bond strengths while retaining the structural integrity of the nanochannels. Before device assembly, the COC cover plate was treated with oxygen plasma consisting of 50 W RF power for 30 s and 10 sccm gas flow rate while the PMMA substrate remained untreated.

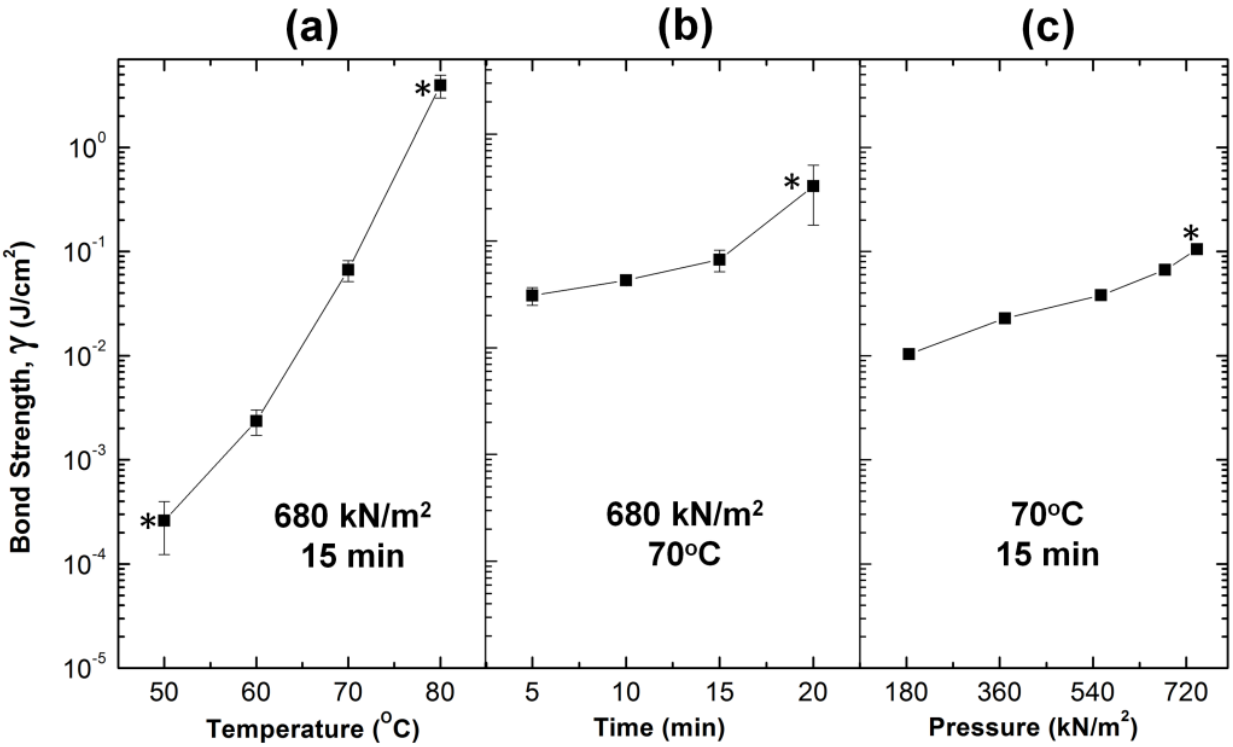

Figure 3.3 Variation of the bond strength with the (a) temperature, (b) bonding time, and (c) pressure for the hybrid assembly scheme.

Variations between the bonding temperature and the bond strength at a constant bonding pressure of 680 kN/m^2 and a bonding time of 15 min are shown in Figure 3.3a. The result revealed that the bond strength varied linearly with the bonding temperature. Based on the work of Tsao *et al.* (Tsao, '07), bond strengths for our nanofluidic devices were comparable to those of microfluidic devices. While the bond strength at 80^{o}C seemed impressively high, our data

revealed that bonding at this temperature resulted in unusable devices. This is likely a result of bulk flow of the cover plate material into the nanochannels due to the bonding temperature being greater than its bulk T_g. In subsequent studies, 70^oC was selected as the optimum bonding temperature.

Next we studied the effect of bonding time on the bond strength using the optimum temperature of 70^oC and a constant force of 680 kN/m^2. As shown in Figure 3.3b, bond strengths were greater than those previously reported in applications involving electrokinetic transport in thermoplastic nanochannels (Chantiwas, '10; Uba, '14) when devices were bonded between 5 and 20 min assembly times. However, we observed that devices bonded at 20 min did not yield reproducible results. We speculate that this may be due to minor deformations in the nanochannels or sagging of the cover plate into the channels similar to previous observations (Cheng, '14). Therefore, 15 min was selected as the optimal assembly time. Lastly, Figure 3.3c shows the effect of bonding pressure on the bond strength under an optimum bonding temperature of 70^oC and a bonding time of 15 min. Bond strengths achieved in the pressure range under study were sufficiently greater than that previously reported for electrokinetic flow in nanofluidic devices (Chantiwas, '10) and comparable to the homogenous polymers bonded at a temperature greater than their T_g (Tsao, '07). However, to prevent sagging of the cover plate into the nanochannels, we selected 680 kN/m^2 as the optimum pressure to minimize this artifact. Based on the aforementioned results, untreated high T_g substrates were bonded to plasma treated low T_g COC cover plates using a bonding pressure, temperature and time of 680 kN/m^2, 70^oC and 15 min, respectively.

Similarly, we evaluated the bond strengths of PL-PMMA, PL-COC and U-COC (COC 5010) substrates bonded to the low T_g COC cover plate. The results are summarized in Table 3.1. Devices 1 – 4 were bonded at the optimized bonding pressure, temperature and time as

previously noted. Device 5 was bonded using a pressure of 370 kN/m^2 at 80^{o}C for ~7 min, as previously reported by our group (Uba, '14). Device 6 was bonded using a pressure of 370 kN/m^2 at 105^{o}C for ~7 min and the bond strength was 0.143 ±0.071 mJ/cm^2 for the U-COC/(PL-COC) device. This bond strength was too low for performing fluidic experiments, because we experienced difficulty in filling the assembled device due to the hydrophobic nature of the untreated substrate. When the COC substrate was treated with oxygen plasma prior to device assembly, there was an increase in the bond strength to 1.04 ±0.01 mJ/cm^2 and an improvement in the wettability. However, using untreated and plasma treated PMMA as the substrates produced devices with bond strengths of 65.92 ±7.13 mJ/cm^2 and 67.92 ±6.97 mJ/cm^2 for U-PMMA/(PL-COC) and PL-PMMA/(PL-COC), respectively, that easily filled easily by capillary action. Though it remains unclear why the bond strength was greater in U-PMMA/(PL-COC) than PL-COC/(PL-COC), we conclude from these results that the bond strength not only depends on the surface wettability - PL-COC has a water contact angle less than U-PMMA - but also on the chemical nature of the surfaces in contact. Nevertheless, U-PMMA/(PL-COC) devices, which we refer to as the hybrid devices, were used in our subsequent experiments.

For comparison, we evaluated the bond strengths from assembled PL-PMMA/(PL-PMMA) and U-PMMA/(U-PMMA) devices. As shown in Table 1, in both cases, the measured bond strengths were lower than that of the hybrid devices. Though PL-PMMA/(PL-PMMA) devices have been useful for surface modification and DNA transport studies (Chantiwas, '10; Uba, '14; Wu, '11), the process yield rate for both devices was relatively low (<50% for PL-PMMA/(PL-PMMA) and <10% for U-PMMA/(U-PMMA)) due primarily to deformation and collapse of the nanochannels following thermal fusion bonding and possible delamination of the cover plate during an experiment (Chantiwas, '10). As a comparison, using the optimized thermal fusion bonding conditions noted above for U-PMMA/(PL-COC) devices, the process yield was

>90% with a similar value noted for devices consisting of U-COC/(PL-COC). AFM measurements taken from the 5 µm × 120 nm nanoslits utilized for the surface charge measurements after removing the cover plate post-assembly revealed no change in the nanoslit dimensions. This was not surprising since device assembly was performed at a temperature ~35^{o}C less than the T_g of the PMMA substrate.

Table 3.1 A summary of the bond strength tests obtained for devices assembled with different substrates and cover plates.

No	Assembled device	Bond Strength (*m*J/cm^2)
1	U-COC/(PL-COC)	0.143 ±0.071
2	PL-COC/(PL-COC)	1.035 ±0.007
3	U-PMMA/(PL-COC)	65.921 ±7.131
4	PL-PMMA/(PL-COC)	67.918 ±6.966
5	PL-PMMA/(PL-PMMA) [80^{o}C]	1.244 ±0.003
6	U-PMMA/(U-PMMA) [106^{o}C]	1.897 ±0.053

3.2.3 Surface Charge Measurements

We recently reported the surface charge density in PL-PMMA/(PL-PMMA) nanofluidic devices assembled under slightly different plasma conditions (5.5 sccm, 35 s and 50 W) (Uba, '14). Herein we evaluated the surface charge density of the hybrid U-PMMA/(PL-COC) devices assembled with the optimum conditions reported above. Ionic conductance plots were used to evaluate the surface charge density of assembled nanofluidic devices comprising an array of five nanoslits, each 5 µm wide, 120 nm deep and 148 µm long. It is well-known that carboxylic acid moieties can be generated on PMMA or COC surfaces following plasma treatment (Roy, '10; Vesel, '12) or UV-activation (Jackson, '14). Figure 3.4a shows the conductance traces measured in PL-PMMA/(PL-COC) compared to PL-PMMA/(PL-PMMA) devices. In the high ionic strength regime (KCl concentrations >10^{-2} M), the ionic conductance in both devices fit linearly to the theoretical bulk conductance with high reproducibility for both devices. This confirmed

that there was no change in the dimensions of the nanochannels during thermal embossing and after assembly for the devices tested. At the low ionic concentration (or surface-charge governed) regime, there was a significant difference in the measured conductance between these devices. For the PL-PMMA/(PL-PMMA) device, the surface charge density $|\sigma_s|$ estimated from the fitted curve was 43.2 mC/m^2 while for the hybrid device, $|\sigma_s|$ was 57.3 mC/m^2, ~32.6% greater than the former. This difference in surface charge density is likely due to the fact that more carboxyl groups are generated on COC compared to PMMA when treated under similar oxygen plasma conditions (Roy, '10; Vesel, '12). Figure 3.4b shows the conductance traces measured in the hybrid device U-PMMA/(PL-COC) before (blue trace) and after (red trace) exposure to UV light. The average conductance in the low ionic strength regime for the unexposed devices was 1.45 × 10^{-9} S with $|\sigma_s|$ equal to 40.7 mC/m^2. After the device was exposed to 350 *m*J/cm^2 of 265 UV light through the plasma-treated COC cover plate, there was a 47.2% increase in $|\sigma_s|$ (59.9 mC/cm^2) as evidenced by the increase in conductance to 1.89 × 10^{-9} S. This suggested that post-assembly UV activation induced more carboxyl groups on the walls of the nanoslits, in particular for the unmodified PMMA substrate.

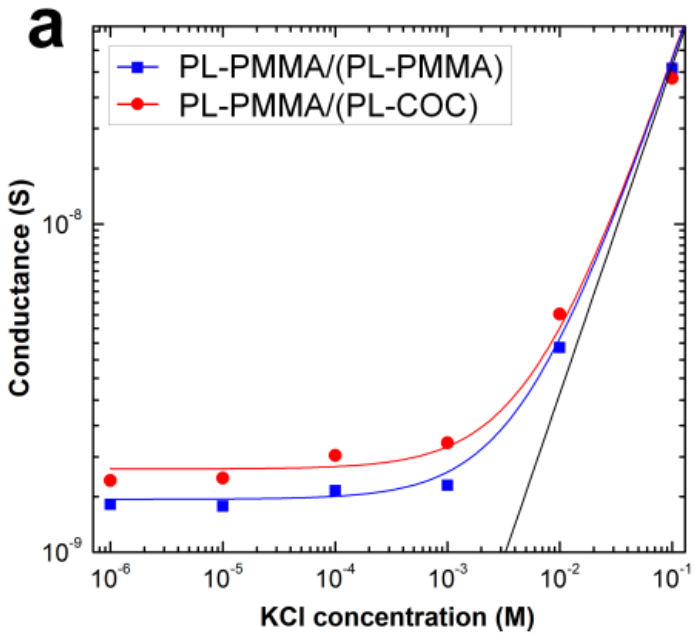

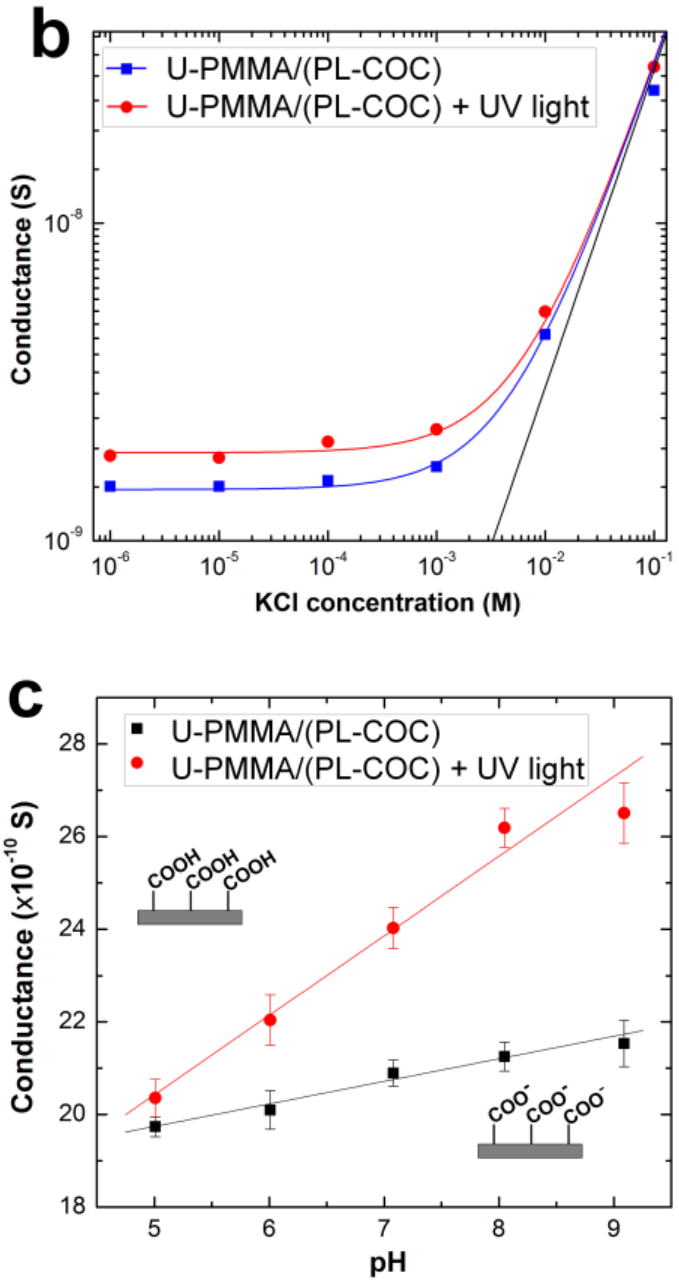

Figure 3.4 (a) Conductance plots for assembled devices with plasma treated PMMA substrate bonded to plasma treated PMMA cover plate, PL-PMMA/(PL-PMMA), and plasma treated PMMA substrate bonded to plasma treated COC cover plate, PL-PMMA/(PL-COC). The latter devices showed a higher conductance at the low ionic conductance regime because more carboxyl moieties are introduced on COC surfaces than PMMA when exposed to the same plasma conditions. (b) Conductance plots for the hybrid devices consisting of untreated PMMA substrate bonded to plasma treated COC cover plate, U-PMMA/(PL-COC), before (blue trace) and after (red trace) UV activation. The device used in all cases consists of an array of five nanoslits (each 5 µm wide, 120 nm deep and 148 µm long) connected to V-shaped assess microchannels at the input and output ends. Each data point represents an average of five measurements with a scatter in the data within 5-8% of the mean value and the solid black line represents the trace of the theoretical bulk conductance. (c) Plot showing the relationship between the conductance and the electrolyte pH for the assembled hybrid devices before (black) and after (red) UV activation. 10^{-4} M KCl solution adjusted to pH between 5.01 and 9.09 was used in the study.

Also, the surface charge density in the UV activated hybrid devices were 4.5% higher than devices with plasma treated substrate (red trace in Fig. 3a). This is because the surface density of carboxylates generated on UV activated PMMA surfaces (14.7 ±2.6 *n*mol/cm^2) (Jackson, '14) is greater than that generated on plasma treated surfaces (2.7 ±0.5 *n*mol/cm^2) (Xu, '07). Figure 3.4c shows the effects of solution pH on the measured conductance for the nanoslits before and after UV activation. As can be seen, in both cases the conductance increased linearly with the pH of the electrolyte. Prior to UV activation, there was an observed change in the measured conductance of the nanochannel from 13.7 (±0.2) × 10^{-10} S at pH 5.0 to 15.5 (±0.5) × 10^{-10} S at pH 9.09 (black trace). Because the PMMA substrate was untreated prior to device assembly, charge contributions from carboxyl moieties on the PMMA surfaces, especially at high pH, will be insignificant compared to that from the plasma treated COC cover plate.

Therefore, the change in conductance is predominantly due to deprotonation of the carboxyl groups on the cover plate. Nevertheless, after UV-activation of the same devices, there was a significant increase in the conductance, ~30% (15.4 (±0.4) × 10^{-10} S at pH 5.0 to ~21.6 (±0.6) × 10^{-10} S at pH 9.1), as evident by an increase in the slope of the red trace in Figure 3.4c. These results confirmed that the nanoslits were successfully functionalized via UV-activation after device assembly.

3.2.4 Operational Characteristics of Nanofluidic Devices

Finally, we assessed the performance of the assembled hybrid nanofluidic devices, for fluorescence imaging, DNA stretching and translocation relative to their non-hybrid counterparts. Figure 3.7a shows an AFM profile and the SEM image (insert) of the UV curable resin stamp consisting of 2-D nanochannels with predefined widths (*w*) × depths (*d*) of 300 × 200 nm, 250 × 155 nm, 190 × 95 nm, 150 × 60 nm, 110 × 25 nm and 35 × 35 nm corresponding to *nc*1, *nc*2, *nc*3, *nc*4, *nc*5, and *nc*6, respectively. The stamp was used to imprint channels into a

PMMA substrate with ~100% replication fidelity. AFM profiles shown in Figure 3.5 suggest effective transfer from Si master to UV resin. Figure 3.6 indicates that there was no significant reduction in the stamp height channel depth even after twenty transfers.

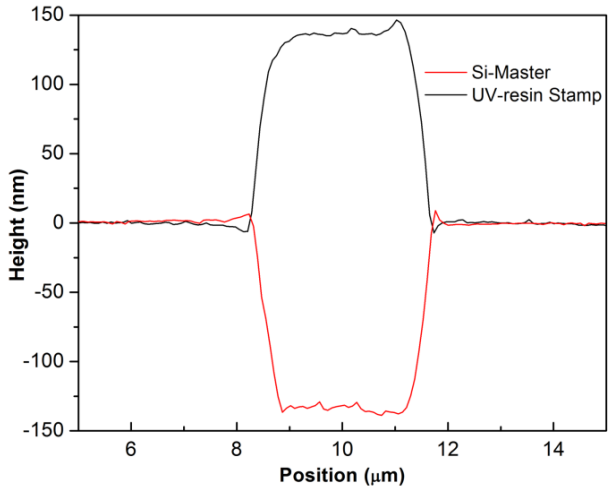

Figure 3.5 AFM profile of a nanoslit in a silicon (Si) master (red trace) and positive structure in the UV resin stamp (black trace) showing the replication fidelity in the structure.

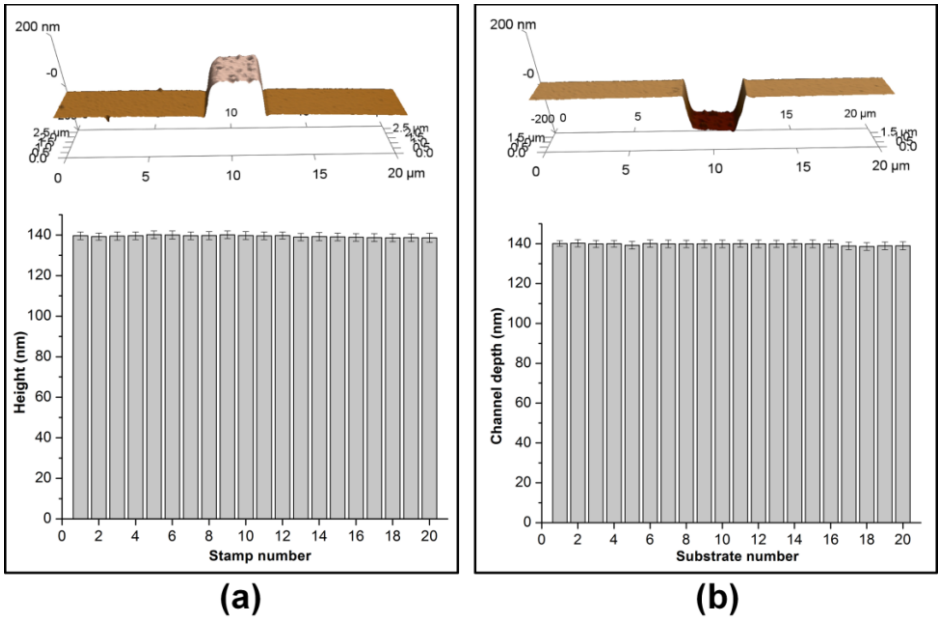

Figure 3.6 (a) Upper panel - AFM image of the first UV resin stamp produced from the Si master. Lower panel – Box plots of the stamp height measured with the AFM from 20 stamps produced from a single Si master. (b) Upper panel – AFM image of the first PMMA device generated after thermal imprinting using a UV-resin stamp. Lower panel – Box plots of the nanoslit depth measured with AFM from 20 substrates produced from a single UV-resin stamp. Both images reveal ~100% replication fidelity of nanostructures from the master to stamp to substrate.

Using the unprocessed images obtained from the fluorescent seeding test with 5 mM FITC, we found that the average SNR was ~3× greater in *nc*1 – *nc*4 and ~4.5× greater in *nc*5 for U-PMMA/(PL-COC) than PL-PMMA/(PL-PMMA) (Figure 3.7b). This enhancement in SNR is most likely due to the superior optical properties (high optical transmission, low autofluorescence/background and high refractive index) of COC at 488 nm compared to PMMA (Piruska, '05). The higher SNR observed for *nc*5 may be an indication of slight collapse of the nanochannel in the non-hybrid devices or an artifact from the high background fluorescence of PMMA.

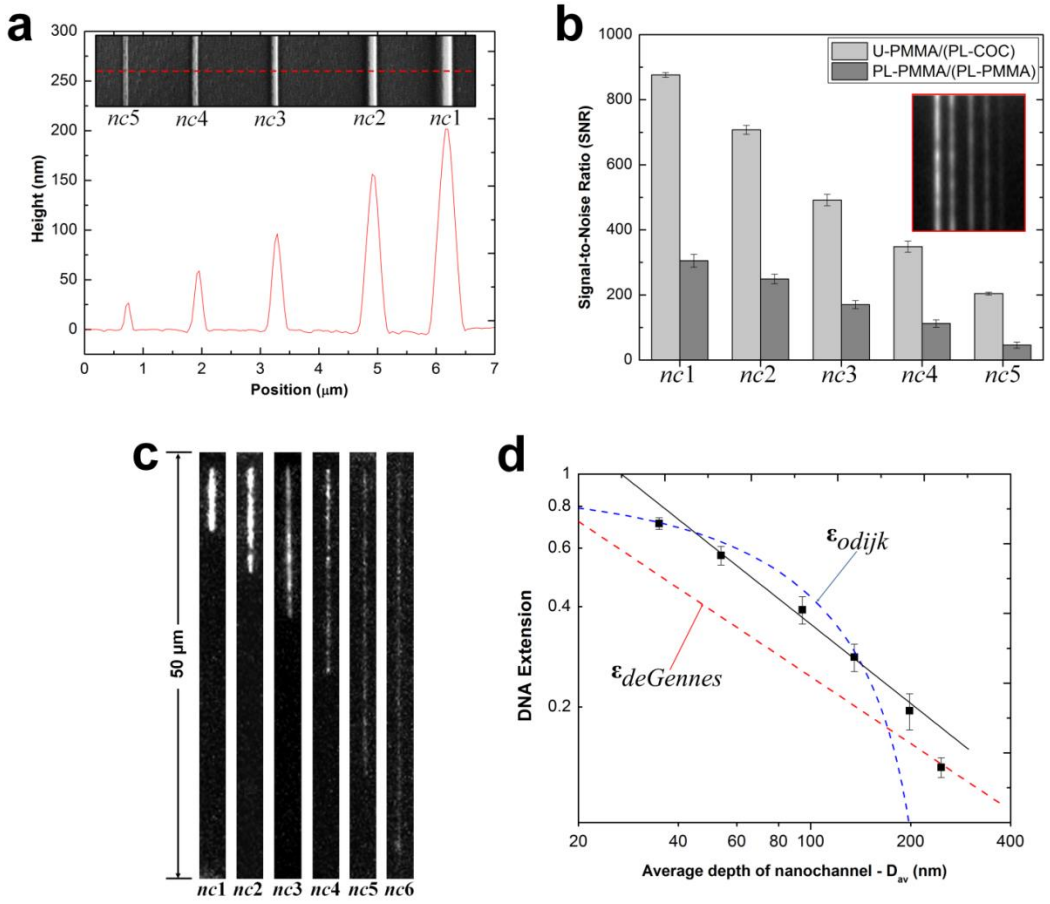

Figure 3.7 (a) AFM scan (and SEM image insert) of the UV curable resin stamp possessing the positive tones of the 2-D nanochannels. Channels were imprinted into PMMA with ~100% replication fidelity and the dimensions (width × depth) were *nc*1 ≈ 300 × 200 nm, *nc*2 ≈ 250 × 155 nm, *nc*3 ≈ 190 × 95 nm and *nc*4 ≈ 150 × 60 nm and *nc*5 ≈ 110 × 25 nm. (b) Bar graphs showing the signal-to-noise ratio (SNR) at 2 s exposure time for the devices with untreated PMMA substrate enclosed with a plasma treated COC cover plate, U-PMMA/(PL-COC), and plasma treated substrate enclosed with a plasma treated PMMA cover plate, PL-PMMA/(PL-PMMA) filled with 5 mM FITC solution. The error bar represents the standard

deviation in measurements from ten separate devices. (Insert shows the unprocessed image of the seeding test for U-PMMA/(PL-COC)). The hybrid devices showed a background that was ~56% lower than that of the non-hybrid devices. (c) Unprocessed representative frames of T4 DNA molecules stretched in the enclosed nanochannels in the hybrid devices. Images were acquired at 10 ms exposure time with the driving field turned-off. (Note that *nc*6 ≈ 35 × 35 nm). (d) Log-log plot showing the T4 DNA extension as a function of the geometric average depth of the nanochannels. The DNA extension was normalized to a total contour length (L_c) of 64 µm for the dye labelled molecules. The red and blue dashed lines are the deGennes and Odijk predictions, respectively, with the respective equations inserted. The black solid line is the best power-law fit to the data points obtained from the nanochannels with an average geometric depth range of 53 nm to 200 nm.

Figure 3.7c shows unprocessed frames of T4 DNA molecules confined in *nc*1 – *nc*6 devices and imaged through the COC cover plate at 10 ms exposure time. The images revealed good contrast and excellent SNR with the degree of polymer stretching increasing as the nanochannel size decreased. Figure 3.7d shows a plot of the DNA extension (ε) versus the geometric average (D_{av}) nanochannel dimension with traces for the deGennes prediction, $\varepsilon_{deGennes} \approx \left(\omega_{eff}\, L_p / D_{av}^2\right)^{1/3}$ and the Odijk prediction, $\varepsilon_{Odijk} \approx \left[1 - 0.361\left(D_{av}/L_p\right)^{2/3}\right]$, where $D_{av} = \sqrt{w \times d}$, ω_{eff} is the effective width (~3 nm) and L_p is the persistence length (50 nm) for dsDNA (Reisner, Morton, , '05).

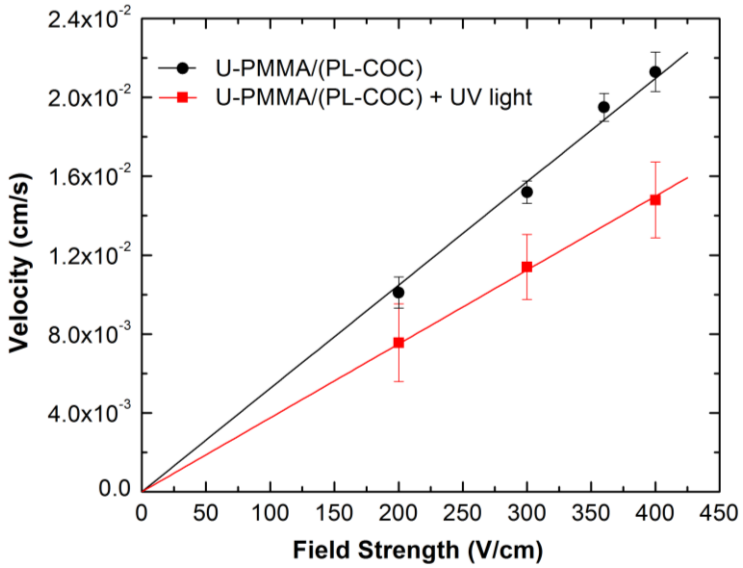

Figure 3.8 Graph showing the relationship between the translocation velocity (cm/s) and the field strength (V/cm) of λ-DNA translocating through the hybrid devices before and after activation with UV light. Each data point represents the mean of 20 events per device measured in 2× TBE buffer.

As seen in Figure 3.7d, the data for the channel with >200 nm D_{av} fits well with the deGennes regime while the nanochannel with D_{av} = 35 nm fits well to the Odijk regime. However, data for *nc*3 – *nc*5, though expected to fit to the deGennes regime, were observed to be greater than the deGennes prediction but less than the Odijk prediction. This enhancement in the degree of extension within this regime is likely due to the hydrophobicity of the nanochannel walls (Bensimon, '95).

Finally, we evaluated the effect of post-assembly UV-activation of the U-PMMA/(PL-COC) devices on the linear velocity of λ-DNA molecules electrokinetically driven through 100 × 100 nm nanochannels. As shown in Figure 3.8, in both cases there was a corresponding linear increase in the velocity of dsDNA as the driving voltage was increased. However, the DNA molecules were observed to migrate slower in the UV-activated devices. This is likely due to an increase in the EOF emanating from increases in the surface charge density after the incorporation of –COOH groups onto the wall of the nanochannel via UV activation.

3.3 Conclusion

In this work, we developed a low temperature hybrid bonding scheme useful for the assembly of thermoplastic devices and demonstrated the utility of these devices for DNA elongation and translocation and post-assembly modification. With this scheme, we have addressed a significant challenge associated with the use of thermoplastics for nanofluidic – the relatively small Young's modulus associated with these materials makes cover plate assembly to the patterned substrate difficult due to cover plate collapse and/or nanostructure deformation using either thermal or chemical assisted bonding to enclose the fluidic network. Our assembly scheme will aid in generating nanofluidic devices with high process yield rates for many analyses that take advantage of the unique physics associated with nano-confinement. We are currently evaluating the extent of distortions in the EOF profile, if any, arising from hybrid

nanochannels as has been shown in microchannels (Ross, '01). We also suspect that these distortions will be observed in PL-COC/(PL-COC) devices due to differences in the norbonene content of the substrate versus cover plate. We are also employing super resolution imaging techniques to assess the surface coverage and uniformity of carboxyl functional groups generated in these nanochannels via UV-activation.

REFERENCES

Abgrall, P.; Low, L.-N.; Nguyen, N.-T. Fabrication of planar nanofluidic channels in a thermoplastic by hot-embossing and thermal bonding. *Lab on a Chip* 2007, 7, 520-522.

Abgrall, P.; Nguyen, N. T. Nanofluidic Devices and Their Applications. *Analytical Chemistry* 2008, 80, 2326-2341.

Bensimon, D.; Simon, A. J.; Croquette, V.; Bensimon, A. Stretching DNA with a Receding Meniscus: Experiments and Models. *Physical Review Letters* 1995, 74, 4754-4757.

Bilenberg, B.; Hansen, M.; Johansen, D.; Özkapici, V.; Jeppesen, C.; Szabo, P.; Obieta, I. M.; Arroyo, O.; Tegenfeldt, J. O.; Kristensen, A. Topas-based lab-on-a-chip microsystems fabricated by thermal nanoimprint lithography. *Journal of Vacuum Science & Technology B* 2005, 23, 2944-2949.

Chai, J.; Lu, F.; Li, B.; Kwok, D. Y. Wettability Interpretation of Oxygen Plasma Modified Poly(methyl methacrylate). *Langmuir* 2004, 20, 10919-10927.

Chantiwas, R.; Hupert, M. L.; Pullagurla, S. R.; Balamurugan, S.; Tamarit-Lopez, J.; Park, S.; Datta, P.; Goettert, J.; Cho, Y.-K.; Soper, S. A. Simple replication methods for producing nanoslits in thermoplastics and the transport dynamics of double-stranded DNA through these slits. *Lab on a Chip* 2010, 10, 3255-3264.

Chantiwas, R.; Park, S.; Soper, S. A.; Kim, B. C.; Takayama, S.; Sunkara, V.; Hwang, H.; Cho, Y.-K. Flexible fabrication and applications of polymer nanochannels and nanoslits. *Chemical Society Reviews* 2011, 40, 3677-3702.

Cheng, E.; Yin, Z.; Zou, H.; Chen, L. Surface modification-assisted bonding of 2D polymer-based nanofluidic devices. *Microfluid. Nanofluid.* 2014, 1-9.

Cheng, E.; Zou, H.; Yin, Z.; Jurcicek, P.; Zhang, X. Fabrication of 2D polymer nanochannels by sidewall lithography and hot embossing. *J. Micromech. Microeng.* 2013, 23.

Cho, Y. H.; Park, J.; Park, H.; Cheng, X.; Kim, B. J.; Han, A. Fabrication of high-aspect-ratio polymer nanochannels using a novel Si nanoimprint mold and solvent-assisted sealing. *Microfluid. Nanofluid.* 2010, 9, 163-170.

Chou, S. Y.; Krauss, P. R.; Renstrom, P. J. Imprint of sub-25 nm vias and trenches in polymers. *Applied Physics Letters* 1995, 67, 3114-3116.

Fang Lim, S.; Karpusenko, A.; Sakon, J. J.; Hook, J. A.; Lamar, T. A.; Riehn, R. DNA methylation profiling in nanochannels. *Biomicrofluidics* 2011, 5.

Firbank, M. J.; Coulthard, A.; Harrison, R. M.; Williams, E. D. A comparison of two methods for measuring the signal to noise ratio on MR images. *Physics in Medicine and Biology* 1999, 44, N261.

Foquet, M.; Korlach, J.; Zipfel, W.; Webb, W. W.; Craighead, H. G. DNA Fragment Sizing by Single Molecule Detection in Submicrometer-Sized Closed Fluidic Channels. *Analytical Chemistry* 2002, 74, 1415-1422.

Guo, L. J.; Cheng, X.; Chou, C.-F. Fabrication of Size-Controllable Nanofluidic Channels by Nanoimprinting and Its Application for DNA Stretching. *Nano Letters* 2003, 4, 69-73.

Han, J.; Turner, S. W.; Craighead, H. G. Entropic Trapping and Escape of Long DNA Molecules at Submicron Size Constriction. *Physical Review Letters* 1999, 83, 1688-1691.

Hu, X.; He, Q.; Zhang, X.; Chen, H. Fabrication of fluidic chips with 1-D nanochannels on PMMA substrates by photoresist-free UV-lithography and UV-assisted low-temperature bonding. *Microfluid. Nanofluid.* 2011, 10, 1223-1232.

Hwang, S.-J.; Tseng, M.-C.; Shu, J.-R.; Her Yu, H. Surface modification of cyclic olefin copolymer substrate by oxygen plasma treatment. *Surface and Coatings Technology* 2008, 202, 3669-3674.

Jackson, J. M.; Witek, M. A.; Hupert, M. L.; Brady, C.; Pullagurla, S.; Kamande, J.; Aufforth, R. D.; Tignanelli, C. J.; Torphy, R. J.; Yeh, J. J.; Soper, S. A. UV activation of polymeric high aspect ratio microstructures: ramifications in antibody surface loading for circulating tumor cell selection. *Lab on a Chip* 2014, 14, 106-117.

Jena, R.; Yue, C. Y.; Lam, Y. C. Micro fabrication of cyclic olefin copolymer (COC) based microfluidic devices. *Microsyst. Technol.* 2012, 18, 159-166.

Junshan, L.; Hongchao, Q.; Zheng, X.; Chong, L.; Junyao, W.; Liqun, D.; Xi, Z.; Liding, W. Fabrication of planar nanofluidic channels in thermoplastic polymers by O₂ plasma etching. *Micro & Nano Letters, IET* 2012, 7, 159-162.

Khanarian, G.; Celanese, H. Optical properties of cyclic olefin copolymers. *OPTICE* 2001, 40, 1024-1029.

Lasse, H. T.; Anna, K.; Anders, K. Stretching DNA in polymer nanochannels fabricated by thermal imprint in PMMA. *Nanotechnology* 2008, 19, 125301.

Levy, S. L.; Craighead, H. G. DNA manipulation, sorting, and mapping in nanofluidic systems. *Chemical Society Reviews* 2010, 39, 1133-1152.

Li, J.-M.; Liu, C.; Ke, X.; Duan, Y.-j.; Fan, Y.; Li, M.; Zhang, K.-p.; Xu, Z.; Wang, L.-d. Fabrication of 1D nanochannels on thermoplastic substrates using microchannel compression. *Microsyst. Technol.* 2013, 19, 1845-1850.

Li, J.-m.; Liu, C.; Ke, X.; Xu, Z.; Duan, Y.-j.; Fan, Y.; Li, M.; Zhang, K.-p.; Wang, L.-d. Microchannel refill: a new method for fabricating 2D nanochannels in polymer substrates. *Lab on a Chip* 2012, 12, 4059-4062.

Li, W. Sacrificial polymers for nanofluidic channels in biological applications. *Nanotechnology* 2003, 14, 578-583.

Liu, J.; Jin, X.; Sun, T.; Xu, Z.; Liu, C.; Wang, J.; Chen, L.; Wang, L. Hot embossing of polymer nanochannels using PMMA moulds. *Microsyst. Technol.* 2013, 19, 629-634.

Odijk, T. Scaling theory of DNA confined in nanochannels and nanoslits. *Physical Review E* 2008, 77, 060901.

Piruska, A.; Nikcevic, I.; Lee, S. H.; Ahn, C.; Heineman, W. R.; Limbach, P. A.; Seliskar, C. J. The autofluorescence of plastic materials and chips measured under laser irradiation. *Lab on a Chip* 2005, 5, 1348-1354.

Prakash, S.; Piruska, A.; Gatimu, E. N.; Bohn, P. W.; Sweedler, J. V.; Shannon, M. A. Nanofluidics: Systems and Applications. *Sensors Journal, IEEE* 2008, 8, 441-450.

Ramm, P.; Lu, J. J.-Q.; Taklo, M. M. *Handbook of Wafer Bonding*. John Wiley & Sons: 2012.

Reisner, W. Statics and dynamics of single DNA molecules confined in nanochannels. *Physical Review Letters* 2005, 94, 196101.

Reisner, W.; Beech, J. P.; Larsen, N. B.; Flyvbjerg, H.; Kristensen, A.; Tegenfeldt, J. O. Nanoconfinement-Enhanced Conformational Response of Single DNA Molecules to Changes in Ionic Environment. *Physical Review Letters* 2007, 99, 058302.

Reisner, W.; Morton, K. J.; Riehn, R.; Wang, Y. M.; Yu, Z.; Rosen, M.; Sturm, J. C.; Chou, S. Y.; Frey, E.; Austin, R. H. Statics and Dynamics of Single DNA Molecules Confined in Nanochannels. *Physical Review Letters* 2005, 94, 196101.

Riehn, R.; Lu, M.; Wang, Y.-M.; Lim, S. F.; Cox, E. C.; Austin, R. H. Restriction mapping in nanofluidic devices. *Proceedings of the National Academy of Sciences of the United States of America* 2005, 102, 10012-10016.

Ross, D.; Johnson, T. J.; Locascio, L. E. Imaging of Electroosmotic Flow in Plastic Microchannels. *Analytical Chemistry* 2001, 73, 2509-2515.

Roy, S.; Yue, C. Y.; Lam, Y. C.; Wang, Z. Y.; Hu, H. Surface analysis, hydrophilic enhancement, ageing behavior and flow in plasma modified cyclic olefin copolymer (COC)-based microfluidic devices. *Sensors and Actuators B: Chemical* 2010, 150, 537-549.

Shao, P. E.; van Kan, A.; Wang, L. P.; Ansari, K.; Bettiol, A. A.; Watt, F. Fabrication of enclosed nanochannels in poly(methylmethacrylate) using proton beam writing and thermal bonding. *Applied Physics Letters* 2006, 88, -.

Sivanesan, P.; Okamoto, K.; English, D.; Lee, C. S.; DeVoe, D. L. Polymer Nanochannels Fabricated by Thermomechanical Deformation for Single-Molecule Analysis. *Analytical Chemistry* 2005, 77, 2252-2258.

Suni, T.; Henttinen, K.; Suni, I.; Mäkinen, J. Effects of Plasma Activation on Hydrophilic Bonding of Si and SiO2. *Journal of The Electrochemical Society* 2002, 149, G348-G351.

Tegenfeldt, J.; Prinz, C.; Cao, H.; Huang, R.; Austin, R.; Chou, S.; Cox, E.; Sturm, J. Micro- and nanofluidics for DNA analysis. *Anal Bioanal Chem* 2004, 378, 1678-1692.

Tong, Q. Y.; Gösele, U. A Model of Low-Temperature Wafer Bonding And Its Applications. *Journal of The Electrochemical Society* 1996, 143, 1773-1779.

Tsao, C. W.; Hromada, L.; Liu, J.; Kumar, P.; DeVoe, D. L. Low temperature bonding of PMMA and COC microfluidic substrates using UV/ozone surface treatment. *Lab on a Chip* 2007, 7, 499-505.

Uba, F. I.; Pullagurla, S.; Sirasunthorn, N.; Wu, J.; Park, S.; Chantiwas, R.; Cho, Y.-K.; Shin, H.; Soper, S. A. Surface charge, electroosmotic flow and DNA extension in chemically modified thermoplastic nanoslits and nanochannels. *Analyst* 2014, 139.

Vesel, A.; Mozetic, M. Surface modification and ageing of PMMA polymer by oxygen plasma treatment. *Vacuum* 2012, 86, 634-637.

Wu, J.; Chantiwas, R.; Amirsadeghi, A.; Soper, S. A.; Park, S. Complete plastic nanofluidic devices for DNA analysis via direct imprinting with polymer stamps. *Lab on a Chip* 2011, 11, 2984-2989.

Xu, F.; Datta, P.; Wang, H.; Gurung, S.; Hashimoto, M.; Wei, S.; Goettert, J.; McCarley, R. L.; Soper, S. A. Polymer Microfluidic Chips with Integrated Waveguides for Reading Microarrays. *Analytical Chemistry* 2007, 79, 9007-9013.

Zhang, L.; Gu, F.; Tong, L.; Yin, X. Simple and cost-effective fabrication of two-dimensional plastic nanochannels from silica nanowire templates. *Microfluid. Nanofluid.* 2008, 5, 727-732.

CHAPTER 4: DEVELOPMENT OF NANOFLUIDIC DEVICES FOR THE ELECTRICAL DETECTION OF DNA

Introduction

Recently, biological (Ashkenasy, '05; Clarke, '09) and solid-state (Fologea, '05; Rhee, '06; Storm, '03) nanopores and nanochannels (Mao, '05; Menard, '10), have served as interesting platforms for the analysis of nucleic acids like Deoxyribonucleic acid (DNA) (Venkatesan, '11). In the case of nanopores, polynucleotides are analyzed by monitoring changes in amplitude of the ionic blockage current generated when the molecules block the flux of buffer ions while traveling through the nanopores with the duration of blockage directly related to the length of the polymer (Kasianowicz, '96; Kasianowicz, '01; Meller, '00). Though nanopores have been useful for the development of nanoscale biosensors, they pose some limitations like poor confinement of the DNA strand within the nanopore (~0.1 % of a 10 kilobase (kb) DNA), poor signal sensitivity and the random motion experienced by the long, supercoiling DNA in solution that results in a large amount of white noise in the signal (Branton, '08).

Nanochannels can serve as alternative platforms to nanopores for bioanalysis due to their increased robustness, great flexibility in terms of shape and size, tunable surface properties and their ability to linearize DNA molecules (Danelon, '06; Lu, '08; Turner, '02). Also, using several robust and well-established techniques, nanochannel biosensors have been fabricated in silicon (Létant, '04), glass (Mao, '05), fused silica (Menard, '10; Steinmann, '04) and polymer (Chantiwas, '11; Wu, '11) substrates. DNA transport through nanochannels has been detected optically by first labeling the DNA biopolymer with a fluorescent reporter dye (Cosa, '01) followed by confinement in the nanochannel (Glazer, '92; Tegenfeldt, '04). The DNA transport

process can also be monitored through changes in the impedance, capacitance, resistance, conductance or quantum mechanical tunneling associated with an unlabeled molecule as it moves through a conduction path (*i.e.,* nanoelectrodes). Although optical detection has been useful for investigating the dynamics of DNA recoiling (Xu, '07), the effects of the channel width (Reisner, '05) and buffer ionic strength (Bilenberg, '05) on the measured end-to-end length of a confined DNA molecule, restriction mapping of DNAs (Riehn, '05) and biomolecular interactions (Wang, '05), it still poses some limitations. Fundamentally, fluorescent labeling of DNA molecules tend to alter its mechanical (Perkins, '95) and electrophoretic (Carlsson, '96) properties and results in light-induced breakage (photonicking) (Akerman, '96). Also, the requirement of sophisticated fluorescence microscopy equipment limits its applicability outside the research laboratory. Indeed, nanogap electrical detectors, which entail integrating nanochannels with nanoscale electrodes, are currently being developed to deal with the limitations posed by fluorescent-based Nanosensors (Li, '10; Liang, '08; Shigeto, '06; Tsutsui, '12). These detectors analyze DNAs by transducing its electrical behavior when resident within the detection volume (formed by the nanoscale gaps) or by monitoring changes in the electrical properties of the electrolyte medium when the DNA occupies the nanogap interstitial volume. Nanogap detectors are capable of detecting single-molecules using simple instrumentation due to their excellent compatibility with advanced semiconductor technology, scalability and low cost (Chen, '10).

In this work, we report the development of novel mixed-scale devices (nm to mm) in thermoplastic (PMMA) and quartz for the molecular-scale sensing of DNA molecules using electrical readout strategies. First, we assessed the capture rate of dsDNA using four nanochannel entrance structures – 3D funnel, funnel populated with pillars, groove and 3D trapezoidal stacks – fabricated in a PMMA substrate. Multi-physics simulations were used to

evaluate the electric field drop across these devices and the results were substantiated with DNA translocation experiments. We also demonstrate the simultaneous optical and longitudinal electrical detection of dsDNA and evaluate the translocation dynamics through a device possessing a single nanochannel. Similarly, we developed a quartz transverse nanogap device possessing a single nanochannel with a 3D funnel entrance (~30 μm; width and length) with two pairs of transverse electron-conducting nano-scale electrodes poised at the input and output ends of a nanochannel with nanometer gaps (~50 nm). The funnel entrance induced uncoiling of the DNA molecules and aided in the efficient entry of DNA into the nanochannel at low electric fields by reducing the entropic barrier for DNA entry into the nanochannel from an adjoining microchannel. This device served as the foundation for a technique for the direct reading and quantification of drug-induced DNA damage (lesion) sites in genomic DNA molecules and a novel DNA sequencing strategy.

4.1 Experimental Methods

4.1.1 Device Fabrication

Devices for the measurement of the longitudinal blockage current was fabricated in poly(methylmethacrylate), PMMA, that was fabricated and assembled using the nanoimprint lithography (NIL) described previously (see Chapter 3 for full details). In a different fabrication protocol, an integrated nanogap device was fabricated in a 500 μm thick 4-inch quartz wafer (RMS roughness of ~0.3 nm) using a combination of conventional lithographic techniques like optical lithography, electron beam lithography (EBL), thin film deposition and Focused Ion Beam (FIB) milling. The fabrication process was carefully organized to ensure that a succeeding fabrication step did not compromise the outcome of previous steps nor interfere with down-stream processing steps. As shown in scheme 4.1, device fabrication involved five steps.

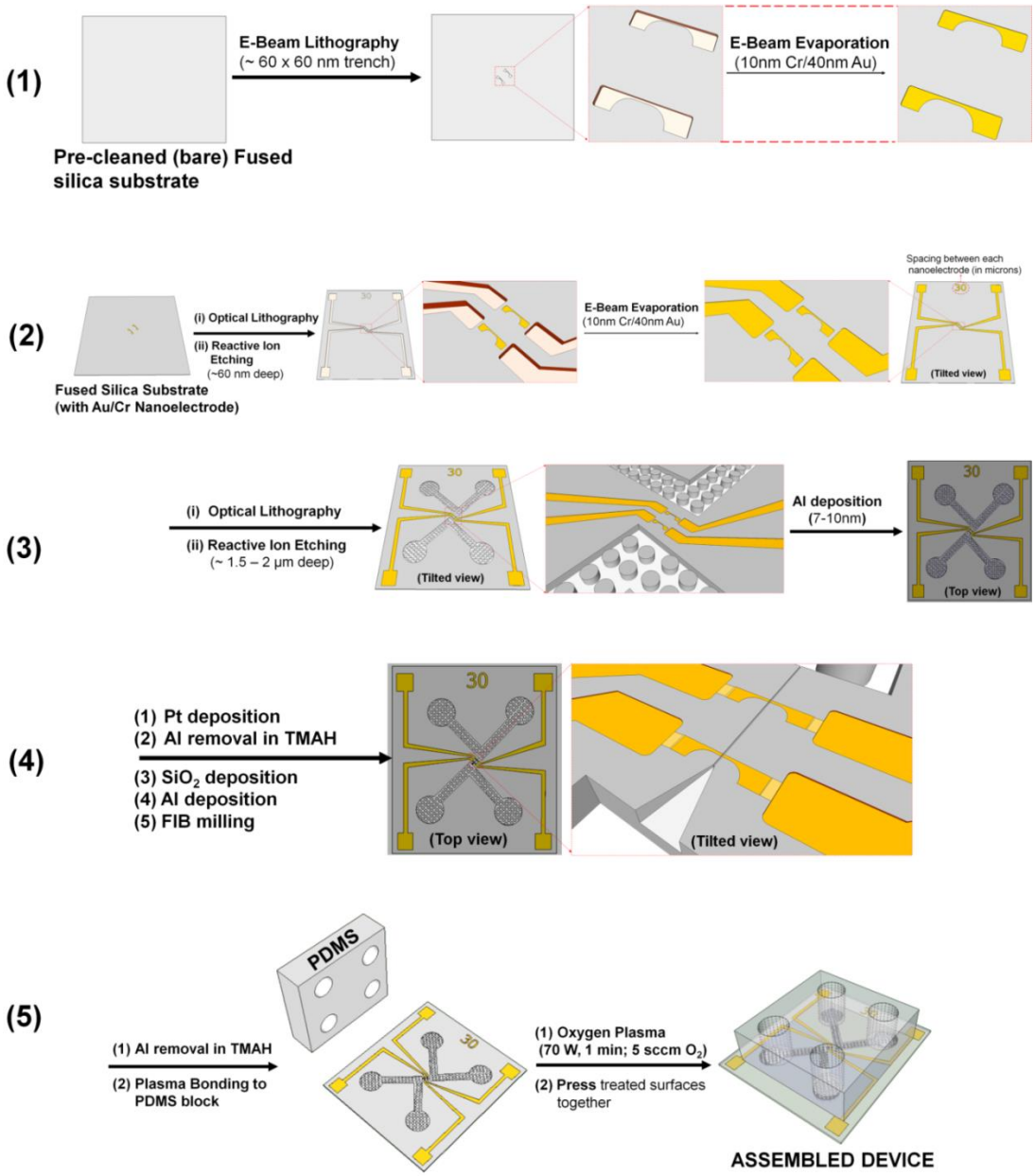

Scheme 4.1 The five processing steps involved in the fabrication of the dual electrode nanogap/nanochannel quartz device utilizing a combination of micro-patterning (optical lithography, e-beam evaporation, reactive ion etching) and nano-patterning (electron beam lithography, FIB and reactive ion etching) techniques.

4.1.1.1 Fabrication of Nanoelectrodes (Step 1, Scheme 4.1)

Device fabrication began with designing the nanoscale electrodes. First, a 100 nm layer of an e-beam resist (Zep520A) was spin coated onto a fused silica wafer at 1,500 rpm. When undertaking e-beam lithography (EBL) on a non-conductive substrate, charge will build up on the substrate during exposure causing broadening of the structures. To prevent this, a 50 nm

layer of Al was deposited on the resist using chemical vapor deposition (CVD). This Al layer had a negligible effect on the forward scattering of electrons during EBL and minimized charging artifacts. Chrome alignment marks were used to align the substrate with respect to the EBL mask.

E-beam writing was performed using an ELS-7000 e-beam writer operating at 100 keV and a current of 30 pA. It took approximately 0.2 s to write 30 nm x 30 nm patterns (12) on a 0.5 mm quartz wafer. After removing the Al layer, the resist was developed using an O-Xyele developer for 1 min. The nano-patterns were then etched into the substrate using ICP-RIE running with the following process conditions: pressure = 150 mTorr, CF_4 = 10 sccm, CHF_3 = 45 sccm, Ar = 10 sccm, power = 150 W and time = 100 s. The nanoelectrodes consisted of a 10 nm Cr adhesion layer and 40 nm Au layer that were electron-beam evaporated using a WOOSUNG e-beam evaporator-1 running at a DC voltage of 8.90 kV with deposition rates of 1.5 Å/s for Cr and 1.0 Å/s for Au.

4.1.1.2 Fabrication of Microelectrode and Contact Pads (Step 2, Scheme 4.1)

As shown in Scheme 4.1, the second fabrication step involves the patterning of microelectrodes and contact pads. This involved; (1) Patterning trenches in a resist by optical lithography, (2) etching with ICP-reactive ion etching, and (3) electron-beam evaporation of the Au electrodes. The wafer possessing the nanoelectrodes was pretreated with hexamethyldisilazane (HMDS) to ensure good adhesion between the photoresist and the quartz substrate and allowed for easy removal of the resist after etching. The treated substrate was spin coated with a positive photoresist, AZ1512, at 4000 rpm for 30 s. The resist thickness was ~1.5 μm. The coated wafer was aligned with a Cr mask followed by UV with an MA6 Mask Aligner (SUSS MICROTEC) with 110 mJ/cm^2 UV energy. The microelectrode mask was designed with AutoCAD software and is shown in Figure 4.1A.

After UV exposure, the photoresist was baked at 105^0C for 1 min and developed in an AZ300MIF developing solution for 60 s. The developed wafer was then cleaned by flushing with deionized water followed by spin drying. A 100 nm Al layer was coated onto the wafer using a DC sputter coater running at 70 W and 10 mTorr. The Al metal layer served to prevent charging and broadening of structures during ICP-RIE. Sixty nanometer deep trenches were created by exposing the coated substrate to a Lab Star TTL model ICP-RIE with the following conditions; CF_4 = 10 sccm, CHF_3 = 45 sccm, Ar = 10 sccm, pressure = 150 mTorr, power = 150 W, time = 100 s. Next, the resist was removed by soaking in piranha solution for 10 min followed by cleaning and N_2 drying. Electrodes consisting of 10 nm Cr (adhesion layer) / 40 nm Au were electron-beam evaporated into the trenches using a WOOSUNG e-beam evaporator-1 (DC voltage = 8.90 kV) with deposition rates of 1.5 Å/s and 1.0 Å/s for Cr and Au, respectively. After deposition, there was a 10 nm space left between the electrode and the quartz surface to allow for tight bonding of the substrate to the PDMS block.

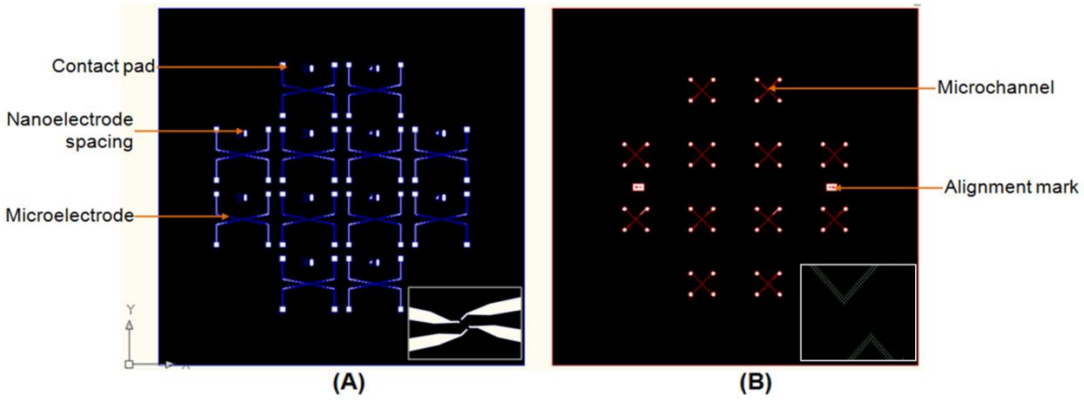

Figure 4.1 (A) Microelectrode mask (insert: connecting points to nanoelectrodes) (B) Microchannel mask (insert: zoom in to view)

4.1.1.3 Microchannel Fabrication (Step 3, Scheme 4.1)

After electrode fabrication, access microchannels were fabricated onto the wafer using optical lithography and ICP-RIE. The wafer containing the micro- and nanoelectrodes was initially coated with a 1 μm thick Al layer, which served to minimize charging during RIE. Next,

the wafer was spin coated at a speed of 3,000 rpm for 30 s with the photoresist consisting of nLOF2035. The coated wafer was pre-baked at 105^0C for 2 min, aligned with respect to the mask (Figure 4.1B) on the SUSS MICROTEC MA6 mask aligner and patterned by exposure to 90 mJ/cm^2 of UV light. The photoresist was subjected to a post exposure bake at 110^0C for 2 min followed by development for 2 min in an AZ300MIF developer. The patterned substrate was then etched using the SNTEK ICP1000 etcher with working conditions of C_4F_8 = 80 sccm, O_2 = 10 sccm, power = 1,300 W and time = 15.5 min. Fifty micron wide and 3 μm deep microchannels populated with an array of 10 µm pillars separated by 15 µm to prevent collapse of the PDMS block into the microchannels. A single wafer accommodated a total of 12 chips.

The Focused Ion Beam (FIB) milling step required that each chip be milled one at a time. The quartz wafer in our experiment was diced along the designed saw lines demarcating each chip using a 200 µm graphite edge blade running at a spindle speed of 20,000 rpm and cutting speed of 1 mm/sec. Each chip of size 20 mm × 20 mm was carefully cut out of the wafer.

4.1.1.4 Fabrication of Nanocontacts, Funnel Input, Nanochannel and Nanogap (Step 4, Scheme 4.1)

Platinum contacts were deposited between the micro-contacts and the nanoelectode of the chips, pre-coated with 100 Å Al using the gas injection system (GIS) on a Dual Beam FIB system (FEI Helios 600 Nanolab) with a milling current of 9.7 pA. Complete electrical contact was verified by resistance measurements. Next, the funnel input and nanochannel/nanogap were fabricated with an FIB milling current of 0.92 *n*A and 9.7 *p*A, respectively. The funnel entrance were milled at the edge of one of the microchannels using an FIB etch bitmap mask designed with AutoCAD. The funnel entrance had a total length of 35 μm from tip-to-base with a base width of 4 μm. The depth at the base and tip were 2.20 μm and 200 nm, respectively. A single 40 nm × 50 nm nanochannel was milled from the apex of the funnel across the nanoelectrodes and

to an exit junction at the opposite microchannel. This process produced the transport nanochannel and the nanogap. Finally, an Al layer was removed using AZ300MIF (TMAH) solution. Complete breakage of the nanoelectrodes was also verified by resistance measurements.

4.1.1.5 Device Assembly (Step 5, Scheme 4.1)

The cleaned quartz chip was sealed with a 0.5 cm thick PDMS block. Thermal heating was avoided to prevent delamination of the Au electrodes and possible collapse of the nanochannel at temperatures close to the glass transition temperature (T_g) of the quartz substrate. Both surfaces were activated with oxygen plasma (30W, 30s, 5.5 sccm) and subsequently brought into close contact and pressed against each other for 3-5 min for permanent sealing. Good bonding was confirmed by seeding the channels with 5 μM FITC and visualized under a fluorescence microscope.

4.1.2 Electric Field Analysis

The electric field at the transition between the micro and nanochannel was analyzed using a Finite Element Analysis tool (ANSYS 11.0, ANSYS Inc). A 3D model with the same dimensions as the real device was designed and a 1 V longitudinal bias applied. Electroosmotic flow, concentration polarization and dielectrophoretic trapping effects were ignored in the simulations.

4.1.3 Simultaneous Optical and Longitudinal Electrical Measurement

Experiments were performed with 0.5 μg/ml solution of Lambda and T4-DNA in 1× TBE buffer stained with YOYO-1 dye at a bp/dye ratio of 20:1. Beta-mercaptoethanol was added to minimize photobleaching and photonicking of the stained DNA molecules. Devices were initially filled with the buffer system followed by the DNA solution. Ag/AgCl electrodes were inserted into the top and bottom reservoirs and an Axopatch 200B amplifier was used to supply the driving voltage and monitor the corresponding current in the voltage clamp mode. A low-

pass Bessel filter on the amplifier was set to 5 kHz and the signal was sampled at 100 kHz using a Digidata 1440A digitizer. To eliminate external noise sources from the HBO light source and EMCCD to the electric current, we incorporated two grounded Faraday cages – one on the sample stage around the fluidic device and another around the microscope frame with the light source, camera, amplifier and digitizer placed outside the cage.

4.1.4 Transverse Electrical Measurements of DNA

Tris Boric acid EDTA (TBE) (1X) buffer (pH 8.3) prepared in Milli-Q water (Milli-pore) was used as the buffer. Preliminary measurements involved the use of 0.33 μg/ml solution of YOYO-1 stained and unstained T4GT7 DNA (Wako Chemicals). The stained sample was used to optimize the required electric field for the entrance of the DNA into the nanochannel while the unstained sample was used in the electrical measurements. The solution was introduced into the channel and electrokinetically transported through the funnel/nanochannel/nanogap assembly using Ag/AgCl electrodes inserted longitudinally across the device. Transverse ionic current across each nanogap was performed by mounting the assembled chip on a custom-designed stage with electrical pin-outs connecting the contact pads to a floating home-built current-to-voltage (I-E) amplifier. Signals were sampled at 500 kHz using an NI-USB 6341 multifunction digitizer (National Instruments) possessing two Analog outputs and 24 Digital I/O. The instrument control and data acquisition program was written and complied in LabView 2010 SP1 (National Instrument).

4.2 Results and Discussions

4.2.1 Enhancing DNA Capture into Nanochannels using Engineered inlet Structures

As previously described, though DNA linearization inside nanochannels allow for consistent and reproducible molecular analysis, nanochannels possess high electrical resistance for electrophoresis and high input entropic barriers that makes it challenging to feed DNA

molecules from microfluidic channels into nanochannels (Liang, '07; Mariam, '10; Storm, '05; Wanunu, '10). Similar to nanopores, a characteristic capture region with radius r* can be defined at the entrance of nanochannels (see Figure 4.2). At a position r > r*, molecular motion is almost purely diffusive (Grosberg, '10; Wanunu, '10; Wong, '07). However, when the molecule is located within a characteristic length r < r*, molecular motion is dominated by the applied electric field and the molecule is attracted towards the nanochannel entrance. Based on the work by Wanunu *et al.*(Wanunu, '10) in nanopores, r* can be represented as;

$$r^* = \frac{D_{av}^2 \mu}{8\, l\, D} \Delta V \qquad (1)$$

where μ is the electrophoretic mobility of the molecule, D_{av} and l are the average depth and length of the nanochannel, D is the diffusion coefficient of the molecule and ΔV is the voltage applied across the nanochannel.

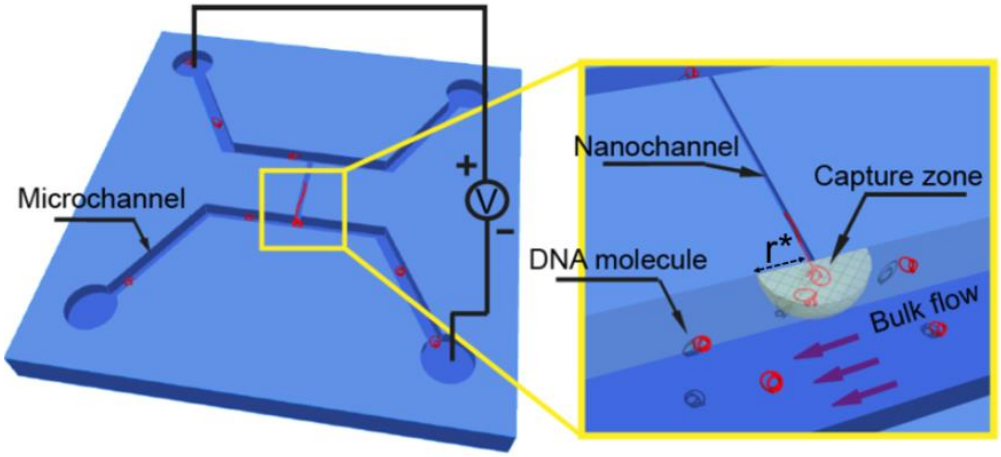

Figure 4.2 Representation of the nanofluidic device with an abrupt nanochannel inlet. The panel on the right is the enlarged view of the nanochannel/microchannel interface showing the capture zone with radius r* and electrokinetically transported DNA molecules.

According to equation 1, for a long nanochannel ($l \geq 5$ μm) such as utilized in our devices and at low electric fields, the radius of the capture zone is short and fewer DNA molecules are captured. Although increasing the driving voltage will increase r* and induce the motion of more molecules into the nanochannel, it is accompanied by high translocation velocity of the

molecules through the nanochannel and overcrowding of the nanochannel entrance. Fast motion of DNA may result in the reduction of the sensitivity and resolution in optical and electrical detection (Liang, '08; Menard, '13; Persson, '10). To mitigate these effects, we engineered micron to sub-micron scale inlet structures at the micro/nanochannel interface to aid the capture of DNA at low fields into nanochannels and slowed down the motion of DNA through the nanochannel and across the nanogap electrical transducer.

We studied the transport dynamics of fluorescently stained T4DNA through five geometrically distinct inlet structures which include; (1) original (abrupt) inlet, (2) nanopillar array inlet, (3) grooved inlet, (4) V-groove inlet (5) trapezoidal funnel inlet and (6) 3-dimensional funnel inlet. In all cases, the nanochannel was 60 µm × 70 nm × 70 nm deep (length × width × depth). The *original inlet* was a nanochannel with an abrupt transition between the micro- and nanochannel. The *nanopillar array inlet* consisted of staggered hexagonally packed pillars with the spacing varied between 220 nm at the bottom to 100 nm at the top (see Figure 4.3a). DNA molecules migrating through these devices were uncoiled as they collided and hooked around the pillars (see Figure 4.3b). The *grooved inlet* consisted of a microgroove that was 24 µm long and 1.5 µm wide and deep (see Figure 4.4c). The motion of DNA through the groove and toward the nanochannel was slow with a velocity of ~3 µm/s using a 0.5 V driving voltage (Figure 4.4d). The V-groove inlet consisted of two V-shaped grooves. The *trapezoidal funnel inlet* consisted of 8 steps of 3-dimensional trapezoidal prism with the width and depth decreasing from 50 µm × 15 µm (width × depth) to 100 nm × 80 nm in discrete steps (see Figure 4.3e and f). The *3-D funnel inlet* consisted of a single funnel structure ~35 µm long and 3.7 µm wide and 2.2 µm deep at the input (base) end (see Figure 4.3g). Both 3D structures prevented a sharp drop in the electric field lines at the microfluidic channel/inlet and inlet/nanochannel interfaces and at the same time increased the opening area toward the nanochannel both in width

and depth. As shown in Figure 4.3h, as the DNA molecules moved through the 3-D funnel inlet towards the nanochannel entrance, they were slowly uncoiled as a result of gradual reduction in entropy. The total migration time through the nanochannel was ~800 ms.

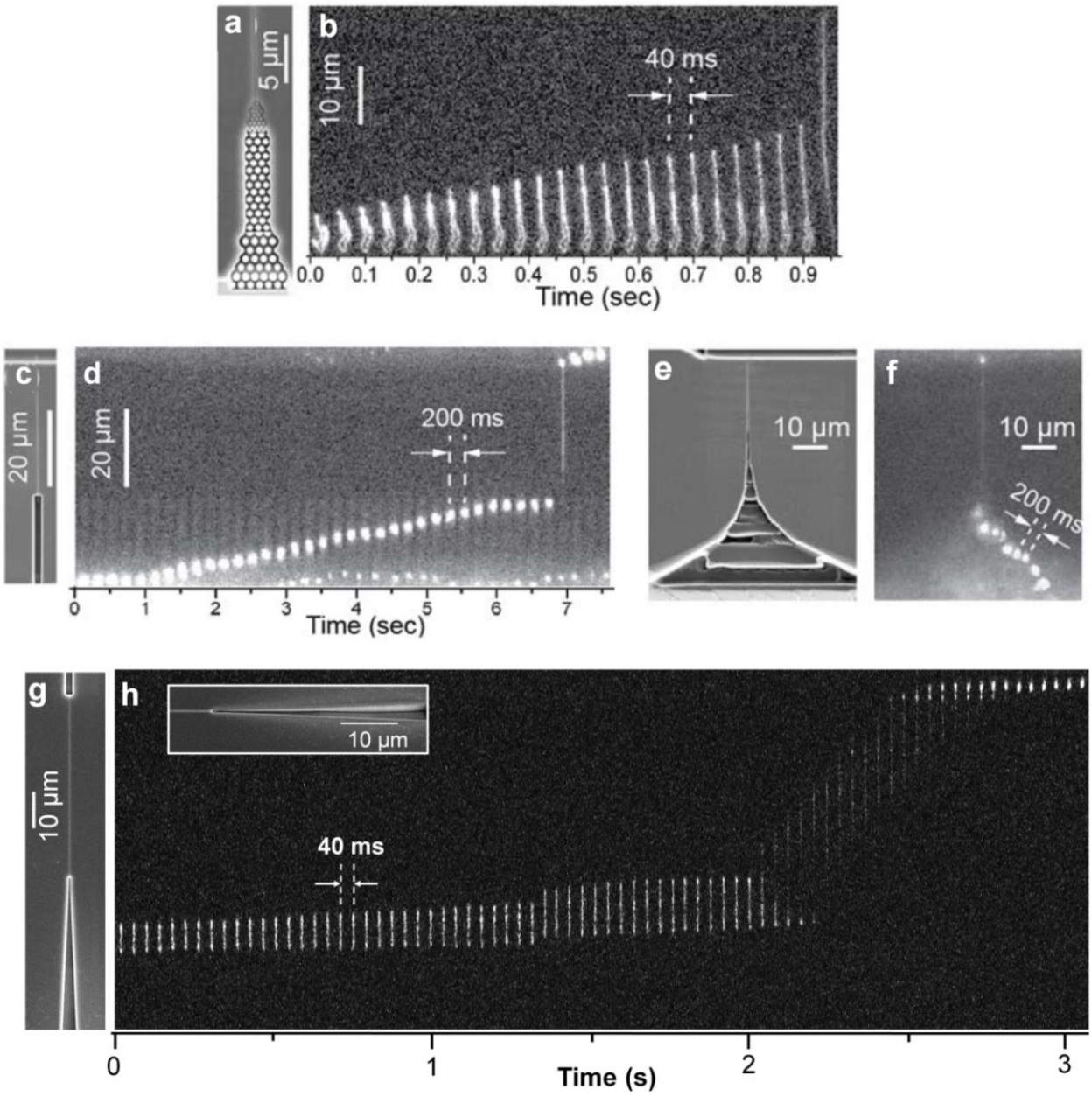

Figure 4.3 (a) On axis SEM image of the pillar inlet. (b) Frames showing the motion of DNA through the nanopillar array showing gradual unravelling by hooking around the pillars. (c) SEM of the grooved inlet and (d) a montage of typical DNA motion inside the grooved inlet. (e) Off axis SEM of the trapezoidal funnel inlet taken at 52^{o}. (f) The fluorescent image DNA captured in the inlet. (g) On axis SEM image of the 3-D funnel inlet, and (h) frames of the DNA migrating from the inlet into the nanochannel. (Insert shows the off-axis SEM image of the 3D-funnel taken at 40^{o}. The funnel was ~35 µm long, 3.7 µm wide and 2.2 µm deep at the base).

The capture rate for different inlets with respect to the capture rate at the original inlet is shown in Figure 4.4a. Compared to the original inlet, all inlet structures had higher capture rates. The grooved and V-grooved inlets presented a capture rate of 342 ±18% and 287 ±25%, respectively, relative to the abrupt inlet. Even though the nanopillar array inlet lowered the entropic barrier for DNA uncoiling prior to entering the nanochannel, it did not lead to a significant enhancement in the DNA capture rate as evidenced by a capture rate of 137 ±15%. The funnel inlet resulted in a capture rate of 770 ±21%; the highest of all inlet geometries.

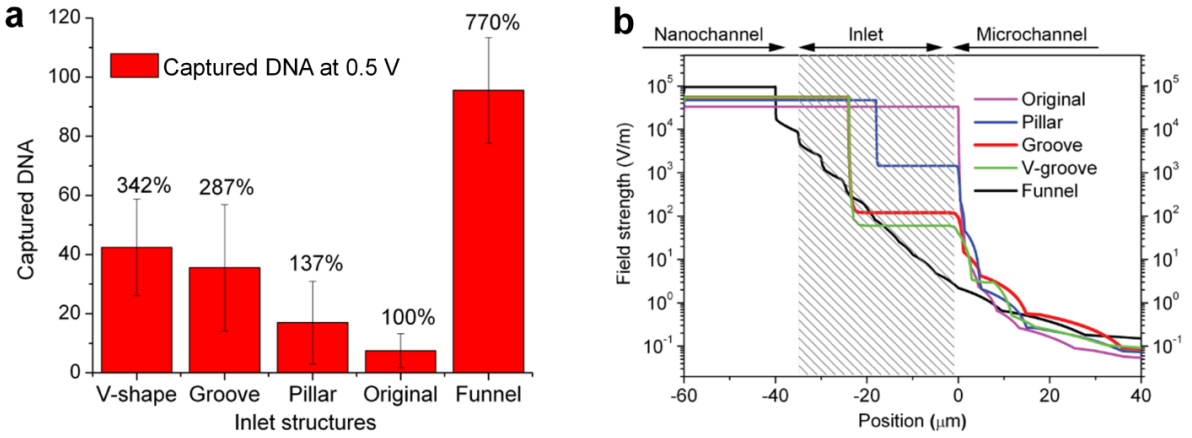

Figure 4.4 (a) The normalized capture rate for various inlet structures under a voltage of 0.5 V. (b) Simulated electric field strength distribution at each inlet structure. An electric potential of 1 V was applied across all inlets

Figure 4.4b shows the simulated electric field lines at the micro/nano interface for different inlets along the direction of the nanochannel. The position in the x-axis set to zero is the interface between inlets and the microfluidic channel. The electric field strength inside the nanochannels was similar in all five inlets. In the abrupt inlets, there was a sharp increase in the electric field from the micro- to the nanochannel. In the devices with the groove and V-groove inlet structures, an almost similar abrupt increase in the electric field was observed. However, the location of the sharp rise was shifted closer to the inlet/nanochannel interface when compared to the original inlet. The pillar inlet also showed a sharp increase in the electric field but to a lesser

extent because the cross-sectional area of the openings was slightly smaller than those of the groove and V-groove inlets.

In the 3D funnel inlet, the simulation results revealed a gradual increase in the electric field strength with multiple small steps from the microchannel to the nanochannel. The implication becomes that low bias voltages will induce slow movement of DNA from the microchannel through the funnel towards the nanochannel entrance. Once it reaches the tip of the funnel, entrance into the nanochannel becomes easier due the lower transition in the electric field and uncoiling as shown in Figure 4.3h.

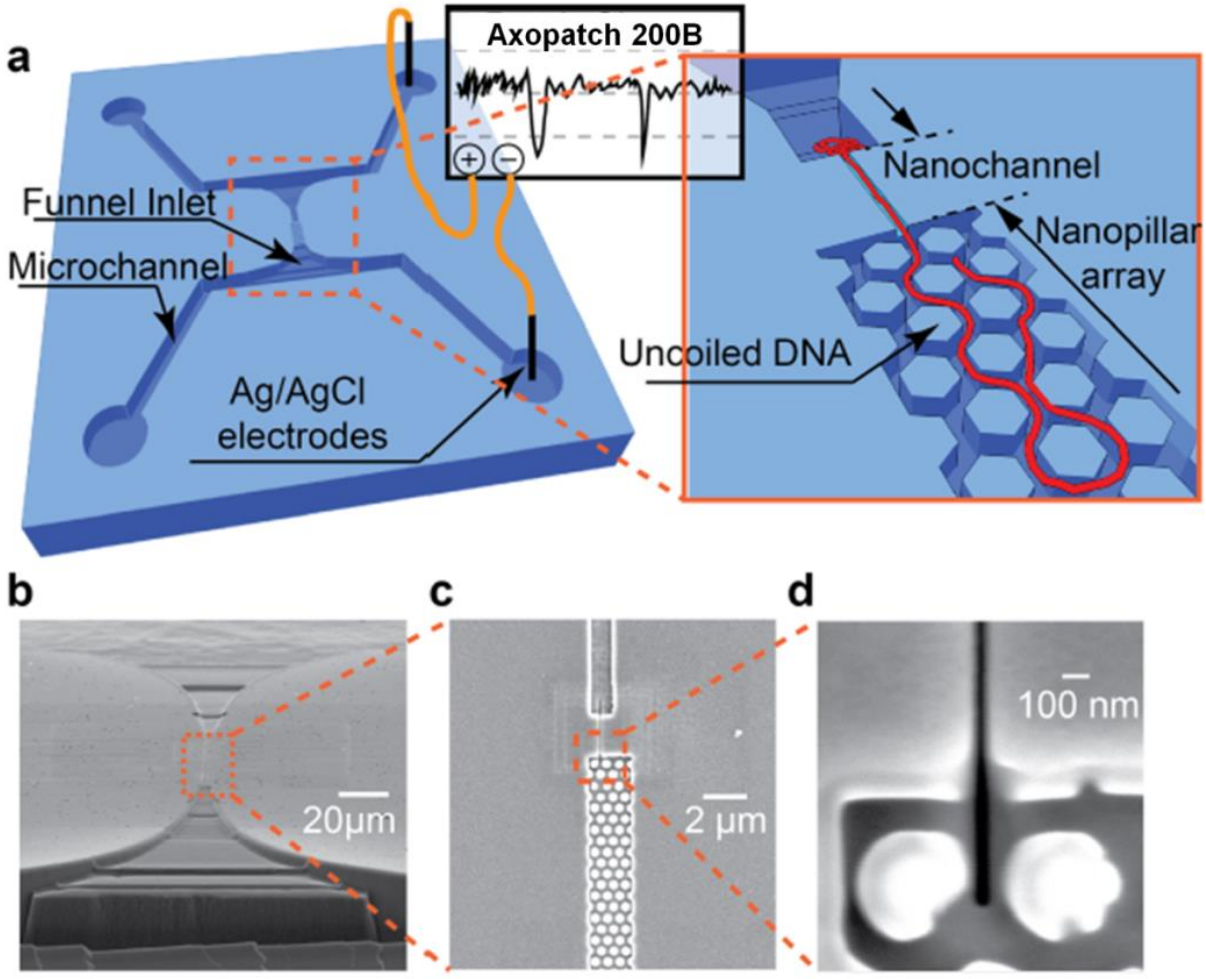

Figure 4.5 (a) Representation of the mode of measurement of the longitudinal blockage current. (b) Off-axis SEM image of the device acquired at 52° showing the assess microchannels and the connecting nanofluidic structures. (c) High magnification view of nanopillar array inlet, nanochannel and groove outlet. (d) High magnification view of the connection between the nanochannel and the nanopillar input.

4.2.2 Simultaneous Optical and Longitudinal Electrical Measurement

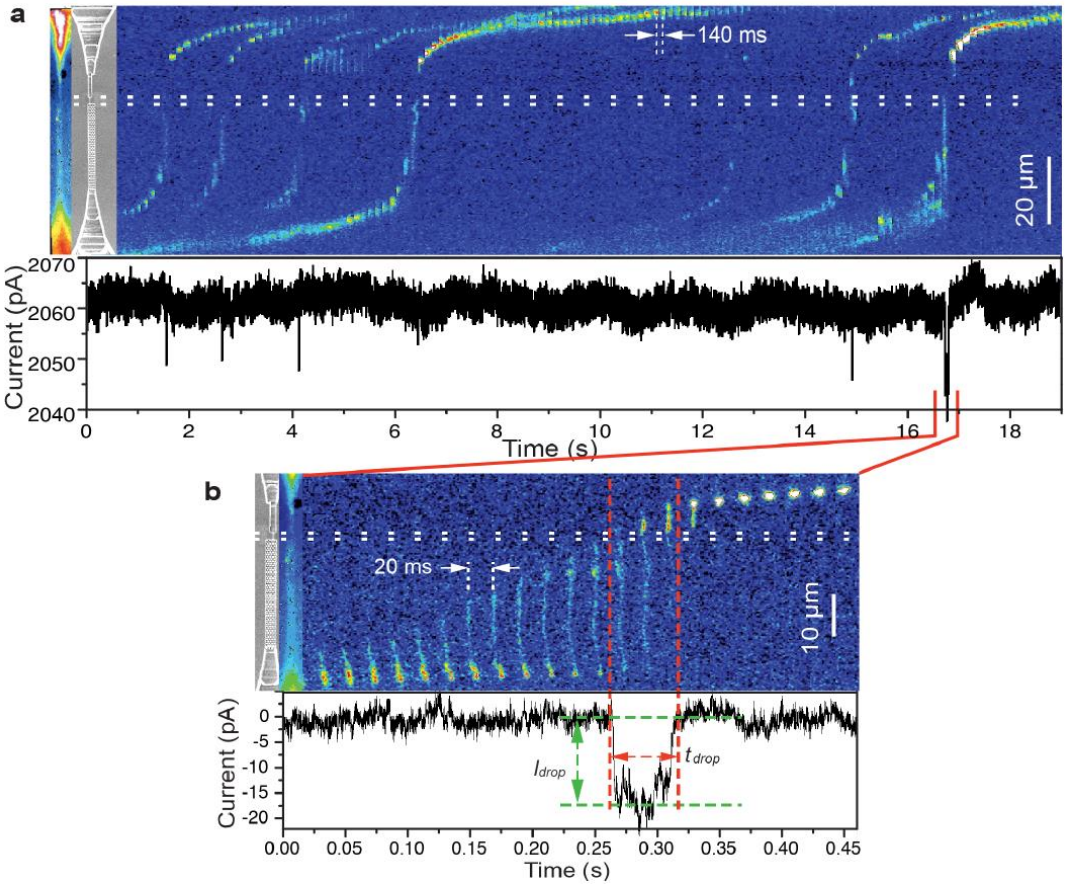

Figure 4.6 (a) Series of frames of seven DNA translocation events and the corresponding current-time trace within 19 s. (b) Enlarged view of a single translocation event showing a drop in the blockage current as the DNA migrated through the nanochannel. SEM image is shown on the left panel of each stack. The position of the nanochannel is marked with a white dashed line. False colors were assigned to the images based on fluorescent signal intensity.

A representation of the measurement modality for the longitudinal blockage current is shown in Figure 4.5a. The device consists of a single 60 × 60 nm nanochannel with an inlet consisting of an array of nanopillars (see Figure 4.5b – d) with pillar diameter of 300 nm and gap size of 90 nm to aid in pre-stretching of the DNA molecules before it entered the nanochannel. Nanochannels with lengths ranging between 200 nm and 55 µm were tested. We found that the when the channel length was > 2 µm, the signal was not distinguishable from the background noise for this nanochannel size. Therefore, we have shown the results obtained from a nanochannel that was ~2 μm long. A groove connected to a 3D funnel was fabricated at the

outlet. DNA molecules were electrokinetically driven though the nanochannel with a 1 V bias voltage and the blockage current was monitored in both high and low ionic strength solutions with simultaneous fluorescent imaging. In all represented frames, the location of the 2 μm long nanochannel is marked with the white dashed lines and the corresponding SEM image is shown on the left side of the image.

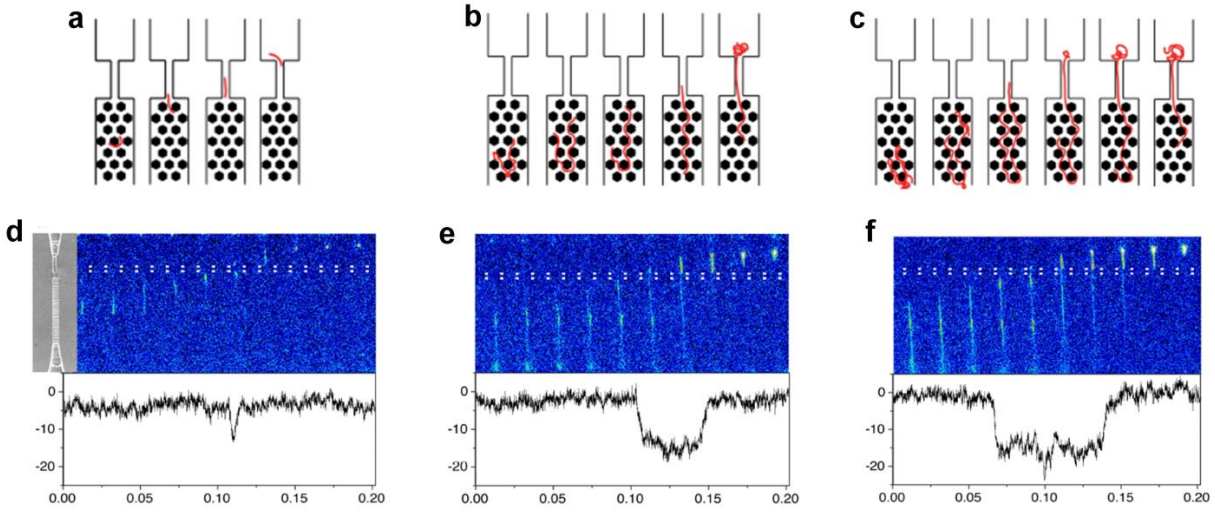

Figure 4.7 Transport modalities observed in (a) ~5 µm DNA fragments, (b) Lambda and (c) T4 DNA. The respective fluorescent images and current-time (I-t) traces are shown in (d), (e) and (f).

Current-time (I-t) traces revealed a reduction in the blockage current (downward spikes) when DNA migrated through the nanochannel. As can be seen on the frames in Figure 4.6a the DNA molecules gradually uncoiled as they moved slowly through the nanopillar array then rapidly migrated through the nanochannel before recoiling at the exit groove. Within a time of 19 s, seven DNA molecules migrated through the nanochannels that resulted in measurable drops in the ionic current (see Figure 4.6a). In all events, current drops occurred exactly when the DNA molecule passed through the nanochannel. The enlarged frames of a single event in Figure 4.6b shows the uncoiling of the DNA molecule in the nanopillar array, rapid translocation through the nanochannel and the recoiling of the DNA after completely exiting the nanochannel. As shown in the corresponding I-t curve, although the DNA molecule was uncoiled and elongated when it

migrated through the nanopillars, the reduction in current only occurred when the DNA migrated through the nanochannel. Also, the magnitude of the current blockage depended on the amount of electrolyte ions excluded from the nanochannel by the DNA molecule while the duration depended on the length of the migrating DNA relative to the nanochannel length.

Depending on the length of the DNA molecule being detected, three transport modalities such as depicted in Figure 4.7a-c were observed. The first mode was observed in DNA fragments ~5 μm long (see Figure 4.7d). We found that the molecules were less impeded by the nanopillars and they migrated through the nanochannels with a total time of 8 ±2 *m*s. Due to their small size, they excluded fewer electrolyte ions from the nanochannel showing a current blockage ~10 ±2 pA. The second modality was observed in full length λ-DNA (~16 μm). The molecules were initially uncoiled at the nanopillar array and they migrated through the nanochannel in ~48 ±5 *m*s (see Figure 4.7e). The measured blockage current was ~18 ±5 *p*A. The third modality was observed in T4DNA (~56.6 μm). As shown in Figure 4.7e, while the entry end of the DNA had completely crossed the nanochannel, the other end still remained hooked around the nanopillars. At a particular instant, the portion of the DNA molecule at the exit end completely blocked the nanochannel and resulted in an additional reduction in current by ~9 ±3 *p*A somewhere midway in the event. Overall, the DNA molecule moved slower through the device and generated an average blockage current of 20 ±3 *p*A and a total duration of 83 ±7 *m*s (see Figure 4.7f).

4.2.3 Transverse Electrical Measurement

4.2.3.1 Scaling Effects for Conductance Measurements using Ion displacement

The scaling effect of a nanogap size on the signal-to-noise ratio (SNR) in transverse electrical measurements was theoretically evaluated with Tris Borate EDTA (TBE) as the buffer. TBE buffer contains Tris base ($(CH_2OH)_3 C NH_2$), Boric acid (H_3BO_3 or $B(OH)_3$) and disodium EDTA salt ($Na_2H_2EDTA.2H_2O$). In solution at 25^{o}C, different reactions occur within the TBE

buffer solution. The complexity of these reactions and the formation of different products make the Henderson-Hasselbach equation inapplicable in the pH calculations (Michov, '86) (Harris, '06).

Tris base (T), *tris hydroxymethyl-aminomethane*, is a primary amine that produces the *Tris cation* and OH^- ions in solution (Bruice, '05). Tris cation is a conjugate (weak) acid of Tris base that can ionize in solution;

$$(HOCH_2)_3CNH_{2(s)} + H_2O_{(l)} \leftrightarrow (HOCH_2)_3CNH_{3\,(aq)} + OH^-_{(aq)} \quad (2)$$

$$(HOCH_2)_3CNH_{3\,(aq)} \leftrightarrow (HOCH_2)_3CNH_{2(s)} + H^+_{(aq)} \quad (3)$$

Boric acid (HB) also ionizes in water to produce *borate anion*, *three-boric acid* (HB_3) and *three-borate anion*; (Michov, '86), (Van Duin, '84)

$$B(OH)_{3(s)} + H_2O_{(l)} \leftrightarrow B(OH)_4^-{}_{(aq)} + H_3O^+_{(aq)} \quad (4)$$

$$3\,B(OH)_{3\,(aq)} \leftrightarrow H_3B_3O_{6\,(aq)} + H_2O_{(l)} \quad (5)$$

$$H_3B_3O_{6\,(aq)} + H_2O_{(l)} \leftrightarrow B_3O_3(OH)_4^-{}_{(aq)} + H^+_{(aq)} \quad (6)$$

In addition to the above products, a complex, weakly acidic, ionizable cyclic salt, *Tris-boric acid*, is produced from the reaction between Tris base and boric acid.(Michov, '86)

$$(HOCH_2)_3CNH_{2\,(aq)} + B(OH)_{3\,(aq)} \leftrightarrow (HO)_2\bar{B}(OH_2C)_2C(CH_2OH)\overset{+}{N}H_{3\,(aq)} + 2H_2O_{(l)} \quad (7)$$

$$(HO)_2\bar{B}(OH_2C)_2C(CH_2OH)\overset{+}{N}H_{3\,(aq)} \leftrightarrow (HO)_2\bar{B}(OH_2C)_2C(CH_2OH)NH_{2\,(aq)} + H^+_{(aq)} \quad (8)$$

The disodium EDTA salt also dissociates in solution;

$$Na_2H_2EDTA_{(s)} \leftrightarrow [H_2EDTA]^{2-}_{(aq)} + 2\,Na^+_{(aq)} \quad (9)$$

As shown in equation 2 of Chapter 1, the bulk conductivity κ_B is represented as;

$$\kappa_B = F \sum_i /z_i/\, u_i\, c_i \quad (10)$$

where F is Faraday's constant (96,485 C/mol), z_i is the ionic charge, u_i is the effective mobility of the ions and c_i is the concentration of ions in solution. Table 4.1 presents a summary of the ions, their charge, symbols and effective ionic mobilities at 25°C.

The equilibrium constants for equations 3 - 8, obtained from Michov (1986) (Michov, '86) and Harris (2006) (Harris, '06) are shown below;

$$K_2 = \frac{[T]\,[H^+]}{[TH^+]}; \qquad pK_2 = 8.03\ (K_2 = 9.333 \times 10^{-9}\ M) \tag{11}$$

$$K_3 = \frac{[B^-]\,[H^+]}{[HB]}; \qquad pK_3 = 9.24\ (K_3 = 5.75 \times 10^{-10}\ M) \tag{12}$$

$$K_4 = \frac{[HB_3]}{[HB]^3}; \qquad pK_4 = -2.08\ (K_4 = 120.226\ M^{-2}) \tag{13}$$

$$K_5 = \frac{[B_3^-][H^+]}{[HB_3]}; \qquad pK_5 = 9.28\ (K_5 = 5.248 \times 10^{-10}\ M) \tag{14}$$

$$K_6 = \frac{[HTB]}{[T][HB]}; \qquad pK_6 = -2.52\ (K_6 = 331.131\ M^{-1}) \tag{15}$$

$$K_7 = \frac{[TB^-][H^+]}{[HTB]}; \qquad pK_7 = 9.44\ (K_7 = 3.63 \times 10^{-10}\ M) \tag{16}$$

Table 4.1 A summary of ions present in a solution of Tris Borate EDTA buffer, charge, symbol and effective ionic mobilities. (Values were obtained from Michov *et al*.(Michov, '88; Michov, '84; Michov, '85))

Ion	Charge (z_i)	Symbol (Michov, '86)	$u_i \times 10^{-5}$ cm^2/Vs
Tris cation	+ 1	TH^+	24.06
Borate	- 1	B^-	- 29.84
Three borate	- 1	B_3^-	- 19.84
Tris-borate	- 1	TB^-	- 9.15
H^+	+ 1	H^+	352.45
OH^-	- 1	OH^-	- 198.60
Na^+	+ 1	Na^+	24.84
$EDTA^{2-}$	- 2	E^{2-}	–

Equations 13 – 20 can be substituted into equation 10 and can be used to calculate the conductivity κ_B in S/m of TBE solution at a known pH and ionic strength with the equation;

$$\kappa_B = F\left[\begin{array}{r} 2.58\times10^{4}[H^+][T] + 3.52\times10^{-3}[H^+] - 1.70\times10^{-13}\frac{[HB]}{[H^+]} - 1.25\times10^{-11}\frac{[HB]^3}{[H^+]} \\ - 1.10\times10^{-11}[T]\frac{[HB]}{[H^+]} - \frac{1.99\times10^{-17}}{[H^+]} + 2.49\times10^{-4}\,[Na^+] \end{array}\right]/10 \tag{17}$$

Figure 4.8 shows a graph of the theoretical and measured conductivities against the ionic strength of the TBE buffer.

If a bias voltage, V, is applied across two opposite electrodes with cross sectional area, A, spaced by a distance, L, occupied by an ionic solution, the measured electric current, I_{DC} is represented by the equation;

$$I_{DC} = \frac{\kappa_B \, A \, V}{L} \tag{18}$$

When a biomolecule with a very low conductivity relative to the ionic solution occupies the detection volume, it excludes buffer ions equal to its volume and results in an overall reduction in the conductivity of the solution within the detection volume and a corresponding reduction in the electric current. This measurable change in electric current (electrical signal) is denoted as;

$$\Delta I = \frac{A \, V}{L}(\kappa_{B1} - \kappa_{B2}) \tag{19}$$

where κ_{B1} and κ_{B2} are the respective conductivities at the detection volume before and after the biomolecule occupies the detection volume.

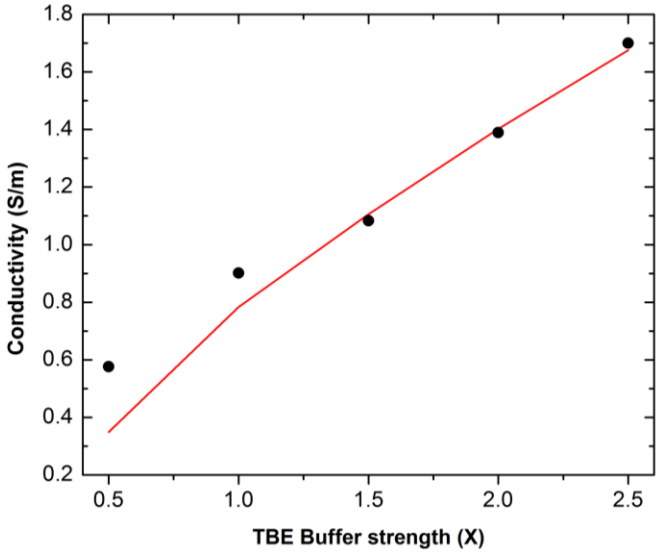

Figure 4.8 Graph of the theoretical (red trace) and measured (data points) conductivities of TBE buffer versus the ionic strengths at pH 8.3.

To compute the SNR, we evaluate the RMS noise contributions of the Johnson-Nyquist, I_{rms}^{nj}, and shot noise, I_{rms}^{ns}, to the electric current from the I-E amplifiers. These were calculated using the following equations;

$$I_{rms}^{nj} = \left[\frac{4\ k\ \mathrm{T\,B}}{\mathrm{R}} \right]^{1/2} \tag{20}$$

$$I_{rms}^{ns} = [\,2\ \mathrm{q}\ \mathrm{I_{DC}}\ \mathrm{B}]^{1/2} \tag{21}$$

where *k* is the Boltzmann's constant, T is the temperature, R is the resistance of the feedback resistor of the amplifier (100 MΩ), B is the bandwidth (Hz) and $\mathrm{I_{DC}}$ is the DC current. The total RMS noise I_{rms}^{nT} can be calculated using;

$$I_{rms}^{nT} = \sqrt{(I_{rms}^{ns})^2 + \left(I_{rms}^{nj}\right)^2}\ ; \tag{22}$$

$$I_{DC}^{n} = I_{rms}^{nT}\sqrt{2} \tag{23}$$

Therefore, the signal-to-noise (SNR) is

$$\boldsymbol{SNR} = \frac{\boldsymbol{\Delta I}}{\boldsymbol{I_{DC}^{n}}} \tag{24}$$

In our preliminary computations, we evaluated the scaling of the SNR with the nanogap size for the detection of a molecule of cytochrome c (cyt c) with 50 × 50 nm nanoelectrodes. Cyt c is a protein with globular structure that possesses one 'Heme' group in a single polypeptide molecule. It can exist in the reduced (ferrocytochrome, +2) and oxidized (ferricytochrome, +3) form with a simple cubic (P) crystal structure shown in Figure 4.9.

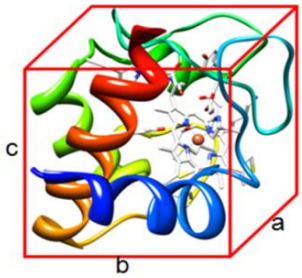

Length [Å]	Angle [°]
a = 82.03	α = 90.00
b = 82.03	β = 90.00
c = 75.19	γ = 90.00

Figure 4.9 The simple cubic crystal structure of Cytochrome C and the respective lengths of the sides as obtained from protein data bank.

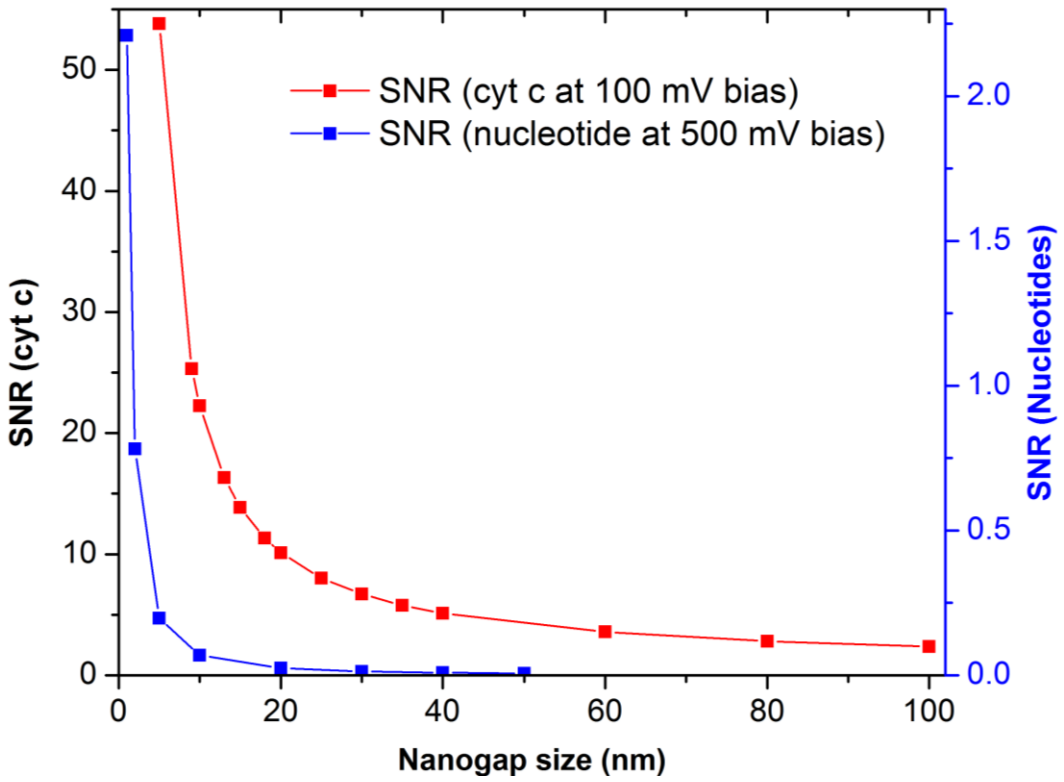

Figure 4.10 Variation between the Signal-to-noise ratio (SNR) and the gap size in the transverse nanogap device with nanosensor 50 × 50 nm. The red trace is the SNR for cyt c at 100 mV and the blue trace is the SNR for a single nucleotide at 500 mV bias voltage

According to Nakahara *et al.* (Nakahara, '77; Nakahara, '80), Szent-Gyorgyi proposed that the characteristic conductivities of proteins depends on the temperature with the equation;

$$\kappa_T = \kappa_o \, exp^{-\left(\frac{\Delta E}{2kT}\right)} \qquad (25)$$

where, κ_T is the conductivity at Kelvin temperature, T, κ_o is the conductivity at zero Kelvin (2.5 S/cm for cyt c) and ΔE is the energy of activation (9.62×10^{-20} J for cyt c). From equation 25, the conductivity of cyt c at 298 K is 1.75×10^{-10} S/cm and the approximate volume occupied by the molecule is 506 nm^3. The graphical representation of the SNR against the nanogap size (L) nm in 1× TBE buffer with a bias voltage of 100 mV is the red trace shown in Figure 4.10. Using the same electrode area (50 × 50 nm), the SNR was also computed for single nucleotides with a volume of 1 nm^3 (blue trace in Figure 4.10). Both results reveal that as the nanogap size reduces or the biomolecule size increases, there is a corresponding exponential increase in the SNR.

4.2.3.2 Device Fabrication and assembly

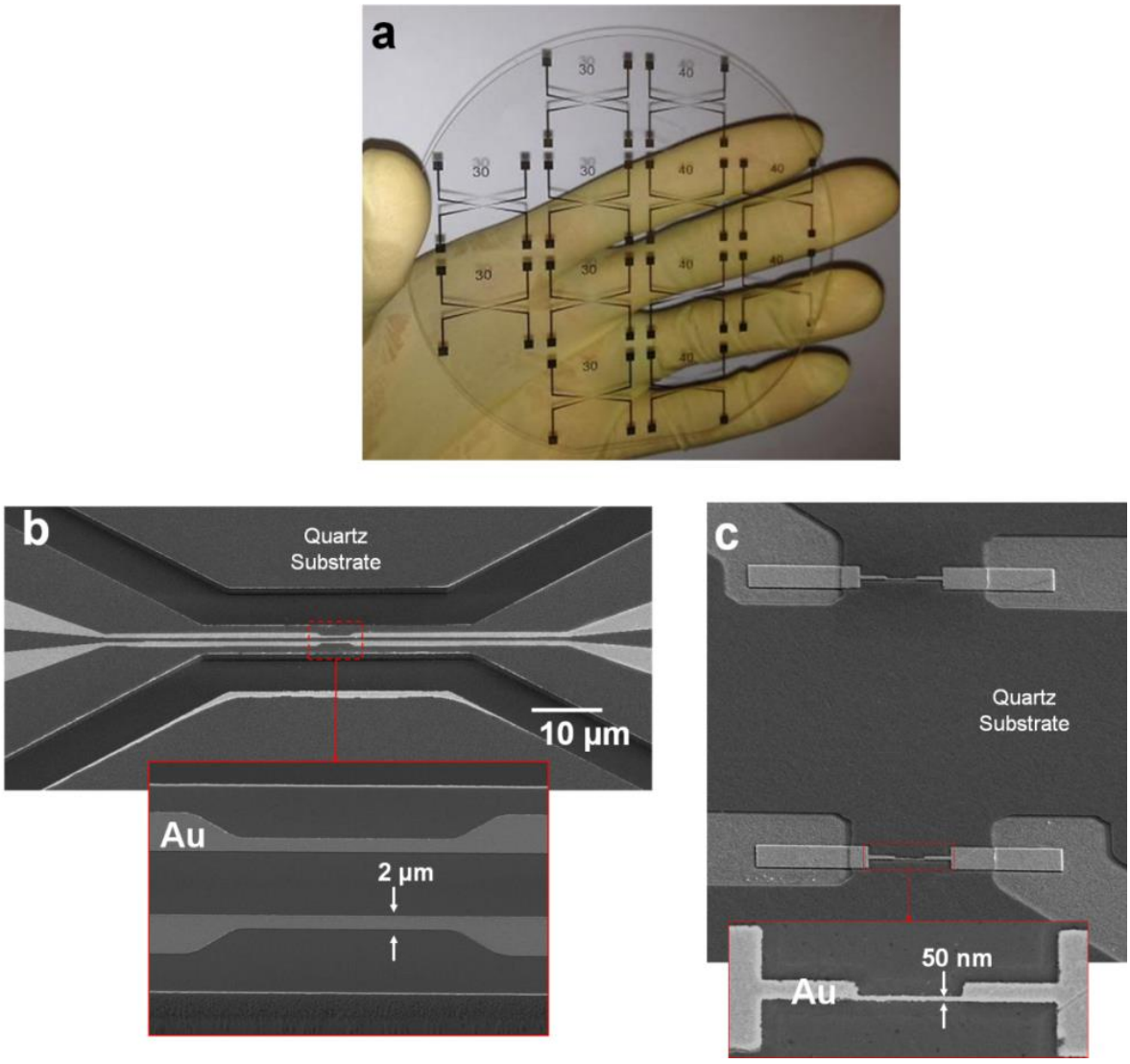

Figure 4.11 (a) Photograph of the dual nanoelectrode device after fabrication in the 4-inch fused Silica wafer. (b) SEM image of the 1-D dual nanoelectrode device. The panel below shows the off axis (520) image taken at a higher magnification. The measured width was 2 µm. (c) SEM images of the 2-D dual nanoelectrodes separated by a distance of 40 µm. The panel below shows the Au-based nanoelectrode with a width of 50 nm

Figure 4.11a shows a photograph of the dual nanoelectrode devices fabricated in a 4-inch fused silica wafer before dicing. With the fabrication scheme previously described (Scheme 4.1), we developed 1-dimensional nanoelectrodes, 2 µm × 50 nm (see SEM in Figure 4.11b) and 2-dimensional nanoelectrodes, 50 nm × 50 nm (see Figure 4.11c) with high reproducibility. The funnel entrance, transport nanochannels and nanogap were fabricated using FIB milling. In FIB,

a beam of gallium ions is incident onto a predefined area on the sample surface at a specific voltage and beam current. As Ga+ primary ion beam hits the sample surface, it sputters a small amount of material which leaves the surface as either secondary ions or neutral atoms along with secondary electrons (see Figure 4.12a) (Orloff, '96). The amount of sample material removed from the surface, *i.e.* the size of the nanotrench, depends on the sputtering yield (or etch rate) of the material and the spot size of the ion beam. The spot size, which is the beam diameter at full width-half-maximum (FWHM), at a specific voltage increases with the beam current. Figure 4.12b shows the variation between the spot size and the beam current at 30 kV and Table 4.2 shows the sputtering yields of the relevant materials at the same voltage.

The nanoelectrode was comprised of 40 nm Au metal and 10 nm Cr adhesion layer deposited onto a pre-patterned trench in the quartz wafer. Because we intended to fabricate the nanochannel and nanogap with a single milling step, we carefully controlled the fabrication conditions by evaluating the width at the nanogap (x_1) and the depth of penetration into the underlying quartz layer denoted as $\boldsymbol{z}$ (see Figure 4.13a) with respect to the width (x_2) and depth h_2 of the nanochannel as shown in Figure 4.13b.

Figure 4.13c shows the variation of the nanogap and nanochannel widths at 9.7 pA beam at 30 kV and a dwell time of 1 µs. Although the graph shows good linearity ($R^2 \sim 0.9971$), each data point showed a nanogap width higher than the nanochannel width by ~71 ±4%. This was corroborated by Figure 4.13d, which shows the variation between the penetration depth into the underlying SiO_2 layer at the nanogap and the nanochannel depth. From the graph, we can deduce that for a 50 nm deep nanogap (with an almost zero underlying layer) fabricated in a single milling step, the resulting nanochannel on the fused silica surface will be ~28.96 nm deep (intercept on the horizontal axis); ~ 72.7% shallower than the nanogap. The depth and width of the nanochannel was different when compared to the nanogap because the combined sputtering

yield of the conductive metals at the nanoelectrode region is higher than that of quartz (SiO_2). This means that a single beam pass will remove more materials from the nanoelectrode region than quartz surface. Nevertheless, the difference in the dimensions can be mitigated by adopting a more controlled multistep fabrication approach where the nanogap is fabricated with a lower beam current (1.5 pA). Figure 4.13e shows a range of nanochannels, 165 × 240 nm, 130 × 187 nm, 95 × 150 nm, 80 × 110 nm and 50 × 52 nm, fabricated in quartz using 9.7 pA milling current.

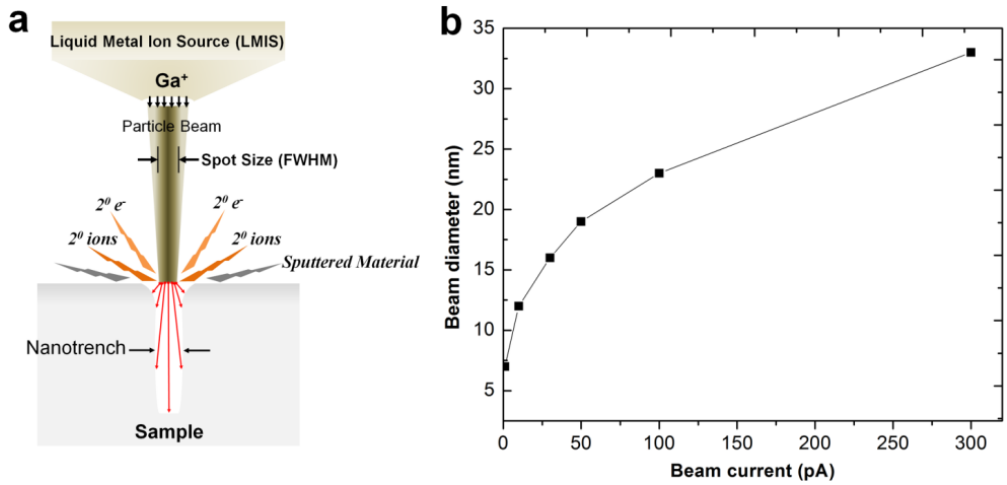

Figure 4.12 (a). Diagram showing the principle of FIB milling. Ga^+ induces the ejection of substrate materials in the form of secondary atoms, ions and electrons simultaneously creating a nanotrench. (b) Variation of the Beam diameter with the beam current at 30 kV obtained from FEI Helios operational manual.

Table 4.2. Sputtering yields of the materials in our device at 30 kV.

Material	Sputtering yield (μm^3/nC)
Al	0.30
Au	1.50
Cr	0.10
SiO_2	0.24

Figure 4.14a shows the SEM image of a1-D nanoelectrode device with a nanogap ~54 nm wide and 50 nm deep with a nanochannel 43.5 nm wide and 30 nm deep as shown in the lower panel. Also, Figure 4.14b shows the 2-D nanoelectrode device with a nanogap ~30 nm wide and 50 nm deep (upper panel). Both devices were milled using a 2-step approach. The

nanogaps were fabricated with 1.5 pA beam current while the 40 × 50 nm nanochannel was fabricated with 9.7 pA milling current. The 3D funnel populated with 800 nm diameter nanopillars and 150 nm spacing was fabricated with 0.48 nA current. A photograph of two chips with 30 µm and 40 µm spacing between the nanogaps, sealed with a PDMS block is shown in Figure 4.14c.

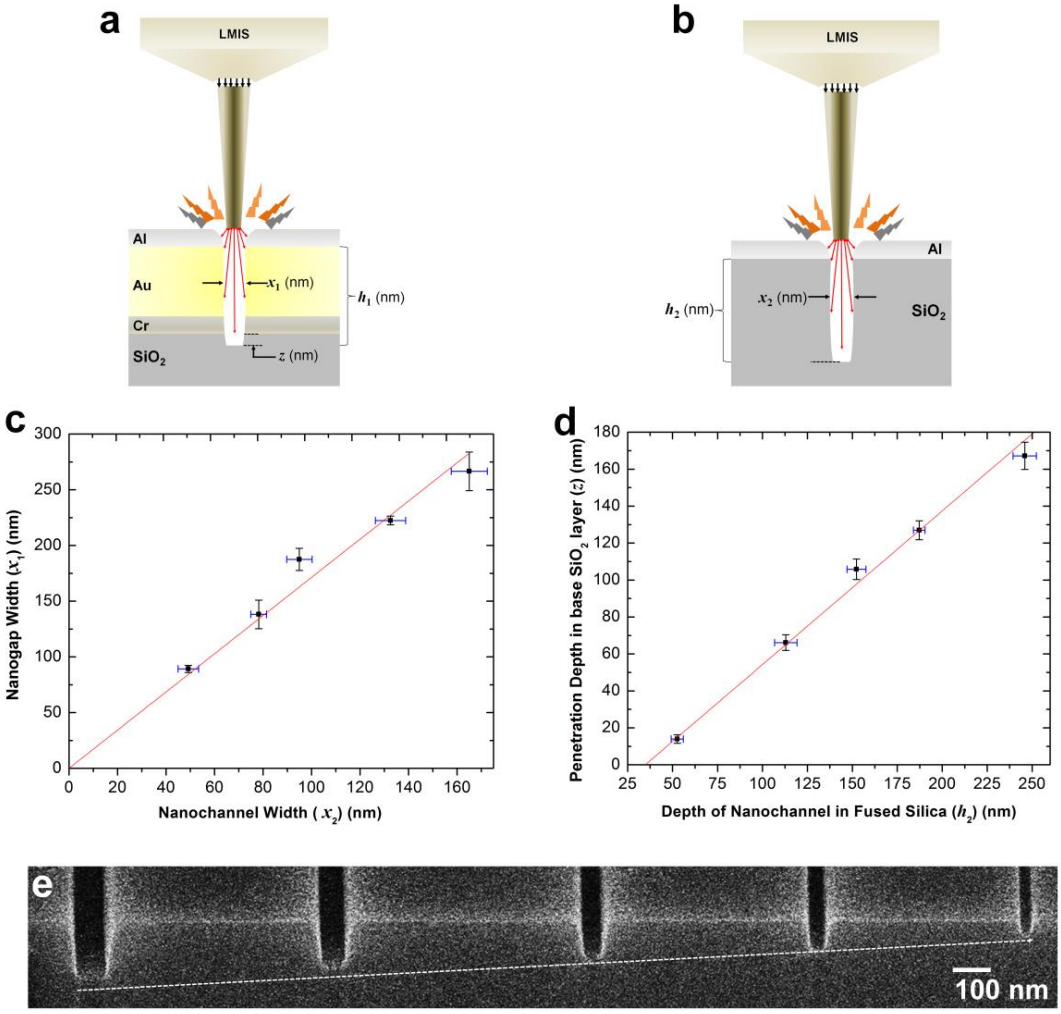

Figure 4.13 Schematic depicting the cross-section of the (a) nanoelectrode and (b) Quartz surface. Both regions were coated with Al prior to FIB milling. The nanoelectrode consists of 40 nm Au and 10 nm Cr adhesion layer. After milling, the final nanogap width is denoted as x_1 and the depth of penetration of the trench into the base SiO_2 layer is denoted as z. The width of the nanochannel fabricated in quartz is denoted as x_2 with the depth denoted as h_2. (c) Variation between the nanogap width and the nanochannel width. (d) Variation between the penetration depth in the base SiO_2 layer beneath the nanoelectrode and the depth of nanochannel in the fused silica after FIB milling. The intercept on the horizontal axis shows the depth of the nanochannel in fused silica when the nanogap depth is exactly 50 nm. (e) Off-axis (52°) SEM images of cross-sections of the FIB milled nanochannels in fused silica. The widths × depths are 165 × 240 nm, 130 × 187 nm, 95 × 150 nm, 80 × 110 nm and 50 × 52 nm (from left to right)

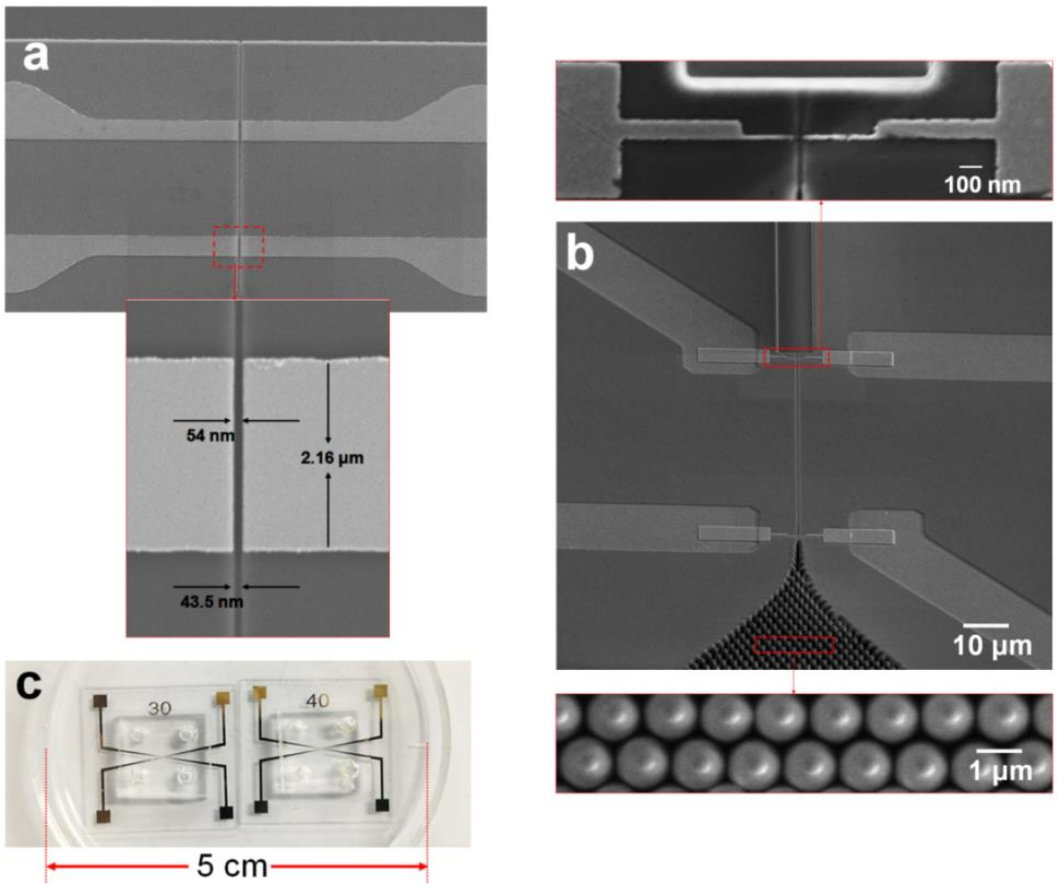

Figure 4.14 (a) SEM image of the FIB milled 1-D dual nanoelectrode device. The panel below shows the on axis image taken at a higher magnification. The measured nanogap width was ~54 nm and the nanochannel width was 43.5 nm. (c) SEM images of the FIB milled 2-D dual nanoelectrodes separated by a distance of 40 µm and connected by a 45 × 45 nm nanochannel with a 3D funnel input populated with nanopillars at the entrance. The top panel shows the nanogap ~30 nm × 50 nm and the bottom panel shows the nanopillars, ~800 nm in diameter spaced by ~150 nm

4.2.3.3 Design of High bandwidth Current-to-Voltage Amplifier and Opto-isolators

The equivalent circuit for the integrated dual electrode nanogap device is shown in Figure 4.15. This circuit ignored the electrical resistance of the micro-contacts and assumed that the major contributors to the overall electrical readouts are the entrance and exit nanogap resistances, $R_{N(ent)}$ and $R_{N(ex)}$ respectively, capacitance (C_{ne}) of the nanoelectrode surface in contact with the buffer and the electrical resistance of the nanoelectrode (R_{ne}). The total impedance across a single nanogap, represented as X_N, is given by;

$$X_N = \left[R_N + 2\left(\frac{1}{2\pi f C_{ne}}\right)\right] \quad (26)$$

From Ohm's law, the bias current (I) across each nanogap equals V/X_N; where V is the bias voltage across the electrodes. Also, since our measurements were performed with the AC field, we assume that the contribution of C_{ne} to the impedance will be very small; hence, $X_N \approx R_N$.

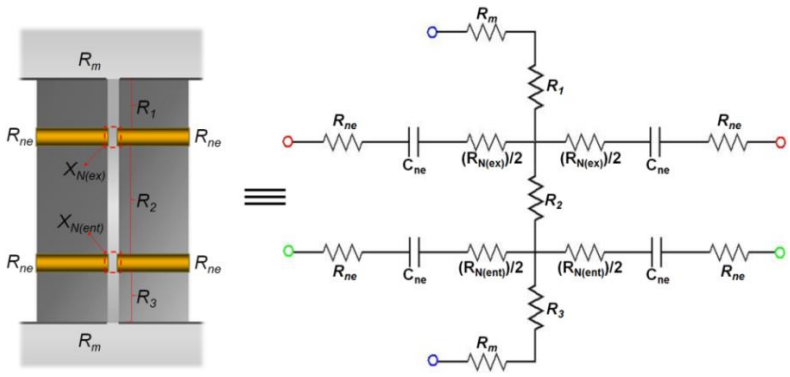

Figure 4.15 Equivalent circuit for the dual nanogap integrated device. (R_{ne} is the Resistance of Nanoelectrodes; $R_{N(ent)}$ and $R_{N(ex)}$ are the Resistance of Entrance and Exit Nanogaps respectively; C_{ne} is the Capacitance on the nanoelectrode surface in contact with the buffer ions; R_m = Resistance of access microchannel; R_1 and R_2 the Resistances of connecting nanochannel and R_3, in our case, is the resistance of the entrance funnel and the short exit nanochannel.

Preliminary measurements performed on our dual nanogap system using two Axopatch 200B amplifiers did not adequately resolve the observed currents at the entrance and exit nanogaps. We also observed that the currents were different in magnitude for the same nanoelectrode size and resident biomolecule. This anomaly occurred because both amplifiers were referenced to the same common point (line ground) at the op-amp and digitizer. As a result, because $R_{N(ent)}$ and $R_{N(ex)}$ are linked by R_2, the transient currents through $R_{N(ent)}$ followed two paths (one through $R_{N(ent)}$ loop and the other through R_2 to $R_{N(exit)}$ loop) and vice versa for the exit nanogap. Therefore, with this arrangement, current transients across one nanogap will be simultaneously detected at the other nanogap and the magnitude will differ in a ratio that depends on the bias voltage across each nanogap and the longitudinal driving voltage. Therefore, to avoid this, we have designed an electronic circuit that is able to isolate one nanogap from the other. As depicted in the interconnect diagram shown in Figure 4.16a, our system consists of two Current-to-Voltage (I-E) converters with two battery powered home-built independent floating

(±15V DC) power supplies and two linear opto-isolators (opto-couplers) – devices that transfer electric signals from their inputs to outputs using light – integrated before and after the A/D and D/A converters to isolate the amplifier from the digitizer. Each opto-isolation circuit consists of an opto-chip (AD215) and four operational amplifiers.

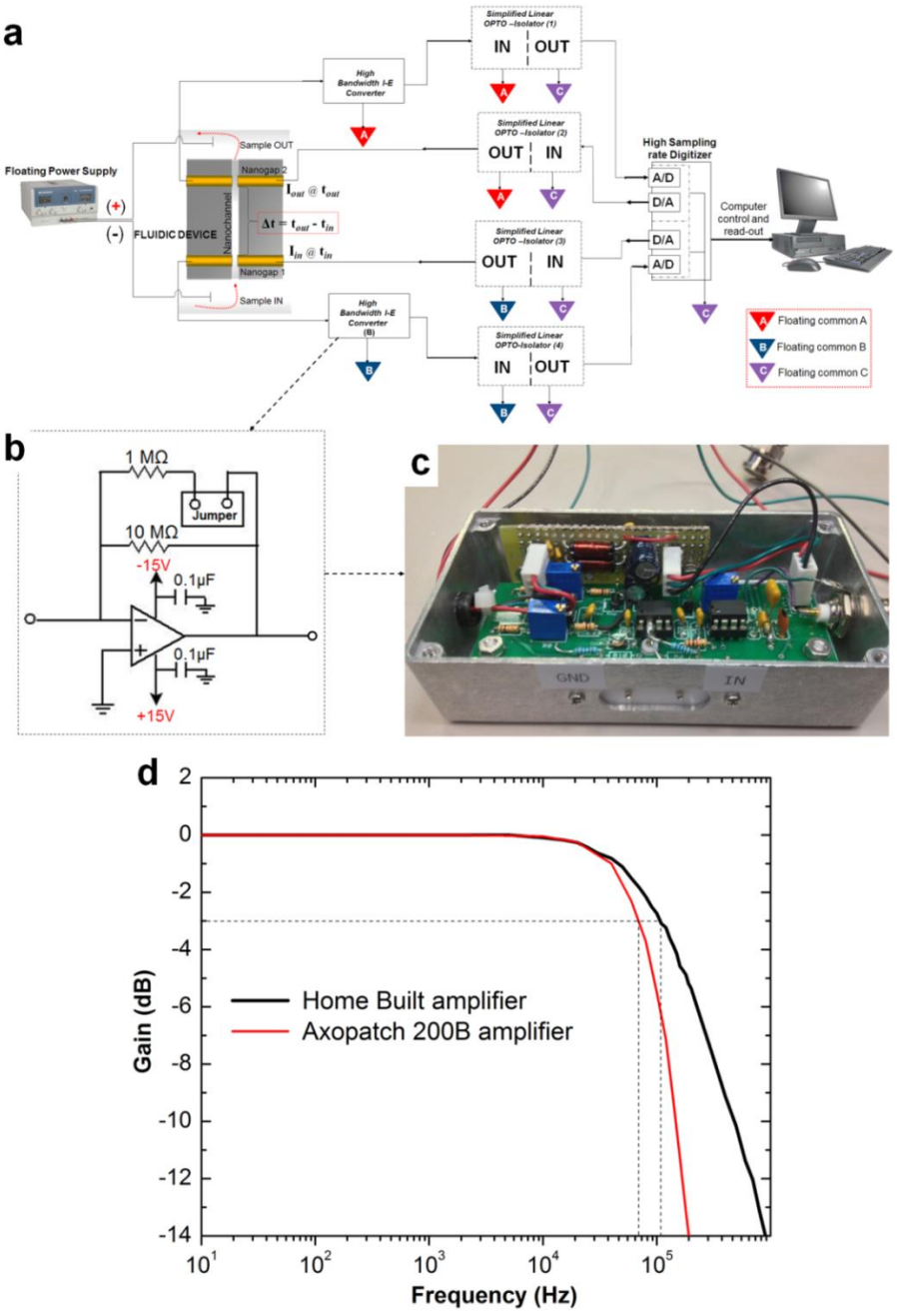

Figure 4.16 (a) Interconnect diagram of the experimental setup showing the nanofluidic device, high bandwidth current-voltage (I-E) amplifiers, opto-isolators and digitizer. (b) Simplified circuit diagram and (c) photograph of the home built I-E amplifier. (d) Bode plot showing the frequency response of the

homebuilt amplifier compared to the commercial axopatch 200B amplifier measured using a digital oscilloscope. The graph shows a bandwidth of ~103 kHz and ~70 kHz for the homebuilt and commercial, respectively.

The current-voltage (I-E) converter used in the measurements was developed using the ADA4627 preamplifier with a feedback circuit that allows the feedback resistance, R_F, to be varied between ~1 and 10 MΩ using a jumper (see Figure 4.16b). Trans-conductance gain of 10nA/V and 1nA/V and resolutions of 30pA and 3pA per step (16bit; ±10V digitization) was achieved for the 1 and 10 MΩ feedback resistors, respectively. The entire I-E converter was encased in a shielded metal chassis and soldered to the external connectors (see Figure 4.16c). and the I-E converter. Plastic shielded BNC cables and connectors were used for all connections between the digitizer. External shielding of the work piece stage, which was mounted on an insulating stage, was achieved using a dual aluminum Faraday cage connected to the floating commons of each amplifier.

The entire setup was placed in a third metal cage which was connected to the ground terminal from the digitizer. This arrangement proved to be very effective in the isolation of external inductively and capacitively coupled noise. Using the 10 MΩ feedback resistors, we recorded a bandwidth of ~103 kHz (comparable to commercial axopatch 200B amplifiers) (see Figure 4.16d) and a peak-peak noise of ~20 pA.

4.2.3.4 Current-Voltage plots along the Nanochannel and across the Nanogap

Figure 4.17a shows current-voltage (I-V) plot generated along the nanochannel (~50 × 50 nm, 35 µm long) with the 3D input funnel filled with 2× TBE. From the slope of the graph, the measured electrical resistance, R, was 10.39 ±0.73 GΩ. The theoretical resistance calculated by substituting V/R for I_{DC} and a buffer conductivity of 1.40 S/m for 2× TBE into equation 18, TBE was ~9.99 GΩ (neglecting the input funnel). The closeness of the theoretical to the measured

resistance indicates that ~ 100% of the voltage drop occurs in the nanochannel and the input funnel does not contribute to the total electrical resistance.

In the same vein, we monitored the I-V plot across the nanogap in the absence of a longitudinal field. From the graph shown in Figure 4.7b, the measured electrical resisance across the nanogap with a solution of 2X TBE was ~14.14 ±0.11 kΩ. Overall, excellent linearity (ohmic behavior) of all plots shown in Figure 4.17, for the I-V across the nanogap and along the length of the nanochannel/input funnel in the voltage range investitgated suggests that reliable quantitative data can be acquired across the device at this voltage range. Current-to-Voltage plots measured with the longitudinal voltages applied did not show a significant difference in the transverse currents when measured using our home-built isolated I-E amplifier.

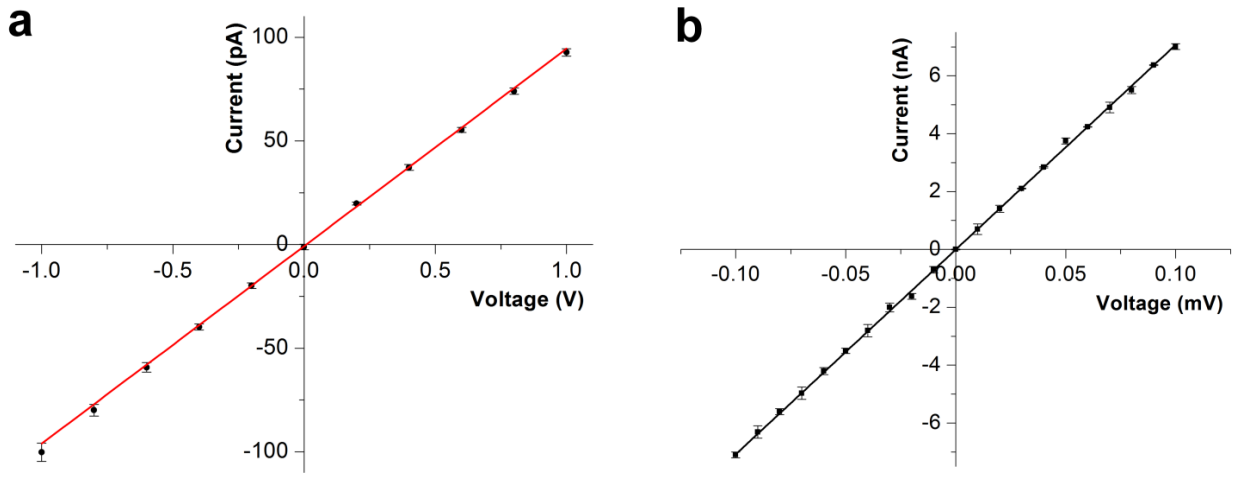

Figure 4.17 Current voltage plots measured (a) longitudinally along the nanochannel/input funnel and (b) transversely across the nanogap with 2× TBE in the absence of a longitudinal field

4.3 Conclusion

In this work, we successfully fabricated nanosensor platforms in thermoplastic and quartz substrate for the optical and electrical detection of biomolecule. Thermoplastic nanofluidic devices were fabricated using simple NIL techniques and utilized for the optical and electrical detection DNA. The integrated quartz fluidic system comprised of a nanofluidic channel (~50 × 50 nm, width × depth) containing two pairs of transverse Au nano-electrodes poised at the

input/output ends of the nanochannel. The nanochannel also possessed a funnel entrance to reduce entropic barriers and allow efficient entry of single molecules. Electrode pairs were poised orthogonal to the nanochannel with a gap ~50 nm situated between them to measure current perturbations induced when single molecules travel through them. Our device measures the change in conductivity in the detection volume defined by the size of the nano-scale electrodes and gap between them. Theoretical computations reveal an exponential increase in the SNR as the nanogap size reduces.

Fabrication of quartz device was accomplished in a clean room environment using five different processing steps which generally involved micro-patterning (optical lithography, e-beam evaporation, reactive ion etching) and nano-patterning (electron beam lithography, FIB milling and reactive ion etching). Resistance measurements across the electrodes were used to check for successful deposition and cutting of the electrodes. The electrical property of the device was found to be ohmic in behavior in the working voltage range investigated.

REFERENCES

Akerman, B.; Tuite, E. Single- and double-strand photocleavage of DNA by YO, YOYO and TOTO. *Nucleic Acids Research* 1996, 24, 1080-1090.

Ashkenasy, N.; Sánchez-Quesada, J.; Bayley, H.; Ghadiri, M. R. Recognizing a Single Base in an Individual DNA Strand: A Step Toward DNA Sequencing in Nanopores. *Angewandte Chemie* 2005, 117, 1425-1428.

Bilenberg, B.; Hansen, M.; Johansen, D.; Özkapici, V.; Jeppesen, C.; Szabo, P.; Obieta, I. M.; Arroyo, O.; Tegenfeldt, J. O.; Kristensen, A. Topas-based lab-on-a-chip microsystems fabricated by thermal nanoimprint lithography. *Journal of Vacuum Science & Technology B* 2005, 23, 2944-2949.

Branton, D.; Deamer, D. W.; Marziali, A.; Bayley, H.; Benner, S. A.; Butler, T.; Di Ventra, M.; Garaj, S.; Hibbs, A.; Huang, X.; Jovanovich, S. B.; Krstic, P. S.; Lindsay, S.; Ling, X. S.; Mastrangelo, C. H., *et al.* The potential and challenges of nanopore sequencing. *Nat Biotech* 2008, 26, 1146-1153.

Bruice, P. Y. *Organic Chemistry*. fourth edition ed.; Pearson: New Jersey, 2005.

Carlsson, C.; Larsson, A.; Jonsson, M. Influence of optical probing with YOYO on the electrophoretic behavior of the DNA molecule. *Electrophoresis* 1996, 17, 642-651.

Chantiwas, R.; Park, S.; Soper, S. A.; Kim, B. C.; Takayama, S.; Sunkara, V.; Hwang, H.; Cho, Y.-K. Flexible fabrication and applications of polymer nanochannels and nanoslits. *Chemical Society Reviews* 2011, 40, 3677-3702.

Chen, X.; Guo, Z.; Yang, G. M.; Li, J.; Li, M. Q.; Liu, J. H.; Huang, X. J. Electrical nanogap devices for biosensing. *Materials Today* 2010, 13, 28-41.

Clarke, J.; Wu, H.-C.; Jayasinghe, L.; Patel, A.; Reid, S.; Bayley, H. Continuous base identification for single-molecule nanopore DNA sequencing. *Nat Nano* 2009, 4, 265-270.

Cosa, G.; Focsaneanu, K. S.; McLean, J. R. N.; McNamee, J. P.; Scaiano, J. C. Photophysical Properties of Fluorescent DNA-dyes Bound to Single- and Double-stranded DNA in Aqueous Buffered Solution¶. *Photochemistry and Photobiology* 2001, 73, 585-599.

Danelon, C.; Santschi, C.; Brugger, J.; Vogel, H. Fabrication and Functionalization of Nanochannels by Electron-Beam-Induced Silicon Oxide Deposition†. *Langmuir* 2006, 22, 10711-10715.

Fologea, D.; Uplinger, J.; Thomas, B.; McNabb, D. S.; Li, J. Slowing DNA Translocation in a Solid-State Nanopore. *Nano Letters* 2005, 5, 1734-1737.

Glazer, A. N.; Rye, H. S. Stable dye-DNA intercalation complexes as reagents for high-sensitivity fluorescence detection. *Nature* 1992, 359, 859-61.

Grosberg, A. Y.; Rabin, Y. DNA capture into a nanopore: Interplay of diffusion and electrohydrodynamics. *The Journal of Chemical Physics* 2010, 133, -.

Harris, D. *Quantitative Chemical Analysis*. Seventh ed.; W.H. Freeman: New York, 2006; p 1008.

Kasianowicz, J. J.; Brandin, E.; Branton, D.; Deamer, D. W. Characterization of individual polynucleotide molecules using a membrane channel. *Proceedings of the National Academy of Sciences of the United States of America* 1996, 93, 13770-13773.

Kasianowicz, J. J.; Henrickson, S. E.; Weetall, H. H.; Robertson, B. Simultaneous multianalyte detection with a nanometer-scale pore. *Analytical Chemistry* 2001, 73, 2268-2272.

Létant, S. E.; van Buuren, T. W.; Terminello, L. J. Nanochannel Arrays on Silicon Platforms by Electrochemistry. *Nano Letters* 2004, 4, 1705-1707.

Li, T.; Hu, W. P.; Zhu, D. B. Nanogap Electrodes. *Advanced Materials* 2010, 22, 286-300.

Liang, X.; Chou, S. Y. Nanogap Detector Inside Nanofluidic Channel for Fast Real-Time Label-Free DNA Analysis. *Nano Letters* 2008, 8, 1472-1476.

Liang, X.; Morton, K. J.; Austin, R. H.; Chou, S. Y. Single Sub-20 nm Wide, Centimeter-Long Nanofluidic Channel Fabricated by Novel Nanoimprint Mold Fabrication and Direct Imprinting. *Nano Letters* 2007, 7, 3774-3780.

Lu, Z. X.; Namboodiri, A.; Collinson, M. M. Self-supporting nanopore membranes with controlled pore size and shape. *Acs Nano* 2008, 2, 993-999.

Mao, P.; Han, J. Fabrication and characterization of 20 nm planar nanofluidic channels by glass-glass and glass-silicon bonding. *Lab on a Chip* 2005, 5, 837-844.

Mariam, A.; Aleksandar, I.; Jongin, H.; Phillip, K.; Emanuele, I.; Joshua, B. E.; Tim, A. Precise electrochemical fabrication of sub-20 nm solid-state nanopores for single-molecule biosensing. *Journal of Physics: Condensed Matter* 2010, 22, 454128.

Meller, A.; Nivon, L.; Brandin, E.; Golovchenko, J.; Branton, D. Rapid nanopore discrimination between single polynucleotide molecules. *Proceedings of the National Academy of Sciences of the United States of America* 2000, 97, 1079-1084.

Menard, L. D.; Ramsey, J. M. Electrokinetically-Driven Transport of DNA through Focused Ion Beam Milled Nanofluidic Channels. *Analytical Chemistry* 2013, 85, 1146-1153.

Menard, L. D.; Ramsey, J. M. Fabrication of Sub-5 nm Nanochannels in Insulating Substrates Using Focused Ion Beam Milling. *Nano Letters* 2010, null-null.

Michov, B. M. Calculating “threeborate” ion mobilities at different ionic strengths and temperatures. *Electrophoresis* 1988, 9, 105-106.

Michov, B. M. Calculation of Tris-Borate Ion Mobility. *Electrophoresis* 1984, 5, 171-171.

Michov, B. M. Ionic Mobility Parameter. *Electrophoresis* 1985, 6, 471-474.

Michov, B. M. Specifying the Equilibrium-Constants in Tris-Borate BUFFERS. *Electrophoresis* 1986, 7, 150-151.

Nakahara, Y.; Kimura, K.; Inokuchi, H. Electrical conductivity of cytochrome c anhydrous film. *Chemical Physics Letters* 1977, 47, 251-254.

Nakahara, Y.; Kimura, K.; Inokuchi, H.; Yagi, T. Electrical conductivity of an anhydrous cytochrome c3 film as a function of temperature and ambient pressure. *Chemical Physics Letters* 1980, 73, 31-34.

Orloff, J.; Swanson, L. W.; Utlaut, M. Fundamental limits to imaging resolution for focused ion beams. *Journal of Vacuum Science & Technology B* 1996, 14, 3759-3763.

Perkins, T. T.; Smith, D. E.; Larson, R. G.; Chu, S. Stretching of a Single Tethered Polymer in a Uniform-Flow. *Science* 1995, 268, 83-87.

Persson, F.; Tegenfeldt, J. O. DNA in nanochannels-directly visualizing genomic information. *Chemical Society Reviews* 2010, 39, 985-999.

Reisner, W.; Morton, K. J.; Riehn, R.; Wang, Y. M.; Yu, Z.; Rosen, M.; Sturm, J. C.; Chou, S. Y.; Frey, E.; Austin, R. H. Statics and dynamics of single DNA molecules confined in nanochannels. *Physical review letters* 2005, 94, 196101.

Rhee, M.; Burns, M. A. Nanopore sequencing technology: research trends and applications. *Trends in Biotechnology* 2006, 24, 580-586.

Riehn, R.; Lu, M.; Wang, Y.-M.; Lim, S. F.; Cox, E. C.; Austin, R. H. Restriction mapping in nanofluidic devices. *Proceedings of the National Academy of Sciences of the United States of America* 2005, 102, 10012-10016.

Shigeto, K.; Kawamura, M.; Kasumov, A. Y.; Tsukagoshi, K.; Kono, K.; Aoyagi, Y. Reproducible formation of nanoscale-gap electrodes for single-molecule measurements by combination of FIB deposition and tunneling current detection. *Microelectronic Engineering* 2006, 83, 1471-1473.

Steinmann, P.; Weaver, J. M. R. Fabrication of sub-5 nm gaps between metallic electrodes using conventional lithographic techniques. *Journal of Vacuum Science & Technology B* 2004, 22, 3178-3181.

Storm, A.; Chen, J.; Zandbergen, H.; Dekker, C. Translocation of double-strand DNA through a silicon oxide nanopore. *Physical Review E* 2005, 71, 051903.

Storm, A. J.; Chen, J. H.; Ling, X. S.; Zandbergen, H. W.; Dekker, C. Fabrication of solid-state nanopores with single-nanometre precision. *Nat Mater* 2003, 2, 537-540.

Tegenfeldt, J. O.; Prinz, C.; Cao, H.; Chou, S.; Reisner, W. W.; Riehn, R.; Wang, Y. M.; Cox, E. C.; Sturm, J. C.; Silberzan, P.; Austin, R. H. The dynamics of genomic-length DNA

molecules in 100-nm channels. *Proceedings of the National Academy of Sciences of the United States of America* 2004, 101, 10979-10983.

Tsutsui, M.; He, Y.; Furuhashi, M.; Rahong, S.; Taniguchi, M.; Kawai, T. Transverse electric field dragging of DNA in a nanochannel. *Sci. Rep.* 2012, 2.

Turner, S. W.; Cabodi, M.; Craighead, H. G. Confinement-induced entropic recoil of single DNA molecules in a nanofluidic structure. *Physical review letters* 2002, 88, 128103.

Van Duin, M.; Peters, J. A.; Kieboom, A. P. G.; Van Bekkum, H. The pH dependence of the stability of esters of boric acid and borate in aqueous medium as studied by ¹¹B NMR. *Tetrahedron* 1984, 40, 2901-2911.

Venkatesan, B. M.; Bashir, R. Nanopore sensors for nucleic acid analysis. *Nat Nano* 2011, 6, 615-624.

Wang, Y. M.; Tegenfeldt, J. O.; Reisner, W.; Riehn, R.; Guan, X.-J.; Guo, L.; Golding, I.; Cox, E. C.; Sturm, J.; Austin, R. H. Single-molecule studies of repressor–DNA interactions show long-range interactions. *Proceedings of the National Academy of Sciences of the United States of America* 2005, 102, 9796-9801.

Wanunu, M.; Morrison, W.; Rabin, Y.; Grosberg, A. Y.; Meller, A. Electrostatic focusing of unlabelled DNA into nanoscale pores using a salt gradient. *Nat Nano* 2010, 5, 160-165.

Wong, C. T. A.; Muthukumar, M. Polymer capture by electro-osmotic flow of oppositely charged nanopores. *The Journal of Chemical Physics* 2007, 126, -.

Wu, J.; Chantiwas, R.; Amirsadeghi, A.; Soper, S. A.; Park, S. Complete plastic nanofluidic devices for DNA analysis via direct imprinting with polymer stamps. *Lab on a Chip* 2011, 11, 2984-2989.

Xu, F.; Datta, P.; Wang, H.; Gurung, S.; Hashimoto, M.; Wei, S.; Goettert, J.; McCarley, R. L.; Soper, S. A. Polymer Microfluidic Chips with Integrated Waveguides for Reading Microarrays. *Analytical Chemistry* 2007, 79, 9007-9013.

CHAPTER 5: ON-GOING DEVELOPMENTS AND FUTURE WORK

The long-term goal of this work is to develop an innovative nanofluidic biosensor for the near real time, rapid and efficient sequencing of biopolymers like DNA, RNA and Proteins based on the time-of-flight (ToF) of single monomer units migrating through a nanocolumn (2D nanochannel) after being enzymatically clipped from the polymer. The basic hypothesis behind our sensor functionality is that individual monomer units moving electrokinetically or hydrodynamically through a 2D nanochannel (with dimensions comparable to the size of the units) will experience flight-times that are dependent upon their molecular identity, chemical nature of the nanochannel wall and dimensions. The ToF, which will provide a signature uniquely specific to the molecule being monitored, will be transduced using a non-labeling electrical approach via conductivity in a detection volume defined by nano-scale electrodes (5-20 nm).

The nanosensor emanating from this project will have as its foundation polymer-based, nanochannels fabricated via nano-replication to allow high rate production of devices. The use of polymer substrates is predicated by their ability to be produced using replication technologies as well as the availability of polymers with a broad range of surface chemistries, which enables optimization of biomolecule/nanochannel wall interactions to facilitate ToF identification. Using this technology, we envision the generation of further innovative discovery efforts for a broader user community due to the systems' low-cost and simple operation. In addition, highly parallel production modalities will be developed to produce the nanosensors in a cost-effective manner to provide realization of platforms that produce sequencing information at the $1,000 level per genome.

5.1 Background Information

The ability to provide chemical or biochemical information at the molecular level offers exciting new opportunities for many applications. Examples include discovery (drugs, molecular recognition elements, new catalysts, biomarkers – genomic or proteomic), basic biology (comparative/functional genomics, proteomics), medicine (molecular profiles for diagnostics), forensics (molecular signatures for human identification), and homeland security (molecular signatures of suspected pathogens). These applications require either single use systems that are field deployable or high-throughput capabilities, due to the large number of samples that must be evaluated, the extensive number of elements to be screened or the need for monitoring an array of targets simultaneously and continuously. Technological platforms that provide reliable, rapid, quantitative, and low-cost identification of biomolecules, such as DNAs, RNAs and proteins, and their structural variants are currently the rate-limiting steps. For example, process pipelines currently available for high-throughput sequencing of DNA/RNAs, based on the pioneering work from Sanger *et al*. (Sanger, '77), include multiple processing steps. Starting with the selection of target cells and extraction of the nucleic acids, most methods require a cloning step and/or PCR to generate adequate copies of each individual target molecule in order to provide sufficient signal-to-noise ratios during detection. This is followed by an electrophoresis step to size-sort the DNA with an optical method of detecting the labeled DNA products. For high throughput protein expression profiling, a sample is digested into small peptides by a proteolytic enzyme, which is followed by a combination of a pre-fractionation step and a gas phase identification step by mass spectrometry. However, these processing pipelines cannot achieve real time readout due to molecular kinetic constraints associated with many processing steps and also, they require large amounts of sample to achieve sufficient identification accuracy.

Previously, biological (Kasianowicz, '96) and solid-state synthetic (Rhee, '06; Storm, '03) nanopores have been fabricated and utilized for DNA sequencing. Iqbal *et al.*(Iqbal, '07) previously demonstrated the ability of solid-state nanopores combined with the appropriate chemistry to sort biomolecules at the single-molecule level. Also, several articles have appeared dealing with the analysis of DNA chains when transported through nanochannels mostly fabricated in glass or fused silica. These works have primarily focused on the stretching of double-stranded DNA molecules for determining contour lengths, restriction mapping, looking for protein/DNA binding or sorting DNA by size. One recent paper investigated the dynamics of double-stranded DNA stretching in square PMMA nanochannels with channel cross-sectional dimensions (250 nm) much larger than the persistence length of the double-stranded DNA (Thamdrup, '08). Another recent paper by Liang *et al.* demonstrated the ability to measure electrical conductance changes of a DNA biopolymer moving through an in-plane electrode nanogap (9 nm) for single 1.1 kbp double-stranded DNAs (Liang and Chou, '08). However, the transport dynamics in the measurement of single nucleotide bases for DNA primary structure determinations has not been demonstrated.

The key issue for identifying single biopolymers using nanopores and nanochannels is the possibility that each monomer unit from the biopolymer will modulate a signal in a specific and measurable way as it passes through the pore or channel; however, there are certain challenges associated with this. For example, the individual base readout for sequencing of DNA molecules requires very high speeds (translocation times are very short) and/or the readout resolution is inadequate for single-base identification (pore thickness is larger than the single base spacing of DNA molecules, ~0.34 nm, and thus multiple bases may simultaneously reside within the pore). Also, a large amount of noise is created in the ionic current measurement due to the large

unoccupied volume in nanopores/nanochannels (Liang, '08). Despite a wealth of new biophysical information obtainable using nanofabricated structures, it is necessary to develop a new sensing mechanism with single molecule sensitivity in order to achieve high throughput identification of biomolecules using nanofabricated structures.

Readout resolution limitations can be mitigated if the monomer units are physically separated from each other. For example, in the case of DNA this has been demonstrated through the addition of a highly processive exonuclease, which sequentially clips individual nucleotides from an intact DNA molecule and then moving these bases through a pore for their identification (Davis, '92). Provided that the clipping process is carried out so as to minimize diffusion misordering of the released bases, these can be directed sequentially through a 2D (long) nanochannel to 'recognize' the mononucleotides using a ToF mechanism through an appropriately prepared 2D nanochannel with the ToF determined by potential target/wall interactions (Zikic, '06). The analogous process can be implemented for protein (and RNA) primary structure elucidation. Single protein molecules can be proteolytically digested and individual units comprising that protein can be identified through characteristic translocation properties.

The single molecule DNA sequencing strategy we are developing in this work is shown in Figure 5.1. A pre-processed double-stranded (ds) DNA fragment (~50 kbp) is electrokinetically directed through a nanochannel ~50 nm in width and height, similar to the persistence length of dsDNA (Tegenfeldt, Cao, , '04; Tegenfeldt, Prinz, , '04) and transduced using a pair of orthogonally placed wires with respect to the nanochannel. This electrical transducer, which measures a perturbation in the bulk solution conductance or tunneling current between the electrodes when a DNA passes through them, provides feedback as to when a

molecule enters the nanosensor and can generate a crude approximation as to its length (Liang and Chou, '08).

5.2 Description of Proposed DNA Sequencing Module

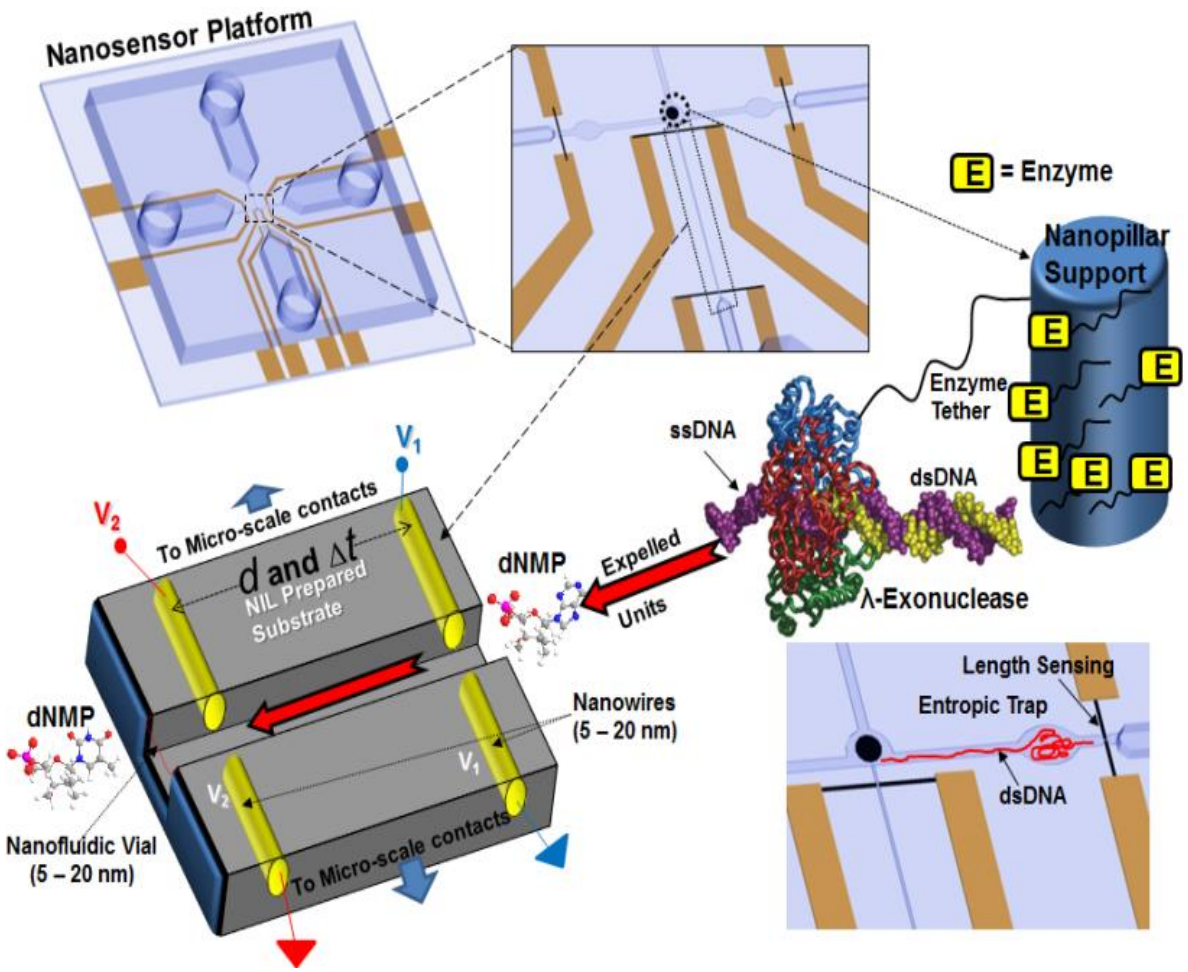

Figure 5.1 Schematic of the nanosensor that accepts dsDNA input molecules and deduces their primary sequence by the sequential clipping of the input dsDNA molecule using an exonuclease enzyme. The single dNMPs generated are moved through a nanochannel that produces a molecular-dependent flight-time used for dNMP identification. The flight-time is measured using a pair of nanoelectrodes poised at the input and output ends of the nanochannel, which is made from the appropriate polymeric material to suit the application need and the structures produced via micro- and nano-replication technologies. The nanosensor uses electrical signatures to monitor the input of dsDNA, immobilized exonuclease to complex the dsDNA, entropic traps to stretch the dsDNA and identify the clipped dNMPs using flight-times through 2D nanochannels.

If the dsDNA entering the nanosensor domain is “complexed” by an exonuclease, which is tethered to a solid support, an electrical signal does not appear at the electrode pair on the opposite side of the bioreactor (see Figure 5.1) signaling the ability to start a sequencing event.

Entropic traps are included to elongate the dsDNA during sequencing. Located within the nanosensor is a highly processive exonuclease, such as λ-exonuclease, that is covalently tethered to a pillar support via a linker using polymer-based modification chemistries developed in our laboratories (McCarley, '06; Wei, '05).

The initiation of the sequencing run is effected by applying an electric field across the nanosensor composed of a < 20 nm channel and the sensing electrodes to measure the flight-time of single dNMPs. The application of this field also introduces Mg^{+2} into the bioreactor to activate the exonuclease (Dapprich, '99; Matsuura, '01; Werner, '05). The released dNMPs are electrokinetically transported through the flight tube (nanochannel) with the travel time determined by the applied electric field, the length of the flight tube and the number of dNTP:channel wall interactions. In cases where the wall interactions are molecular dependent, the flight-times will provide a direct indicator of the identity of the dNMPs. Therefore, our base identification protocol is predicated on molecular-specific solute/wall interactions, similar to what has been demonstrated for nucleotides using chromatographic techniques (Czarnecka, '05). The major difference is that in our approach, the flight-time of single molecules must be monitored as opposed to ensemble measurements typically performed in chromatography due to the stochastic nature of the exonuclease.

We are currently investigating the translocation dynamics of dsDNA through an entropic trap/nanopillar/nanochannel assembly as depicted in Figure 5.2a. The SEM image and the equivalent circuit are shown in Figure 5.2b and c, respectively. The nanochannels around the single pillar serve as resistors for shaping and channeling dsDNA while the entropic trap (400 n m diameter and 80 nm deep) acts as a capacitor for storing the DNA. This can be observed in the fluorescent frames shown in Figure 5.2d. Under a longitudinal voltage of 0.1V, the DNA

molecules migrated from the microchannels through the entrance funnel into the entropic trap. It coiled up and remained in the trap for ~15 ms (see Figure 5.2e) before exiting the trap and migrating through the nanochannel in a total time of ~ 650 ms.

5.2.1 Translocation dynamics of dsDNA through Entropic Trap/Nanopillar structures

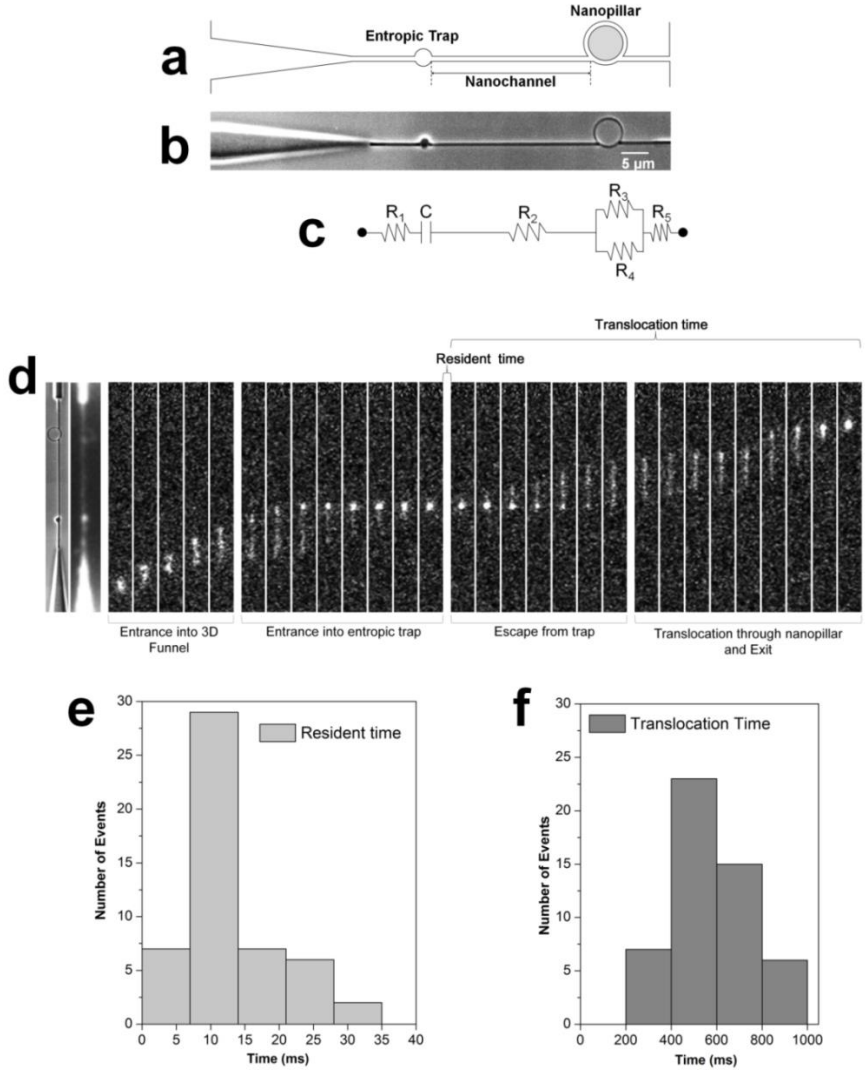

Figure 5.2 (a) Illustration, (b) SEM image and (c) Equivalent circuit of the multi-structured 3D Funnel/Entropic trap/Nanopillar device. Nanochannels are represented as resistors and the entropic trap is represented as a capacitor. (d) Frames showing the translocation of lambda DNA through the device. (e) and (f) shows the histograms of the resident time and translocation time of the migrating DNA, respectively under a 0.1 V driving voltage

Subsequently, it will be interesting to investigate the effect of changing the size of the trap and the nanochannel length on the translocation modality of dsDNA. In the long run, results

obtained from this device will serve as a basis for the development of the single-molecule solid-phase bioreactor in which exonuclease enzymes can be covalently attached to the pillar support. As the processive enzyme lathes unto the 5′ end of the dsDNA and exerts a pulling force while clipping the molecule, the entropic trap will exert an equal but opposite pulling force on the other end of the DNA. The single mononucleotides are electrokinetically fed into the flight tube.

5.2.2 Single Molecule real time Fluorescent Tracking of Nucleotides

The realization of our proposed DNA sequencing platform will require a fundamental understanding of the motion of nucleotides interacting with material surfaces (walls of the nanochannels) in buffers and the transport dynamics of the free mononucleotides to the nanosensor. Previously, we reported the fluorescence tracking of single molecules in polymer microchannels (Okagbare, '09) and single DNA molecules stained with intercalating dyes in nanochannels with widths well below the diffraction limit.

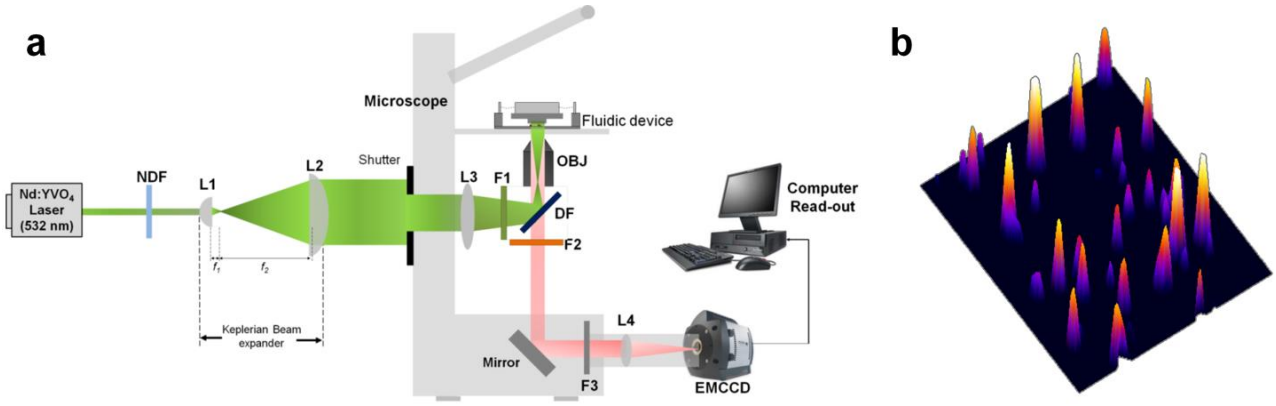

Figure 5.3 (a) Optical set-up of the imaging system. The Gaussian beam from the Laser (Nd:VYAG (λex = 532 nm; P = 0.01-5W; 2.2 mm beam diameter) was initially passed through a Neutral density filter (NDF) then expanded 10 times with a Kaplerian beam expander (focal lengths are 20mm and 200mm for L1 and L2 plano-convex lenses, respectively) and the wings knocked out with a shutter that ensures uniform laser intensity in the field of view and complete back-filling of the objective (OBJ). The beam was focused through an iris into the back end of a 100x oil immersion objective lens (OBJ) using lens (L3) through a 532nm laser line filter (F1) and the reflection from a dichroic filter (DF). A collimated laser beam is impinged upon the polymer nanofluidic device. The fluorescence signal generated from the single molecule was collected by this same objective, passed through the DF and spectrally selected using a long pass filter (F2). A mirror was used to steer the fluorescence signal onto an EMCCD after through a band-pass filter (F3) and focused using lens (L4). (b) 3D surface plot of the fluorescent image of the dye labelled nucleotides viewed under the system

In a following work, we will investigate the electrophoretic properties of single mononucleotides by fluorescently tracking them while being electrokinetically transported through the nanochannel. This will provide information on the effect of the surface chemistry within the nanofluidic channel on the ToF from single molecules. As the molecules travel through the nanochannel, they can interact with the walls of the channels. A change in the surface functional groups within the nano-channel will translate into a change in the EOF and/or surface charge density within the channel, hence, a corresponding change in the ToF of the single molecule traveling through the channel.

To initiate these experiments, we have developed a microscope instrumentation shown in Figure 5.3a with Nd:YVO_4 as the light source and ATTO532 as the fluorescent reporter. Our setup consists of an epi-fluorescence inverted microscope containing a high numerical aperture oil emersion objective (100×, NA = 1.3). The excitation beam will be a variable power Nd:YVO_4 laser (λex = 532 nm; P = 0.01 – 5W) that is shaped to provide a field-of-view of 10-50 μm to allow imaging the entire length of the polymer nanochannels. The emission was collected with the same objective and transmitted through a dichroic mirror and onto an EMCCD. The EMCCD camera we will use is a frame transfer EMCCD equipped with signal enhancement via on-chip gain configured in a 512 × 512 front illumination format.

To track the dye reporter with minimal photobleaching, we have chosen ATTO532 dye (λ_{ex} = 532 nm; λ_{em} = 556 nm) due to its high photochemical stability and also a functional group to allow facile conjugation to the dNMP targets. We have also added the appropriate anti-bleaching reagents (Trolox and Beta-Mercaptoethanol) (Vogelsang, '08) or Glucose Oxidase – Catalase (GODCAT) enzymatic-based scavenging system for the removal of molecular oxygen, which can serve as a reactive species that can significantly reduce the photostability of the

molecular dye. The polymers that will be selected for the present examinations will be those that have excellent optical properties (*i.e.*, low autofluorescence backgrounds), such as PMMA and COC (Shadpour, '06). Preliminary imaging through a COC cover plate reveals individual dye molecules with good SNR (see Figure 5.3b for the 3D surface plot of the dye labelled nucleotides). These experiments will eventually be coupled with the single-molecule electrical measurements.

5.2.3 Reducing Nanoelectrode and Nanogap sizes for Single Nucleotide Sensing

In this work, we have successfully fabricated a nanosensor platform in quartz comprising of a nanofluidic channel (~50 × 50 nm, width × depth) containing two pairs of transverse Au nano-electrodes (50 × 50 nm) poised at the input/output ends of the nanochannel. Our current device will be useable in the measurement of dsDNA. However, preliminary theoretical computations, shown in Figure 5.4, revealed that the SNR increases linearly as the nanoelectrode size reduces and exponentially as the nanogap size reduces. Towards achieving our goal of DNA sequencing via ToF, we will need to further reduce the nanoelectrode size to ≤ 10 nm and nanogap sizes ≤ 3 nm.

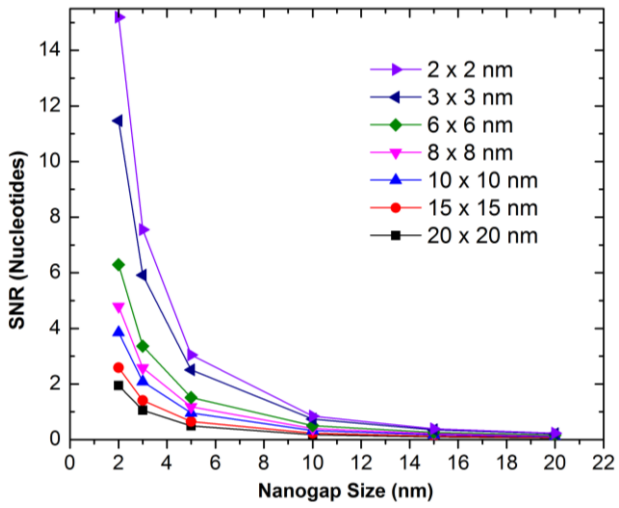

Figure 5.4 Variation between the electrical signal-to-noise (SNR) ratio and the nanogap size for different nanoelectrode areas for single mononucleotide units at 500 mV bias. As the nanoelectrode area reduces, there is a reduction in the detection volume and a corresponding increase in the SNR

5.2.4 Adopting Alternative Schemes for fabricating Nanoelectrodes in Thermoplastics

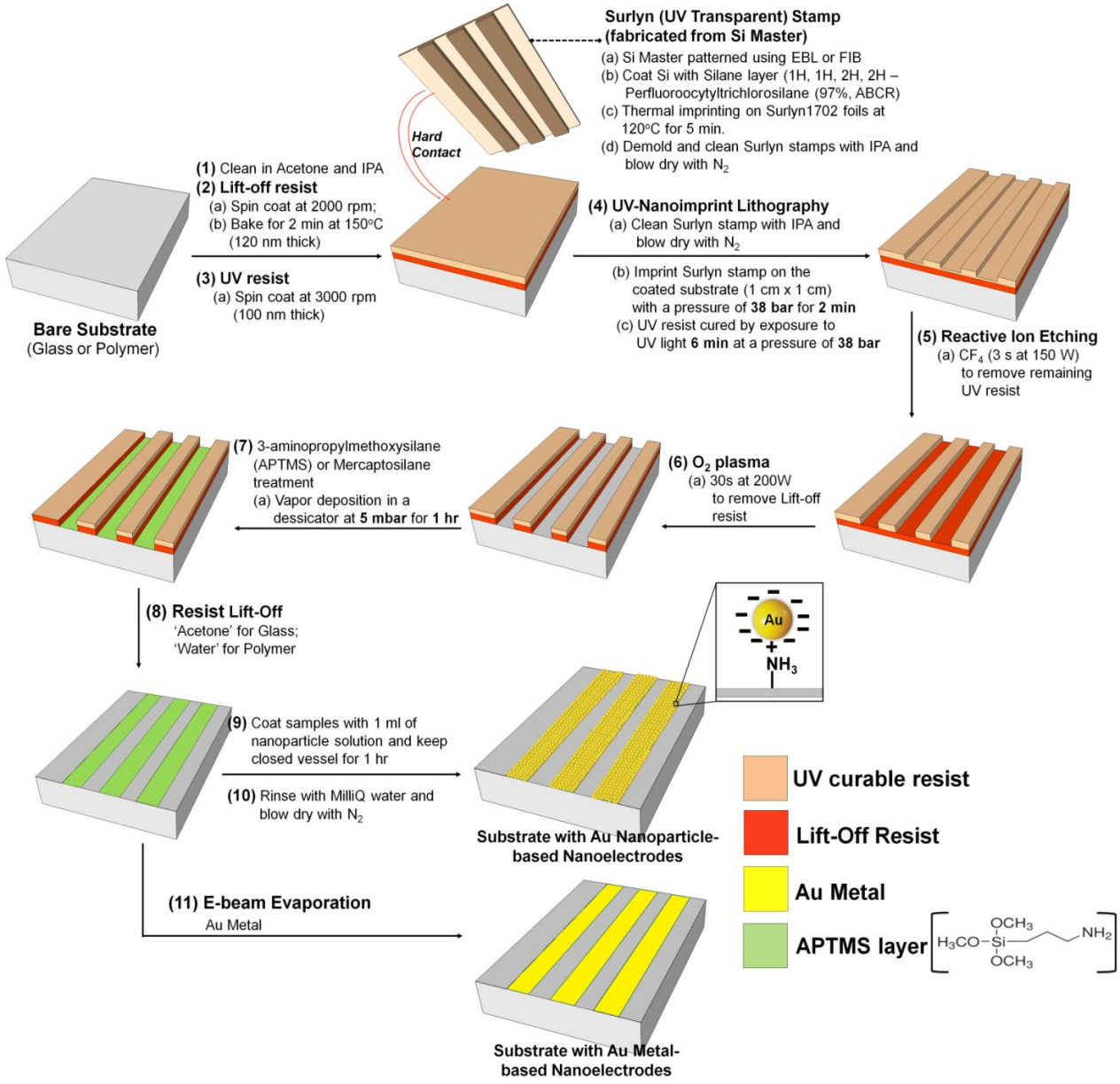

Figure 5.5 Full description of the newly proposed scheme for the fabrication of Au nanoparticle or Au metal based nanoscale electrode in a glass or Polymer substrate

As an alternative to the fabrication scheme described in Chapters 4 for the development of nanoelectrodes in fused silica, we intend to investigate other routes especially for the fabrication of nanoelectrodes in thermoplastic substrates. This proposed fabrication scheme, as depicted in Figure 5.4, involves ~10 steps.

Fabrication will begin by spin coating a lift-off resist (water based for polymer and Acetone based for glass) onto the surface of the cleaned substrate followed by the UV resist. A Surlyn or PDMS stamp fabricated from a Si master (as described in Chapter 2) will be used to create nanotrenches into the substrate via UV-NIL. This will be followed by reactive ion etching to remove the cured UV resist from the trenches and oxygen plasma to remove the lift-off resist. A mercaptosilane layer which will serve as the adhesion layer will be deposited in vapor phase into the trenches. Next, the lift-off resist will be removed using the appropriate solvent (water or acetone) followed by the assembly of AuNPs or electron beam evaporation of Au metal into the trenches.

5.3 Conclusion

In our nanosensor, a nanochannel serves as a flight tube to provide molecular-dependent flight times of single-molecules electrokinetically driven through this tube. The entrance and exit of single molecules from this tube is transduced using single-molecule conductivity measurements from molecules generated enzymatically from a surface immobilized enzyme acting on a target biopolymer.

The sensor will provide the ability to secure data that can provide identification of sequence variations in both DNA and RNA biopolymers and the identification of single proteins using peptide mass fingerprinting. Molecule dependent flight times can be generated either through differences in electrophoretic mobilities and/or solute/wall interactions (CE and CEC). Using polymer modification chemistries, monolayers of different chemical entities can be appended to the walls of the flight tube to generate unique stationary phases to improve identification efficiency by improving electrophoretic resolution.

REFERENCES

Czarnecka, J.; Cieslak, M.; Michal, K. Application of solid phase extraction and high-performance liquid chromatography to qualitative and quantitative analysis of nucleotides and nucleosides in human cerebrospinal fluid. *Journal of Chromatography B* 2005, 822, 85-90.

Dapprich, J. Single-molecule DNA digestion by lambda-exonuclease. *Cytometry* 1999, 36, 163-168.

Davis, L. M., Fairfield, F.R., Hammond, M.L., Harger, C.A., Jett, J.H., Keller, R.A., Hahn, J.H., Krakowski, L.A., Marrone, B., Martin, J.C., Nutter, H.L., Ratliff, R.R., Shera, E.B., Simpson, D.J., Soper, S.A., Wilkerson, C.W. *Rapid DNA Sequencing Based on Single Molecule Detection*; 1992.

Iqbal, S. M.; Akin, D.; Bashir, R. Solid-state nanopore channels with DNA selectivity. *Nat. Nanotechnol.* 2007, 2, 243-248.

Kasianowicz, J. J.; Brandin, E.; Branton, D.; Deamer, D. W. Characterization of individual polynucleotide molecules using a membrane channel. *Proceedings of the National Academy of Sciences* 1996, 93, 13770-13773.

Liang, X. G.; Chou, S. Y. Nanogap detector inside nanofluidic channel for fast real-time label-free DNA analysis. *Nano Letters* 2008, 8, 1472-1476.

Liang, X. G., Chou, S.Y. Nanogap detector inside nanofluidic channel for fast real-time label-free DNA analysis. *Nano Letters* 2008, 8, 1472-1476.

Matsuura, S.; Komatsu, K.; Hirano, K.; Yasuda, H.; Takashima, K.; Katsura, S.; Mizuno, A. Real time observation of a single DNA digestion by lambda exonulease under a fluorescence microscope field. *Nucleic Acids Research* 2001, 29, e79.

McCarley, R. L.; Vaidya, B.; Wei, S. Y.; Smith, A. F.; Patel, A. B.; Feng, J.; Murphy, M. C.; Soper, S. A. Resist-free patterning of surface architectures in polymer-based microanalytical devices. *Journal of the American Chemical Society* 2006, 127, 842-843.

Okagbare, P. I.; Soper, S. A. High throughput single molecule detection for monitoring biochemical reactions. *Analyst* 2009, 134, 97-106.

Rhee, M.; Burns, M. A. Nanopore sequencing technology: research trends and applications. *Trends in Biotechnology* 2006, 24, 580-586.

Sanger, F.; Nicklen, S.; Coulson, A. R. DNA sequencing with chain-terminating inhibitors. *Proceedings of the National Academy of Sciences* 1977, 74, 5463-5467.

Shadpour, H.; Musyimi, H.; Chen, J.; Soper, S. A. Physiochemical properties of various polymer substrates and their effects on microchip electrophoresis performance. *Journal of Chromatography A* 2006, 1111, 238-251.

Storm, A. J.; Chen, J. H.; Ling, X. S.; Zandbergen, H. W.; Dekker, C. Fabrication of solid-state nanopores with single-nanometre precision. *Nat Mater* 2003, 2, 537-540.

Tegenfeldt, J. O.; Cao, H.; Reisner, W. W.; Prinz, C.; Austin, R. H.; Chou, S. Y.; Cox, E. C.; Sturm, J. C. Stretching DNA in nanochannels. *Biophysical Journal* 2004, 86, 596A-596A.

Tegenfeldt, J. O.; Prinz, C.; Cao, H.; Chou, S.; Reisner, W. W.; Riehn, R.; Wang, Y. M.; Cox, E. C.; Sturm, J. C.; Silberzan, P.; Austin, R. H. The dynamics of genomic-length DNA molecules in 100-nm channels. *Proceedings of the National Academy of Sciences of the United States of America* 2004, 101, 10979-10983.

Thamdrup, L. H.; Klukowska, A.; Kristensen, A. Stretching DNA in polymer nanochannels fabricated by thermal imprint in PMMA. *Nanotechnology* 2008, 19, 1-6.

Vogelsang, J.; Kasper, R.; Steinhauer, C.; Person, B.; Heilemann, M.; Sauer, M.; Tinnefeld, P. A Reducing and Oxidizing System Minimizes Photobleaching and Blinking of Fluorescent Dyes. *Angewandte Chemie* 2008, 47, 5465-5469.

Wei, S.; Vaidya, B.; Patel, A. B.; Soper, S. A.; McCarley, R. L. Photochemically Patterned Poly(methyl methacrylate) Surfaces Used in the Fabrication of Microanalytical Devices. *Journal of Physical Chemistry B* 2005, 109, 16988-16996.

Werner, J. H.; Cai, H.; Keller, R. A.; Goodwin, P. M. Exonuclease I hydrolyzes DNA with a distribution of rates. *Biophysical Journal* 2005, 88, 1403-1412.

Zikic, R.; Krstic, P. S.; Zhang, X. G.; Fuentes-Cabrera, M.; Wells, J.; Zhao, X. C. Characterization of the tunneling conductance across DNA bases. *Physical Review E* 2006, 74.